Nitrido-, Oxonitrido-, and Oxonitridocarbidosilicates

for Solid-State Lighting by a

Multiple Cation and Anion Approach

Christian Andreas Maak

aus

Bad Aibling, Deutschland

2019

Erklärung

Diese Dissertation wurde im Sinne von § 7 der Promotionsordnung vom 28. November 2011 von Herrn Prof. Dr. Wolfgang Schnick betreut.

Eidesstattliche Versicherung

Diese Dissertation wurde eigenständig und ohne unerlaubte Hilfe erarbeitet.

München, den 20.05.2019

....

(Christian Andreas Maak)

Dissertation eingereicht am   02.04.2019

1. Gutachter   Prof. Dr. Wolfgang Schnick

2. Gutachter   Prof. Dr. Oliver Oeckler

Mündliche Prüfung am   17.05.2019

Meiner Familie

Danksagung

„ Logik bringt dich von A nach B.

Deine Phantasie bringt dich überall hin "

(Albert Einstein)

Table of Contents

1   Introduction

The continuously growing world population as well as the expanding technologization lead to a massive increase in energy consumption and thus to an increased emission of the greenhouse gas CO_2. At the same time, CO_2 emissions urgently need to be reduced in order to comply with the Paris Agreement, which aims to limit global warming to 1.5 °C on average.[1] Renewable energies as well as the invention and development of sustainable and energy-efficient technologies, e.g. in the sectors automotive and lighting, are therefore of utmost importance. The lighting market has been revolutionized in the last decade by the introduction of white phosphor-converted light-emitting diodes (pcLEDs) to replace conventional incandescent light bulbs and compact fluorescent lamps (CFLs). Although incandescent lamps are still superior in terms of color rendering with a color rendering index (CRI) close to 100 (the maximum value 100 corresponds to daylight or black-body radiation), the EU decided in 2009 to phase-out such lamps due to their poor energy balance.[2,3] Whereas only 5–10% of the consumed energy is irradiated as visible light, 90–95% are wasted through heat production and emission in the infrared spectral range.[4] As a consequence, the aim was to replace incandescent lamps by CFLs, which enable significantly higher energy efficiency. However, CFLs also exhibit some major drawbacks such as poor color rendering (CRI 70–90) and above all the usage of toxic mercury. For these reasons, CFLs have never really been accepted as an alternative to conventional light bulbs. In contrast to incandescent lamps and CFLs, pcLEDs convince with improved lifetime, environmental friendliness, and high efficiency.[5] The U.S. Department of Energy (DOE) forecasted that compared to the year 2013 pcLEDs will reduce the energy consumed by lighting in the US by 15% in 2020 and even 40% in 2030. More optimistic calculations even predicted energy-savings of 60% compared to a no-LED scenario.[6] In order to achieve these goals, some major leaps in the development of pcLEDs still need to be made. These include improvements in packaging and engineering as well as the synthesis and development of novel phosphor materials with superior emission properties. However, applications of pcLEDs are not limited to lighting in general including e.g. residential, street, and city lighting. Further application fields arise such as automotive lighting, backlighting in liquid crystal displays (LCD), or horticultural lighting.[7] For all named application fields novel phosphor materials with specific emission profiles are required to improve the state-of-the-art pcLEDs in terms of lighting quality and energy-consumption. Therefore, basic research with regard to luminescent materials (phosphors) is in full swing.

The basis for the breakthrough of pcLEDs was the access to highly efficient UV to blue-emitting $Ga_{1-x}In_xN$ LEDs, mainly achieved by Nakamura, Akasaki, and Amano. The 2014 Nobel Prize in Physics awarded to these three researchers demonstrates the great significance of this invention.[8] The UV to blue light emitted by $Ga_{1-x}In_xN$ LEDs is down-converted by phosphors, which then emit radiation in the blue to red part of the visible spectrum. White light can be produced by additive color-mixing of different phosphors. Figure 1 illustrates three possible approaches to white pcLEDs. In a single-phosphor approach (1pcLED), a yellow phosphor (e.g. $(Y,Gd,Lu)_3Al_5O_{12}:Ce^{3+}$, YAG:Ce)[9,10] with broad emission band is excited by a blue $Ga_{1-x}In_xN$ LED. Due to missing red components, such 1pcLEDs exhibit poor color rendition and are not suitable for residential lighting. High CRI white pcLEDs are obtained by adding a second phosphor (2pcLED) with emission in the red spectral range.[11] The third approach is called full-conversion. Thereby, red, green and blue phosphors (RGB pcLED) are excited by a near-UV primary LED. If the blue phosphor exhibits a very small Stokes shift and a narrow emission band, these devices may exhibit improved color rendering and color point stability compared to 2pcLEDs.[12]
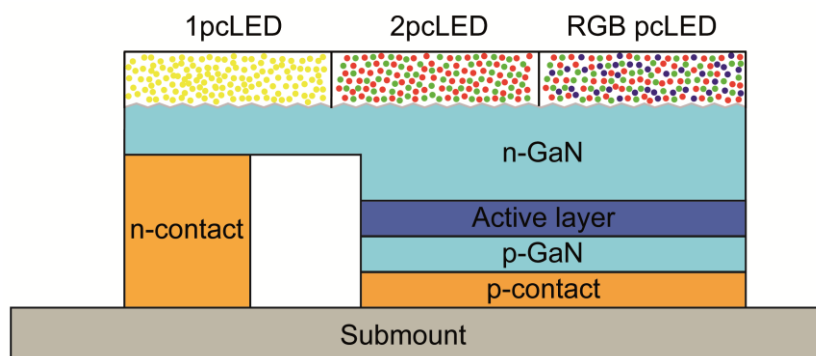
Figure 1. Schematic build-up of a pcLED. A thin-film, flip-chip LED emitting in the blue or near-UV excites yellow (1pcLED), red and green (2pcLED), or red, green and blue phosphors (RGB). Additive color-mixing results in the emission of white light.[7]

The luminescence of phosphors originates from electronic transitions, i.e. electronic excitation and relaxation in so called activator ions (e.g. Eu^{2+}, Yb^{2+}, Ce^{3+}, Eu^{3+}, $Mn^{2+/4+}$), which are incorporated into the crystal structures of the host materials. The most common activators used in pcLEDs are Eu^{2+} and Ce^{3+}.[13] The UV to blue photons of the pump LED excite electrons of these rare-earth (*RE*) atoms from the occupied 4*f* orbitals into unoccupied 5*d* orbitals. Due to the strong interaction of the outer-lying 5*d* orbitals with ligands, the energetic position of the excited states with respect to the ground state level strongly depends on the ligand field surrounding the activator ions. The energetic position

of the 5*d* orbitals is influenced through two factors, the interelectron repulsion and the crystal field splitting (Figure 2). The interelectron repulsion of the *d*-orbitals is always lowered upon placing the free ions in a ligand field trough two processes. Firstly, the effective charges of the metal ions are lowered and thus the *d*-orbitals expand (nephelauxetic effect). Secondly, *d*-electrons can be delocalized into ligand orbitals. Both effects lead to a lowering of the interelectronic repulsion and are related to covalency. Hence, the higher the covalence of the activator-ligand bonds (e.g. S > N > O), the lower the energy of the excited state. The crystal field splitting describes the suspension of the degeneracy of free-ion terms in a ligand field. The form and magnitude of the energetic splitting of the *d*-electron energies for each term is a complex function dependent on the coordination geometry and strength of activator–ligand interactions.[14] Summarizing, the described effects determine the energetic position of the excited states of a phosphor, as illustrated in Figure 2.
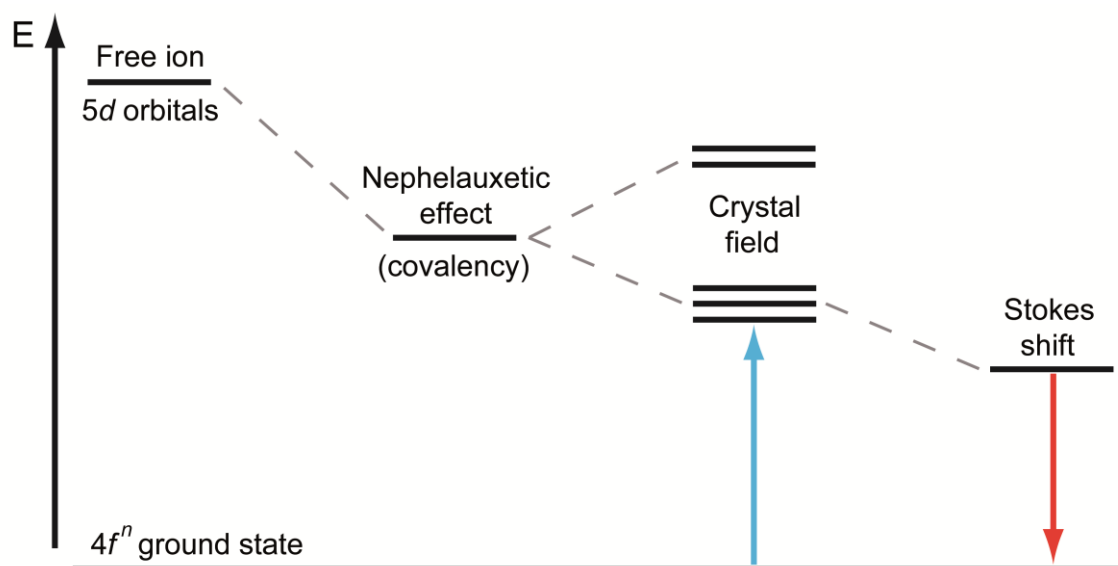
Figure 2. Stylized energy diagram showing major impacts on the excitation (blue arrow) and emission (red arrow) energy of Eu^{2+} and Ce^{3+}.[15]

After the excitation, nonradiative relaxation of the excited electrons to the vibrational ground state of the excited state occurs. Subsequently, the electrons relax to the electronic ground state, whereby the energy difference is emitted as photons. Due to the nonradiative relaxation process in the excited state, the incident radiation of higher energy is phosphor-converted through the phosphor and photons with lower energy are emitted. The energy difference between the maxima of the excitation and emission spectra is called Stokes shift.[16,17] Beside the energetic position of the emission bands, the Stokes

shift correlates with the width of the excitation and emission bands (Figure 3). Furthermore, a large Stokes shift has a negative effect on the thermal quenching behavior and consequently on the efficiency of phosphors due to increased probability for nonradiative decay (Figure 3a, NR). The Stokes shift can be quantified by equation 1.[18]

$$E_{Stokes} = 2S \cdot \hbar\omega \qquad (1)$$

S is called the Huang-Rhys parameter, which is a measure for the magnitude of electron-phonon coupling. Accordingly, S strongly depends on the rigidity of the host structure, whereby high rigidity corresponds to small values of S.[17] ω corresponds to phonon frequencies and is associated to the atomic weight of the atoms in a host material. Similar to the energy states of a harmonic oscillator, ω is typically smaller for larger molar masses.
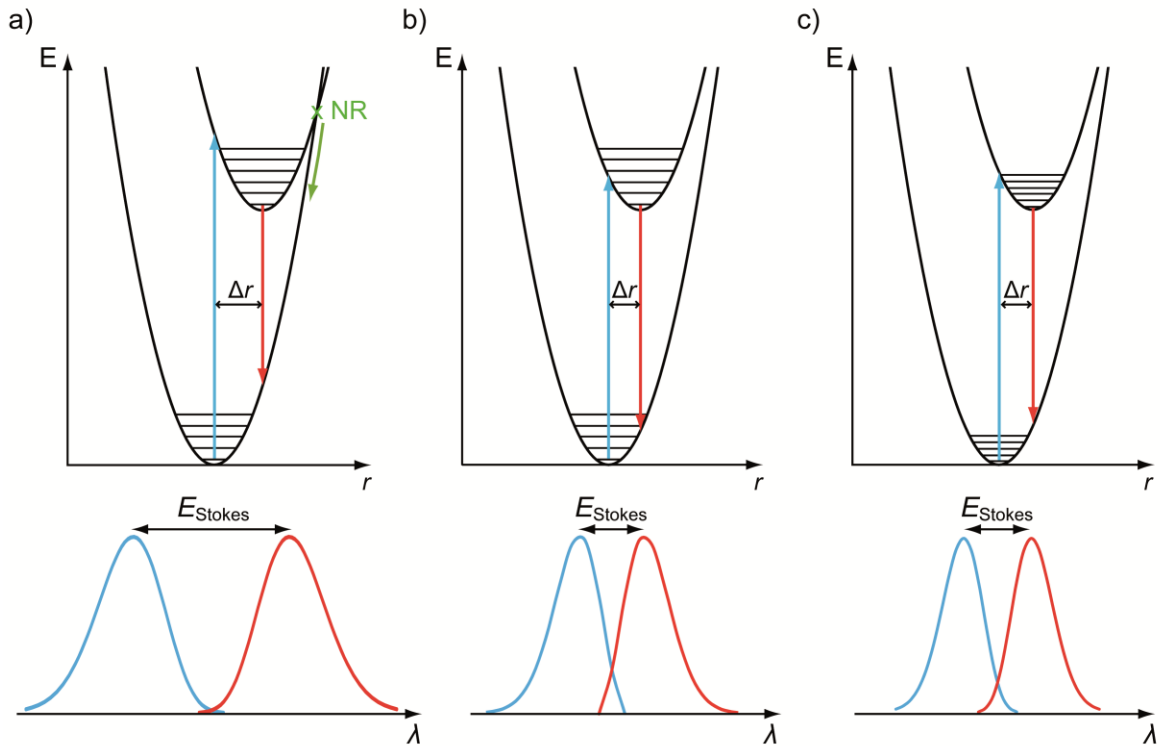
Figure 3. Configurational coordinate diagrams (top) and corresponding excitation and emission spectra (bottom), excitation blue and emission red, respectively. Δr gives the parabola offset between the ground states and the excited states. (a) Large S and ω. NR indicates nonradiative decay from the excited state to the ground state. (b) Reduced S. (c) Reduced ω.[17–19]

The configurational coordinate diagrams in Figure 3 illustrate the dependence of the Stokes shift as well as the shapes of excitation and emission bands from S and ω.[19] In

general, the foregoing considerations demonstrate that Eu^{2+} and Ce^{3+} emissions can be tuned in a wide range with regard to emission energy and shape by varying structural parameters, e.g. structure type, covalency of activator–ligand bonds, or atomic weight of surrounding atoms.

In recent years, basic research on Eu^{2+} doped phosphors has primarily focused on narrow-band emitting materials. Such phosphors have the potential to improve white pcLEDs used for residential lighting and LCD displays, but also amber pcLEDs, which are used, for example, as turn signals or in outdoor lighting.[20] Narrow-band red-emitting materials allow for fabrication of white pcLEDs with high color rendering and, simultaneously, high efficiency due to decreased losses in the infrared spectral range in contrast to pcLEDs with broad-emitting red phosphors.[21] Narrow-band blue-emitting phosphors are the basis for efficient white RGB pcLEDs that can exceed 2pcLEDs in terms of color rendering and color point stability.[22] Narrow-band red- and blue-emitting phosphors are also relevant for the improvement of LCD displays, in which white pcLEDs are used as a backlighting component.[23] In this context, however, narrow-band green phosphors play a more crucial role due to the high wavelength-sensitivity of the human eye in the green spectral range.[24,25] By using a very narrow-band green-emitting phosphor the color gamut in the Comission Internationale de l'Éclairage (CIE) diagram can be increased. This enables to produce a large number of different green color shades and consequently to improve the quality of LCD displays. For the fabrication of next-generation amber pcLEDs with high color purity and luminous efficacy (LE), narrow-band yellow-orange phosphors are required. The increase in LE (SI unit: lumen/Watt) would result from the wavelength-dependent sensitivity of the human eye. Currently used amber-emitting $(Ba,Sr)Si_5N_8:Eu^{2+}$ suffers from its broad emission band and hence losses in LE due to the low eye sensitivity in the red spectral range.[26] However, there are hardly any other suitable yellow-orange luminescent materials so far and especially phosphors with narrow-band emission have not yet become accessible at all.

In the case of Ce^{3+} as an activator, basic research is going into a completely different direction due to the intrinsically broadened Ce^{3+} luminescence. This broadening originates from the splitting of the Ce^{3+} ground state into two energy levels ($^2F_{5/2}$, $^2F_{7/2}$), resulting in two emission bands with an energy difference of about 2000 cm^{-1}.[27] Due to their broad emission bands, Ce^{3+} doped phosphors with yellow luminescence allow for fabrication of white LEDs with a single phosphor approach (1pcLED). This approach is cheaper than 2pcLEDs and RGB LEDs, as only one phosphor material has to be applied to the blue primary LED chip. However, the emission bands of currently used phosphors YAG:Ce do not cover the red spectral range, resulting in cool-white 1pcLEDs with poor color rendition.

Consequently, Ce^{3+} doped phosphors with red-shifted emission compared to YAG:Ce are desired to obtain 1pcLEDs with acceptable color-rendition, for example for application in outdoor lighting.[28] If the phosphor converted into infrared light, further applications, e.g. in horticultural lighting, would be conceivable for Ce^{3+} doped luminescent materials.

In the search for suitable host materials to realize the desired Eu^{2+}/Ce^{3+} luminescence properties, the compound class of (oxo)nitridosilicates has demonstrated to be promising. The fundamental structural building units of these materials are $Si(O/N)_4$ tetrahedra. In contrast to oxosilicates, in which SiO_4 tetrahedra solely exhibit oxygen in terminal ($O^{[1]}$) or in twofold bridging positions ($O^{[2]}$), the partial or complete replacement of oxygen by nitrogen results in significantly increased structural possibilities through additional structural motifs.[29] Nitrogen is able to connect three ($N^{[3]}$) and even four ($N^{[4]}$) tetrahedral centers. The first reported compound with ammonia-like $N^{[4]}$ atoms in so called star-shaped $[N^{[4]}(SiN_3)_4]$ units is $BaYbSi_4N_7$.[30] Furthermore, edge-sharing of SiN_4 tetrahedra can appear in nitridosilicates, e.g. observed in $Ba_5Si_2N_6$.[31] The replacement of O by N atoms can also result in a significantly increased degree of condensation, which is defined as the atomic ratio of tetrahedral centers to ligands, i.e. $\kappa = n(Si):n(O,N)$. The lower limit $\kappa = 1/4$ is observed for structures with noncondensed $Si(O/N)_4$ tetrahedra. The upper limit for oxosilicates of $\kappa = 1/2$ is observed for the binary oxide SiO_2.[32] In contrast, the degree of condensation in nitridosilicates can reach values up to $\kappa = 3/4$, as is the case for Si_3N_4.[33] The nitridosilicate with the highest degree of condensation so far is $BaSi_7N_{10}$ with $\kappa = 0.7$.[34] The high rigidity of highly condensed ($\kappa \geq 1/2$), covalent networks can contribute to a small Stokes shift and hence narrow and efficient luminescence as illustrated in Figure 3.[24,35] Furthermore, the smaller electronegativity of nitrogen leads to an increased covalency of activator–ligand interactions in contrast to oxygen,[36] which in turn results in a decrease of the energy difference between excited state and ground state (nephelauxetic effect, Figure 2). Accordingly, the spectral range accessible with the dopants Eu^{2+}/Ce^{3+} is significantly red-shifted by (oxo)nitridosilicates. In addition, (oxo)nitridosilicates often benefit from high chemical inertness and large band gaps, which are key prerequisites for state-of-the-art luminescent materials.[37] Consequently, there are several industrially relevant (oxo)nitridosilicates such as narrow-band cyan-emitting $BaSi_2O_2N_2$:Eu^{2+}, green-emitting $SrSi_2O_2N_2$:Eu^{2+}, $La_3Si_6N_{11}$:Ce^{3+} with yellow emission, or the red phosphors $(Ba,Sr)_2Si_5N_8$:Eu^{2+} and $(Sr,Ca)AlSiN_3$:Eu^{2+}.[38–48]

Synthesis and investigation of new materials with specific luminescence properties is highly important to address the current challenges in solid-state lighting. Novel compounds can be obtained, for example, by extending the compositional range and

examining complex systems with multiple cations and anions. Providing cations and anions with different valences during syntheses enables unprecedented crystal structures, which are inaccessible with only one kind of cation and anion. Over the last years, a couple of new nitridosilicates with intriguing crystal structures have been reported when trivalent *RE* atoms and bivalent alkaline earth metal (*AE*) atoms were simultaneously incorporated as counter ions. Examples are the already mentioned $BaYbSi_4N_7$ and $Ca_3RE_3[Si_9N_{17}]$ (*RE* = Sm,Yb), both containing star-shaped $[N^{[4]}(SiN_3)_4]$ units and additional $[Si_5N_{16}]$ supertetrahedra in the case of the latter.[30,49] By extending this concept of multiple cations to multiple anions, the research field of nitridosilicates will be greatly extended once again. With a raising number of components the number of possible systems and hence the number of new materials can be increased as illustrated by *Jansen*.[50] A promising example in the context of phosphor research is the oxonitridosilicate $La_3BaSi_5N_9O_2$:Ce^{3+}, which exhibits broadened and red-shifted green-yellow emission compared to YAG:Ce and is discussed as phosphor for 1pcLEDs with improved color rendition.[51] However, the concept of multiple anions is not limited to the expansion from nitridosilicates to oxonitridosilicates. The incorporation of carbon into anionic silicate networks, as it is observed in the only known nitridocarbidosilicates $RE_2[Si_4N_6C]$ (*RE* = Ho, Tb, La, Gd, Lu, Y, Sc),[52–56] as well as the incorporation of halide anions as counter ions also appear auspicious.[57,58] Due to the differing characteristics of the incorporated cations and anions regarding atomic weight, ionic radii, charge, electronegativity, and polarizability numerous adjusting screws are obtained to tailor the optical properties of such phosphors according to the respective demands.[59] Consequently, the multiple cation/anion approach can make a huge contribution to mastering the current challenges in solid-state lighting. While the concept appears simple, only a small number of nitridosilicate based compounds with multiple cations and anions have been synthesized so far. Up to now, mostly ternary and quaternary compounds have been investigated as these are usually simpler, for example with regard to synthesis optimization. However, as combinatorial screening algorithms and high-throughput exploration methods become more and more successful in taking known structure types and optimizing synthesis and elemental compositions with regard to desired luminescence properties,[50,60,61] it is now becoming more and more feasible to explore complex multinary systems. The aim of this work is to put a focus on nitridosilicate based materials with multiple cations and anions and to find new systems and structure types that are promising for applications in the lighting industry.

This thesis focuses on the explorative synthesis and characterization of novel Eu^{2+} and Ce^{3+} doped phosphors through incorporation of multiple cations and anions with different valences. Various synthesis routes such as metathesis and carbothermal reactions were utilized to synthesize the presented (oxo)nitrido(carbido)silicate compounds in high-temperature reactions. The complex crystal structures of the multinary compounds were elucidated using state-of-the-art methods such as laboratory X-ray diffraction, transmission electron microscopy, and synchrotron microdiffraction. The optical properties of the phosphors were investigated in detail, especially with regard to luminescence characteristics and possible applications in solid-state lighting.

References

[1]   https://unfccc.int/process-and-meetings/the-paris-agreement/the-paris-agreement, visited on October 10th, 2018.

[2]   CIE. Method of Measuring and Specifying Colour Rendering Properties of Light Sources (CIE 13.3, 1995). Vienna: Commission Internationale de l'Éclairage, 1995.

[3]   http://europa.eu/rapid/press-release_MEMO-09-368_en.htm, visited on November 19th, 2018.

[4]   Feldmann, C. Technical Revolution Underway: Nitride-based Phosphors for LED Application. *Z. Anorg. Allg. Chem.* **2012**, *638*, 2169–2171.

[5]   McKittrick, J.; Shea-Rohwer, L. E. Review: Down Conversion Materials for Solid-State Lighting. *J. Am. Ceram. Soc.* **2014**, *97*, 1327–1352.

[6]   https://www.energy.gov/eere/ssl/led-lighting-forecast, visited on October 10th, 2018.

[7]   Pust, P.; Schmidt, P. J.; Schnick, W. A revolution in lighting. *Nat. Mater.* **2015**, *14*, 454–458.

[8]   https://www.nobelprize.org/nobel_prizes/physics/laureates/2014/, visited on November 19th, 2018.

[9]   Blasse, G.; Bril, A. A new phosphor for flying-spot cathode-ray tubes for color television: yellow-emitting $Y_3Al_5O_{12}$-Ce^{3+}. *Appl. Phys. Lett.* **1967**, *11*, 53–55.

[10] Xia, Z.; Meijerink, A. Ce^{3+}-Doped garnet phosphors: composition modification, luminescence properties and applications. *Chem. Soc. Rev.* **2017**, *46*, 275–299.

[11] Leaño Jr., J. L.; Fang, M.-H.; Liu, R.-S. Review—Narrow-Band Emission of Nitride Phosphors for Light-Emitting Diodes: Perspectives and Opportunities. *ECS J. Solid State Sci. Technol.* **2018**, *7*, R3111–R3133.

[12] Piquette, A.; Bergbauer, W.; Galler, B.; Mishra, K. C. On Choosing Phosphors for Near-UV and Blue LEDs for White Light. *ECS J. Solid State Sci. Technol.* **2016**, *5*, R3146–R3159.

[13] Wang, L.; Xie, R.-J.; Suehiro, T.; Takeda, T.; Hirosaki, N. Down-Conversion Nitride Materials for Solid State Lighting: Recent Advances and Perspectives. *Chem. Rev.* **2018**, *118*, 1951–2009.

[14] Figgis, B. N.; Hitchman, M. A. *Ligand Field Theory and Its Applications*; Wiley-VCH, New York, 2000.

[15] Schmiechen, S.; Pust, P.; Schmidt, P. J.; Schnick, W. Weißes Licht aus Nitriden. *Nachr. Chem.* **2014**, *62*, 847–851.

[16] Stokes, G. G. On the change of refrangibility of light. *Phil. Trans. R. Soc. Lond.* **1852**, *142*, 463–562.

[17]   Blasse, G.; Bril, A. Characteristic luminescence. *Philips Tech. Rev.* **1970**, *31*, 304–332.

[18]   Blasse, G. Luminescence of inorganic solids: from isolated centres to concentrated systems. *Prog. Solid State Chem.* **1988**, *18*, 79–171.

[19]   Shionoya, S.; Yen, W. M. *Phosphor Handbook*; CRC Press, New York, 1998.

[20]   Fang, M.-H.; Leaño Jr., J. L.; Liu, R.-S. Control of Narrow-Band Emission in Phosphor Materials for Application in Light-Emitting Diodes. *ACS Energy Lett.* **2018**, *3*, 2573–2586.

[21]   Pust, P.; Weiler, V.; Hecht, C.; Tücks, A.; Wochnik, A. S.; Henß, A.-K.; Wiechert, D.; Scheu, C.; Schmidt, P. J.; Schnick, W. Narrow-band red-emitting Sr[LiAl$_3$N$_4$]:Eu^{2+} as a next-generation LED-phosphor material. *Nat. Mater.* **2014**, *13*, 891–896.

[22]   Strobel, P.; Maak, C.; Weiler, V.; Schmidt, P. J.; Schnick, W. Ultra-Narrow-Band Blue-Emitting Oxoberyllates AELi$_2$[Be$_4$O$_6$]:Eu^{2+} (AE = Sr,Ba) Paving the Way to Efficient RGB pc-LEDs. *Angew. Chem., Int. Ed.* **2018**, *57*, 8739–8743; *Angew. Chem.* **2018**, *130*, 8875–8879.

[23]   Liao, H.; Zhao, M.; Molokeev, M. S.; Liu, Q.; Xia, Z. Learning from a Mineral Structure toward an Ultra-Narrow-Band Blue-Emitting Silicate Phosphor RbNa$_3$(Li$_3$SiO$_4$)$_4$:Eu^{2+}. *Angew. Chem., Int. Ed.* **2018**, *57*, 11728–11731; *Angew. Chem.* **2018**, *130*, 11902–11905.

[24]   Strobel, P.; Schmiechen, S.; Siegert, M.; Tücks, A.; Schmidt, P. J.; Schnick, W. Narrow-Band Green Emitting Nitridolithoalumosilicate Ba[Li$_2$(Al$_2$Si$_2$)N$_6$]:Eu^{2+} with Framework Topology *whj* for LED/LCD-Backlighting Applications. *Chem. Mater.* **2015**, *27*, 6109–6115.

[25]   Zhao, M.; Liao, H.; Ning, L.; Zhang, Q.; Liu, Q.; Xia, Z. Next-Generation Narrow-Band Green-Emitting RbLi(Li$_3$SiO$_4$)$_2$:Eu^{2+} Phosphor for Backlight Display Application. *Adv. Mater.* **2018**, *30*, 1802489.

[26]   Mueller-Mach, R.; Mueller, G.; Krames, M. R.; Höppe, H. A.; Stadler, F.; Schnick, W.; Juestel, T.; Schmidt, P. Highly efficient all-nitride phosphor-converted white light emitting diode. *Phys. Status Solidi A* **2005**, *202*, 1727–1732.

[27]   Blasse, G.; Grabmaier, B. C. *Luminescent Materials*; Springer, Berlin, 1994.

[28]   Chen, Z.; Zhang, Q.; Li, Y.; Wang, H.; Xie, R.-J. A promising orange-yellow-emitting phosphor for high power warm-light white LEDs: Pure-phase synthesis and photoluminescence properties. *J. Alloys Compd.* **2017**, *715*, 184–191.

[29]   Schnick, W.; Huppertz, H. Nitridosilicates – A Significant Extension of Silicate Chemistry. *Chem. - Eur. J.* **1997**, *3*, 679–683.

[30]   Huppertz, H.; Schnick, W. BaYbSi$_4$N$_7$ – Unexpected Structural Possibilities in Nitridosilicates. *Angew. Chem., Int. Ed. Engl.* **1996**, *35*, 1983–1984; BaYbSi$_4$N$_7$ – überraschende strukturelle Möglichkeiten in Nitridosilicaten. *Angew. Chem.* **1996**, *108*, 2115–2116.

[31]   Yamane, H.; DiSalvo F. Preparation and crystal structure of a new barium silicon nitride, Ba$_5$Si$_2$N$_6$. *J. Alloys Compd.* **1996**, *240*, 33–36.

[32]   Jay, A. H. The Thermal Expansion of Quartz by X-ray Measurements. *Proc. Royal Soc. A* **1933**, *142*, 237–247.

[33]   Hardie, D.; Jack, K. H. Crystal Structures of Silicon Nitride. *Nature* **1957**, *180*, 332–333.

[34]   Huppertz, H.; Schnick, W. Edge-sharing SiN$_4$ Tetrahedra in the Highly Condensed Nitridosilicate BaSi$_7$N$_{10}$. *Chem. - Eur. J.* **1997**, *3*, 249–252.

[35]   Wagatha, P.; Pust, P.; Weiler, V.; Wochnik, A. S.; Schmidt, P. J.; Scheu, C.; Schnick, W. Ca$_{18.75}$Li$_{10.5}$[Al$_{39}$N$_{55}$]:Eu^{2+} – Supertetrahedron Phosphor for Solid-State Lighting. *Chem. Mater.* **2016**, *28*, 1220–1226.

[36]   Kloß, S. D.; Janka, O.; Block, T.; Pöttgen, R.; Glaum, R.; Schnick, W. Open-Shell 3d Transition Metal Nitridophosphates M^{II}P$_8$N$_{14}$ (M^{II} = Fe, Co, Ni) by High-Pressure Metathesis. *Angew. Chem., Int. Ed.* **2019**, *58*, 4685–4689; *Angew. Chem.* **2019**, *131*, 4733–4737.

[37]   Zeuner, M.; Pagano, S.; Schnick, W. Nitridosilicates and Oxonitridosilicates: From Ceramic Materials to Structural and Functional Diversity. *Angew. Chem., Int. Ed.* **2011**, *50*, 7754–7775; Nitridosilicate und Oxonitridosilicate: von keramischen Materialien zu struktureller und funktioneller Diversität. *Angew. Chem.* **2011**, *123*, 7898–7920.

[38]   Li, Y. Q.; Delsing, A. C. A.; de With, G.; Hintzen, H. T. Luminescence Properties of Eu^{2+}-Activated Alkaline-Earth Silicon-Oxynitride MSi$_2$O$_{2-\delta}$N$_{2+2/3\delta}$ (M = Ca, Sr, Ba): A Promising Class of Novel LED Conversion Phosphors. *Chem. Mater.* **2005**, *17*, 3242–3248.

[39]   Kechele, J. A.; Oeckler, O.; Stadler, F.; Schnick, W. Structure elucidation of BaSi$_2$O$_2$N$_2$ – A host lattice for rare-earth doped luminescent materials in phosphor-converted (pc)-LEDs. *Solid State Sci.* **2009**, *11*, 537–543.

[40]   Oeckler, O.; Stadler, F.; Rosenthal, T.; Schnick, W. Real structure of SrSi$_2$O$_2$N$_2$. *Solid State Sci.* **2007**, *9*, 205–212.

[41]   Seibald, M.; Rosenthal, T.; Oeckler, O.; Maak, C.; Tücks, A.; Schmidt, P. J.; Wiechert, D.; Schnick, W. New Polymorph of the Highly Efficient LED-Phosphor

SrSi$_2$O$_2$N$_2$:Eu^{2+} – Polytypism of a Layered Oxonitridosilicate. *Chem. Mater.* **2013**, *25*, 1852–1857.

[42] Bachmann, V.; Ronda, C.; Oeckler, O.; Schnick, W.; Meijerink, A. Color Point Tuning for (Sr,Ca,Ba)Si$_2$O$_2$N$_2$:Eu^{2+} for White Light LEDs. *Chem. Mater.* **2009**, *21*, 316–325.

[43] Woike, M.; Jeitschko, W. Preparation and Crystal Structure of the Nitridosilicates Ln$_3$Si$_6$N$_{11}$ (Ln = La, Ce, Pr, Nd, Sm) and LnSi$_3$N$_5$ (Ln = Ce, Pr, Nd). *Inorg. Chem.* **1995**, *34*, 5105–5108.

[44] Kijima, N.; Seto, T.; Hirosaki, N. A New Yellow Phosphor La$_3$Si$_6$N$_{11}$:Ce^{3+} for White LEDs. *ECS Trans.* **2009**, *25(9)*, 247–252.

[45] Schlieper, T.; Milius, W.; Schnick, W. Nitrido-silicate. II. Hochtemperatur-Synthesen und Kristallstrukturen von Sr$_2$Si$_5$N$_8$ und Ba$_2$Si$_5$N$_8$. *Z. Anorg. Allg. Chem.* **1995**, *621*, 1380–1384.

[46] Höppe, H. A.; Lutz, H.; Morys, P.; Schnick, W.; Seilmeier, A. Luminescence in Eu^{2+}-doped Ba$_2$Si$_5$N$_8$: fluorescence, thermoluminescence, and upconversion. *J. Phys. Chem. Solids* **2000**, *61*, 2001–2006.

[47] Uheda, K.; Hirosaki, N.; Yamamoto, Y.; Naito, A.; Nakajima, T.; Yamamoto, H. Luminescence Properties of a Red Phosphor, CaAlSiN$_3$:Eu^{2+}, for White Light-Emitting Diodes. *Electrochem. Solid-State Lett.* **2006**, *9*, H22–H25.

[48] Watanabe, H.; Kijima, N. Crystal structure and luminescence properties of Sr$_x$Ca$_{1-x}$AlSiN$_3$:Eu^{2+} mixed nitride phosphors. *J. Alloys Compd.* **2009**, *475*, 434–439.

[49] Huppertz, H.; Oeckler, O.; Lieb, A.; Glaum, R.; Johrendt, D.; Tegel, M.; Kaindl, R.; Schnick, W. Ca$_3$Sm$_3$[Si$_9$N$_{17}$] and Ca$_3$Yb$_3$[Si$_9$N$_{17}$] Nitridosilicates with Interpenetrating Nets that Consist of Star-Shaped [N$^{[4]}$(SiN$_3$)$_4$] Units and [Si$_5$N$_{16}$] Supertetrahedra. *Chem. - Eur. J.* **2012**, *18*, 10857–10864.

[50] Jansen, M. A Concept for Synthesis Planning in Solid-State Chemistry. *Angew. Chem., Int. Ed.* **2002**, *41*, 3746–3766; Ein Konzept zur Syntheseplanung in der Festkörperchemie. *Angew. Chem.* **2002**, *114*, 3896–3917.

[51] Durach, D.; Neudert, L.; Schmidt, P. J.; Oeckler, O.; Schnick, W. La$_3$BaSi$_5$N$_9$O$_2$:Ce^{3+} – A Yellow Phosphor with an Unprecedented Tetrahedra Network Structure Investigated by Combination of Electron Microscopy and Synchrotron X-ray Diffraction. *Chem. Mater.* **2015**, *27*, 4832–4838.

[52] Höppe, H. A.; Kotzyba, G.; Pöttgen, R.; Schnick, W. High-temperature synthesis, crystal structure, optical properties, and magnetism of the carbidonitridosilicates Ho$_2$[Si$_4$N$_6$C] and Tb$_2$[Si$_4$N$_6$C]. *J. Mater. Chem.* **2001**, *11*, 3300–3306.

[53]   Zhang, H.; Horikawa, T.; Machida, K.-i. Preparation, Structure, and Luminescence Properties of $Y_2Si_4N_6C:Ce^{3+}$ and $Y_2Si_4N_6C:Tb^{3+}$. *J. Electrochem. Soc.* **2006**, *153*, H151–H154.

[54]   Yan, C.; Liu, Z.; Zhuang, W.; Liu, R.; Xing, X.; Liu, Y.; Chen, G.; Li, Y.; Ma, X. $YScSi_4N_6C:Ce^{3+}$ – A Broad Cyan-Emitting Phosphor To Weaken the Cyan Cavity in Full-Spectrum White Light-Emitting Diodes. *Inorg. Chem.* **2017**, *56*, 11087–11095.

[55]   Liddell, K.; Thompson, D. P.; Bräuniger T.; Harris, R. K. $M_2(Si,Al)_4(N,C)_7$ (M = La,Y,Ca) carbonitrides: I. Synthesis and structural characterisation by XRD and NMR. *J. Eur. Ceram. Soc.* **2005**, *25*, 37–47.

[56]   Duan, C.; Zhang, Z.; Rösler, S.; Rösler, S.; Delsing, A.; Zhao, J.; Hintzen, H. T. Preparation, Characterization, and Photoluminescence Properties of Tb^{3+}-, Ce^{3+}-, and Ce^{3+}/Tb^{3+}-Activated $RE_2Si_4N_6C$ (RE = Lu, Y, and Gd) Phosphors. *Chem. Mater.* **2011**, *23*, 1851–1861.

[57]   Marchuk, A.; Schnick, W. $Ba_3P_5N_{10}Br:Eu^{2+}$: A Natural-White-Light Single Emitter with a Zeolite Structure Type. *Angew. Chem., Int. Ed.* **2015**, *54*, 2383–2387; *Angew. Chem.* **2015**, *127*, 2413–2417.

[58]   Marchuk, A.; Wendl, S.; Imamovic, N.; Tambornino, F.; Wiechert, D.; Schmidt, P. J.; Schnick, W. Nontypical Luminescence Properties and Structural Relation of $Ba_3P_5N_{10}X:Eu^{2+}$ (X = Cl, I): Nitridophosphate Halides with Zeolite-like Structure. *Chem. Mater.* **2015**, *27*, 6432–6441.

[59]   Kageyama, H.; Hayashi, K.; Maeda, K.; Attfield, J. P.; Hiroi, Z.; Rondinelli, J. M.; Poeppelmeier, K. R. Expanding frontiers in materials chemistry and physics with multiple anions. *Nat. Commun.* **2018**, *9*, 772.

[60]   Park, W. B.; Son, K. H.; Singh, S. P.; Sohn, K.-S. Solid-State Combinatorial Screening of $ARSi_4N_7:Eu^{2+}$ (A = Sr, Ba, Ca; R = Y, La, Lu) Phosphors. *ACS Comb. Sci.* **2012**, *14*, 537–544.

[61]   Park, W. B.; Singh, S. P.; Kim, M.; Sohn, K.-S. Combinatorial Screening of Luminescent and Structural Properties in a Ce^{3+}-Doped Ln-Al-Si-O-N (Ln = Y, La, Gd, Lu) System: The Discovery of a Novel $Gd_3Al_{3+x}Si_{3-x}O_{12+x}N_{2-x}:Ce^{3+}$ Phosphor. *Inorg. Chem.* **2015**, *54*, 1829–1840.

2   Nitridolithosilicates Li$_{38.7}$*RE*$_{3.3}$*AE*$_{5.7}$[Li$_2$Si$_{30}$N$_{59}$]O$_2$F as Promising Host Materials for Ce^{3+} Doping

2.1   Unprecedented Deep-Red Ce^{3+} Luminescence of the Nitrido-lithosilicates Li$_{38.7}$*RE*$_{3.3}$Ca$_{5.7}$[Li$_2$Si$_{30}$N$_{59}$]O$_2$F (*RE* = La, Ce, Y)
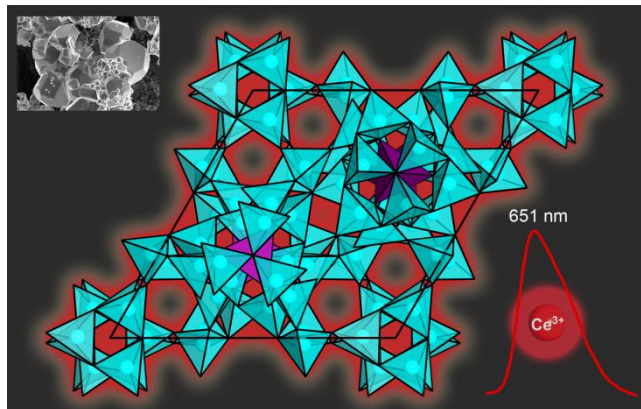
Abstract. Ce^{3+} doped solids find broad application, e.g. in phosphor converted light emitting diodes, utilizing the usually broad blue to yellow-orange emission of the respective phosphors. The red to infrared spectral range was not yet accessible with the activator Ce^{3+}, even in nitride host materials. Here, we report on the nitridolithosilicates Li$_{38.7}$*RE*$_{3.3}$Ca$_{5.7}$[Li$_2$Si$_{30}$N$_{59}$]O$_2$F (*RE* = La, Ce, Y) with unique, red-shifted Ce^{3+} luminescence. The materials were synthesized by solid-state metathesis reactions in tantalum ampules. The isotypic crystal structures exhibit a highly condensed three-dimensional network made up of SiN$_4$ and LiN$_4$ tetrahedra. Crystal structures were refined from single-crystal and powder X-ray diffraction data. The results are supported by

energy-dispersive X-ray spectroscopy as well as charge distribution, lattice energy, and bond valence sum calculations. Optical band gaps of ≈ 4 eV were determined from diffuse reflectance UV/Vis data using Tauc plots. The nitridolithosilicates are highly excitable from the UV to the green-yellow spectral range with a preferred excitation wavelength of λ_{exc} ≈ 540 nm. The emission spectra peak is in the deep-red with λ_{em} = 638–651 nm (*fwhm* ≈ 3600 cm^{-1}). According to the unique absorption and emission properties, application as luminescent solar concentrators or in horticultural lighting appears promising.

2.1.1 Introduction

Phosphor converted light emitting diodes (pcLEDs) have replaced traditional light sources such as incandescent and fluorescent lamps in the last few years. Nevertheless, synthesis and investigation of novel luminescent materials are still required to improve pcLEDs for applications such as automotive, horticultural, or general lighting.[1,2] In this context, Ce^{3+} doped (oxo)nitridosilicates have been extensively investigated and established on the LED market.[3] So far, the Ce^{3+} emission of known compounds ranges from the blue to orange-red spectral range.[4,5] (Oxo)nitridosilicates with blue emission are, e.g., RESiO$_2$N:Ce^{3+} (RE = La/Y: λ_{em} = 416/442 nm) and LaSi$_3$N$_5$:Ce^{3+} (λ_{em} = 465 nm).[6–8] Green emission is observed, e.g. for RE_4Si$_2$O$_7$N$_2$:Ce^{3+} (RE = La/Y: λ_{em} = 488/504 nm) and Y$_6$Si$_3$O$_9$N$_4$:Ce^{3+} (λ_{em} = 525 nm).[6,7,9] An outstanding green-yellow emitting phosphor is Y$_{3-x}$Gd$_x$Al$_{5-y}$Ga$_y$O$_{12}$:Ce^{3+} (YAG) with garnet structure type. With its broad emission in the λ_{em} = 530–560 nm range, it is applied, e.g., in state-of-the-art white pcLEDs.[10,11] However, due to the lack of red components in the spectrum, additional red emitting phosphors such as (Ca,Sr)SiAlN$_3$:Eu^{2+}, (Ba,Sr)$_2$Si$_5$N$_8$:Eu^{2+}, or Sr[LiAlN$_3$]:Eu^{2+} are necessary to achieve improved color rendering.[12–14] Consequently, Ce^{3+} doped phosphors with a red-shifted Ce^{3+} emission compared to YAG are of considerable interest to achieve improved color rendering with a single phosphor approach (1pcLEDs). In this context, nitridosilicates are promising host materials due to the high covalency of the activator–nitrogen bond (nephelauxetic effect).[15] In recent years, a couple of (oxo)nitridosilicates with significantly red-shifted Ce^{3+} emission compared to YAG have been reported, e.g. La$_3$BaSi$_5$N$_9$O$_2$:Ce^{3+} (λ_{em} = 578 nm), (La,Ca–Ba)$_3$Si$_6$N$_{11}$:Ce^{3+} (λ_{em} = 540–595 nm), CaAlSiN$_3$:Ce^{3+} (λ_{em} = 570–603 nm), and SrAlSi$_4$N$_7$:Ce^{3+} (λ_{em} = 590 nm).[16–21] In addition to the red-shifted emission, luminescent nitridosilicates such as La$_3$Si$_6$N$_{11}$:Ce^{3+} and SrAlSi$_4$N$_7$:Ce^{3+} show improved thermal stability of emission compared to that of YAG. This also makes them promising materials, e.g. for automotive

forward lighting, as the maximum drive conditions are limited due to rather strong thermal quenching of currently used (Y,Gd)AG.[11,17,21] The Ce³⁺ doped luminescent materials with the most red-shifted emission up to date are the orange-red emitting materials Y$_3$Si$_5$N$_9$O:Ce³⁺ (λ_{em} = 620 nm) and cubic CaSiN$_2$:Ce³⁺ (λ_{em} = 625 nm). These luminophors have been considered for application in high color rendering white pcLEDs and for plant growth enhancement.[22,23] The red to infrared spectral range, however, has not been accessible with Ce³⁺ doped host materials so far. In this contribution, we report on the nitridolithosilicates Li$_{38.7}$$RE_{3.3}Ca_{5.7}$[Li$_2Si_{30}N_{59}$]O$_2$F ($RE$ = La, Ce, Y). These materials show unique long-wavelength absorption and emission behavior compared to that of all known Ce³⁺ phosphors. Accordingly, the presented nitridolithosilicates exhibit promising properties required for application in pcLEDs, e.g. for horticultural lighting. Additionally, application as luminescent solar concentrators in photovoltaic cells, due to the unprecedented absorption properties and the broad-band red emission, appears promising.

2.1.2 Experimental Section

2.1.2.1 Synthesis

All synthesis steps were performed in an argon-filled glovebox (Unilab, MBraun, Garching; O$_2$ < 1 ppm; H$_2$O < 1 ppm) or in flame-dried glassware. The title compounds were obtained from solid-state metathesis reactions starting from REF$_3$ (YF$_3$: Chempur, 99.999%; LaF$_3$/CeF$_3$: Sigma-Aldrich, 99.99%), CaF$_2$ (Alfa Aesar, 99.99%), amorphous Si$_3$N$_4$ (Ube Industries, > 99%), Li$_3$N (Alfa Aesar, 99.4%), and RE_2O$_3$ (Y$_2$O$_3$: Sigma-Aldrich, 99.999%; La$_2$O$_3$: Chempur, 99.999%) or CeO$_2$ (Auer-Remy, 99.9%), respectively. Substitution of Ce³⁺ into the host compounds Li$_{38.7}$La$_{3.3}$Ca$_{5.7}$[Li$_2$Si$_{30}$N$_{59}$]O$_2$F and Li$_{38.7}$Y$_{3.3}$Ca$_{5.7}$[Li$_2$Si$_{30}$N$_{59}$]O$_2$F was done by using CeF$_3$. Details on the amounts of starting materials are summarized in Table S1 in the Supporting Information. Starting materials were ground in an agate mortar and then transferred into tantalum crucibles. The crucibles were welded shut using the tungsten inert gas (TIG) welding method.[24] Water-cooling was applied during welding to prevent any chemical reactions. The sealed ampules were placed in a silica glass tube, evacuated, and then heated in a tube furnace. The reaction mixtures were heated to 950 °C for 1 h, maintained at 950 °C for 10 h, cooled to 500 °C for 3 h, and finally quenched to room temperature.

2.1.2.2 Electron Microscopy

The chemical composition and morphology of all samples were investigated using a scanning electron microscope (SEM) NanoLab G3 (Helios). To prevent electrostatic charging, the samples were carbon-coated (BAL-TEC MED 020, Bal Tec AG). Energy dispersive X-ray (EDX) measurements were performed with an acceleration voltage of 20 kV using an X-Max 80 SDD detector (Oxford Instruments).

2.1.2.3 Single-Crystal X-ray Diffraction

Single-crystal X-ray diffraction data of $Li_{38.7}Y_{3.3}Ca_{5.7}[Li_2Si_{30}N_{59}]O_2F$ were acquired using a Bruker D8 Venture diffractometer with rotating anode (Mo Kα radiation). The isolated single crystals were mounted on MicroMounts (MiTeGen) with an aperture size of 20 μm. Absorption effects were corrected with SADABS.[25] The crystal structure was solved using Direct Methods (SHELXS-97)[26] and refined by least-squares method (SHELXL-97).[27,28]

2.1.2.4 Powder X-ray Diffraction

Powder X-ray diffraction (PXRD) data of powder samples in glass capillaries (0.2 mm diameter, wall thickness 0.01 mm, Hilgenberg GmbH, Malsfeld, Germany) were obtained using a STOE STADI P diffractometer (Cu Kα_1 radiation, Ge(111) monochromator, Mythen1K detector) with parafocusing Debye-Scherrer geometry. For Rietveld refinements, the TOPAS-Academic V4.1 software package was used, applying the fundamental parameters approach (direct convolution of source emission profiles, axial instrument contributions, crystallite size, and microstrain effects).[29–32] Absorption effects were corrected using the calculated absorption coefficient. Preferred orientation was handled with the spherical harmonics model of fourth order. The structure model of $Li_{38.7}Y_{3.3}Ca_{5.7}[Li_2Si_{30}N_{59}]O_2F$, obtained from single-crystal X-ray data, was used as a starting point for the refinements.

2.1.2.5 Crystallographic Data

Details on the single-crystal structure investigation on $Li_{38.7}RE_{3.3}Ca_{5.7}[Li_2Si_{30}N_{59}]O_2F$ (RE = La, Ce, Y) can be obtained from the Cambridge Crystallographic Data Centre (CCDC) upon quoting the depository codes CCDC 1840986 (RE = Y), CCDC 1840987 (RE = Ce), and CCDC 1840988 (RE = La).

2.1.2.6 UV/Vis Spectroscopy

Diffuse reflectance UV/Vis spectroscopy was performed in the range of 240–800 nm (1 nm step size) using a Jasco V-650 UV/Vis spectrophotometer. The device is equipped with a deuterium and a halogen lamp (Czerny-Turner monochromator with 1200 lines/mm concave grating, photomultiplier tube detector).

2.1.2.7 Luminescence

Luminescence properties of Li$_{38.7}$Y$_{3.3}$Ca$_{5.7}$[Li$_2$Si$_{30}$N$_{59}$]O$_2$F:Ce^{3+} were investigated on crystals sealed in glass capillaries. Measurements were performed using a HORIBA Fluoromax4 spectrofluorimeter system, attached via optical fibers to an Olympus BX51 microscope. Emission spectra were captured with 2 nm step size in a wavelength range between 400 and 800 nm. In the case of Li$_{38.7}$La$_{3.3-x}$Ce$_x$Ca$_{5.7}$[Li$_2$Si$_{30}$N$_{59}$]O$_2$F (x = 0.1–3.3), luminescence was measured on microcrystalline powder samples in PTFE sample holders. Measurements were carried out using an in-house built system based on a 5.3 in. integrating sphere and a spectrofluorimeter equipped with a 150 W Xe lamp, two 500 mm Czerny-Turner monochromators, 1800 1/mm lattices, and 250/500 nm lamps with a spectral range from 230 to 820 nm. Obtained spectra were merged with additional data from a spectrometer sensitive in the 600–1100 nm wavelength range (Avantes) to measure the complete emission bands. The internal quantum efficiencies (IQE) of powder samples were determined by comparing integrated emission intensities and absorption at excitation wavelength with reference materials (BaSO$_4$, Merck p.a.; commercial (Sr,Ca)AlSiN$_3$:Eu^{2+}, Mitsubishi Chemical, and Y$_3$Al$_5$O$_{12}$:Ce^{3+}, Philips).

2.1.3 Results and Discussion

2.1.3.1 Synthesis and Chemical Analysis

Li$_{38.7}$La$_{3.3}$Ca$_{5.7}$[Li$_2$Si$_{30}$N$_{59}$]O$_2$F was obtained as colorless powder. Doping with Ce^{3+} yields reddish samples with darker body color for increasing Ce contents. Accordingly, Li$_{38.7}$Ce$_{3.3}$Ca$_{5.7}$[Li$_2$Si$_{30}$N$_{59}$]O$_2$F exhibits a dark-red body color. Samples of Li$_{38.7}$Y$_{3.3}$Ca$_{5.7}$[Li$_2$Si$_{30}$N$_{59}$]O$_2$F exhibit a grayish to reddish body color, irrespective of the Ce^{3+} content. This may result from yttrium nitride as a minor side phase or point defects (color centers) in the title compound. All materials are sensitive to air and moisture. Rietveld refinements on powder X-ray data were performed to validate that the investigated Li$_{38.7}$Y$_{3.3}$Ca$_{5.7}$[Li$_2$Si$_{30}$N$_{59}$]O$_2$F single crystal is representative for the bulk. A

comparison of the measured PXRD data and the calculated diffraction pattern for Li$_{38.7}$Y$_{3.3}$Ca$_{5.7}$[Li$_2$Si$_{30}$N$_{59}$]O$_2$F are exemplarily shown in Figure 1. Rietveld refinements and results for the three title compounds are shown in the Supporting Information (Figures S1−3, Table S2). The accuracy of the fits and the reflection profiles indicate that the crystallites have a homogeneous chemical composition. The Rietveld refinements for the samples with RE = La, Ce yielded RE:Ca ratios of 3.3:5.7, corresponding to the single-crystal structure analysis of Li$_{38.7}$Y$_{3.3}$Ca$_{5.7}$[Li$_2$Si$_{30}$N$_{59}$]O$_2$F. Chemical composition was investigated by means of EDX spectroscopy. The data are summarized in Table 1, and detailed results are listed in the Supporting Information (Tables S3–5 and Figures S4–6). Accordingly, the chemical compositions determined with EDX spectroscopy agree well with the results from single-crystal X-ray data and Rietveld refinements on X-ray powder data.

Figure 1. Measured X-ray powder diffraction pattern (black) and calculated pattern (red) for Li$_{38.7}$Y$_{3.3}$Ca$_{5.7}$[Li$_2$Si$_{30}$N$_{59}$]O$_2$F.

2.1.3.2   Crystal Structure Refinement and Description

The crystal structure of Li$_{38.7}$Y$_{3.3}$Ca$_{5.7}$[Li$_2$Si$_{30}$N$_{59}$]O$_2$F was solved and refined from single-crystal X-ray data in the trigonal space group P3c1 (no. 165).[26,27] All atom sites were refined with anisotropic displacement parameters (Table S7). The small amounts of Ce^{3+} (1 atom% referred to Y/Ca) were disregarded during the refinement due to the small contribution to the structure factor. Crystallographic data of the refinement are summarized in Table 2. The crystal structures of Li$_{38.7}$RE$_{3.3}$Ca$_{5.7}$[Li$_2$Si$_{30}$N$_{59}$]O$_2$F with RE = La, Ce were refined from powder X-ray diffraction data starting from the structural model of Li$_{38.7}$Y$_{3.3}$Ca$_{5.7}$[Li$_2$Si$_{30}$N$_{59}$]O$_2$F. For detailed information regarding the structure

refinements from X-ray powder data, see Table S2 with explanations. Fractional atomic coordinates and isotropic displacement parameters for the three materials are summarized in Tables S6, S8, and S9.

Table 1. EDX Results.

	Theoretical atom%	Experimental atom%		
		RE = La	RE = Ce	RE = Y
RE	3.3	3.1(4)	3.0(7)	3.4(4)
Ca	5.6	5.4(7)	5.1(7)	5.3(4)
Si	29.7	26(2)	26(3)	28.1(12)
N	58.4	58(3)	59(4)	57.1(14)
O	2.0	5.2(9)	5.4(8)	4.1(7)
F	1.0	2.2(5)	1.3(5)	2.0(3)

Variation of the lattice parameters corresponds to the ionic radii of the RE^{3+} atoms incorporated into the crystal structures (La^{3+}: 110 pm, Ce^{3+}: 107 pm, Y^{3+}: 96 pm; CN = 7).[33] Accordingly, the lattice parameters and the cell volume (Table 3) decrease in the order RE = La/Ce/Y. The title compounds' crystal structures (Figure 2) are isotypic, exhibiting a highly condensed three-dimensional network, made up by all side vertex-sharing (Q^4-type) SiN$_4$ and LiN$_4$ tetrahedra in the atomic ratio of 15:1. The degree of condensation [n(Si,Li):n(N)] is κ = 0.542. Two structural motifs are connected to build the anionic network (Figure 3c). The first one can be described as a cage formed by three siebener rings of SiN$_4$ tetrahedra. This cage is filled with one LiN$_4$ tetrahedra (Figure 3a). The second motif is a double dreier ring with six additional SiN$_4$ tetrahedra at the vertices (Figure 3b).[34] Both motifs are connected by common vertices. Accordingly, the anionic network is topologically equivalent to that of known nitridolithosilicates Li$_{33}$$RE_9$[Li$_2Si_{30}N_{59}$]O$_2$F ($RE$ = Ce, Pr).[35] Both crystal structures exhibit two heavy cation sites, which are mixed occupied with RE^{3+} (RE = La, Ce, Y) and Ca^{2+} atoms in the case of Li$_{38.7}$$RE_{3.3}Ca_{5.7}$[Li$_2Si_{30}N_{59}$]O$_2$F ($RE$ = La, Ce, Y). The refined site occupancies are shown in Table 3. As the trivalent RE^{3+} atoms in the Li$_{33}$$RE_9$[Li$_2Si_{30}N_{59}$]O$_2$F ($RE$ = Ce, Pr) structure type are partially substituted by Ca^{2+} in Li$_{38.7}$$RE_{3.3}Ca_{5.7}$[Li$_2Si_{30}N_{59}$]O$_2$F ($RE$ = La, Ce, Y), charge balance is necessary.

Table 2. Crystallographic Data of the Single-Crystal Structure Determination of Li$_{38.7}$Y$_{3.3}$Ca$_{5.7}$[Li$_2$Si$_{30}$N$_{59}$]O$_2$F.

formula	Li$_{38.7}$Y$_{3.3}$Ca$_{5.7}$[Li$_2$Si$_{30}$N$_{59}$]O$_2$F
formula mass / g·mol^{-1}	2524.61
crystal system	trigonal
space group	$P\overline{3}c1$ (no. 165)
lattice parameters / Å	a = 14.6748(4), c = 15.2552(5)
cell volume / Å^3	2845.1(2)
formula units/unit cell	2
X-ray density / g·cm^{-3}	2.948
abs. coefficient / μ·mm^{-1}	4.607
absorption correction	multiscan[25]
temperature / K	300(2)
diffractometer	Bruker D8 Venture
radiation / Å	Mo Kα (λ = 0.71073)
F(000)	2446
θ range / °	3.011 ≤ θ ≤ 30.508
observed reflections	48829
independent reflections	2912 (R_{int} = 0.0715)
refined parameters	220
GoF	1.112
R indices ($I > 2\sigma(I)$)	R_1 = 0.0318, wR_2 = 0.0641
R indices (all data)	R_1 = 0.0421, wR_2 = 0.0674
$\Delta\rho_{max}$, $\Delta\rho_{min}$ / e·Å^{-3}	0.638, −0.803

The single-crystal X-ray data for RE = Y show that charge balance is achieved by incorporation of Li on an additional crystallographic site. Consequently, ten Li sites are present in Li$_{38.7}$RE$_{3.3}$Ca$_{5.7}$[Li$_2$Si$_{30}$N$_{59}$]O$_2$F (RE = La, Ce, Y) in contrast to nine Li$^+$ sites in homeotypic Li$_{33}$RE$_9$[Li$_2$Si$_{30}$N$_{59}$]O$_2$F (RE = Ce, Pr).[35] The site occupancy factor of the additional Li10 site was constrained to 0.95 to provide charge balance.

The Si–N distances in the anionic network range from 1.701(2)–1.7868(10) Å for RE = Y, 1.69(2)–1.82(2) Å for RE = La, and 1.66(2)–1.82(2) Å for RE = Ce. The Li–N distances in the LiN$_4$ tetrahedra are 2.066(4)–2.071(10) Å for RE = Y. For RE = La, Ce similar values were obtained. However, these values are less meaningful as Li sites were not refined during Rietveld analysis. All values are in typical ranges compared to other nitridosilicates or nitridolithosilicates.[36,37]
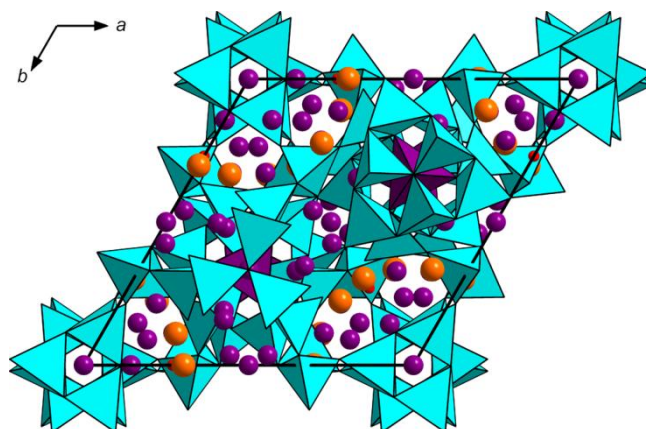
Figure 2. Crystal structure of Li$_{38.7}$*RE*$_{3.3}$Ca$_{5.7}$[Li$_2$Si$_{30}$N$_{59}$]O$_2$F (*RE* = Y, La, Ce), viewed along [001] with SiN$_4$ tetrahedra (turquoise), LiN$_4$ tetrahedra (violet), O/F atoms (red), Li atoms (violet), and *RE*/Ca atoms (orange). Unit cell in black.
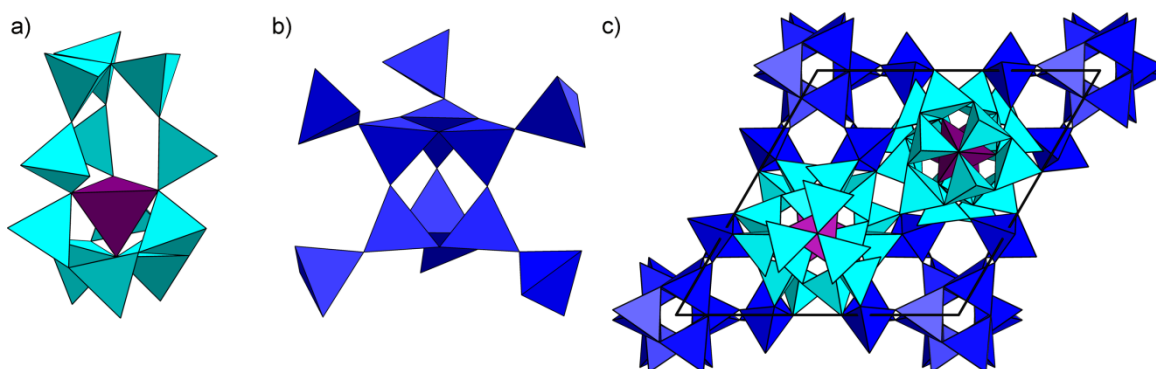
Figure 3. (a) Cage of SiN$_4$ tetrahedra (turquoise) containing a LiN$_4$ tetrahedra (violet). (b) Double dreier ring with additional SiN$_4$ tetrahedra at the vertices (blue). (c) Three-dimensional tetrahedra network, viewing direction [001].

The two mixed occupied *RE*/Ca sites are surrounded by seven anions. The site *RE*1/Ca1 is coordinated by seven N atoms, the *RE*2/Ca2 by six N atoms, and a mixed-occupied O/F site (Figure 4). The noncondensed anion site occupied by O/F atoms does not belong to the anionic network. The *RE*/Ca–ligand distances are listed in Table S10. All atomic distances are similar for the three title compounds and in typical ranges compared to other *RE*- and Ca-(oxo)nitridosilicates.[35,36,38,39] Li atoms exhibit coordination numbers from 4 to 7. The surroundings of the ten Li sites are shown in Figure S7. The calculated charge distribution (CHARDI) values for the cation sites (Table S11) prove the electrostatic plausibility of the structure models.[40] The trends in the calculated values for *RE*/Ca sites

can be directly correlated to the site occupancy factors refined from X-ray diffraction data (Table 3). The values for Si and most Li sites agree well with the expected values. Solely values for the Li10 site are significantly smaller than expected with values of ≈ 0.7. This may explain why the Li10 site is unoccupied in the Li$_{33}$RE$_9$[Li$_2$Si$_{30}$N$_{59}$]O$_2$F (RE = Ce, Pr) structure type with no required charge balance.

Table 3. Comparison of Crystallographic Data for Li$_{38.7}$RE$_{3.3}$Ca$_{5.7}$[Li$_2$Si$_{30}$N$_{59}$]O$_2$F (RE = La, Ce, Y) and Site Occupancy Factors (*s.o.f.*) for the Sites *RE*1/Ca1 and *RE*2/Ca2.

	RE = La	*RE* = Ce	*RE* = Y
cell parameters / Å	a = 14.7789(3) c = 15.3370(3)	a = 14.75380(11) c = 15.3132(2)	a = 14.6748(4) c = 15.2552(5)
volume / Å^3	2901.07(13)	2886.72(5)	2845.1(2)
*s.o.f. RE*1/Ca1	0.494(8)/0.506(8)	0.668(10)/0.334(10)	0.846(5)/0.154(5)
*s.o.f. RE*2/Ca1	0.307(3)/0.693(3)	0.221(3)/0.779(3)	0.128(3)/0.872(3)

For the isolated anion site, occupation with O and F was assumed and constrained to a ratio of O:F = 2:1, analogous to Li$_{33}$RE$_9$[Li$_2$Si$_{30}$N$_{59}$]O$_2$F (RE = Ce, Pr). This is in accordance with the EDX results (Table 1). Additionally, lattice energy (MAPLE)[33,41–43] and bond valence sum (BVS)[44,45] calculations were performed to verify the assignment of the anions. Partial MAPLE values for all cations and anions are in the expected ranges. The total MAPLE sums for all phases agree well with MAPLE sums of hypothetical reactions of binary starting materials. Detailed explanations and results of the MAPLE calculations are summarized in Table S12. The BVS calculations (Table S13) are also in good agreement with the assignment of N atoms to the anionic network and O/F to the isolated anion site. The BVS values for the O1/F1 site are close to −1.66, which is expected for an occupation O:F = 2:1. Combined CHARDI, MAPLE, and BVS calculations demonstrate the electrostatic consistency of the structural models.
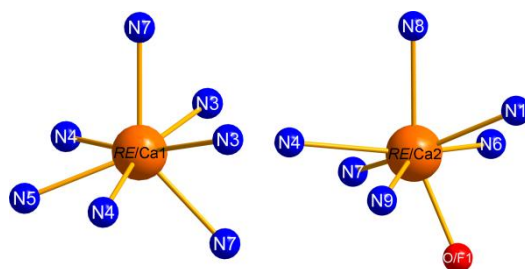
Figure 4. Coordination spheres of *RE*/Ca sites in Li$_{38.7}$RE$_{3.3}$Ca$_{5.7}$[Li$_2$Si$_{30}$N$_{59}$]O$_2$F (RE = La, Ce, Y).

2.1.3.3 UV/Vis Spectroscopy

Solid-state UV/Vis spectroscopy was performed to estimate the optical band gaps of the title compounds. For nondoped samples with RE = La, Y measured diffuse reflectance spectra were converted to pseudoabsorption spectra using the Kubelka-Munk function $F(R) = (1 − R)^2/2R$.[46] Optical band gaps were then determined from Tauc plots by drawing a line tangent at the inflection point.[47] For the Tauc plots, the Kubelka-Munk exponent n = 1/2 was chosen, assuming direct allowed transitions. The diffuse reflectance spectrum of Li$_{38.7}$La$_{3.3}$Ca$_{5.7}$[Li$_2$Si$_{30}$N$_{59}$]O$_2$F (Figure S8) exhibits a broad absorption band around 275 nm, corresponding to the colorless sample. The optical band gap is approximately 4.1 eV. The Tauc plot for Li$_{38.7}$La$_{3.3}$Ca$_{5.7}$[Li$_2$Si$_{30}$N$_{59}$]O$_2$F is exemplarily shown in Figure 5. Li$_{38.7}$Y$_{3.3}$Ca$_{5.7}$[Li$_2$Si$_{30}$N$_{59}$]O$_2$F exhibits an unexpected grayish to reddish body color, possibly due to point defects.
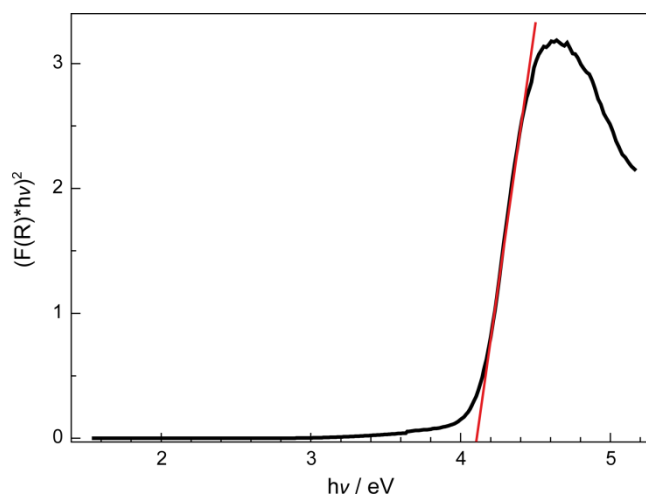
Figure 5. Tauc plot (n = 1/2) for nondoped Li$_{38.7}$La$_{3.3}$Ca$_{5.7}$[Li$_2$Si$_{30}$N$_{59}$]O$_2$F.

Accordingly, the UV/Vis spectrum exhibits an absorption band in the visible range additionally to the absorption band around 275 nm (Figure S9). An optical band gap of ≈ 4.0 eV was obtained from the Tauc plot (Figure S10). Li$_{38.7}$Ce$_{3.3}$Ca$_{5.7}$[Li$_2$Si$_{30}$N$_{59}$]O$_2$F with its high dopant concentration shows strong absorption in the visible to blue range with absorption bands around 530 and 420 nm (Figure S11). Large band gaps ≥ 4 eV are a prerequisite for RE doped host materials for application in pcLEDs.

2.1.3.4 Luminescence

Luminescence properties were either obtained from single particles in glass capillaries (RE = Y) or thick bed powder samples (Li$_{38.7}$La$_{3.3-x}$Ce$_x$Ca$_{5.7}$[Li$_2$Si$_{30}$N$_{59}$]O$_2$F, x = 0.1–3.3). The title compounds show strong deep-red Ce^{3+} luminescence when irradiated with UV to green-yellow light. Excitation and emission spectra (λ_{exc} = 440 nm) are illustrated in Figure 6. All excitation spectra have two maxima around 405 and 540 nm. Li$_{38.7}$Y$_{3.3}$Ca$_{5.7}$[Li$_2$Si$_{30}$N$_{59}$]O$_2$F:Ce^{3+} (3 atom% Ce, nominal) emits at λ_{em} = 638 nm with full width at half-maximum (*fwhm*) of 144 nm/3420 cm^{-1}. Li$_{38.7}$La$_{3.3}$Ca$_{5.7}$[Li$_2$Si$_{30}$N$_{59}$]O$_2$F:Ce^{3+} (3 atom% Ce, nominal) shows similar emission with a maximum at λ_{em} = 638 nm and slightly increased *fwhm* of 156 nm/3540 cm^{-1}. Li$_{38.7}$Ce$_{3.3}$Ca$_{5.7}$[Li$_2$Si$_{30}$N$_{59}$]O$_2$F in contrast exhibits strongly red-shifted emission with λ_{em} = 651 nm and *fwhm* = 175 nm/3650 cm^{-1}.
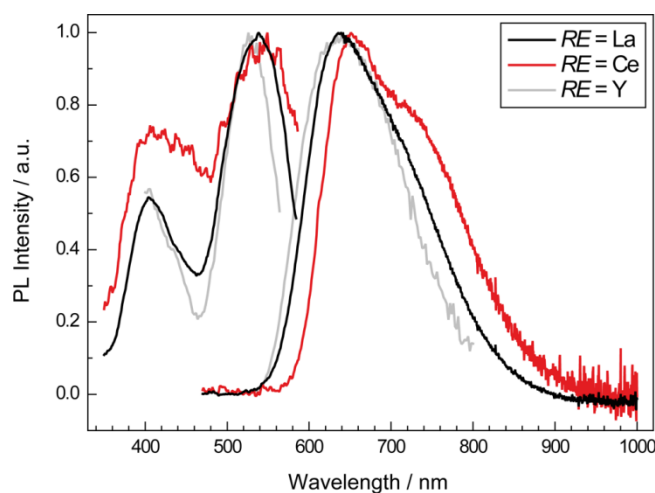
Figure 6.   Normalized   excitation   and   emission   spectra   (λ_{exc} = 440 nm)   of Li$_{38.7}$RE$_{3.3}$Ca$_{5.7}$[Li$_2$Si$_{30}$N$_{59}$]O$_2$F (RE = La, Ce, Y). Samples with RE = La, Y were doped with 3 atom% Ce (nominal).

The red shift of the emission compared to Li$_{38.7}$La$_{3.3}$Ca$_{5.7}$[Li$_2$Si$_{30}$N$_{59}$]O$_2$F:Ce^{3+} (3 atom% Ce, nominal) is possibly caused by reabsorption due to the increased Ce^{3+} content and emission at lower energy.[48] Consequently, the emission of the solid-solution Li$_{38.7}$La$_{3.3-x}$Ce$_x$Ca$_{5.7}$[Li$_2$Si$_{30}$N$_{59}$]O$_2$F (x = 0.1–3.3) shows a continuous red shift from λ_{em} = 638 to 651 nm with rising activator concentration. The respective emission spectra are illustrated in Figure S12, details on luminescence properties are listed in Table S14. The slightly smaller activator–ligand distances seem to play a minor role in the red-shift, as for RE = La and RE = Y (distances in Table S10), almost identical excitation and emission spectra are observed. *IQE*s were determined for all samples of

$Li_{38.7}La_{3.3-x}Ce_xCa_{5.7}[Li_2Si_{30}N_{59}]O_2F$ (x = 0.1–3.3) with an excitation wavelength λ_{exc} = 440 nm. The samples with x = 0.1/0.3 (3%/9% Ce) have the highest IQE values of 14%. With higher Ce contents, the samples show concentration quenching. Consequently, the IQE of $Li_{38.7}Ce_{3.3}Ca_{5.7}[Li_2Si_{30}N_{59}]O_2F$ is small with ≈ 4%. For the most promising samples with x = 0.1/0.3, the IQEs were also measured with excitation wavelengths of 405 and 540 nm, which are the most suitable energies according to the excitation spectra (Figure 6). The IQEs show a strong increase, most of all for λ_{exc} = 540 nm with IQEs of 35% (x = 0.1) and 32% (x = 0.3). All IQEs are summarized in Table 4.

Table 4. Internal Quantum Efficiencies of $Li_{38.7}La_{3.3-x}Ce_xCa_{5.7}[Li_2Si_{30}N_{59}]O_2F$ (x = 0.1–3.3).

x	λ_{exc} = 440 nm	λ_{exc} = 405 nm	λ_{exc} = 540 nm
0.1	0.14	0.20	0.35
0.3	0.14	0.19	0.32
0.6	0.11		
1.2	0.06		
3.3	0.04		

The thermal behavior of $Li_{38.7}La_{3.3-x}Ce_xCa_{5.7}[Li_2Si_{30}N_{59}]O_2F$ (x = 0.1–3.3) deteriorates with rising Ce content (Figures 7 and S13). Relative quantum efficiencies at 423 K (related to values at room temperature) range from 52% for x = 0.1 to 27% for x = 3.3. Compared to other Ce^{3+} doped phosphors the presented materials absorb light in an unprecedented large energy range, between the UV and remarkably low energies in the green-yellow spectral range. This may be explained by the strong covalency of the activator–ligand interaction (nephelauxetic effect) due to the coordination by N atoms combined with the occupation of dopant sites with low site symmetry. Ce^{3+} is expected to occupy the heavy metal sites RE/Ca1 (Wyckoff position 6f) with site symmetry 2, and the RE/Ca2 site (Wyckoff position 12g) with site symmetry 1. This leads to a splitting of the Ce^{3+} 5d levels into five separated energy levels. The combination of the low site symmetry and a strong nephelauxetic effect in the nitridolithosilicates probably shift the lowest 5d state strongly toward the 4f ground state.[22,49] This results in the low energy of the lowest Ce^{3+} 5d state and the absorption in the green-yellow spectral range. Corresponding to the low energy absorption, the title compounds emit light in the deep-red region. Luminescent materials with comparable Ce^{3+} luminescence properties are orange-red emitting $Y_3Si_5N_9O$:Ce^{3+} and cubic $CaSiN_2$:Ce^{3+}.[22,23] The longest wavelength maxima in the excitation spectra of these phosphors are 506 nm ($Y_3Si_5N_9O$:Ce^{3+}) and 535 nm ($CaSiN_2$:Ce^{3+}), respectively.

Y$_3$Si$_5$N$_9$O:Ce^{3+} with a very broad emission band (*fwhm* = 178 nm) peaks at λ_{em} = 620 nm. Cubic CaSiN$_2$:Ce^{3+} shows more narrow emission (80 nm) with a maximum at λ_{em} = 625 nm. Therefore, the title compounds exhibit, to the best of our knowledge, the lowest energy Ce^{3+} excitation and emission band positions reported so far.
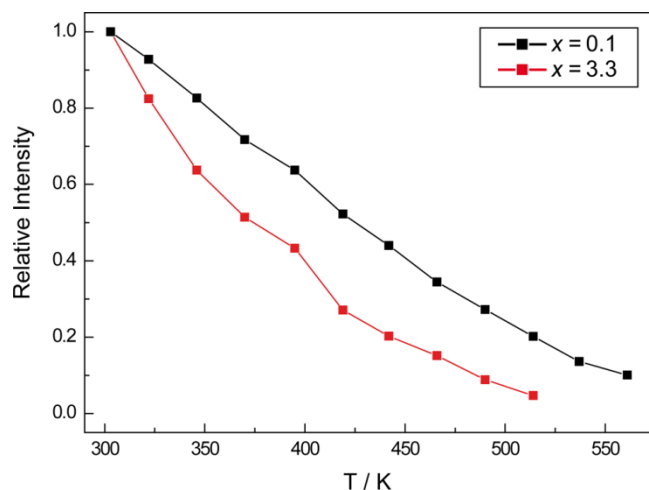
Figure 7. Temperature dependent integrated luminescence intensities of Li$_{38.7}$La$_{3.3-x}$Ce$_x$Ca$_{5.7}$[Li$_2$Si$_{30}$N$_{59}$]O$_2$F.

2.1.4 Conclusion

In this contribution, we reported on the nitridolithosilicates Li$_{38.7}$RE$_{3.3}$Ca$_{5.7}$[Li$_2$Si$_{30}$N$_{59}$]O$_2$F (RE = La, Ce, Y) with intriguing Ce^{3+} luminescence properties. The materials were synthesized in solid-state metathesis reactions. The structural models were refined from single-crystal and powder X-ray diffraction data. The highly condensed anionic networks of these compounds are made up by SiN$_4$ and LiN$_4$ tetrahedra. The crystal structure is homeotypic to that of known Li$_{33}$RE$_9$[Li$_2$Si$_{30}$N$_{59}$]O$_2$F (RE = Ce, Pr). Charge balance, which is required as bivalent Ca^{2+} atoms substitute trivalent ions, is provided by incorporation of lithium on an additional crystallographic site. These results are supported by EDX investigations as well as CHARDI, MAPLE, and BVS calculations. Compared to previously known Ce^{3+} doped phosphors, the reported nitridolithosilicates exhibit strikingly different luminescence properties. Usually, Ce^{3+} doped (oxo)nitridosilicates are most effectively excited in the UV to blue and emit in the blue to yellow-orange spectral range. In contrast, the title compounds absorb light from the UV to the green-yellow spectral range with an excitation maximum at around 540 nm. This is probably caused by a strong nephelauxetic effect due to coordination by nitrogen with short contact lengths combined with the low point symmetry of the sites occupied by the activator ions. The emission is therefore

observed in the deep-red to IR range, peaking between 638–651 nm. Accordingly, the title compounds exhibit an unrivaled long-wavelength Ce^{3+} excitation and emission, significantly extending the spectral range accessible with the activator Ce^{3+}. It is the subject of further research to improve the efficiency and thermal stability of the emission, e.g. through further substitution on the cation sites with elements *RE* = La–Lu, Y and *AE* = Mg–Ba. Luminescent materials with the described characteristics may, for example, be applied as luminescent solar concentrators in solar cells, as they can convert an extended range of high-energetic light into red light, as it is required to increase the conversion efficiency of solar cells. Furthermore, application in horticultural lighting appears promising because green light, which cannot be utilized in the photosynthetic process, is down-converted into deep-red to infrared photons by the reported nitridolithosilicates.

2.1.5 References

[1]   Xia, Z.; Liu, Q. Progress in discovery and structural design of color conversion phosphors for LEDs. *Prog. Mater. Sci.* **2016**, *84*, 59–117.

[2]   McKittrick, J.; Shea-Rohwer, L. E. Review: Down Conversion Materials for Solid-State Lighting. *J. Am. Ceram. Soc.* **2014**, *97*, 1327–1352.

[3]   Wang, L.; Xie, R.-J.; Suehiro, T.; Takeda, T.; Hirosaki, N. Down-Conversion Nitride Materials for Solid State Lighting: Recent Advances and Perspectives. *Chem. Rev.* **2018**, *118*, 1951–2009.

[4]   Xie, R.-J.; Hirosaki, N.; Takeda, T. Rare-Earth Activated Nitride Phosphors: Synthesis, Luminescence and Applications. *Materials* **2010**, *3*, 3777–3793.

[5]   Xie, R.-J.; Hintzen, H. T. Optical Properties of (Oxy)Nitride Materials: A Review. *J. Am. Ceram. Soc.* **2013**, *96*, 665–687.

[6]   van Krevel, J. W. H.; Hintzen, H. T.; Metselaar, R.; Meijerink, A. Long Wavelength Ce^{3+} Emission in Y−Si−O−N Materials. *J. Alloys Compd.* **1998**, *268*, 272–277.

[7]   Dierre, B.; Xie, R.-J.; Hirosaki, N.; Sekiguchi, T. Blue emission of Ce^{3+} in Lanthanide Silicon Oxynitride Phosphors. *J. Mater. Res.* **2007**, *22*, 1933–1941.

[8]   Suehiro, T.; Hirosaki, N.; Xie, R.-J.; Sato, T. Blue-Emitting LaSi$_3$N$_5$:Ce^{3+} Fine Powder Phosphor for UV-Converting White Light-Emitting Diodes. *Appl. Phys. Lett.* **2009**, *95*, 051903.

[9]   Deng, D.; Xu, S.; Su, X.; Wang, Q.; Li, Y.; Li, G.; Hua, Y.; Huang, L.; Zhao, S.; Wang, H.; Li, C. Long wavelength Ce^{3+} emission in Y$_6$Si$_3$O$_9$N$_4$ phosphors for white-emitting diodes. *Mater. Lett.* **2011**, *65*, 1176–1178.

[10] Blasse, G.; Bril, A. A new phosphor for flying-spot cathode-ray tubes for color television: yellow-emitting Y$_3$Al$_5$O$_{12}$-Ce^{3+}. *Appl. Phys. Lett.* **1967**, *11*, 53–55.

[11] Xia, Z.; Meijerink, A. Ce^{3+}-Doped garnet phosphors: composition modification, luminescence properties and applications. *Chem. Soc. Rev.* **2017**, *46*, 275–299.

[12] Watanabe, H.; Kijima, N. Crystal structure and luminescence properties of Sr$_x$Ca$_{1-x}$AlSiN$_3$:Eu^{2+} mixed nitride phosphors. *J. Alloys Compd.* **2009**, *475*, 434–439.

[13] Höppe, H. A.; Lutz, H.; Morys, P.; Schnick, W.; Seilmeier, A. Luminescence in Eu^{2+}-doped Ba$_2$Si$_5$N$_8$: fluorescence, thermoluminescence, and upconversion. *J. Phys. Chem. Solids* **2000**, *61*, 2001–2006.

[14] Pust, P.; Weiler, V.; Hecht, C.; Tücks, A.; Wochnik, A. S.; Henß, A.-K.; Wiechert, D.; Scheu, C.; Schmidt, P. J.; Schnick, W. Narrow-band red-emitting Sr[LiAl$_3$N$_4$]:Eu^{2+} as a next-generation LED-phosphor material. *Nat. Mater.* **2014**, *13*, 891–896.

[15] Feldmann, C. Technical Revolution Underway – Nitride-based Phosphors for LED Application. *Z. Anorg. Allg. Chem.* **2012**, *638*, 2169–2171.

[16] Durach, D.; Neudert, L.; Schmidt, P. J.; Oeckler, O.; Schnick, W. La$_3$BaSi$_5$N$_9$O$_2$:Ce^{3+} – A Yellow Phosphor with an Unprecedented Tetrahedra Network Structure Investigated by Combination of Electron Microscopy and Synchrotron X-ray Diffraction. *Chem. Mater.* **2015**, *27*, 4832–4838.

[17] Kijima, N.; Seto, T.; Hirosaki, N. A New Yellow Phosphor La$_3$Si$_6$N$_{11}$:Ce^{3+} for White LEDs. *ECS Trans.* **2009**, *25(9)*, 247–252.

[18] Suehiro, T.; Hirosaki, N.; Xie, R.-J. Synthesis and Photoluminescent Properties of (La,Ca)$_3$Si$_6$N$_{11}$:Ce^{3+} Fine Powder Phosphors for Solid-State Lighting. *ACS Appl. Mater. Interfaces* **2011**, *3*, 811–816.

[19] Chen, Z.; Zhang, Q.; Li, Y.; Wang, H.; Xie, R.-J. A promising orange-yellow-emitting phosphor for high power warm-light white LEDs: Pure-phase synthesis and photoluminescence properties. *J. Alloys Compd.* **2017**, *715*, 184–191.

[20] Li, Y. Q.; Hirosaki, N.; Xie, R.-J.; Takeda, T.; Mitomo, M. Yellow-Orange-Emitting CaAlSiN$_3$:Ce^{3+} Phosphor: Structure, Photoluminescence, and Application in White LEDs. *Chem. Mater.* **2008**, *20*, 6704–6714.

[21] Ruan, J.; Xie, R.-J.; Funahashi, S.; Tanaka, Y.; Takeda, T.; Suehiro, T.; Hirosaki, N.; Li, Y.-Q. A novel yellow-emitting SrAlSi$_4$N$_7$:Ce^{3+} phosphor for solid state lighting: Synthesis, electronic structure and photoluminescence properties. *J. Solid State Chem.* **2013**, *208*, 50–57.

[22] Zhu, Q.-Q.; Wang, L.; Hirosaki, N.; Hao, L. Y.; Xu, X.; Xie, R.-J. Extra-Broad Band Orange-Emitting Ce^{3+}-Doped Y$_3$Si$_5$N$_9$O Phosphor for Solid-State Lighting:

Electronic, Crystal Structures and Luminescence Properties. *Chem. Mater.* **2016**, *28*, 4829–4839.

[23] Le Toquin, R.; Cheetham, A. K. Red-emitting cerium-based phosphor materials for solid-state lighting applications. *Chem. Phys. Lett.* **2006**, *423*, 352–356.

[24] Pöttgen, R.; Janka, O.; Dronskowski, R.; Kikkawa, S.; Stein, A. High-Temperature Methods. *Handbook of Solid State Chemistry* **2017**, 1–22.

[25] Sheldrick, G. M. *SADABS, v. 2: Multi-Scan Absorption Correction*; Bruker-AXS: Billerica, MA, 2012.

[26] Sheldrick, G. M. *SHELXS-97: A Program for Crystal Structure Solution*; University of Göttingen: Göttingen, Germany, 1997.

[27] Sheldrick, G. M. *SHELXL-97: A Program for Crystal Structure Refinement*; University of Göttingen: Göttingen, Germany, 1997.

[28] Sheldrick, G. M. A short history of SHELX. *Acta Crystallogr., Sect. A: Found. Crystallogr.* **2008**, *64*, 112–122.

[29] Rietveld, H. M. A profile refinement method for nuclear and magnetic structures. *J. Appl. Crystallogr.* **1969**, *2*, 65–71.

[30] Coelho, A. A. *TOPAS, v. 4.1: A program for Rietveld refinement*; Coelho Software: Brisbane, Australia, 2007.

[31] Bergmann, J.; Kleeberg, R.; Haase, A.; Breidenstein, B. Advanced fundamental parameter model for improved profile analysis. *Mater. Sci. Forum* **2000**, *347–349*, 303–308.

[32] Cheary, R. W.; Coelho, A. A.; Cline, J. P. Fundamental Parameters Line Profile Fitting in Laboratory Diffractometers. *J. Res. Natl. Inst. Stand. Technol.* **2004**, *109*, 1–25.

[33] Shannon, R. D. Revised effective ionic radii and systematic studies of interatomic distances in halides and chalcogenides. *Acta Crystallogr., Sect. A: Cryst. Phys., Diffr., Theor. Gen. Crystallogr.* **1976**, *32*, 751–767.

[34] The term *siebener* (*dreier*) ring was coined by Liebau and is derived from the German word "siebener" ("dreier"); a *siebener* (*dreier*) ring comprises seven (three) tetrahedra centers.

[35] Lupart, S.; Durach, D.; Schnick, W. Li$_{35}$Ln$_9$Si$_{30}$N$_{59}$O$_2$F with Ln = Ce, Pr − Highly Condensed Nitridosilicates. *Z. Anorg. Allg. Chem.* **2011**, *637*, 1841–1844.

[36] Wilhelm, D.; Seibald, M.; Baumann, D.; Wurst, K.; Huppertz, H. Further Representatives of the Type RE$_3$[Si$_5$N$_9$O] (RE = Dy–Er, Yb). *Eur. J. Inorg. Chem.* **2018**, 731–738.

[37] Poesl, C.; Schnick, W. Crystal Structure and Nontypical Deep-Red Luminescence of Ca$_3$Mg[Li$_2$Si$_2$N$_6$]:Eu^{2+}. *Chem. Mater.* **2017**, *29*, 3778–3784.

[38] Maak, C.; Niklaus, R.; Friedrich, F.; Mähringer, A.; Schmidt, P. J.; Schnick, W. Efficient Yellow-Orange Phosphor Lu$_4$Ba$_2$[Si$_9$ON$_{16}$]O:Eu^{2+} and Orange-Red Emitting Y$_4$Ba$_2$[Si$_9$ON$_{16}$]O:Eu^{2+}: Two Oxonitridosilicate Oxides with Outstanding Structural Variety. *Chem. Mater.* **2017**, *29*, 8377–8384.

[39] Schlieper, T.; Schnick, W. Nitrido-silicate. I. Hochtemperatur-Synthesen und Kristallstrukturen von Ca$_2$Si$_5$N$_8$. *Z. Anorg. Allg. Chem.* **1995**, *621*, 1037–1041.

[40] Hoppe, R.; Voigt, S.; Glaum, H.; Kissel, J.; Müller, H. P.; Bernet, K. A new route to charge distributions in ionic solids. *J. Less-Common Met.* **1989**, *156*, 105–122.

[41] Hoppe, R. Madelung constants. *Angew. Chem., Int. Ed. Engl.* **1966**, *5*, 95–106; Über Madelungfaktoren. *Angew. Chem.* **1966**, *78*, 52–63.

[42] Hoppe, R. The Coordination Number – an "Inorganic Chameleon". *Angew. Chem., Int. Ed. Engl.* **1970**, *9*, 25–34; Die Koordinationszahl – ein „anorganisches Chamäleon". *Angew. Chem.* **1970**, *82*, 7–16.

[43] Hübenthal, R. *Maple, Program for the Calculation of MAPLE values, version 4*; University of Gießen: Gießen, Germany, 1993.

[44] Brown, I. D.; Altermatt, D. Bond–valence parameters obtained from a systematic analysis of the Inorganic Crystal Structure Database. *Acta Crystallogr., Sect. B: Struct. Sci.* **1985**, *41*, 244–247.

[45] Brese, N. E.; O'Keeffe, M. Bond–Valence Parameters for Solids. *Acta Crystallogr., Sect. B: Struct. Sci.* **1991**, *47*, 192–197.

[46] López, R.; Gómez, R. Band-gap energy estimation from diffuse reflectance measurements on sol-gel and commercial TiO$_2$: a comparative study. *J. Sol-Gel Sci. Technol.* **2012**, *61*, 1–7.

[47] Tauc, J.; Grigorovici, R.; Vancu, A. Optical Properties and Electronic Structure of Amorphous Germanium. *Phys. Status Solidi B* **1966**, *15*, 627–637.

[48] Sakuma, K.; Hirosaki, N.; Xie, R.-J. Red-shift of emission wavelength caused by reabsorption mechanism of europium activated Ca-*α*-SiAlON ceramic phosphors. *J. Lumin.* **2007**, *126*, 843–852.

[49] Van Eijk, C. W. Development of inorganic scintillators. *Nucl. Instrum. Methods Phys. Res., Sect. A* **1997**, *392(1)*, 285–290.

2.2 Unpublished Results in the System $Li_{38.7}RE_{3.3}AE_{5.7}[Li_2Si_{30}N_{59}]O_2F$

Following on from the results presented in chapter 2.1, further syntheses were performed to study the impact of different *RE*/*AE* (*RE* = La–Lu, Y and *AE* = Mg–Ba) element combinations on the luminescence properties. The aim of the investigations was to find out in which wavelength range the emission of $Li_{38.7}RE_{3.3}AE_{5.7}[Li_2Si_{30}N_{59}]O_2F:Ce^{3+}$ phosphors can be tuned and whether the internal quantum efficiency (*IQE*) and the thermal quenching behavior can be improved by cation substitution. In this context the two phases with the nominal compositions $Li_{38.7}Y_{3.3}Sr_{5.7}[Li_2Si_{30}N_{59}]O_2F:Ce^{3+}$ and $Li_{38.7}Lu_{3.3}Ca_{5.7}[Li_2Si_{30}N_{59}]O_2F:Ce^{3+}$ were obtained. Both compounds were synthesized in tantalum ampules according to chapter 2.1.2.1. Detailed amounts of starting materials are summarized in Table S15 in the Supporting Information. Rietveld refinements of X-ray powder diffraction data (chapter 2.1.2.4) show that the Y/Sr compound was obtained with yields of 61 wt% (Figure S14). In the case of the Lu/Ca compound the yields are significantly smaller with 28 wt% (Figure S15). LiF, Li_2SiN_2, $Li_2AESi_2N_4$, *RE*N and $LiSi_2N_3$ have been identified as side phases. The results of the Rietveld refinements are summarized in Table S16. The target phases were refined using the structure model of $Li_{38.7}Y_{3.3}Ca_{5.7}[Li_2Si_{30}N_{59}]O_2F$ (Tables S6 and S7). A significant refinement of atomic coordinates and site occupancy factors for the *RE*/*AE* sites was not possible. In the case of the Y/Sr compound, the latter is prevented by the very similar atomic form factors of Y^{3+} and Sr^{2+} for X-rays. In the case of Lu/Ca, the phase fraction of the target phase is too low. Accordingly, solely lattice parameters were refined.

The particles which were selected for optical characterization were first investigated by means of EDX spectroscopy (see chapter 2.1.2.2). The results essentially correspond to the nominal composition $Li_{38.7}RE_{3.3}AE_{5.7}[Li_2Si_{30}N_{59}]O_2F$ (Table S17). Luminescence characteristics of these particles were measured with a luminescence microscope (see chapter 2.1.2.7). The obtained excitation and emission spectra are illustrated in Figure 1 and compared to spectra of $Li_{38.7}Y_{3.3}Ca_{5.7}[Li_2Si_{30}N_{59}]O_2F:Ce^{3+}$ with $\lambda_{em} \approx 639$ nm and *fwhm* ≈ 144 nm/3420 cm^{-1} (orange). The Y/Sr compound exhibits blue-shifted excitation and emission with $\lambda_{em} \approx 616$ nm and *fwhm* ≈ 139 nm/3550 cm^{-1}. The blue-shift can be explained by the larger ionic radius of Sr^{2+} compared to Ca^{2+} (Sr^{2+}: 121 pm, Ca^{2+}: 106 pm; CN = 7).[1] The increased lattice parameters of the Y/Sr compound (Tables S2 and S16) probably result in increased activator–ligand distances and consequently a reduced crystal field splitting. The Lu/Ca compound shows an almost identical excitation spectrum compared to $Li_{38.7}Y_{3.3}Ca_{5.7}[Li_2Si_{30}N_{59}]O_2F:Ce^{3+}$. The emission spectrum ($\lambda_{em} \approx 629$ nm, *fwhm* ≈ 132 nm/3200 cm^{-1}) in contrast is blue-shifted and more narrow due to a slightly

smaller Stokes shift. This may be explained by almost identical ionic radii (Y^{3+}: 90 pm, Lu^{3+}: 86 pm; CN = 6) but significantly higher atomic weight of Lu^{3+} compared to Y^{3+}.[1,2] However, detailed information on the crystal structure and improved spectra would be necessary for a reliable discussion of structure-property-relationships.
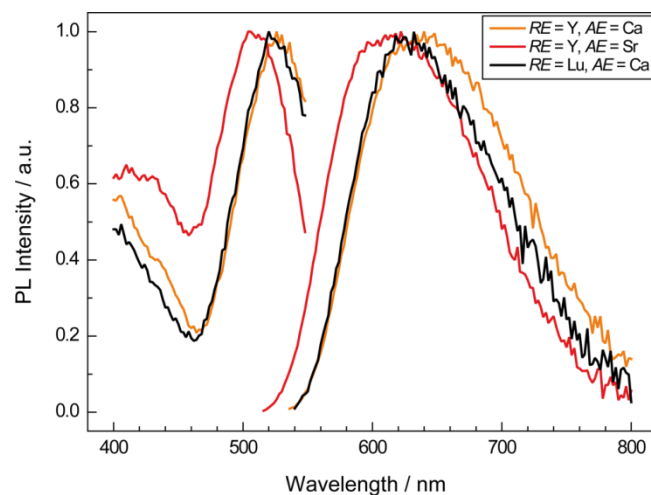
Figure 1. Normalized excitation and emission spectra of particles with the nominal composition $Li_{38.7}Y_{3.3}Sr_{5.7}[Li_2Si_{30}N_{59}]O_2F{:}Ce^{3+}$ and $Li_{38.7}Lu_{3.3}Ca_{5.7}[Li_2Si_{30}N_{59}]O_2F{:}Ce^{3+}$ compared to spectra of $Li_{38.7}Y_{3.3}Ca_{5.7}[Li_2Si_{30}N_{59}]O_2F{:}Ce^{3+}$.

IQE values and thermal quenching data could not be obtained for the Ce^{3+} doped Y/Sr and Lu/Ca samples. Such investigations require phase-pure samples or at least samples with optically inactive side phases. Nevertheless, the results demonstrate that the system $Li_{38.7}RE_{3.3}AE_{5.7}[Li_2Si_{30}N_{59}]O_2F$ exhibits high potential for further substitution on the *RE/AE* sites. Syntheses optimization for the two presented materials and other potential substitution variants will allow for a more detailed elucidation of the compositions, the crystal structures and the optical properties.

References

[1]   Shannon, R. D. Revised effective ionic radii and systematic studies of interatomic distances in halides and chalcogenides. *Acta Crystallogr., Sect. A: Cryst. Phys., Diffr., Theor. Gen. Crystallogr.* **1976**, *32*, 751–767.

[2]   Shionoya, S.; Yen, W. M. *Phosphor Handbook*; CRC Press, New York, 1998.

3 Narrow-Band Yellow-Orange Emitting La$_{3-x}$Ca$_{1.5x}$Si$_6$N$_{11}$:Eu^{2+} ($x \approx 0.77$): A Promising Phosphor for Next-Generation Amber pcLEDs

authors: Christian Maak, Dajana Durach, Christoph Martiny, Peter J. Schmidt, and Wolfgang Schnick
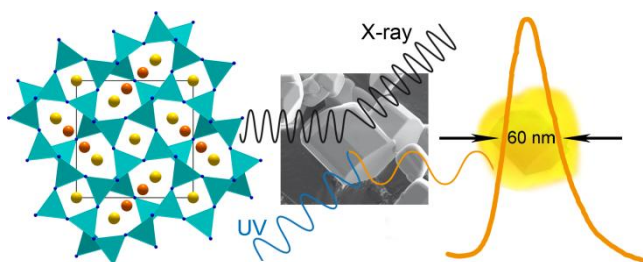
Abstract. The nitridosilicate La$_{3-x}$Ca$_{1.5x}$Si$_6$N$_{11}$:Eu^{2+} ($x \approx 0.77$) was synthesized in a radiofrequency furnace starting from LaF$_3$, La(NH$_2$)$_3$, CaH$_2$, Si(NH)$_2$, and EuF$_3$. The crystal structure was solved and refined from single-crystal X-ray data in the tetragonal space group $P4bm$ (no. 100) with $a = 10.1142(6)$, $c = 4.8988(3)$ Å, and $Z = 2$. Thereby, the so far unknown charge balance mechanism in the system (La,Ca)$_3$Si$_6$N$_{11}$, which is necessary as bivalent Ca^{2+} substitutes trivalent La^{3+}, was clarified. Accordingly, charge balance is achieved by incorporation of Ca^{2+} on three cation sites, including an additional third site compared to the homeotypic La$_3$Si$_6$N$_{11}$ structure type. The results are supported by Rietveld refinement on powder X-ray diffraction data as well as energy-dispersive X-ray spectroscopy. Fourier transform infrared spectroscopy indicates absence of N–H bonds. An optical band gap of ≈ 4.0 eV was determined using UV/Vis reflectance spectroscopy. The Eu^{2+} doped compound exhibits a remarkably narrow emission in the yellow-orange spectral range ($\lambda_{em} \approx 587$ nm, *fwhm* ≈ 60 nm/1700 cm^{-1}). Because of the intriguing yellow-orange luminescence, La$_{3-x}$Ca$_{1.5x}$Si$_6$N$_{11}$:Eu^{2+} ($x \approx 0.77$) is a promising candidate for application in next-generation amber phosphor-converted light emitting diodes.

3.1   Introduction

Since the invention of efficient blue light-emitting diodes (LEDs),[1] much progress has been made in the search for suitable down-conversion materials, bringing phosphor-converted LEDs (pcLEDs) into widespread applications.[2–6] Due to enhanced efficiency, lifetime, and sustainability, warm white pcLEDs have been replacing traditional incandescent light bulbs and fluorescent lamps.[7] However, there is still need for luminescent materials (phosphors) with improved luminescence properties to improve pcLEDs for general lighting and other special applications. In recent years, particular attention was paid to the discovery and investigation of phosphors with narrow-band emission. Narrow-band red emitting phosphors, for example, are required for general lighting to obtain energy-saving white pcLEDs with high color rendition. The high energy-saving potential of such phosphors arises from the decreased spillover with the infrared range[8] compared to commercially established red phosphors such as (Sr,Ca)AlSiN$_3$:Eu^{2+}.[9]   In   this   context,   nitridomagnesosilicates   such   as Li$_2$Ca$_2$[Mg$_2$Si$_2$N$_6$]:Eu^{2+} and   Sr[Mg$_3$SiN$_4$]:Eu^{2+},   nitridolithoaluminates   such   as Sr[LiAl$_3$N$_4$]:Eu^{2+}, Sr$_4$[LiAl$_{11}$N$_{14}$]:Eu^{2+} and Ca$_{18.75}$Li$_{10.5}$[Al$_{39}$N$_{55}$]:Eu^{2+}, and nitridomagneso-aluminates such as Sr[Mg$_2$Al$_2$N$_4$]:Eu^{2+} attracted a lot of attention.[10–15] Furthermore, novel narrow-band   green   emitting   phosphors   such   as   the   nitridolithoalumosilicates Ba[Li$_2$(Al$_2$Si$_2$)N$_6$]:Eu^{2+} and Ba$_2$LiSi$_7$AlN$_{12}$:Eu^{2+} were reported.[16,17] These phosphors are promising candidates for white pcLEDs in LCD backlighting applications, as the color gamut in the green spectral range is enhanced.[8] Besides the need for narrow-band red or green phosphors, narrow-band yellow-orange phosphors are of interest for fabrication of amber pcLEDs with high color purity and luminous efficacy. Performance of state-of-the-art amber emitting pcLEDs is limited due to the broad emission band of typically used (Ba,Sr)$_2$Si$_5$N$_8$:Eu^{2+} (*fwhm* $\approx$ 90–100 nm).[18,19] Up to now, no narrow-band yellow-orange phosphors have been reported.

Next to the above-named compound classes, nitridosilicates are auspicious candidates to overcome this deficiency. A familiar representative of this compound class, known for over 20 years,   is   La$_3$Si$_6$N$_{11}$.[20]   Luminescence   properties   of   La$_3$Si$_6$N$_{11}$:Ce^{3+} have   been intensively studied, as this yellow phosphor with a broad Ce^{3+} emission is a promising candidate for warm white pcLEDs.[21–23] Improved emission properties and synthesis by addition of alkaline earth metals have been reported for (La,*AE*)$_3$Si$_6$N$_{11}$:Ce^{3+} (*AE* = Ca, Sr, Ba).[24,25] However, structure–property relationships have not been discussed properly, and it remains unclear where the alkaline earth ions are incorporated as well as how

charge balance is achieved in this system. Furthermore, the question arises if such materials may also be suitable host lattices for Eu^{2+} as activator.

In this contribution, we report on the synthesis and characterization of the nitridosilicate La$_{3-x}$Ca$_{1.5x}$Si$_6$N$_{11}$ ($x \approx 0.77$), thereby clarifying the structural effects of Ca-substitution into La$_3$Si$_6$N$_{11}$. Additionally, Eu^{2+}-doped samples exhibit intriguing luminescence properties in the yellow-orange spectral range. This makes La$_{3-x}$Ca$_{1.5x}$Si$_6$N$_{11}$:Eu^{2+} ($x \approx 0.77$) a promising phosphor for next-generation amber pcLEDs.

3.2 Experimental Section

3.2.1 Synthesis

All synthesis steps were performed under exclusion of moisture and oxygen either in an argon-filled glovebox (Unilab, MBraun, Garching; O$_2$ < 1 ppm; H$_2$O < 1 ppm) or in flame-dried glassware on a Schlenk line attached to a vacuum line. La$_{3-x}$Ca$_{1.5x}$Si$_6$N$_{11}$ ($x \approx 0.77$) was synthesized from LaF$_3$ (0.31 mmol, 61.2 mg; Sigma-Aldrich, 99.99%), La(NH$_2$)$_3$ (0.33 mmol, 61.1 mg),[26] CaH$_2$ (1.46 mmol, 61.5 mg; Materion, 99.7%), and Si(NH)$_2$ (1.84 mmol, 106.7 mg).[27] Starting materials were thoroughly ground in an agate mortar and filled into a tungsten crucible. Then, the crucible was placed in a water-cooled silica glass reactor of a radiofrequency furnace (type AXIO 10/450, maximal electrical output 10 kW, Hüttinger Elektronik, Freiburg) heated under purified N$_2$-atmosphere to 800 °C for 0.5 h and then to 1650 °C within 5 min, maintained at that temperature for 10 h, cooled to 900 °C for 5 h, and finally quenched to room temperature by switching off the furnace. The resulting product consists of colorless crystals of La$_{3-x}$Ca$_{1.5x}$Si$_6$N$_{11}$ ($x \approx 0.77$). Addition of EuF$_3$ (Sigma-Aldrich, 99.99%) to the starting materials yielded yellow to orange powders of La$_{3-x}$Ca$_{1.5x}$Si$_6$N$_{11}$:Eu^{2+}, dependent on the dopant concentration. Samples with dopant concentrations of 1, 2, and 4 mol% (0.015 mmol, 3.1 mg; 0.03 mmol, 6.2 mg; 0.06 mmol, 12.3 mg EuF$_3$) related to Ca were synthesized. All samples show strong yellow-orange luminescence under irradiation with blue light. The doped and nondoped compounds are highly stable toward air, water, and concentrated mineral acids.

3.2.2   Electron Microscopy

The chemical composition and morphology of La$_{3-x}$Ca$_{1.5x}$Si$_6$N$_{11}$:Eu^{2+} ($x \approx 0.77$) samples were examined with a scanning electron microscope (SEM) NanoLab G3 (Helios). The samples were carbon-coated (BAL-TEC MED 020, Bal Tec AG) to prevent electrostatic charging. Energy dispersive X-ray (EDX) measurements were performed with an acceleration voltage of 20 kV using an X-Max 80 SDD detector (Oxford Instruments).

3.2.3   Fourier Transform Infrared Spectroscopy

Fourier transform infrared (FTIR) spectroscopy on La$_{3-x}$Ca$_{1.5x}$Si$_6$N$_{11}$:Eu^{2+} ($x \approx 0.77$) was carried out with a Jasco FT/IR-4100 spectrometer using the ATR method.

3.2.4   Single-Crystal X-ray Diffraction

Single crystals of La$_{3-x}$Ca$_{1.5x}$Si$_6$N$_{11}$:Eu^{2+} ($x \approx 0.77$) were isolated and mounted on MicroMounts (MiTeGen) with an aperture size of 20 µm. X-ray diffraction (XRD) data were measured with a Bruker D8 Venture diffractometer with rotating anode (Mo Kα radiation). An absorption correction was executed using SADABS.[28] The crystal structure was solved using Direct Methods (SHELXS)[29] and refined by least-squares method (SHELXL).[30,31] Details on the crystal structure investigation can be obtained from the Cambridge Crystallographic Data Centre (CCDC) upon quoting the CCDC code 1821482.

3.2.5   Powder X-ray Diffraction

For powder diffraction (PXRD) measurements, samples were ground and loaded into glass capillaries with 0.2 mm diameter and a wall thickness of 0.01 mm (Hilgenberg GmbH, Malsfeld, Germany). Diffraction data were obtained using a STOE STADI P diffractometer (Mo Kα_1 radiation, Ge(111) monochromator, Mythen1K detector) in parafocusing Debye-Scherrer geometry. Rietveld refinements were carried out with TOPAS-Academic V4.1 software applying the fundamental parameters approach (direct convolution of source emission profiles, axial instrument contributions, crystallite size, and microstrain effects).[32–35] Absorption effects were corrected using the calculated absorption coefficient. Preferred orientation was handled with the spherical harmonics model of the fourth order.

3.2.6 UV/Vis Spectroscopy

A diffuse reflectance spectrum of nondoped La$_{3-x}$Ca$_{1.5x}$Si$_6$N$_{11}$ ($x \approx 0.77$) was measured with a Jasco V-650 UV/Vis spectrophotometer in the range of 200–800 nm with 1 nm step size. The device is equipped with a deuterium and a halogen lamp (Czerny-Turner monochromator with 1200 lines/mm concave grating, photomultiplier tube detector).

3.2.7 Luminescence

Photoluminescence measurements were performed on microcrystalline powder samples in PTFE sample holders using an in-house built system based on a 5.3 in. integrating sphere and a spectrofluorimeter equipped with a 150 W Xe lamp, two 500 mm Czerny-Turner monochromators, 1800 1/mm lattices, and 250/500 nm lamps, with a spectral range from 230 to 820 nm. The internal quantum efficiency (*IQE*) of the samples was determined by comparing integrated emission intensities and absorption at excitation wavelength with standard materials (BaSO$_4$, Merck p.a.; commercial (Sr,Ca)AlSiN$_3$:Eu^{2+}, Mitsubishi Chemical, and Y$_3$Al$_5$O$_{12}$:Ce^{3+}, Philips).

3.3 Results and Discussion

3.3.1 Synthesis and Chemical Analysis

For the synthesis of La$_{3-x}$Ca$_{1.5x}$Si$_6$N$_{11}$:Eu^{2+} ($x \approx 0.77$), highly reactive starting materials such as LaF$_3$, La(NH$_2$)$_3$, Si(NH)$_2$, and CaH$_2$ were used. An excess of CaH$_2$ had to be applied as Ca partially evaporates due to a high reaction temperature of 1650 °C. During the reaction, CaF$_2$ is formed on the inside of the water-cooled silica glass reactor, as is shown by PXRD analysis of the deposited powder (Figure S1). Consequently, fluorine was never detected in numerous EDX measurements. The synthesis route yields single crystals with size up to 40 μm. The morphology of the crystals is depicted in Figure 1. The obtained, averaged sum formula from EDX measurements is La$_{2.2(3)}$Ca$_{1.2(2)}$Si$_{5.9(4)}$N$_{10.7(8)}$. Therefore, the results are in good agreement with the stoichiometry refined from single-crystal XRD data. Furthermore, the EDX data show that Ca is homogeneously distributed in the sample, as similar values are obtained for 15 measurements on 15 different crystals. For detailed results of individual measurements, see Table S1. An EDX spectrum is exemplarily shown in Figure S2, illustrating that no significant amounts of oxygen and

no fluorine were detected. FTIR spectroscopy corroborates the absence of N–H groups (Figure S3).
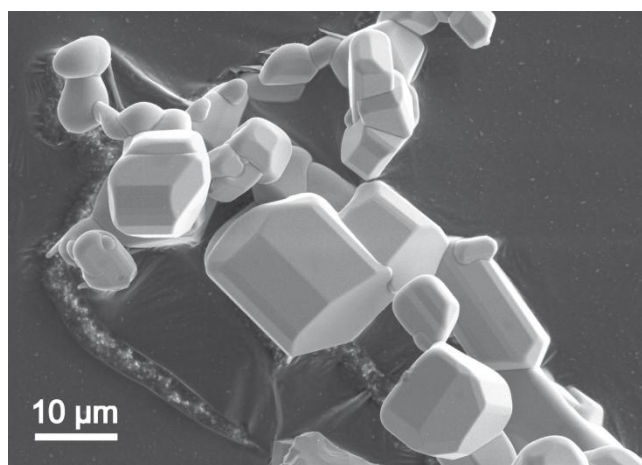
Figure 1. Representative SEM image for La$_{3-x}$Ca$_{1.5x}$Si$_6$N$_{11}$:Eu^{2+} ($x \approx 0.77$).

3.3.2   Crystal Structure

The crystal structure of La$_{3-x}$Ca$_{1.5x}$Si$_6$N$_{11}$:Eu^{2+} ($x \approx 0.77$) was solved and refined in the tetragonal space group *P*4*bm* (no. 100). The dopant Eu^{2+} was neglected during the refinement because of the small contribution (2 mol% referred to Ca) to the structure factor. All atoms were refined anisotropically. The crystallographic details are given in Table 1. Atomic coordinates, isotropic displacement parameters, and site occupancy factors (Table S2) as well as anisotropic displacement parameters (Table S3) are summarized in the Supporting Information. The crystal structure of La$_{3-x}$Ca$_{1.5x}$Si$_6$N$_{11}$:Eu^{2+} ($x \approx 0.77$) exhibits a three-dimensional network of all side vertex sharing (Q^4-type) SiN$_4$ tetrahedra and a degree of condensation of $\kappa = 0.545$. The nitridosilicate network contains twofold bridging (N$^{[2]}$) and threefold bridging (N$^{[3]}$) N atoms. The SiN$_4$ tetrahedra are condensed to *vierer* and *achter* rings, forming planes perpendicular to [001] (Figures 2a and b).[36,37] These planes are interlinked by pairs of vertex sharing SiN$_4$ tetrahedra (Figure 2c). Therefore, the 3D anionic network in La$_{3-x}$Ca$_{1.5x}$Si$_6$N$_{11}$:Eu^{2+} is topologically equivalent with that in La$_3$Si$_6$N$_{11}$. However, both phases differ in the number of heavy cation sites. Whereas the La$_3$Si$_6$N$_{11}$ structure type exhibits only two cation sites for La atoms, there are three crystallographically independent cation sites in La$_{3-x}$Ca$_{1.5x}$Si$_6$N$_{11}$:Eu^{2+}. Accordingly, both structures are homeotypic. The La2,Ca2 site in La$_{3-x}$Ca$_{1.5x}$Si$_6$N$_{11}$:Eu^{2+} is coordinated by eight N atoms in a slightly distorted quadratic antiprism arrangement, analogous to La$_3$Si$_6$N$_{11}$. The second site is described by a split

position La,Ca1A/La,Ca1B, which is coordinated by eight (La,Ca1A) or seven (La,Ca1B) N atoms, respectively.

Table 1. Crystallographic Data of the Single-Crystal Structure Determination of La$_{3-x}$Ca$_{1.5x}$Si$_6$N$_{11}$ (x = 0.77).

formula	La$_{2.23}$Ca$_{1.16}$Si$_6$N$_{11}$
formula mass / g·mol^{-1}	678.42
crystal system	Tetragonal
space group	$P4bm$ (no. 100)
lattice parameters / Å	a = 10.1142(6), c = 4.8988(3)
cell volume / Å^3	501.13(7)
formula units/unit cell	2
X-ray density / g·cm^{-3}	4.496
abs. coefficient / μ·mm^{-1}	10.663
absorption correction	multiscan[28]
temperature / K	295(2)
diffractometer	Bruker D8 Venture
radiation / Å	Mo Kα (λ = 0.71073)
F(000)	622
θ range / °	4.030 ≤ θ ≤ 32.469
independent reflections	947 (R_{int} = 0.0307)
refined parameters/restraints	68/4
GoF	1.173
$R$1 (all data/for $I > 2\sigma(I)$)	0.0162/0.0162
wR2 (all data/for $I > 2\sigma(I)$)	0.0372/0.0372
$\Delta\rho_{max}$, $\Delta\rho_{min}$ / e·Å^{-3}	0.855, −1.751

The splitting of the La1/Ca1 position in La$_{3-x}$Ca$_{1.5x}$Si$_6$N$_{11}$ results from the statistical incorporation of Ca^{2+} on an under-occupied third cation site. The La,Ca1A site in La$_{3-x}$Ca$_{1.5x}$Si$_6$N$_{11}$, which corresponds to the La1 site in La$_3$Si$_6$N$_{11}$, is split to avoid short La,Ca1A–Ca3 distances of only 2.7347(1) Å. The Ca3 site is coordinated by six N atoms. The coordination of the three cation sites is illustrated in Figure 3. Atomic distances for the heavy cation surroundings are shown in Table S4. To obtain charge neutrality, sum formula constraints were applied during the refinement. Thereby, a mixed occupancy with La and Ca was refined for the sites La,Ca1A/La,Ca1B and La2,Ca2. As the additional third cation site is under-occupied, it cannot be determined with certainty whether this position is occupied by La, Ca, or mixed-occupied. However, single-crystal XRD data

strongly indicate that this site is solely occupied with Ca atoms. Refinement of La on this site leads to significantly worse R values and physically implausible displacement parameters of Si and N atoms. Additionally, the atomic ratio La:Ca obtained when La is refined on the third site does not match the EDX results. The XRD data together with EDX data clearly show that charge balance in La$_{3-x}$Ca$_{1.5x}$Si$_6$N$_{11}$ is achieved by incorporation of Ca^{2+} on the two cation sites also present in La$_3$Si$_6$N$_{11}$ as well as on an additional third site.
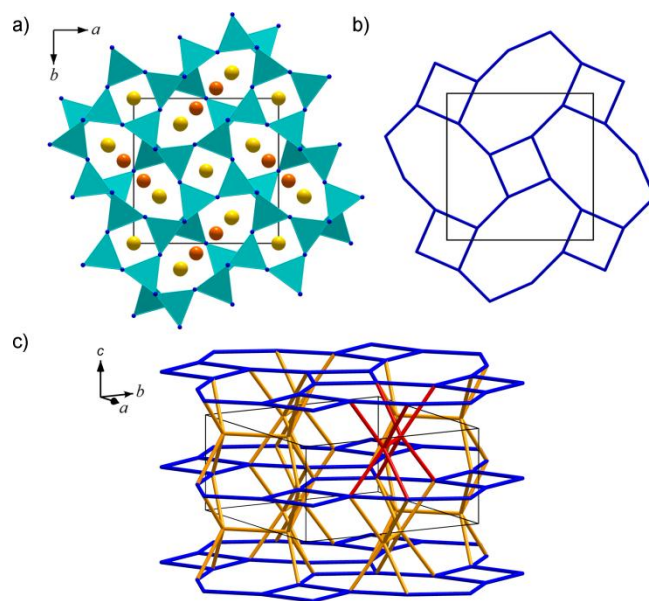
Figure 2. (a) Crystal structure of La$_{3-x}$Ca$_{1.5x}$Si$_6$N$_{11}$:Eu^{2+} in projection along [001] with SiN$_4$ tetrahedra (turquoise), N atoms (blue), La,Ca atoms (yellow), and Ca atoms (orange). (b) Topological representation of layers formed by *achter* and *vierer* rings (blue). (c) Topological representation with layer-linking pairs (yellow, one unit highlighted in red). Unit cell shown in black.
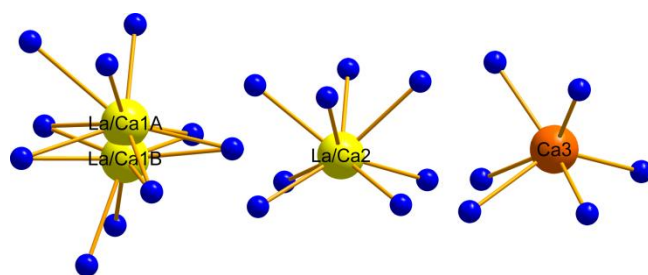
Figure 3. Coordination spheres of the heavy atom sites in La$_{3-x}$Ca$_{1.5x}$Si$_6$N$_{11}$:Eu^{2+}. Mixed occupied La/Ca sites are yellow, Ca orange, and N atoms blue.

The Si–N bond lengths [1.704(2)–1.780(2) Å] are in good agreement with comparable compounds such as Ca$_2$Si$_5$N$_8$ [1.671(5)–1.796(4) Å][38] and Sr$_2$Si$_5$N$_8$ [1.653(9)–

1.786(5) Å].[39] The La/Ca–N [2.556(3)–2.917(4) Å] and Ca–N [2.462(4)–2.674(9) Å]
distances also correspond to those in other La and Ca nitridosilicates.[20,38] To determine
the composition of the samples as well as the accuracy of the structure elucidation from
single-crystal XRD data, Rietveld refinements of PXRD data were carried out. The
refinements (Figure S4, Table S5) show that the described synthesis route yields single-
phase products of La$_{3-x}$Ca$_{1.5x}$Si$_6$N$_{11}$:Eu^{2+} ($x \approx 0.77$).

3.3.3   UV/Vis Spectroscopy

The optical band gap was determined for a nondoped sample of La$_{3-x}$Ca$_{1.5x}$Si$_6$N$_{11}$
($x \approx 0.77$) by means of UV/Vis spectroscopy. Due to the absorption of the host lattice, the
reflectance spectra show a broad absorption band around 285 nm (Figure S5). This
corresponds to the colorless sample. For determination of the optical band gap, the
reflectance (R) spectrum was converted to pseudoabsorption with the Kubelka-Munk
function $F(R) = (1 - R)^2/2R$.[40] Then, a Tauc plot was used to determine the band gap by
drawing a line tangent at the inflection point (Figure 4).[41] The evaluated band gap of
La$_{3-x}$Ca$_{1.5x}$Si$_6$N$_{11}$ ($x \approx 0.77$) is approximately 4.0 eV. For the calculations, the Kubelka-
Munk exponent $n = 1/2$ was chosen, assuming a direct allowed transition as was reported
elsewhere for La$_3$Si$_6$N$_{11}$.[42] The calculated band gap of 4 eV for La$_3$Si$_6$N$_{11}$ (using HSE06
functional) is comparable to that of La$_{3-x}$Ca$_{1.5x}$Si$_6$N$_{11}$ ($x \approx 0.77$).[23]
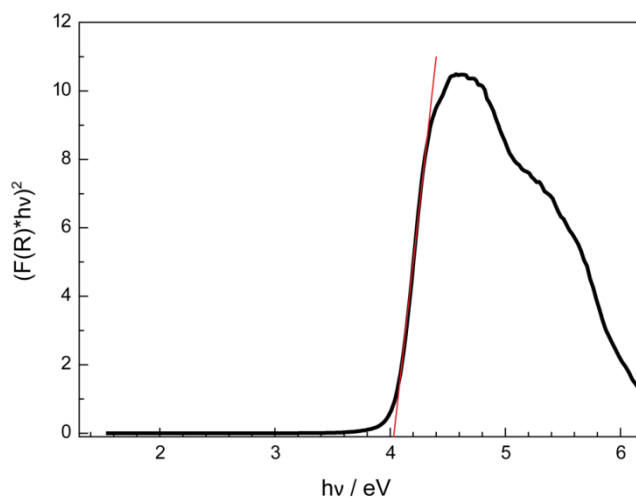
Figure 4. Tauc plot ($n = 1/2$) for nondoped La$_{3-x}$Ca$_{1.5x}$Si$_6$N$_{11}$ ($x \approx 0.77$).

3.3.4   Luminescence

Luminescence measurements were performed on thick bed powder samples of Eu^{2+} doped La$_{3-x}$Ca$_{1.5x}$Si$_6$N$_{11}$ ($x \approx 0.77$). Excitation of the samples with UV to blue light leads to a remarkably narrow emission in the yellow-orange spectral range. The excitation and emission spectra of a sample with a nominal doping content of 1 mol% referred to Ca are shown in Figure 5. The excitation spectrum shows a maximum at around 435 nm. Therefore, the phosphor can be effectively excited by an (In,Ga)N-LED. The emission spectrum peaks at 587 nm and exhibits a full width at half-maximum (*fwhm*) of $\approx$ 60 nm/1700 cm^{-1}. The color coordinates (CIE) are $x = 0.553$ and $y = 0.441$. As depicted by Figure 3, the title compound provides a highly symmetric, quadratic antiprismatic coordination around site La/Ca2 with eight almost identical La/Ca–N distances (Table S4). The coordination is comparable to that in the narrow-band green emitting phosphor Ba[Li$_2$(Al$_2$Si$_2$)N$_6$]:Eu^{2+}.[16] This symmetric coordination sphere probably leads to the remarkably narrow yellow-orange emission of La$_{3-x}$Ca$_{1.5x}$Si$_6$N$_{11}$:Eu^{2+} ($x \approx 0.77$). We assume that the Eu^{2+} atoms (ionic radius: 125 pm for 8-fold coordination)[43] preferably occupy the La2,Ca2 site. For increasing dopant concentrations, the occupation of the La,Ca1A/La,Ca1B and Ca3 site also increases. This can be observed in the excitation and emission spectra (Figure 6, lines) of samples with different doping concentrations (1, 2, and 4 mol% Eu referred to Ca). Although λ_{em} (587 nm) and the *fwhm* ($\approx$ 60 nm/1700 cm^{-1}) remain constant, the shapes of the emission spectra change. According to the partially shorter Eu–N distances on the sites La,Ca1 and Ca3, the emission exhibits additional intensity in the red spectral range for larger dopant concentrations. In the corresponding excitation spectra (Figure 6, dotted lines), an additional peak arises around 500 nm.
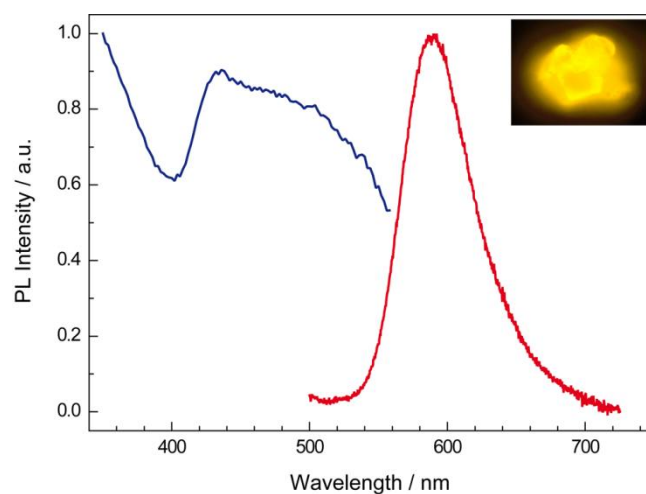
Figure 5. Excitation (blue) and emission (red, λ_{exc} = 440 nm) spectra of La$_{3-x}$Ca$_{1.5x}$Si$_6$N$_{11}$:Eu^{2+} ($x \approx 0.77$) bulk material with a nominal dopant concentration of 1%.

The internal quantum efficiency (*IQE*) is rather low for all samples, showing a further decrease for increasing nominal dopant concentrations. The determined *IQE* values are 11.4% (1 mol% Eu), 8.6% (2 mol% Eu), and 8.0% (4 mol% Eu), respectively. The low efficiencies probably result from reabsorption of the Eu^{2+} emission from the La2/Ca2 site by Eu^{2+} on the sites La,Ca1A/La,Ca1B and/or Ca3 as well as energy transfer to these sites, whose lowest lying absorption states overlap with the main emission energy. This is also indicated by the large rest absorption values (17–19%) observed in the diffuse reflection spectra in the emission range. Consequently, the highest *IQE* is observed for the sample with the smallest Eu^{2+} concentration.
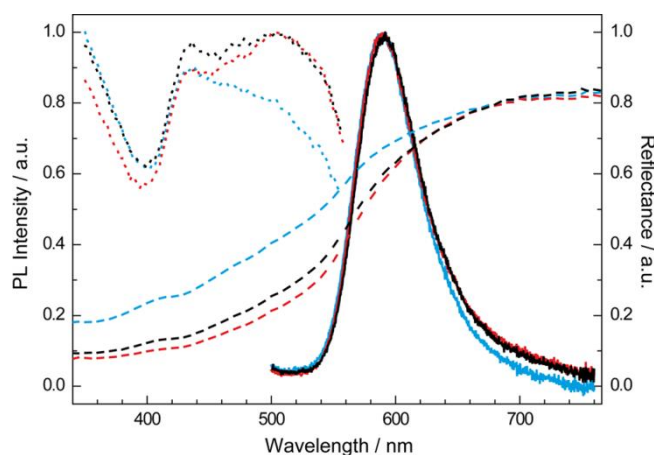
Figure 6. Excitation (dotted line), emission (line), and diffuse reflectance (dashed line) spectra of La$_{3-x}$Ca$_{1.5x}$Si$_6$N$_{11}$:Eu^{2+} ($x \approx 0.77$) for varying Eu concentrations (1 mol%: cyan; 2 mol%: black; 4 mol%: red).

To quantify the influence of thermal quenching to the low *IQE*, temperature-dependent measurements were conducted from 6 to 300 K for a sample with 1 mol% Eu. The integrated luminescence intensity shows a strong drop starting at around 100 K (Figure 7), and a relative increase of the long wavelength tail emission intensity is observed (Figure 8, see also Figures S6 and S7). At room temperature, the relative emission intensity is about one-third of the intensity at 6 K. Therefore, at 6 K, the *IQE* of the phosphor is still rather low with approximately 34%. This indicates that the main issue to increase the *IQE* of the phosphor is to decrease the large reabsorption and consequently to prevent the occupation of the sites La,Ca1A/La,Ca1B and Ca3 by Eu^{2+}. The emission wavelength of La$_{3-x}$Ca$_{1.5x}$Si$_6$N$_{11}$:Eu^{2+} ($x \approx 0.77$) resembles that of the oxonitrido-alumosilicate CaSi$_9$Al$_3$ON$_{15}$:Eu^{2+} (Ca-α-SiAlON, λ_{em} = 581 nm, *fwhm* $\approx$ 2890 cm^{-1})[44,45] and the oxonitridosilicate oxide Lu$_4$Ba$_2$[Si$_9$ON$_{16}$]O:Eu^{2+} (λ_{em} = 586 nm, *fwhm* = 2530 cm^{-1}).[46] It

is also comparable to amber emitting $(Ba,Sr)_2Si_5N_8$:Eu^{2+} ($\lambda_{em} \approx 590$–625 nm, *fwhm* ≈ 2050–2600 cm^{-1}), a phosphor used, for example, in warning signs or automotive turn signals.[18,19] Compared to all above named materials, $La_{3-x}Ca_{1.5x}Si_6N_{11}$:$Eu^{2+}$ ($x \approx 0.77$) exhibits a significantly more narrow emission in the yellow-orange spectral range.
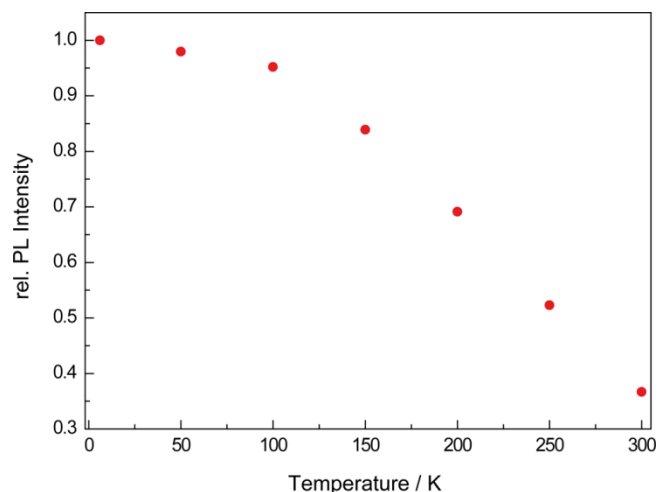
Figure 7. Relative integrated emission intensity of $La_{3-x}Ca_{1.5x}Si_6N_{11}$:$Eu^{2+}$ ($x \approx 0.77$) with 1 mol% Eu (nominal).
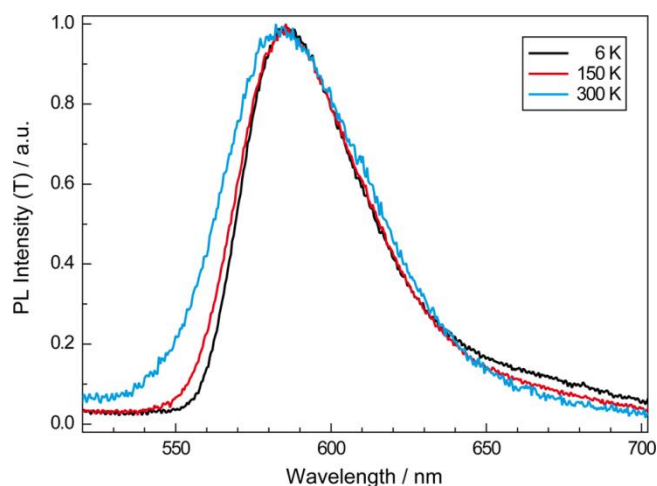
Figure 8. Normalized temperature dependent emission spectra for $La_{3-x}Ca_{1.5x}Si_6N_{11}$:$Eu^{2+}$ ($x \approx 0.77$) with 1 mol% Eu (nominal).

3.4 Conclusion

In this contribution, we reported on the crystal structure and luminescence properties of the nitridosilicate La$_{3-x}$Ca$_{1.5x}$Si$_6$N$_{11}$:Eu^{2+} ($x \approx$ 0.77). The crystal structure and composition refined from single-crystal X-ray data are supported by powder X-ray diffraction data and EDX spectroscopy. Accordingly, the structure is homeotypic to that of the commercially used yellow phosphor La$_3$Si$_6$N$_{11}$:Ce^{3+}. Ca atoms are incorporated on the two La sites also present in La$_3$Si$_6$N$_{11}$:Ce^{3+} as well as on an additional third site. An optical band gap of 4.0 eV was determined by means of UV/Vis spectroscopy. The Eu^{2+} doped compound shows intense luminescence ($\lambda_{em} \approx$ 587 nm, *fwhm* $\approx$ 60 nm/1700 cm^{-1}) in the yellow-orange spectral range when excited by UV to blue light. The internal quantum efficiency is probably limited by large reabsorption of the synthesized bulk materials as well as strong thermal quenching due to more efficient energy transfer to energetically lower lying Eu^{2+} centers at higher temperatures. It is the subject of further research to investigate the influence of different synthesis conditions, Ca contents or incorporation of Mg/Sr/Ba instead of Ca on the luminescence properties, rest absorption, and thermal quenching. The emission of La$_{3-x}$Ca$_{1.5x}$Si$_6$N$_{11}$:Eu^{2+} ($x \approx$ 0.77) is significantly more narrow compared to all known yellow-orange phosphors such as Ca-α-SiAlON, Lu$_4$Ba$_2$[Si$_9$ON$_{16}$]O:Eu^{2+}, or (Ba,Sr)$_2$Si$_5$N$_8$:Eu^{2+}.[19,44–46] Luminescent materials with such a narrow yellow-orange emission are required to increase the color purity and luminous efficacy compared to state-of-the-art amber pcLEDs. Therefore, La$_{3-x}$Ca$_{1.5x}$Si$_6$N$_{11}$:Eu^{2+} ($x \approx$ 0.77) is a promising candidate for application in next-generation amber pcLEDs, which could be used for example in warning signs or automotive turn signals.

3.5   References

[1]   Heber, J. Nobel Prize 2014: Akasaki, Amano & Nakamura. *Nat. Phys.* **2014**, *10,*
      791.

[2]   Xie, R.-J.; Hirosaki, N.; Takeda, T. Rare-Earth Activated Nitride Phosphors:
      Synthesis, Luminescence and Applications. *Materials* **2010**, *3*, 3777–3793.

[3]   Narukawa, Y.; Narita, J.; Sakamoto, T.; Yamada, T.; Narimatsu, H.; Sano, M.;
      Mukai, T. Recent progress of high efficiency white LEDs. *Phys. Status Solidi A*
      2007, *204*, 2087–2093.

[4]   Höppe, H. A. Recent developments in the field of inorganic phosphors. *Angew.
      Chem., Int. Ed.* **2009**, *48*, 3572–3582; Aktuelle Entwicklungen auf dem Gebiet der
      anorganischen Leuchtstoffe. *Angew. Chem.* **2009**, *121*, 3626–3636.

[5]   Xia, Z.; Liu, Q. Progress in discovery and structural design of color conversion
      phosphors for LEDs. *Prog. Mater. Sci.* **2016**, *84*, 59–117.

[6]   Xia, Z.; Xu, Z.; Chen, M.; Liu, Q. Recent developments in the new inorganic solid-
      state LED phosphors. *Dalton Trans.* **2016**, *45*, 11214–11232.

[7]   Schubert, E. F.; Kim, J.-K. Solid-State Light Sources Getting Smart. *Science* **2005**,
      308, 1274–1278.

[8]   Pust, P.; Schmidt, P. J.; Schnick, W. A revolution in lighting. *Nat. Mater.* **2015**, *14,*
      454–458.

[9]   Watanabe, H.; Kijima, N. Crystal structure and luminescence properties of
      Sr$_x$Ca$_{1-x}$AlSiN$_3$:Eu^{2+} mixed nitride phosphors. *J. Alloys Compd.* **2009**, *475*, 434–439.

[10] Strobel, P.; Weiler, V.; Hecht, C.; Schmidt, P. J.; Schnick, W. Luminescence of the
      Narrow-band Red Emitting Nitridomagnesosilicate Li$_2$(Ca$_{1-x}$Sr$_x$)$_2$[Mg$_2$Si$_2$N$_6$]:Eu^{2+}
      (x = 0–0.06). *Chem. Mater.* **2017**, *29*, 1377–1383.

[11] Schmiechen, S.; Schneider, H.; Wagatha, P.; Hecht, C.; Schmidt, P. J.; Schnick, W.
      Toward New Phosphors for Application in Illumination-Grade White pc-LEDs: The
      Nitridomagnesosilicates Ca[Mg$_3$SiN$_4$]:Ce^{3+}, Sr[Mg$_3$SiN$_4$]:Eu^{2+}, and Eu[Mg$_3$SiN$_4$].
      Chem. Mater. **2014**, *26*, 2712–2719.

[12] Pust, P.; Weiler, V.; Hecht, C.; Tücks, A.; Wochnik, A. S.; Henß, A.-K.; Wiechert, D.;
      Scheu, C.; Schmidt, P. J.; Schnick, W. Narrow-band red-emitting Sr[LiAl$_3$N$_4$]:Eu^{2+} as
      a next-generation LED-phosphor material. *Nat. Mater.* **2014**, *13*, 891–896.

[13] Wilhelm, D.; Baumann, D.; Seibald, M.; Wurst, K.; Heymann, G.; Huppertz, H.
      Narrow-Band Red Emission in the Nitridolithoaluminate Sr$_4$[LiAl$_{11}$N$_{14}$]:Eu^{2+}. *Chem.
      Mater.* **2017**, *29*, 1204–1209.

[14] Wagatha, P.; Pust, P.; Weiler, V.; Wochnik, A. S.; Schmidt, P. J.; Scheu, C.; Schnick, W. Ca$_{18.75}$Li$_{10.5}$[Al$_{39}$N$_{55}$]:Eu^{2+} – Supertetrahedron Phosphor for Solid-State Lighting. *Chem. Mater.* **2016**, *28*, 1220–1226.

[15] Pust, P.; Hintze, F.; Hecht, C.; Weiler, V.; Locher, A.; Zitnanska, D.; Harm, S.; Wiechert, D.; Schmidt, P. J.; Schnick, W. Group (III) Nitrides M[Mg$_2$Al$_2$N$_4$] (M = Ca, Sr, Ba, Eu) and Ba[Mg$_2$Ga$_2$N$_4$] – Structural Relation and Nontypical Luminescence Properties of Eu^{2+} Doped Samples. *Chem. Mater.* **2014**, *26*, 6113–6119.

[16] Strobel, P.; Schmiechen, S.; Siegert, M.; Tücks, A.; Schmidt, P. J.; Schnick, W. Narrow-Band Green Emitting Nitridolithoalumosilicate Ba[Li$_2$(Al$_2$Si$_2$)N$_6$]:Eu^{2+} with Framework Topology *whj* for LED/LCD-Backlighting Applications. *Chem. Mater.* **2015**, *27*, 6109–6115.

[17] Takeda, T.; Hirosaki, N.; Funahshi, S.; Xie, R.-J. Narrow-Band Green-Emitting Phosphor Ba$_2$LiSi$_7$AlN$_{12}$:Eu^{2+} with High Thermal Stability Discovered by a Single Particle Diagnosis Approach. *Chem. Mater.* **2015**, *27*, 5892–5898.

[18] Höppe, H. A.; Lutz, H.; Morys, P.; Schnick, W.; Seilmeier, A. Luminescence in Eu^{2+}-doped Ba$_2$Si$_5$N$_8$: fluorescence, thermoluminescence, and upconversion. *J. Phys. Chem. Solids* **2000**, *61*, 2001–2006.

[19] Krames, M.; Mueller, G. O.; Mueller-Mach, R.; Bechtel, H.; Schmidt, P. J. Wavelength conversion for producing white light from high power blue led, *PCT Int. Appl.*. WO 2010131133 A1, 2010.

[20] Woike, M.; Jeitschko, W. Preparation and Crystal Structure of the Nitridosilicates Ln$_3$Si$_6$N$_{11}$ (Ln = La, Ce, Pr, Nd, Sm) and LnSi$_3$N$_5$ (Ln = Ce, Pr, Nd). *Inorg. Chem.* **1995**, *34*, 5105–5108.

[21] Kijima, N.; Seto, T.; Hirosaki, N. A New Yellow Phosphor La$_3$Si$_6$N$_{11}$:Ce^{3+} for White LEDs. *ECS Trans.* **2009**, *25(9)*, 247–252.

[22] Park, W. B.; Kwon, T. H.; Sohn, K.-S. Decay Behavior in Ce^{3+}-Doped La$_3$Si$_6$N$_{11}$ and Lu$_3$Al$_5$O$_{12}$ Phosphors. *J. Am. Ceram. Soc.* **2015**, *98*, 490–494.

[23] George, N. C.; Birkel, A.; Brgoch, J.; Hong, B.-C.; Mikhailovsky, A. A.; Page, K.; Llobet, A.; Seshadri, R. Average and Local Structural Origins of the Optical Properties of the Nitride Phosphor La$_{3-x}$Ce$_x$Si$_6$N$_{11}$ (0 < x ≤ 3). *Inorg. Chem.* **2013**, *52*, 13730–13741.

[24] Suehiro, T.; Hirosaki, N.; Xie, R.-J. Synthesis and Photoluminescent Properties of (La,Ca)$_3$Si$_6$N$_{11}$:Ce^{3+} Fine Powder Phosphors for Solid-State Lighting. *Appl. Mater. Interfaces*, **2011**, *3*, 811–816.

[25] Chen, Z.; Zhang, Q.; Li, Y.; Wang, H.; Xie, R.-J. A promising orange-yellow-emitting phosphor for high power warm-light white LEDs: Pure-phase synthesis and photoluminescence properties. *J. Alloys Compd.* **2017**, *715*, 184–191.

[26] Hadenfeldt, C.; Gieger, B.; Jacobs, H. Die Kristallstruktur von Lanthanamid, La(NH$_2$)$_3$. *Z. Anorg. Allg. Chem.* **1974**, *410*, 104–112.

[27] Lange, H.; Wötting, G.; Winter, G. Silicon Nitride - From Powder Synthesis to Ceramic Materials. *Angew. Chem., Int. Ed. Engl.* **1991**, *30,* 1579–1597; Siliciumnitrid - vom Pulver zum keramischen Werkstoff. *Angew. Chem.* **1991**, *103*, 1606–1625.

[28] Sheldrick, G. M. *SADABS, v. 2: Multi-Scan Absorption Correction*; Bruker-AXS: Billerica, MA, 2012.

[29] Sheldrick, G. M. *SHELXS-97: A Program for Crystal Structure Solution*; University of Göttingen: Göttingen, Germany, 1997.

[30] Sheldrick, G. M. *SHELXL-97: A Program for Crystal Structure Refinement*; University of Göttingen: Göttingen, Germany, 1997.

[31] Sheldrick, G. M. A short history of SHELX. *Acta Crystallogr., Sect. A: Found. Crystallogr.* **2008**, *64*, 112–122.

[32] Rietveld, H. M. A profile refinement method for nuclear and magnetic structures. *J. Appl. Crystallogr.* **1969**, *2*, 65–71.

[33] Coelho, A. A. *TOPAS, v. 4.1: A program for Rietveld refinement*; Coelho Software: Brisbane, Australia, 2007.

[34] Bergmann, J.; Kleeberg, R.; Haase, A.; Breidenstein, B. Advanced fundamental parameter model for improved profile analysis. *Mater. Sci. Forum* **2000**, *347–349*, 303–308.

[35] Cheary, R. W.; Coelho, A. A.; Cline, J. P. Fundamental Parameters Line Profile Fitting in Laboratory Diffractometers. *J. Res. Natl. Inst. Stand. Technol.* **2004**, *109*, 1–25.

[36] Liebau, F. *Structural Chemistry of Silicates*; Springer: Berlin, 1985.

[37] The term *vierer* (*achter*) ring was coined by Liebau and is derived from the German word "vierer" ("achter"); a *vierer* (*achter*) ring comprises four (eight) tetrahedra centers.

[38] Schlieper, T.; Schnick, W. Nitrido-silicate. I. Hochtemperatur-Synthesen und Kristallstrukturen von Ca$_2$Si$_5$N$_8$. *Z. Anorg. Allg. Chem.* **1995**, *621*, 1037–1041.

[39] Schlieper, T.; Milius, W.; Schnick, W. Nitrido-silicate. II. Hochtemperatur-Synthesen und Kristallstrukturen von Sr$_2$Si$_5$N$_8$ und Ba$_2$Si$_5$N$_8$. *Z. Anorg. Allg. Chem.* **1995**, *621*, 1380–1384.

[40] López, R.; Gómez, R. Band-gap energy estimation from diffuse reflectance measurements on sol-gel and commercial TiO$_2$: a comparative study. *J. Sol-Gel Sci. Technol.* **2012**, *61*, 1–7.

[41] Tauc, J.; Grigorovici, R.; Vancu, A. Optical Properties and Electronic Structure of Amorphous Germanium. *Phys. Status Solidi B* **1966**, *15*, 627–637.

[42] Jia, Y.; Miglio, A.; Poncé, S.; Gonze, X.; Mikami, M. First-principles Study of Ce^{3+} doped Lanthanum Silicate Nitride Phosphors: Neutral Excitation, Stokes Shift and Luminescent Center Identification. *Phys. Rev. B: Condens. Matter Mater. Phys.* **2016**, *93*, 1–11.

[43] Shannon, R. D. Revised effective ionic radii and systematic studies of interatomic distances in halides and chalcogenides. *Acta Crystallogr., Sect. A: Cryst. Phys., Diffr., Theor. Gen. Crystallogr.* **1976**, *32*, 751–767.

[44] Xie, R.-J.; Hirosaki, N.; Takeda, T.; Suehiro, T. On the performance enhancement of nitride phosphors as spectral conversion materials in solid state lighting. *ECS J. Solid State Sci. Technol.* **2013**, *2*, R3031–R3040.

[45] Xie, R.-J.; Hirosaki, N.; Sakuma, K.; Yamamoto, Y.; Mitomo, M. Eu^{2+} doped Ca-α-SiAlON: A yellow phosphor for white light-emitting diodes. *Appl. Phys. Lett.* **2004**, *84*, 5404–5406.

[46] Maak, C.; Niklaus, R.; Friedrich, F.; Mähringer, A.; Schmidt, P. J.; Schnick, W. Efficient Yellow-Orange Phosphor Lu$_4$Ba$_2$[Si$_9$ON$_{16}$]O:Eu^{2+} and Orange-Red Emitting Y$_4$Ba$_2$[Si$_9$ON$_{16}$]O:Eu^{2+}: Two Oxonitridosilicate Oxides with Outstanding Structural Variety. *Chem. Mater.* **2017**, *29*, 8377–8384.

4   Efficient Yellow-Orange Phosphor Lu$_4$Ba$_2$[Si$_9$ON$_{16}$]O:Eu^{2+} and Orange-Red Emitting Y$_4$Ba$_2$[Si$_9$ON$_{16}$]O:Eu^{2+}: Two Oxonitridosilicate Oxides with Outstanding Structural Variety

Abstract. The oxonitridosilicate oxides Y$_4$Ba$_2$[Si$_9$ON$_{16}$]O:Eu^{2+} and Lu$_4$Ba$_2$[Si$_9$ON$_{16}$]O:Eu^{2+} have been synthesized starting from *RE*F$_3$, *RE*$_2$O$_3$ (*RE* = Y, Lu), BaH$_2$, Si(NH)$_2$, and EuF$_3$ in a radiofrequency furnace at 1550 °C. The crystal structures were solved and refined from single-crystal X-ray data supported with Rietveld refinement on X-ray powder diffraction data. Both compounds are isotypic and crystallize in monoclinic space group *P*2$_1$/*c* (no. 14) with *Z* = 4 and *a* = 6.0756(2), *b* = 27.0606(9), *c* = 9.9471(3) Å, and *β* = 91.0008(8)° for *RE* = Y and *a* = 6.0290(3), *b* = 26.7385(12), *c* = 9.8503(5) Å, and *β* = 90.7270(30)° for *RE* = Lu. The unique crystal structure exhibits a three-dimensional network made up from Q^4-type SiN$_4$ and Q^3-type SiON$_3$ tetrahedra. Containing 4-fold bridging N$^{[4]}$ atoms in star-shaped units [N$^{[4]}$(SiN$_3$)$_4$] next to N$^{[3]}$, N$^{[2]}$, O$^{[1]}$, and noncondensed oxide ions, the title compounds illustrate the vast structural variety in (oxo)nitridosilicates. Under excitation with UV to blue light, Y$_4$Ba$_2$[Si$_9$ON$_{16}$]O:Eu^{2+} shows emission in the orange-red spectral range (*λ*$_{max}$ = 622 nm, full width at half-maximum (*fwhm*) ≈ 2875 cm^{-1}). Yellow-orange emitting Lu$_4$Ba$_2$[Si$_9$ON$_{16}$]O:Eu^{2+} (*λ*$_{max}$ = 586 nm,

fwhm ≈ 2530 cm^{-1}) exhibits high internal quantum efficiency (*IQE*) ≈ 85%. This makes Lu$_4$Ba$_2$[Si$_9$ON$_{16}$]O:Eu^{2+} a promising phosphor for low color rendering index (CRI) warm white phosphor converted light emitting diodes (pcLEDs).

4.1   Introduction

In recent years, light emitting diodes (LEDs) have been replacing traditional incandescent light bulbs and fluorescent tubes due to longer lifetime, higher energy efficiency, and improved sustainability. White LED light is most commonly generated by down-conversion using green and red emitting phosphors on top of a blue emitting (In,Ga)N-LED.[1–4] Red components used in pcLEDs (phosphor converted LEDs) are, for example, the nitridosilicates (Ba,Sr)$_2$Si$_5$N$_8$:Eu^{2+} and (Sr,Ca)AlSiN$_3$:Eu^{2+}.[5,6] However, these phosphors show broad emission bands (90–100 nm) leading to energy loss caused by emission in the infrared range. Therefore, narrow-band red emitting phosphors with reduced emission in the infrared range are of crucial importance in developing energy saving high CRI (color rendering index) pcLEDs.[7,8] Compounds with narrow-band red emission are nitridolithoaluminates such as Sr[LiAl$_3$N$_4$]:Eu^{2+} and Ca$_{18.75}$Li$_{10.5}$[Al$_{39}$N$_{55}$]:Eu^{2+} and nitridomagnesoaluminates like Sr[Mg$_2$Al$_2$N$_4$]:Eu^{2+}, as well as the nitridomagnesosilicates Li$_2$(Ca$_{1-x}$Sr$_x$)$_2$[Mg$_2$Si$_2$N$_6$]:Eu^{2+} and Sr[Mg$_3$SiN$_4$]:Eu^{2+} (SMS).[9–13] To the best of our knowledge, SMS is the most narrow red emitting Eu^{2+} doped nitride phosphor (λ_{em} = 615 nm, full width at half-maximum (*fwhm*) = 1170 cm^{-1}) reported so far. Because of the intriguing emission properties of known phosphors, novel (oxo)nitridosilicate compounds are promising materials for investigation and application in pcLEDs. A number of materials of this class of compounds also combine crucial properties for state-of-the-art phosphors like optical transparency, high thermal and chemical stability, low thermal quenching, and high conversion efficiency.[14,15] Recently, we reported on several novel (oxo)nitridosilicates(chlorides) synthesized by reaction of LaX_3 (X = F, Cl), AEH$_2$ (AE = Sr, Ba), and different silicon sources (e.g., Si(NH)$_2$, Si$_2$(NH)$_3$·6 NH$_4$Cl) in a radiofrequency furnace. The formation of highly stable binary salts AEX_2 from LaX_3 and AEH$_2$ is discussed to be the thermodynamic driving force of this reaction type.[16–18] Besides an intriguing structural chemistry of the formed silicates, La$_3$BaSi$_5$N$_9$O$_2$:Ce^{3+} is a promising phosphor for single phosphor luminescence conversion due to its quite broad yellow emission.[16]

In this contribution, we used the reaction type described above to synthesize the two oxonitridosilicates   Y$_4$Ba$_2$[Si$_9$ON$_{16}$]O:Eu^{2+} and   Lu$_4$Ba$_2$[Si$_9$ON$_{16}$]O:Eu^{2+}.   The materials

crystallize in a unique structure type and show strong orange-red and yellow-orange luminescence, respectively, when excited with UV to blue light. Especially the highly efficient Lu compound with emission in the yellow-orange spectral range seems promising for application in low CRI warm white pcLEDs.

4.2   Experimental Section

4.2.1   Synthesis

All steps were carried out in a glovebox (Unilab, MBraun, Garching; O$_2$ < 1 ppm; H$_2$O < 1 ppm) under argon atmosphere. For the synthesis of single crystals of Y$_4$Ba$_2$[Si$_9$ON$_{16}$]O:Eu^{2+} ([1]), YF$_3$ (0.40 mmol, 58.4 mg; Chempur, 99.999%), Y$_2$O$_3$ (0.04 mmol, 9.0 mg; Sigma-Aldrich, 99.999%), BaH$_2$ (0.76 mmol, 105.9 mg; Chemco, 99.7%), Si(NH)$_2$ (0.40 mmol, 23.3 mg),[19] and EuF$_3$ (0.004 mmol, 0.7 mg; Sigma-Aldrich, 99.99%) were ground in an agate mortar and filled into a tungsten crucible. Lu$_4$Ba$_2$[Si$_9$ON$_{16}$]O:Eu^{2+} ([2]) was synthesized from LuF$_3$ (0.35 mmol, 81.1 mg; Chempur, 99.9%), Lu$_2$O$_3$ (0.035 mmol, 13.9 mg; Chempur, 99.99%), BaH$_2$ (0.66 mmol, 92.6 mg), Si(NH)$_2$ (0.35 mmol, 20.3 mg),[19] and EuF$_3$ (0.003 mmol, 0.6 mg). Subsequently, the crucibles were placed in a water-cooled silica glass reactor of a radiofrequency furnace (type IG 10/600; Hüttinger Elektronik Freiburg). Crucibles were heated to 1550 °C for 3 h, maintained at 1550 °C for 9 h, cooled to 900 °C for 50 h, and finally quenched to room temperature. Reactions were carried out under N$_2$ atmosphere. Inhomogeneous reddish samples containing a few transparent yellowish crystals of [1] and [2], respectively, were obtained. Crystals from both reactions show strong orange-red ([1]) or yellow-orange ([2]) luminescence under excitation with blue light. Both compounds are stable toward air, water, and 6M hydrochloric acid. The yield of [1] was optimized by heating to 1500 °C for 1 h, maintaining for 8 h, and then quenching to room temperature. By additionally washing the product with 6M hydrochloric acid, [1] was obtained as single phase according to powder X-ray diffraction data with a yield of ≈ 20%.

4.2.2   Electron Microscopy

Chemical composition and morphology of crystals of [1] and [2] were investigated using a scanning electron microscope (SEM) JSM 6500F (JEOL). Energy dispersive X-ray (EDX) spectra were collected with a Si/Li EDX detector (Oxford instruments, model 7418) applying an acceleration voltage of 30 kV.

4.2.3   Fourier Transform Infrared Spectroscopy

A Fourier transform infrared (FTIR) spectrum of [**1**] was recorded with a Jasco FT/IR-4100 spectrometer using the ATR method.

4.2.4   Single-Crystal X-ray Diffraction

Single crystals of [**1**] and [**2**] were isolated from the inhomogeneous reaction mixtures and mounted on MicroMounts (MiTeGen) with an aperture size of 20 µm. Diffraction data of [**1**] were collected on a Bruker D8 Venture diffractometer with rotating anode. A single crystal of [**2**] was analyzed on a Bruker D8 Quest diffractometer with microfocus (both devices with Mo Kα radiation and Goebel mirror optics). Absorption correction was performed using SADABS.[20] The crystal structures were solved using Direct Methods (SHELXS)[21] and refined by least-squares method (SHELXL).[22,23] Details on crystal structure investigations may be obtained from the Fachinformationszentrum Karlsruhe, 76344 Eggenstein-Leopoldshafen, Germany (fax: (+49)7247–808–666; e-mail: crysdata@fiz-karlsruhe.de) upon quoting the Cambridge Structural Database depository numbers CSD-433302 for [**1**] and CSD-433303 for [**2**].

4.2.5   Powder X-ray Diffraction

Powder X-ray diffraction (PXRD) data of [**1**] and [**2**] were collected using a STOE STADI P diffractometer (Cu Kα_1 radiation, Ge(111) monochromator, Mythen1K detector) in parafocusing Debye-Scherrer geometry. Therefore, samples were loaded into glass capillaries with 0.1 mm diameter and a wall thickness of 0.01 mm (Hilgenberg GmbH, Malsfeld, Germany). Rietveld refinement was performed with TOPAS-Academic V4.1 software applying the fundamental parameter approach (direct convolution of source emission profiles, axial instrument contributions, crystallite size, and microstrain effects).[24–27] Absorption effects were corrected using the calculated absorption coefficient. Preferred orientation was handled with the spherical harmonics model of fourth order.

4.2.6   UV/Vis Spectroscopy

A diffuse reflectance spectrum of $Y_4Ba_2[Si_9ON_{16}]O$ was recorded on a Jasco V-650 UV/Vis spectrophotometer with a deuterium and a halogen lamp (Czerny-Turner monochromator

with 1200 lines/mm concave grating, photomultiplier tube detector). The spectrum was obtained in a range of 200 to 800 nm with 1 nm step size.

4.2.7 DFT Calculations

Structural relaxations were carried out with the *Vienna ab initio simulation package* (VASP).[28–30] Convergence of total energies of the unit cell ($< 10^{-7}$ eV/atom) and of residual atomic forces ($< 1 \times 10^{-2}$ eV/Å) was obtained. The exchange correlation was calculated within the generalized gradient approximation (GGA) of *Perdew*, *Burke*, and *Ernzerhof* (PBE)[31,32] and the projector-augmented-wave (PAW) method.[33,34] The plane-wave cutoff was set to 535 eV, and for sampling of the Brillouin zone, Γ-centered *k*-meshes of $9 \times 3 \times 6$ were obtained according to the method of Monkhorst and Pack.[35]

4.2.8 Luminescence

Single crystals of [**1**] and [**2**] as well as powder samples of [**1**] were investigated. Measurements on crystals were carried out with a HORIBA Fluoromax4 spectrofluorimeter system, attached via optical fibers to an Olympus BX51 microscope. Crystals were measured inside glass capillaries with $\lambda_{exc} = 440$ nm. The spectral width of the excitation wavelength at 440 nm was 10 nm. Emission spectra were captured with 2 nm step size in a wavelength range between 400 and 800 nm. Excitation spectra were obtained with monitoring wavelength of 636 ([**1**]) and 600 nm ([**2**]), respectively. Photoluminescence measurements on microcrystalline powder samples in PTFE sample holders were carried out using an in-house built system based on a 5.3 in. integrating sphere and a spectrofluorimeter equipped with a 150 W Xe lamp, two 500 mm Czerny-Turner monochromators, 1800 1/mm lattices, and 250/500 nm lamps, with a spectral range from 230 to 820 nm. Internal quantum efficiency (*IQE*) of [**1**] was determined by comparing integrated emission intensities and absorption at excitation wavelength with standard materials ($BaSO_4$, Merck p.a.; commercial $(Sr,Ca)AlSiN_3:Eu^{2+}$, Mitsubishi Chemical, and $Y_3Al_5O_{12}:Ce^{3+}$, Philips), according to equation 1.[36]

$$IQE = \frac{N_{emi}}{N_{abs}} = \frac{\int \frac{\lambda}{hc}[I_{emi}^{sample}(\lambda) - I_{emi}^{standard}(\lambda)]d\lambda}{\int \frac{\lambda}{hc}[I_{abs}^{sample}(\lambda) - I_{abs}^{standard}(\lambda)]d\lambda} \tag{1}$$

4.3   Results and Discussion

4.3.1   Synthesis and Chemical Analysis

The described synthesis procedure with a final cooling ramp of 50 h to 900 °C yielded single crystals of [**1**] and [**2**] for single-crystal X-ray diffraction analysis. Figure 1 shows the typical needle-like morphology of such crystals. EDX spectra were measured on different crystals of each phase. The results (Table 1) are in good accordance with the results from single-crystal structure refinement. No other elements were detected. The absence of N−H and O–H groups was checked by FTIR spectroscopy of [**1**] (Figure S1).
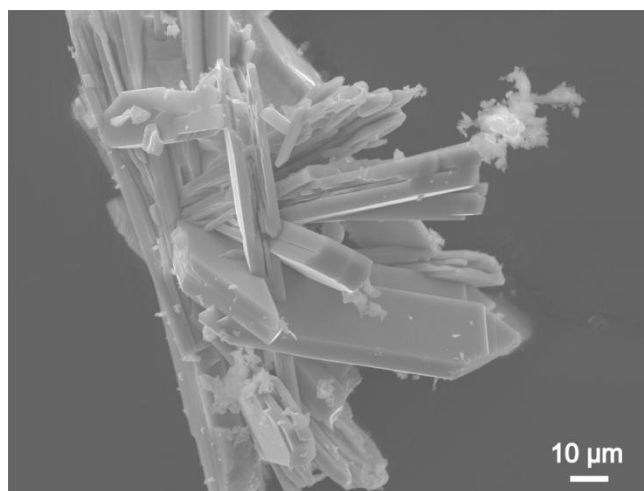
Figure 1. SEM image of Y$_4$Ba$_2$[Si$_9$ON$_{16}$]O:Eu^{2+}.

4.3.2   Crystal Structure

The crystal structures of [**1**] and [**2**] were solved (SHELXS-97) and refined (SHELXL-97) in space group $P2_1/c$ (no. 14).[21,22] The compounds are isotypic with $Z = 4$ and $a = 6.0756(2)$, $b = 27.0606(9)$, $c = 9.9471(3)$ Å, and $\beta = 91.0008(8)°$ for [**1**] and $a = 6.0290(3)$, $b = 26.7385(12)$, $c = 9.8503(5)$ Å, and $\beta = 90.7270(30)°$ for [**2**]. The smaller lattice parameters for the Lu containing phase originate from the smaller ionic radius of Lu^{3+} compared to Y^{3+} (lanthanide contraction).[37] Crystallographic data are summarized in Table 2. Atomic coordinates, Wyckoff positions, and isotropic displacements parameters (Tables S1 and S2) as well as anisotropic displacement parameters (Tables S3 and S4) are listed in the Supporting Information. Eu^{2+} content was not taken into account during

structure refinement. Due to low content and similar number of electrons compared to Ba^{2+}, its contribution to the scattering density is insignificant. Regarding the large ionic radius of Eu^{2+} (117 pm for coordination number (CN) = 6) compared to Y^{3+} (90 pm for CN = 6), we assume that Eu^{2+} (see chapter 4.3.4) occupies Ba^{2+} sites.[37]

Table 1. EDX Results.

	Theoretical atom%	Experimental atom%	
		RE = Y	*RE* = Lu
RE	12.1	10	12
Ba	6.1	5	6
Si	27.3	23	23
O	6.1	12	10
N	48.5	49	50

$RE_4Ba_2[Si_9ON_{16}]O:Eu^{2+}$ (*RE* = Y, Lu) compounds are built up by a three-dimensional network of vertex-sharing Q^4-type SiN_4 and Q^3-type SiN_3O tetrahedra (Figure 2). Ordering of O and N atoms is strongly supported by the refinement itself, as terminal and nonbridging anion sites could only be refined as O atoms (N atoms would have negative displacement parameters for [**1**] and are close to zero for [**2**]). These findings are confirmed by MAPLE[37–40] calculations (Table S5) and also agree with Pauling's rules.[41] Characteristic for the crystal structure are $[N^{[4]}(SiN_3)_4]$ building blocks, also referred to as star-shaped units, with 4-fold bridging $N^{[4]}$ atoms.[42] Furthermore, the network contains $N^{[3]}$ and $N^{[2]}$ atoms as well as terminal $O^{[1]}$ atoms, giving $[Si_9O^{[1]}N_{14}{}^{[2]}N^{[3]}N^{[4]}]^{14-}$ for the anionic network and a degree of condensation of $\kappa = 0.53$. With additional noncondensed oxide ions outside the network, $RE_4Ba_2[Si_9ON_{16}]O:Eu^{2+}$ (*RE* = Y, Lu) are to our knowledge the first (oxo)nitridosilicate compounds containing N or O atoms in connecting types ranging from $X^{[0]}$ to $X^{[4]}$. $[N^{[4]}(SiN_3)_4]$ building blocks are stacked along [001] with rotation of 180° forming highly condensed strands of star-shaped units (Figure 3b, A, green). These strands are interconnected in the *ac*-plane by $N^{[2]}$ atoms. The second type of strands (Figure 3c, B turquoise) consists of two less condensed units (Figure 3b, turquoise) compared to strand A. These units are connected by common corners and can be transformed into each other by inversion. Units building B strand can be derived from A strands by alternate replacement of $N^{[4]}$ atoms by $N^{[3]}$ and $N^{[2]}$ atoms. A and B strands are interconnected by $N^{[2]}$ atoms, leading to a 3D network. Orientation of both strands alternates according to a 2_1-screw-axis as can be seen in viewing direction [001], where tetrahedra tips of A strands either point into or out of the *ab*-plane (Figure 3a).

Table 2. Crystallographic Data of [**1**] and [**2**].

	$Y_4Ba_2[Si_9ON_{16}]O$	$Lu_4Ba_2[Si_9ON_{16}]O$
formula mass / g·mol^{-1}	1139.29	1483.53
crystal system	monoclinic	
space group	$P2_1/c$ (no. 14)	
cell parameters / Å, °	a = 6.0756(2)	a = 6.0290(3)
	b = 27.0606(9)	b = 26.7385(12)
	c = 9.9471(3)	c = 9.8503(5)
	β = 91.0008(8)	β = 90.727(3)
volume / Å^3	1635.15(9)	1587.80(13)
formula units / cell	4	
X-ray density / g·cm^{-3}	4.628	6.206
abs. coefficient / μ·mm^{-1}	19.489	30.248
F(000)	2088	2600
crystal dimensions / mm^3	0.030 × 0.030 × 0.010	0.087 × 0.075 × 0.047
diffractometer	D8 Venture	D8 Quest
radiation	Mo Kα (λ = 0.71073 Å)	
temperature / K	303(2)	296(2)
absorption correction	multiscan[20]	
θ range / °	3.011–36.34	2.285–32.032
observed reflections	30149	37062
independent reflections	6227 [R_{int} = 0.0350]	5514 [R_{int} = 0.0390]
independent reflection ($I \geq 2\sigma(I)$)	5313	5223
min./max. transmission	0.3735/0.4977	0.2828/0.4470
refined parameters	298	209
GoF	1.107	1.251
R indices ($F_o^2 \geq 2\sigma(F_o^2)$)	R_1 = 0.0273/wR_2 = 0.0542	R_1 = 0.0262/wR_2 = 0.0547
R indices (all data)	R_1 = 0.0375/wR_2 = 0.0565	R_1 = 0.0285/wR_2 = 0.0553
min./max. residual electron density / e·Å^{-3}	−1.634/1.876	−2.064/1.521

The presence of star-shaped $[N^{[4]}(SiN_3)_4]$ units has already been reported for $AERE[Si_4N_7]$ (AE = Sr, Ba, Eu; RE = Y, Yb, Lu)[43–47] and isotypic sialons $AERE[Si_{4-x}Al_xO_xN_{7-x}]$ (AE = Eu, Sr, Ba; RE = Ho, Er, Tm, Yb),[48,49] nitridoalumosilicate oxide $BaSm_5[Si_9Al_3N_{20}]O$,[42] and the nitridosilicates $CaRE[Si_9N_{17}]$ (RE = Sm, Yb).[50] The $BaYb[Si_4N_7]$ structure type exhibits further similarities to $RE_4Ba_2[Si_9ON_{16}]O:Eu^{2+}$ as $[N^{[4]}(SiN_3)_4]$ building blocks and their interconnection is equal for both structure types. In contrast to $RE_4Ba_2[Si_9ON_{16}]O:Eu^{2+}$, the 3D network in $BaYb[Si_4N_7]$ is exclusively made up of highly condensed strands of star-shaped units pointing into the same direction. This

leads to a higher degree of condensation ($\kappa = 0.57$) and noncentrosymmetric crystal symmetry ($P6_3mc$, no. 186) for the BaYb[Si$_4$N$_7$] structure type (Figure 4).[43]
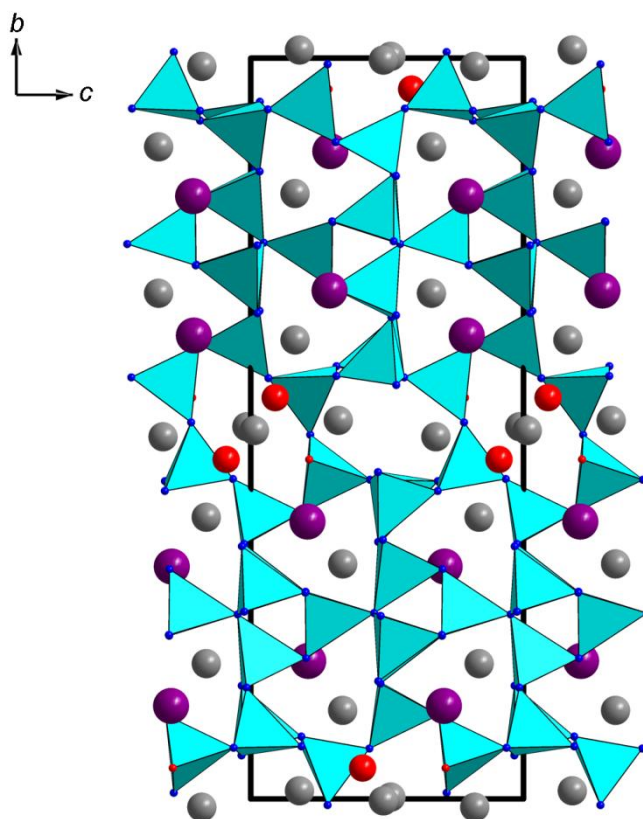
Figure 2. Crystal structure of RE_4Ba$_2$[Si$_9$ON$_{16}$]O:Eu^{2+} (RE = Y, Lu), view along [100] with SiN$_4$/SiN$_3$O tetrahedra (turquoise), N atoms (blue), O atoms (red), Y/Lu atoms (gray), and Ba atoms (violet). Unit cell outlined in black.

In RE_4Ba$_2$[Si$_9$ON$_{16}$]O:Eu^{2+} (RE = Y, Lu) compounds, the Si–N$^{[4]}$ distances range between 189.6(3) and 198.4(3) pm for [**1**] and 188.3(5) and 196.5(5) pm in the case of [**2**]. These values correspond well with Si–N$^{[4]}$ distances of 186–196 pm reported for BaYb[Si$_4$N$_7$].[43,44] The Si–N$^{[2]}$ and Si–N$^{[3]}$ distances range from 171 to 180 pm for RE = Y and from 169 to 180 pm for RE = Lu. The more ionic character of Si–O bonds compared to Si–N bonds leads to shorter Si–O$^{[1]}$ distances (167 pm for RE = Y, Lu). The Si−N$^{[3]}$/N$^{[2]}$/O$^{[1]}$ distances are in the typical ranges compared to other (oxo)nitridosilicates.[51,52] Summarizing, all equivalent Si–N/O bonds in [**2**] are slightly shorter than in [**1**] according to smaller lattice constants.
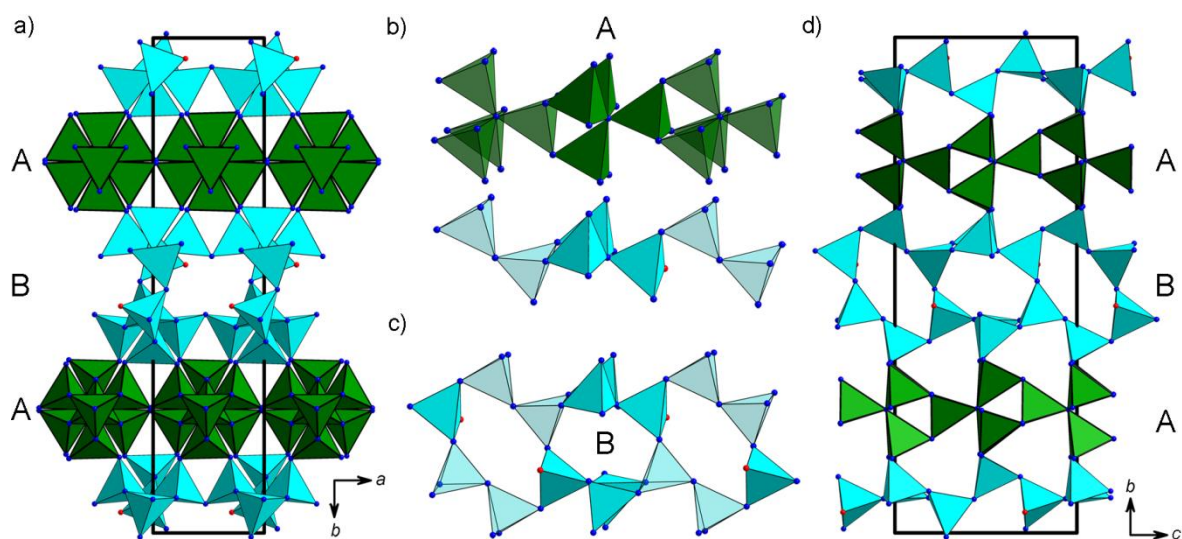
Figure 3. (a) Three-dimensional silicate network of RE_4Ba$_2$[Si$_9$ON$_{16}$]O:Eu^{2+} (RE = Y, Lu) along [001] with highly condensed strands of star-shaped [N$^{[4]}$(SiN$_3$)$_4$] units (A, green) and less condensed strands (B, turquoise). (b) A strands of [N$^{[4]}$(SiN$_3$)$_4$] units (green) and half a B strand (turquoise). (c) B strand. (d) Structure in projection along [100]. N atoms blue, O atoms red, and unit cell outlined in black.
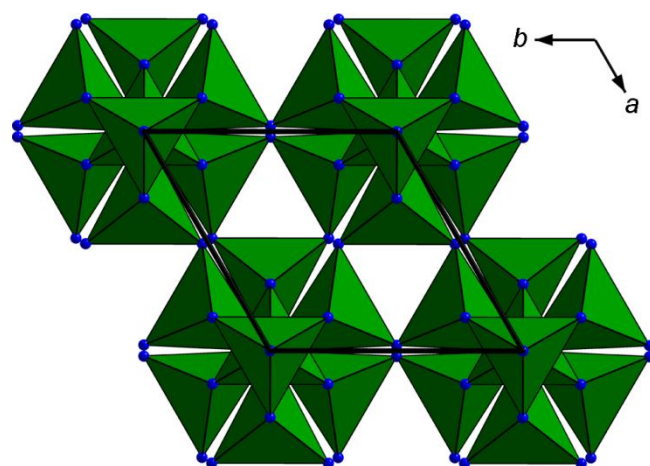
Figure 4. Silicate network of BaYb[Si$_4$N$_7$] along [001], SiN$_4$ tetrahedra green, N atoms blue, and unit cell outlined in black.

Ba and Y/Lu are ordered and occupy six crystallographically independent atom sites (Figure 5). Y1/Lu1, Y2/Lu2, and Y4/Lu4 are coordinated in a distorted octahedral way. Y1/Lu1 is exclusively coordinated by N, Y2/Lu2, and Y4/Lu4 sites by N and O atoms. The Y3/Lu3 site shows 7-fold coordination by N and O atoms forming a distorted, capped trigonal prismatic coordination. Ba1 site is coordinated by N in a distorted

anticuboctahedral way. The 10-fold coordination of Ba2 by N and O corresponds to no regular polyhedron. Y–N (231.1(3)–255.5(3) pm) and Y–O (214.2(2)–245.8(2) pm) distances are 5 and 2.5 pm longer on average than Lu–N (225.6(4)–252.5(4) pm) and Lu−O (211.1(4)–249.1(4) pm) bond lengths, respectively (Table S6).
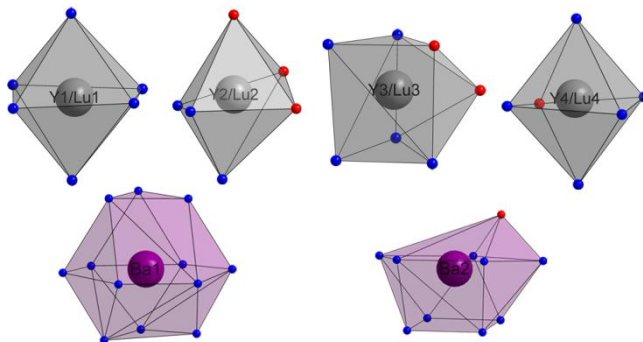
Figure 5. Coordination spheres of Y/Lu and Ba in $RE_4Ba_2[Si_9ON_{16}]O:Eu^{2+}$ (RE = Y, Lu).

Averaged Ba–N (284.6(4)–340.0(5) pm) distances in [**1**] are enlarged by 2.5 pm compared to Ba–N bond lengths (282.5(3)–344.0(3) pm) in [**2**]. In contrast, Ba–O bond length in [**1**] (267.2(2) pm) is slightly shorter compared to Ba–O (269.7(4) pm) in [**2**]. These values correspond to bond lengths reported for other yttrium, lutetium, and barium (oxo)nitridosilicates.[46,51–53] Rietveld refinements of $Y_4Ba_2[Si_9ON_{16}]O:Eu^{2+}$ (Figure S2) and $Lu_4Ba_2[Si_9ON_{16}]O:Eu^{2+}$ (Figure S3) samples support the structure models from single-crystal X-ray diffraction results. Data of the Rietveld refinements are summarized in Table S7.

4.3.3 UV/Vis Spectroscopy

Solid-state UV/Vis spectroscopy was exemplarily performed for both compounds with a nondoped sample of $Y_4Ba_2[Si_9ON_{16}]O$ as samples of $Lu_4Ba_2[Si_9ON_{16}]O$ contain large amounts of LuN (Figure S3). The reflectance spectrum (Figure S4) shows a broad absorption band in the UV region around 260 nm. In order to determine the optical band gap, the reflectance (R) spectrum was first converted to pseudoabsorption through Kubelka-Munk function $F(R) = (1 − R)^2/2R$.[54] Then, the band gap was determined using Tauc plot by drawing a line tangent at the inflection point (Figure 6).[55] The evaluated band gap of $Y_4Ba_2[Si_9ON_{16}]O$ is approximately 4.0 eV.
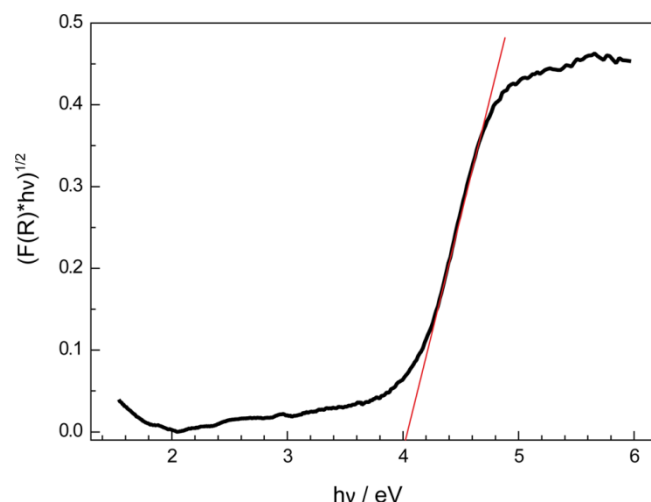
Figure 6. Tauc plot (*n* = 2) for nondoped Y$_4$Ba$_2$[Si$_9$ON$_{16}$]O.

For the calculations, the Kubelka-Munk exponent *n* = 2 for an indirect allowed transition
was chosen. The type of transition was determined from DFT calculations of the electronic
band structures of Y$_4$Ba$_2$[Si$_9$ON$_{16}$]O and Lu$_4$Ba$_2$[Si$_9$ON$_{16}$]O. The DFT calculations show
indirect band gaps (Figure 7) for both compounds and an increased band gap of 3.0 eV
for Lu$_4$Ba$_2$[Si$_9$ON$_{16}$]O compared to 2.8 eV for Y$_4$Ba$_2$[Si$_9$ON$_{16}$]O. The large difference
between calculation and experimental band gap for Y$_4$Ba$_2$[Si$_9$ON$_{16}$]O is caused by typical
underestimation of band gap values by the DFT method.[56]

4.3.4   Luminescence

The Eu^{2+}-doped oxonitridosilicate oxides [**1**] and [**2**] show strong luminescence when
excited with UV to blue light. The nominal Eu^{2+} content of investigated samples is 0.5%
related to Ba, as we assume that the activator occupies both Ba^{2+} sites. Measurements
were performed on nonoptimized samples regarding Eu^{2+} content. Single crystals of [**1**]
and [**2**] with the same nominal Eu^{2+} content and very similar morphology were selected for
luminescence studies in order to obtain comparable absorption and light propagation
properties. Shape and energetic position of excitation and emission spectra of single
crystals and powder samples of [**1**] are comparable (Figure S5). Therefore, only spectra of
single crystals are shown in Figure 8. The quite similar excitation spectra of [**1**] (dark blue)
and [**2**] (cyan) show absorption maxima around 410 nm. Hence, both phosphors are
effectively excited by UV to blue light of an (In,Ga)N-LED.
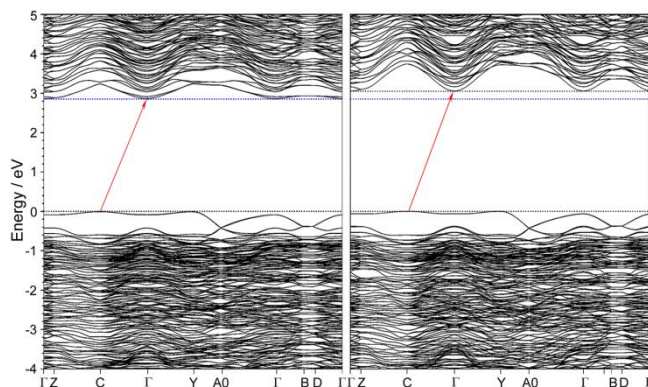
Figure 7. Calculated band structures for $Y_4Ba_2[Si_9ON_{16}]O$ (left) and $Lu_4Ba_2[Si_9ON_{16}]O$ (right). Red arrows indicate indirect transitions.

$Y_4Ba_2[Si_9ON_{16}]O:Eu^{2+}$ shows orange-red band emission with maximum at 622 nm and full width at half-maximum (*fwhm*) of 111 nm/2875 cm^{-1} (λ_{exc} = 440 nm). Color coordinates (CIE) are x = 0.59 and y = 0.40. The phosphor exhibits low thermal quenching at 150 °C with a relative emission intensity of ≈ 80% (Figure S6). Internal quantum efficiency (*IQE*) of the powder sample is 20% (λ_{exc} = 440 nm). In contrast, $Lu_4Ba_2[Si_9ON_{16}]O:Eu^{2+}$ shows narrower, blue-shifted emission peaking at 586 nm with *fwhm* = 88 nm/2530 cm^{-1} (λ_{exc} = 440 nm) and CIE at x = 0.51 and y = 0.47.
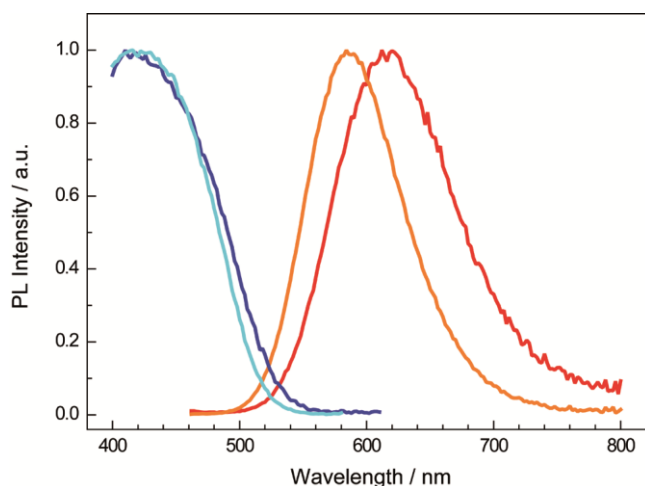
Figure 8. $Y_4Ba_2[Si_9ON_{16}]O:Eu^{2+}$: normalized excitation spectrum (λ_{mon} = 636 nm) dark blue, normalized emission spectrum (λ_{exc} = 440 nm) red; $Lu_4Ba_2[Si_9ON_{16}]O:Eu^{2+}$: normalized excitation spectrum (λ_{mon} = 600 nm) cyan, emission spectrum (λ_{exc} = 440 nm) orange.

Slightly shorter activator–ligand distances are expected for [2], as averaged Ba–N (284.6(4)–340.0(5) pm) distances in [2] are smaller by 2.5 pm compared to Ba–N bond lengths (282.5(3)–344.0(3) pm) in [1]. This should lead to slightly larger crystal field splitting and therefore red-shifted excitation and emission spectra for [2]. However, the similar energetic positions of the excitation maxima indicate that activator–ligand distances play a minor role. Comparing the emission of both phosphors, a rather large blue-shift is observed for [2]. The blue-shifted and more narrow emission of [2] is most likely caused by reduced phonon frequencies ω of local lattice vibrations to which the electronic transitions of the activator ions in [2] are coupled. This can be referred to nearly doubled atomic weight of Lu^{3+} compared to Y^{3+}. According to equation 2, smaller phonon frequencies lead to smaller Stokes shift coming along with a decreased *fwhm* (with dimensionless Huang-Rhys factor S, $x = 0–1$), as is observed for [2].[57] Stokes shifts for both phases were estimated by fitting the emission spectra with data generated using the single configuration coordinate model,[58] giving $E_{Stokes} \approx 4200$ cm^{-1}, $\hbar\omega \approx 601$ cm^{-1} and $S \approx 4$ for [1] and $E_{Stokes} \approx 3700$ cm^{-1}, $\hbar\omega \approx 567$ cm^{-1}, and $S \approx 3.8$ for [2] (assuming $x = 1$, Figure S7).

$$E_{Stokes} = (2S - x) \cdot \hbar\omega \qquad\qquad (2)$$

Single crystals of [2] emit light more intense than single crystals of [1]. This observation is supported by measurements on single crystals of same size and nominal Eu^{2+} content. For comparison of conversion efficiency, emission spectra of single crystals of [1] and [2] were normalized to the same excitation peak intensity at 440 nm (Figure 9). Subsequently, the areas under the emission spectra were integrated in order to allow comparison between the efficiencies of the two phosphors (Figure S8). Thereby, a 4.3 times stronger emission was found for [2], indicating a rather high *IQE* $\approx 85\%$ if compared to powder luminescence measurement results of [1] and commercial phosphor materials of known *IQE*. The higher conversion efficiency of [2] at room temperature should also be caused by lower phonon frequencies of the vibrations that couple to the electronic transitions of the luminescence center ion as the energetic barrier for nonradiative transitions is being increased.[59] Smaller Stokes shifts and higher quantum efficiencies for Lu nitridosilicates compared to isotypic Y compounds are also reported for other host lattices as well as the technically important isotypic garnet phosphors $RE_3Al_5O_{12}:Ce^{3+}$ (RE = Y, Lu).[60,61]

Peak position and *fwhm* of [1] are comparable to commercially used red phosphors $(Ba,Sr)_2Si_5N_8:Eu^{2+}$ ($\lambda_{em} \approx 590–625$ nm, *fwhm* $\approx 2050–2600$ cm^{-1})[4,5,62] and

(Sr,Ca)AlSiN$_3$:Eu^{2+} (λ_{em} ≈ 610–660 nm,   *fwhm* ≈ 2100–2500 cm^{-1}).[6,63,64]   Yellow-orange luminescence of [**2**] resembles emission of oxonitridoalumosilicate CaSi$_9$Al$_3$ON$_{15}$:Eu^{2+} (Ca-*α*-SiAlON, λ_{em} = 581 nm, *fwhm* ≈ 2890 cm^{-1}), a phosphor material proposed for warm white illumination applications.[65,66]
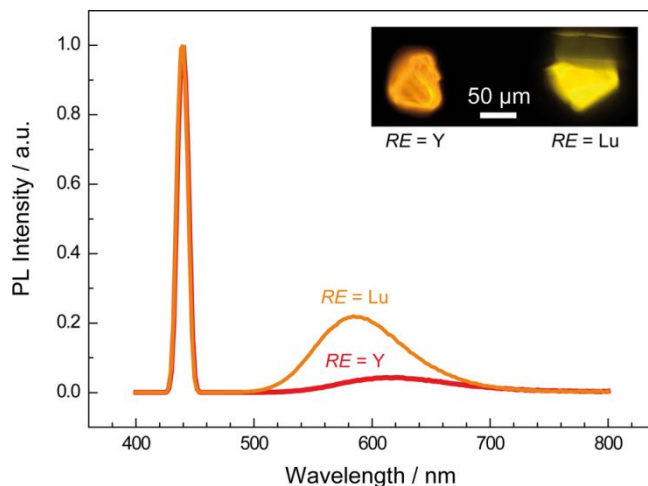
Figure 9. Comparison of luminescence intensities of Y$_4$Ba$_2$[Si$_9$ON$_{16}$]O:Eu^{2+} (red) and Lu$_4$Ba$_2$[Si$_9$ON$_{16}$]O:Eu^{2+} (orange) single crystals. Normalized excitation peaks at 440 nm.

4.4 Conclusion

The novel oxonitridosilicate oxides Y$_4$Ba$_2$[Si$_9$ON$_{16}$]O:Eu^{2+} and Lu$_4$Ba$_2$[Si$_9$ON$_{16}$]O:Eu^{2+} have been synthesized in high temperature reactions. Structural characterization was carried out using X-ray data (single-crystal and PXRD) and is supported by FTIR spectroscopy as well as lattice energy calculations. Both materials are isotypic, crystallizing in a unique structure type. The three-dimensional silicate network is the first one exhibiting 4-fold bridging, ammonia type N$^{[4]}$ atoms as well as N$^{[3]}$, N$^{[2]}$, terminal O$^{[1]}$ atoms, and noncondensed oxide ions. Therefore, these materials illustrate nicely the structural possibilities and diversity in (oxo)nitridosilicates. In general, presence of trivalent and divalent anions and cations should open up the way to further intriguing crystal structures in this compound class. When doped with Eu^{2+}, the title compounds show strong luminescence when excited by blue light of a (In,Ga)N-LED. Because of a smaller Stokes shift due to a beneficial lattice phonon structure, Lu$_4$Ba$_2$[Si$_9$ON$_{16}$]O:Eu^{2+} exhibits narrower and highly efficient (*IQE* ≈ 85%) emission in the yellow-orange spectral region. The observed chemical stability, high *IQE*, and yellow-orange emission make this phosphor a promising candidate for high luminous efficiency warm white pcLEDs, for example, in outdoor illumination applications. Furthermore, especially the system Lu–Ba–Si–O–N

seems quite intriguing regarding narrow-band Eu^{2+}-doped luminophors. In particular, crystal structures with only one highly symmetric alkaline earth cation site, like in narrow emitting Sr[Mg$_3$SiN$_4$]:Eu^{2+}, Ba[Li(Al$_2$Si$_2$)N$_6$]:Eu^{2+}, or BaSi$_2$O$_2$N$_2$:Eu^{2+}, are of interest.[13,67–69] Low frequencies of phonons coupled to the electronic transitions of the Eu^{2+} activator ions, because of the large atomic weight of Lu^{3+}, will additionally contribute to narrow emission and high efficiency of such phosphors.

4.5   References

[1]   Xie, R.-J.; Hirosaki, N.; Takeda, T. Rare-Earth Activated Nitride Phosphors: Synthesis, Luminescence and Applications. *Materials* **2010**, *3*, 3777–3793.

[2]   McKittrick, J.; Shea-Rohwer, L. E. Review: Down Conversion Materials for Solid-State Lighting. *J. Am. Ceram. Soc.* **2014**, *97*, 1327–1352.

[3]   Höppe, H. A. Recent developments in the field of inorganic phosphors. *Angew. Chem., Int. Ed.* **2009**, *48*, 3572–3582; Aktuelle Entwicklungen auf dem Gebiet der anorganischen Leuchtstoffe. *Angew. Chem.* **2009**, *121*, 3626–3636.

[4]   Mueller-Mach, R.; Mueller, G.; Krames, M. R.; Höppe, H. A.; Stadler, F.; Schnick, W.; Juestel, T.; Schmidt, P. Highly efficient all-nitride phosphor-converted white light emitting diode. *Phys. Status Solidi A* **2005**, *202*, 1727–1732.

[5]   Höppe, H. A.; Lutz, H.; Morys, P.; Schnick, W.; Seilmeier, A. Luminescence in Eu^{2+}-doped Ba$_2$Si$_5$N$_8$: fluorescence, thermoluminescence, and upconversion. *J. Phys. Chem. Solids* **2000**, *61*, 2001–2006.

[6]   Watanabe, H.; Kijima, N. Crystal structure and luminescence properties of Sr$_x$Ca$_{1−x}$AlSiN$_3$:Eu^{2+} mixed nitride phosphors. *J. Alloys Compd.* **2009**, *475*, 434−439.

[7]   Pust, P.; Schmidt, P. J.; Schnick, W. A revolution in lighting. *Nat. Mater.* **2015**, *14*, 454–458.

[8]   Wang, X.-J.; Funahashi, S.; Takeda, T.; Suehiro, T.; Hirosaki, N.; Xie, R.-J. Structure and luminescence of a novel orange-yellow-emitting Ca$_{1.62}$Eu$_{0.38}$Si$_5$O$_3$N$_6$ phosphor for warm white LEDs, discovered by a single-particle-diagnosis approach. *J. Mater. Chem. C* **2016**, *4*, 9968–9975.

[9]   Pust, P.; Weiler, V.; Hecht, C.; Tücks, A.; Wochnik, A. S.; Henß, A.-K.; Wiechert, D.; Scheu, C.; Schmidt, P. J.; Schnick, W. Narrow-band red-emitting Sr[LiAl$_3$N$_4$]:Eu^{2+} as a next-generation LED-phosphor material. *Nat. Mater.* **2014**, *13*, 891–896.

[10]   Wagatha, P.; Pust, P.; Weiler, V.; Wochnik, A. S.; Schmidt, P. J.; Scheu, C.; Schnick, W. Ca$_{18.75}$Li$_{10.5}$[Al$_{39}$N$_{55}$]:Eu^{2+} – Supertetrahedron Phosphor for Solid-State Lighting. *Chem. Mater.* **2016**, *28*, 1220–1226.

[11] Pust, P.; Hintze, F.; Hecht, C.; Weiler, V.; Locher, A.; Zitnanska, D.; Harm, S.;
      Wiechert, D.; Schmidt, P. J.; Schnick, W. Group (III) Nitrides M[Mg$_2$Al$_2$N$_4$] (M = Ca,
      Sr, Ba, Eu) and Ba[Mg$_2$Ga$_2$N$_4$] – Structural Relation and Nontypical Luminescence
      Properties of Eu^{2+} Doped Samples. *Chem. Mater.* **2014**, *26*, 6113–6119.

[12] Strobel, P.; Weiler, V.; Hecht, C.; Schmidt, P. J.; Schnick, W. Luminescence of the
      Narrow-band Red Emitting Nitridomagnesosilicate Li$_2$(Ca$_{1-x}$Sr$_x$)$_2$[Mg$_2$Si$_2$N$_6$]:Eu^{2+}
      (x = 0−0.06). *Chem. Mater.* **2017**, *29*, 1377–1383.

[13] Schmiechen, S.; Schneider, H.; Wagatha, P.; Hecht, C.; Schmidt, P. J.; Schnick, W.
      Toward New Phosphors for Application in Illumination-Grade White pc-LEDs: The
      Nitridomagnesosilicates Ca[Mg$_3$SiN$_4$]:Ce^{3+}, Sr[Mg$_3$SiN$_4$]:Eu^{2+}, and Eu[Mg$_3$SiN$_4$].
      Chem. Mater. **2014**, *26*, 2712–2719.

[14] Feldmann, C. Technical Revolution Underway − Nitride-based Phosphors for LED
      Application. *Z. Anorg. Allg. Chem.* **2012**, *638*, 2169–2171.

[15] Zeuner, M.; Pagano, S.; Schnick, W. Nitridosilicates and Oxonitridosilicates: From
      Ceramic Materials to Structural and Functional Diversity. *Angew. Chem., Int. Ed.*
      2011, *50*, 7754–7775; Nitridosilicate und Oxonitridosilicate: von keramischen
      Materialien zu struktureller und funktioneller Diversität. *Angew. Chem.* **2011**, *123*,
      7898–7920.

[16] Durach, D.; Neudert, L.; Schmidt, P. J.; Oeckler, O.; Schnick, W.
      La$_3$BaSi$_5$N$_9$O$_2$:Ce^{3+} – A Yellow Phosphor with an Unprecedented Tetrahedra
      Network Structure Investigated by Combination of Electron Microscopy and
      Synchrotron X-ray Diffraction. *Chem. Mater.* **2015**, *27*, 4832–4838.

[17] Durach, D.; Fahrnbauer, F.; Oeckler, O.; Schnick, W. La$_6$Ba$_3$[Si$_{17}$N$_{29}$O$_2$]Cl – An
      Oxonitridosilicate Chloride with Exceptional Structural Motifs. *Inorg. Chem.* **2015**,
      54, 8727–8732.

[18] Schultz, P.; Durach, D.; Schnick, W.; Oeckler, O. Ba$_{1.63}$La$_{7.39}$Si$_{11}$N$_{23}$Cl$_{0.42}$:Ce^{3+} – A
      Nitridosilicate Chloride with a Zeolite-Like Structure. *Z. Anorg. Allg. Chem.* **2016**,
      642, 603–608.

[19] Lange, H.; Wötting, G.; Winter, G. Silicon Nitride - From Powder Synthesis to
      Ceramic Materials. *Angew. Chem., Int. Ed. Engl.* **1991***, 30,* 1579–1597;
      Siliciumnitrid - vom Pulver zum keramischen Werkstoff. *Angew. Chem.* **1991**, *103*,
      1606–1625.

[20] Sheldrick, G. M. *SADABS, v. 2: Multi-Scan Absorption Correction*; Bruker-AXS:
      Billerica, MA, 2012.

[21] Sheldrick, G. M. *SHELXS-97: A Program for Crystal Structure Solution*; University of
      Göttingen: Göttingen, Germany, 1997.

[22]   Sheldrick, G. M. *SHELXL-97: A Program for Crystal Structure Refinement*; University of Göttingen: Göttingen, Germany, 1997.

[23]   Sheldrick, G. M. A short history of SHELX. *Acta Crystallogr., Sect. A: Found. Crystallogr.* **2008**, *64*, 112–122.

[24]   Rietveld, H. M. A profile refinement method for nuclear and magnetic structures. *J. Appl. Crystallogr.* **1969**, *2*, 65–71.

[25]   Coelho, A. A. *TOPAS, v. 4.1: A program for Rietveld refinement*; Coelho Software: Brisbane, Australia, 2007.

[26]   Bergmann, J.; Kleeberg, R.; Haase, A.; Breidenstein, B. Advanced fundamental parameter model for improved profile analysis. *Mater. Sci. Forum* **2000**, *347−349*, 303–308.

[27]   Cheary, R. W.; Coelho, A. A.; Cline, J. P. Fundamental Parameters Line Profile Fitting in Laboratory Diffractometers. *J. Res. Natl. Inst. Stand. Technol.* **2004**, *109*, 1–25.

[28]   Kresse, G.; Hafner, J. *Ab initio* molecular dynamics for liquid metals. *Phys. Rev. B: Condens. Matter Mater. Phys.* **1993**, *47*, 558–561.

[29]   Kresse, G.; Hafner, J. *Ab initio* molecular-dynamics simulation of the liquid-metal–amorphous-semiconductor transition in germanium. *Phys. Rev. B: Condens. Matter Mater. Phys.* **1994**, *49*, 14251–14269.

[30]   Kresse, G.; Furthmüller, J. Efficiency of ab-initio total energy calculations for metals and semiconductors using a plane-wave basis set. *Comput. Mater. Sci.* **1996**, *6*, 15–50.

[31]   Perdew, J. P.; Burke, K.; Ernzerhof, M. Generalized Gradient Approximation Made Simple. *Phys. Rev. Lett.* **1996**, *77*, 3865–3868.

[32]   Perdew, J. P.; Burke, K.; Ernzerhof, M. Generalized Gradient Approximation Made Simple. *Phys. Rev. Lett.* **1997**, *78*, 1396–1396.

[33]   Blöchl, P. E. Projector augmented-wave method. *Phys. Rev. B: Condens. Matter Mater. Phys.* **1994**, *50*, 17953–17979.

[34]   Kresse, G.; Joubert, D. From ultrasoft pseudopotentials to the projector augmented-wave method. *Phys. Rev. B: Condens. Matter Mater. Phys.* **1999**, *59*, 1758–1775.

[35]   Monkhorst, H. J.; Pack, J. D. Special points for Brillouin-zone integrations. *Phys. Rev. B* **1976**, *13*, 5188–5192.

[36]   Blasse, G.; Grabmaier, B. C. *Luminescent Materials*; Springer: Berlin, 1994.

[37]   Shannon, R. D. Revised effective ionic radii and systematic studies of interatomic distances in halides and chalcogenides. *Acta Crystallogr., Sect. A: Cryst. Phys., Diffr., Theor. Gen. Crystallogr.* **1976**, *32*, 751–767.

[38] Hoppe, R. Madelung constants. *Angew. Chem., Int. Ed. Engl.* **1966**, *5*, 95–106; Über
      Madelungfaktoren. *Angew. Chem.* **1966**, *78*, 52–63.

[39] Hoppe, R. The Coordination Number – an "Inorganic Chameleon". *Angew. Chem.,
      Int. Ed. Engl.* **1970**, *9*, 25–34; Die Koordinationszahl – ein „anorganisches
      Chamäleon". *Angew. Chem.* **1970**, *82*, 7–16.

[40] Hübenthal, R. *Maple, Program for the Calculation of MAPLE values, version 4*;
      University of Gießen: Gießen, Germany, 1993.

[41] Morgan, P. E. D. Pauling's second crystal rule for nitrogen-substituted crystal
      structures. *J. Mater. Sci.* **1986**, *21*, 4305–4309.

[42] Lieb, A.; Schnick, W. BaSm$_5$[Si$_9$Al$_3$N$_{20}$]O – a nitridoaluminosilicate oxide with a new
      structure type composed of "star-shaped" [N$^{[4]}$((Si,Al)N$_3$)$_4$] units as secondary
      building units. *Solid State Sci.* **2006**, *8*, 185–191.

[43] Huppertz, H.; Schnick, W. BaYbSi$_4$N$_7$ – Unexpected Structural Possibilities in
      Nitridosilicates. *Angew. Chem., Int. Ed. Engl.* **1996**, *35*, 1983–1984; BaYbSi$_4$N$_7$ –
      überraschende strukturelle Möglichkeiten in Nitridosilicaten. *Angew. Chem.* **1996**,
      108, 2115–2116.

[44] Huppertz, H.; Schnick, W. Synthesis, Crystal Structure, and Properties of the
      Nitridosilicates SrYbSi$_4$N$_7$ and BaYbSi$_4$N$_7$. *Z. Anorg. Allg. Chem.* **1997**, *623*, 212–
      217.

[45] Huppertz, H.; Schnick, W. Eu$_2$Si$_5$N$_8$ and EuYbSi$_4$N$_7$. The First Nitridosilicates with a
      Divalent Rare Earth Metal. *Acta Crystallogr., Sect. C: Cryst. Struct. Commun.* **1997**,
      53, 1751–1753.

[46] Li, Y. Q.; de With, G.; Hintzen, H. T. Synthesis, structure, and luminescence
      properties of Eu^{2+} and Ce^{3+} activated BaYSi$_4$N$_7$. *J. Alloys Compd.* **2004**, *385*, 1–11.

[47] Park, W. B.; Son, K. H.; Singh, S. P.; Sohn, K.-S. Solid-State Combinatorial
      Screening of ARSi$_4$N$_7$:Eu^{2+} (A = Sr, Ba, Ca; R = Y, La, Lu) Phosphors. *ACS Comb.
      Sci.* **2012**, *14*, 537–544.

[48] Vinograd, V. L.; Juarez-Arellano, E. A.; Lieb, A.; Knorr, K.; Schnick, W.; Gale, J. D.;
      Winkler, B. Coupled Al/Si and O/N order/disorder in BaYb[Si$_{4-x}$Al$_x$O$_x$N$_{7-x}$] sialon:
      neutron powder diffraction and Monte Carlo simulations. *Z. Kristallogr.* **2007**, *222*,
      402–415.

[49] Lieb, A.; Kechele, J. A.; Kraut, R.; Schnick, W. The Sialons *MLn*[Si$_{4-x}$Al$_x$O$_x$N$_{7-x}$] with
      M = Eu, Sr, Ba and *Ln* = Ho-Yb – Twelve Substitution Variants with the *M*Yb[Si$_4$N$_7$]
      Structure Type. *Z. Anorg. Allg. Chem.* **2007**, *633*, 166–171.

[50] Huppertz, H.; Oeckler, O.; Lieb, A.; Glaum, R.; Johrendt, D.; Tegel, M.; Kaindl, R.;
      Schnick, W. Ca$_3$Sm$_3$[Si$_9$N$_{17}$] and Ca$_3$Yb$_3$[Si$_9$N$_{17}$] Nitridosilicates with Interpenetrating

Nets that Consist of Star-Shaped $[N^{[4]}(SiN_3)_4]$ Units and $[Si_5N_{16}]$ Supertetrahedra. *Chem. - Eur. J.* **2012**, *18*, 10857–10864.

[51] Liddell, K.; Thompson, D. P. The crystal structure of $Y_3Si_5N_9O$ and revision of the compositions of some high nitrogen-containing M−Si−O−N (M = Y, La) phases. *J. Mater. Chem.* **2001**, *11*, 507–512.

[52] Schlieper, T.; Milius, W.; Schnick, W. Nitrido-silicate. II: Hochtemperatur-Synthesen und Kristallstrukturen von $Sr_2Si_5N_8$ und $Ba_2Si_5N_8$. *Z. Anorg. Allg. Chem.* **1995**, *621*, 1380–1384.

[53] Takahashi, J.; Yamane, H.; Shimada, M.; Yamamoto, Y.; Hirosaki, N.; Mitomo, M.; Oikawa, K.; Torii, S.; Kamiyama, T. Crystal Structure of $Lu_4Si_2O_7N_2$ Analyzed by the Rietveld Method Using the Time-of-Flight Neutron Powder Diffraction Pattern. *J. Am. Ceram. Soc.* **2002**, *85*, 2072–2077.

[54] López, R.; Gómez, R. Band-gap energy estimation from diffuse reflectance measurements on sol-gel and commercial TiO_2: a comparative study. *J. Sol-Gel Sci. Technol.* **2012**, *61*, 1–7.

[55] Tauc, J.; Grigorovici, R.; Vancu, A. Optical Properties and Electronic Structure of Amorphous Germanium. *Phys. Status Solidi B* **1966**, *15*, 627–637.

[56] Perdew, J. P. Density functional theory and the band gap problem. *Int. J. Quantum Chem.* **1986**, *19*, 497–523.

[57] de Jong, M.; Seijo, L.; Meijerink, A.; Rabouw, F. T. Resolving the ambiguity in the relation between Stokes shift and Huang-Rhys parameter. *Phys. Chem. Chem. Phys.* **2015**, *17*, 16959–16969.

[58] Shionoya, S.; Yen, W. M. *Phosphor Handbook*; CRC Press, New York, 1998.

[59] Blasse, G. Luminescence of inorganic solids: from isolated centres to concentrated systems. *Prog. Solid State Chem.* **1988**, *18*, 79–171.

[60] Xu, X.; Cai, C.; Hao, L.; Wang, Y.; Li, Q. The photoluminescence of Ce-doped $Lu_4Si_2O_7N_2$ green phosphors. *Mater. Chem. Phys.* **2009**, *118*, 270–272.

[61] Xia, Z.; Meijerink, A. Ce^{3+}-Doped garnet phosphors: composition modification, luminescence properties and applications. *Chem. Soc. Rev.* **2017**, *46*, 275–299.

[62] Krames, M.; Mueller, G. O.; Mueller-Mach, R.; Bechtel, H.; Schmidt, P. J. Wavelength conversion for producing white light from high power blue led, *PCT Int. Appl.* WO 2010131133 A1, 2010.

[63] Uheda, K.; Hirosaki, N.; Yamamoto, Y.; Naito, A.; Nakajima, T.; Yamamoto, H. Luminescence properties of a red phosphor, $CaAlSiN_3:Eu^{2+}$, for white light-emitting diodes. *Electrochem. Solid-State Lett.* **2006**, *9*, H22–H25.

[64] Uheda, K.; Hirosaki, N.; Yamamoto, H. Host lattice materials in the system Ca$_3$N$_2$−AlN−Si$_3$N$_4$ for white light emitting diode. *Phys. Status Solidi A* **2006**, *203*, 2712–2717.

[65] Xie, R.-J.; Hirosaki, N.; Takeda, T.; Suehiro, T. On the performance enhancement of nitride phosphors as spectral conversion materials in solid state lighting. *ECS J. Solid State Sci. Technol.* **2013**, *2*, R3031–R3040.

[66] Xie, R.-J.; Hirosaki, N.; Sakuma, K.; Yamamoto, Y.; Mitomo, M. Eu^{2+} doped Ca-*α*-SiAlON: A yellow phosphor for white light-emitting diodes. *Appl. Phys. Lett.* **2004**, *84*, 5404–5406.

[67] Strobel, P.; Schmiechen, S.; Siegert, M.; Tücks, A.; Schmidt, P. J.; Schnick, W. Narrow-Band Green Emitting Nitridolithoalumosilicate Ba[Li$_2$(Al$_2$Si$_2$)N$_6$]:Eu^{2+} with Framework Topology *whj* for LED/LCD-Backlighting Applications. *Chem. Mater.* **2015**, *27*, 6109–6115.

[68] Kechele, J. A.; Oeckler, O.; Stadler, F.; Schnick, W. Structure elucidation of BaSi$_2$O$_2$N$_2$ – A host lattice for rare-earth doped luminescent materials in phosphor-converted (pc)-LEDs. *Solid State Sci.* **2009**, *11*, 537–543.

[69] Bachmann, V.; Ronda, C.; Oeckler, O.; Schnick, W.; Meijerink, A. Color Point Tuning for (Sr,Ca,Ba)Si$_2$O$_2$N$_2$:Eu^{2+} for White Light LEDs. *Chem. Mater.* **2009**, *21*, 316–325.

5 $RE_4Ba_2[Si_{12}O_2N_{16}C_3]$:Eu^{2+} ($RE$ = Lu, Y): Green-Yellow Emitting Oxonitridocarbidosilicates with a Highly Condensed Network Structure Unraveled through Synchrotron Microdiffraction
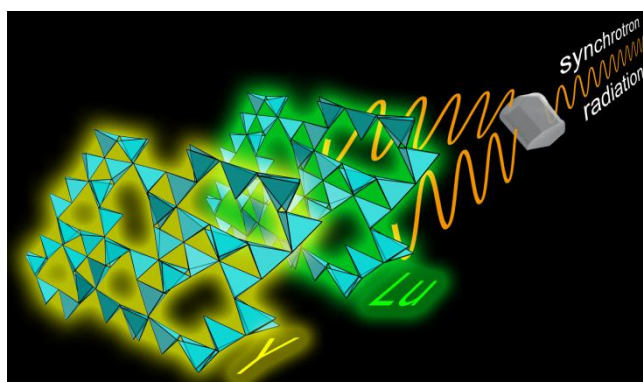
Abstract. The oxonitridocarbidosilicates $RE_4Ba_2[Si_{12}O_2N_{16}C_3]$:Eu^{2+} ($RE$ = Lu, Y) were synthesized by carbothermal reactions starting from RE_2O_3, graphite, $Ba_2Si_5N_8$, $Si(NH)_2$, and Eu_2O_3. The crystal structure of $Lu_4Ba_2[Si_{12}O_2N_{16}C_3]$:Eu^{2+} was elucidated on a submicron-sized single crystal by a combination of transmission electron microscopy and microfocused synchrotron radiation. The compound crystallizes in trigonal space group $P3$ (no. 143) with a = 16.297(4) Å, c = 6.001(2) Å, and Z = 3 ($R1$ = 0.0332, $wR2$ = 0.0834, GoF = 1.034). According to Rietveld refinements on powder X-ray diffraction data, $Y_4Ba_2[Si_{12}O_2N_{16}C_3]$:Eu^{2+} is isotypic with a = 16.41190(6) Å and c = 6.03909(3) Å. The crystal structures are built up of vertex-sharing SiC(O/N)$_3$ tetrahedra forming star-shaped units $[C^{[4]}(Si(O/N)_3)_4]$ with carbon atoms in fourfold bridging positions. Energy-dispersive X-ray spectroscopy and CHNS analysis correspond to the sum formula, lattice energy,

and charge distribution calculations support the assignment of O/N/C atoms. When excited with UV to blue light, Eu^{2+}-doped samples show green luminescence for RE = Lu ($\lambda_{em} \approx 538$ nm, full width at half-maximum (*fwhm*) ≈ 3600 cm^{-1}) and yellow emission in the case of RE = Y ($\lambda_{em} \approx 556$ nm, *fwhm* ≈ 4085 cm^{-1}).

5.1   Introduction

(Oxo)nitridosilicates are highly important for modern solid-state lighting, as Eu^{2+} or Ce^{3+} doped materials can show emission all over the visible spectral range and are applied in phosphor-converted light emitting diodes (pcLEDs).[1,2] Commercially applied nitridosilicate phosphors include $(Sr,Ca)AlSiN_3$:Eu^{2+}, $La_3Si_6N_{11}$:Ce^{3+}, and $(Ba,Sr)_2Si_5N_8$:Eu^{2+}.[3–5] Key features of such host materials are rigid silicate networks and high chemical and thermal stability. In (oxo)nitridosilicates, these features arise from the high covalency of Si–N bonds and the high connectivity of nitrogen, which can interconnect up to four tetrahedra.[6] The resulting $[N^{[4]}(SiN_3)_4]$-type units are present in the crystal structures of the nitridosilicates $BaYbSi_4N_7$ and $Ca_3RE_3[Si_9N_{17}]$ (RE = Sm, Yb), the nitridoalumosilicate $BaSm_5[Si_9Al_3N_{20}]O$, and the oxonitridosilicates $RE_4Ba_2[Si_9ON_{16}]O$ (RE = Y, Lu).[7–10] The replacement of fourfold bridging nitrogen atoms by carbon is feasible as Si–C bonds are even more covalent than Si–N bonds, and a high rigidity and stability of the network structure can be expected. The resulting $[C^{[4]}(SiN_3)_4]$ units resemble both nitridosilicates and silicon carbide.[11] Nevertheless, compounds with general formula $RE_2[Si_4N_6C]$ (RE = Ho, Tb, La, Gd, Lu, Y, Sc)[12–16] represent the only nitridocarbidosilicates reported so far. Therefore, new synthesis routes, such as carbothermal approaches, are worthwhile to be explored, targeting further (oxo)nitridocarbidosilicate host structures for rare earth doping. However, even when such materials have been synthesized successfully, another challenge arises if the syntheses solely yield crystals too small for conventional single-crystal X-ray diffraction. Structure solution from powder diffraction data is often challenging as rather phase pure samples are required. These, however, are hard to obtain if the exact sum formulas of multinary products are still unknown. In addition, (oxo)nitridosilicates often exhibit complicated structures, superstructure phenomena,[17,18] and light atoms next to heavy ones such as Lu suffer from imprecise atomic parameters. In recent years, such problems have been overcome by collecting X-ray diffraction data employing synchrotron radiation. The development of compound refractive lenses[19] enable high brilliance of the radiation and investigations on single crystals in the (sub)micrometer range due to the very small beam cross section.[20–24] In this contribution, we report on the oxonitridocarbidosilicates $RE_4Ba_2[Si_{12}O_2N_{16}C_3]$:$Eu^{2+}$ (RE = Lu, Y),

accessible by carbothermal reactions. These highly stable materials are suitable for optical Eu^{2+} activation and emit in the green to yellow spectral range upon high-energy irradiation. The structure elucidation is based on data obtained from a submicron-sized single crystal of Lu$_4$Ba$_2$[Si$_{12}$O$_2$N$_{16}$C$_3$]:Eu^{2+}, thereby employing synchrotron microdiffraction at its limits.

5.2   Experimental Section

5.2.1   Synthesis

As some starting materials are sensitive to air and moisture, all preparation steps were carried out under an argon atmosphere either in an argon-filled glovebox (Unilab, MBraun, Garching; O$_2$ < 1 ppm; H$_2$O < 1 ppm) or in argon filled glassware (Schlenk technique). Lu$_4$Ba$_2$[Si$_{12}$O$_2$N$_{16}$C$_3$]:Eu^{2+} was obtained by reacting Lu$_2$O$_3$ (0.30 mmol, 120.7 mg; Chempur, 99.99%), graphite (1.52 mmol, 18.2 mg; Chempur, 99.9%), Ba$_2$Si$_5$N$_8$ (0.15 mmol, 80.0 mg),[25] Si(NH)$_2$ (1.06 mmol, 61.7 mg),[26] and Eu$_2$O$_3$ (0.003 mmol, 1.1 mg; ABCR, 99.99%). Y$_4$Ba$_2$[Si$_{12}$O$_2$N$_{16}$C$_3$]:Eu^{2+} was synthesized starting from Y$_2$O$_3$ (0.30 mmol, 68.5 mg; Sigma-Aldrich, 99.999%), graphite (1.52 mmol, 18.2 mg; Chempur, 99.9%), Ba$_2$Si$_5$N$_8$ (0.15 mmol, 80.0 mg),[25] Si(NH)$_2$ (1.06 mmol, 61.7 mg),[26] and Eu$_2$O$_3$ (0.003 mmol, 1.1 mg; ABCR, 99.99%). The phase-pure synthesis of the starting material Ba$_2$Si$_5$N$_8$ is described in the Supporting Information (Tables S1 and S2, Figure S1). Starting materials were mixed in an agate mortar, filled into a tungsten crucible, and then transferred into a water-cooled silica glass reactor of a radiofrequency furnace (type IG 10/600; Hüttinger Elektronik Freiburg). The crucibles were heated to 1750 °C for 1 h, maintained at that temperature for 8 h, cooled down to 900 °C for 8 h, and finally quenched to room temperature. Lu$_4$Ba$_2$[Si$_{12}$O$_2$N$_{16}$C$_3$]:Eu^{2+} was obtained as a greenish powder; Y$_4$Ba$_2$[Si$_{12}$O$_2$N$_{16}$C$_3$]:Eu^{2+} exhibits yellowish body color. When excited with UV to blue light, the materials show strong green or yellow emission, respectively. Both compounds are insensitive toward air, moisture, and concentrated hydrochloric acid.

5.2.2   Transmission Electron Microscopy

Crystals of Lu$_4$Ba$_2$[Si$_{12}$O$_2$N$_{16}$C$_3$]:Eu^{2+} were ground in absolute ethanol and drop-cast on copper finder grids covered with a continuous carbon film (Plano GmbH, Germany). The grids were mounted on a double-tilt holder and transferred into an FEI Tecnai G20 transmission electron microscope (TEM) with a thermal emitter (LaB$_6$) operating at

200 keV. SAED patterns and bright-field images were recorded using a TVIPS camera (TemCam F216, Tietz) with a resolution of 2048 × 2048 pixels. Suitable crystals for structure determination were identified by means of selected area electron diffraction (SAED) patterns and energy-dispersive X-ray spectroscopy (EDX, Apollo XLT detector, EDAX). Maps of the grids enable subsequent positioning of the selected crystals in the synchrotron beam. For EDX measurements, crystals of the title compounds were ground in absolute ethanol and drop-cast on copper grids covered with holey carbon film (S166-2, Plano GmbH, Germany). The grids were mounted on a double-tilt holder and transferred into a C_s DCOR probe-corrected Titan Themis 300 TEM (FEI, USA) equipped with an X-FEG, post-column filter (Enfinium ER-799), a US1000XP/FT camera system (Gatan, Germany), and a windowless, 4-quadrant Super-X EDX detector. TEM images were recorded using a 4k × 4k FEI Ceta CMOS camera. The microscope was operated at 300 kV accelerating voltage. TEM data were evaluated with Digital Micrograph (SAED patterns), ProcessDiffraction7, JEMS (SAED simulations), and ES Vision (EDX).[27−31]

5.2.3   Single-Crystal X-ray Diffraction

The TEM grid was mounted on a SYMETRIE NanoPos hexapod, and the $Lu_4Ba_2[Si_{12}O_2N_{16}C_3]$:Eu^{2+} crystal of about 1.6 × 0.45 × 1 µm^3 in size (Figure S2) was recovered at beamline ID11 (ESRF, Grenoble) by a telescope with large magnification, using the copper crossbars of the grid as landmarks. The crystallite was centered using Ba X-ray fluorescence scans. The single-crystal data set was then collected using a microfocused synchrotron beam of 1 × 1 µm^2. Semiempirical absorption correction and scaling were executed using SADABS.[32] The crystal structure was solved by direct methods and refined by least-squares methods with SHELX-2014.[33]

5.2.4   Powder X-ray Diffraction

Powder X-ray diffraction (PXRD) of samples in glass capillaries (0.1 mm diameter, Hilgenberg GmbH) were carried out on STOE STADIP diffractometers with modified Debye-Scherrer geometry using Cu Kα_1 or Mo Kα_1 radiation (Stoe & Cie., Darmstadt, Germany, Ge(111) monochromator; Mythen1K detector, DECTRIS Ltd., Baden-Daettwil, Switzerland). For Rietveld refinements, the TOPAS Academic V4.1 software package was used, applying the fundamental parameters approach, i.e., direct convolution of source emission profiles, axial instrument contributions, crystallite size, and microstrain effects.[34−36]

5.2.5   CHNS Analysis

Conventional elemental analysis was performed using a Vario Micro Cube device (Elementar, Langenselbold, Germany).

5.2.6   IR Spectroscopy

Fourier transform infrared (FTIR) spectra were recorded with a Spectrum BX FT-IR System (PerkinElmer, Rodgau, Germany) device using the ATR method.

5.2.7   UV/Vis Spectroscopy

For diffuse reflectance UV/Vis spectroscopy, a Jasco V-650 UV/Vis spectrophotometer with a deuterium and a halogen lamp was used (JASCO, Pfungstadt, Germany, Czerny-Turner monochromator with 1200 lines/mm, concave grating, photomultiplier tube detector).

5.2.8   Luminescence

Luminescence properties of $RE_4Ba_2[Si_{12}O_2N_{16}C_3]:Eu^{2+}$ (RE = Lu, Y) were determined on microcrystalline powder samples in PTFE sample holders. Measurements were carried out using an in-house built system based on a 5.3″ integrating sphere and a spectrofluorimeter equipped with a 150 W Xe lamp, two 500 mm Czerny-Turner monochromators, 1800 mm^{-1} lattices, and 250/500 nm lamps, with a spectral range from 230 to 820 nm. The internal quantum efficiencies (IQEs) of the samples were determined by comparing integrated emission intensities and absorption at excitation wavelength with reference materials ($BaSO_4$, Merck for white standard DIN 5033 commercial $(Sr,Ca)AlSiN_3:Eu^{2+}$, Mitsubishi Chemical, and $Y_3Al_5O_{12}:Ce^{3+}$, Philips).

5.3   Results and Discussion

5.3.1   Synthesis and Chemical Analysis

RE_4Ba$_2$[Si$_{12}$O$_2$N$_{16}$C$_3$]:Eu^{2+} (RE = Lu, Y) were obtained from carbothermal reactions starting from RE_2O$_3$, C, Ba$_2$Si$_5$N$_8$, and Si(NH)$_2$ according to eq 1.

$$2\ RE_2O_3 + 7\ C + Ba_2Si_5N_8 + 7\ Si(NH)_2 \rightarrow RE_4Ba_2[Si_{12}O_2N_{16}C_3] + 4\ CO + 3\ N_2 + 7\ H_2 \qquad (1)$$

Nonstoichiometric amounts of the reactants (see Experimental Section) resulted in the highest yields. Chemical compositions were investigated by EDX after plasma-cleaning the samples for 20 min. Measurements were performed using STEM mode (probe size ≈ 1 Å). To avoid influence of the support film on C quantification, point measurements of crystals not fully supported by carbon film were recorded. The EDX results (Table S3) are in good agreement with calculated values for RE_4Ba$_2$[Si$_{12}$O$_2$N$_{16}$C$_3$] (RE = Lu, Y). The phase compositions of the obtained powders were determined by Rietveld refinements on powder X-ray diffraction data. These show that the structure model obtained from the Lu$_4$Ba$_2$[Si$_{12}$O$_2$N$_{16}$C$_3$] single crystal is representative for the bulk materials with RE = Lu as well as RE = Y. The target phases were obtained with yields of ca. 85 wt % (Figures S3 and S4, Table S4). CHNS analyses agree well with expected values according to the sum formula (Tables S5 and S6). Side-phase fractions as obtained from Rietveld refinements were taken into account for the calculation of the expected values. IR spectroscopy shows no O–H, N–H, and C–H vibrations (Figures S5 and S6).

5.3.2   Crystal Structure Determination

The crystallites obtained from the carbothermal syntheses have volumes < 1 µm^3. As this is too small for conventional single-crystal X-ray diffraction and structure solution from PXRD data was not successful, single-crystal data were collected for RE = Lu using microfocused synchrotron radiation. The crystal structure was initially solved in space group $P$6. Merohedral twinning toward Laue symmetry 6/mmm was taken into account, and refinements yielded $R$1 values of ≈ 0.04. However, the mirror plane perpendicular to [001] led to three split N atom sites, i.e., tetrahedra with alternative vertex positions. These could be resolved in the *translationengleiche* subgroup $P$3. Consequently, fourfold twinning was taken into account during refinement (twin matrices: $\bar{1}$00 0$\bar{1}$0 001; 010 100 00$\bar{1}$; 0$\bar{1}$0 $\bar{1}$00 001). Refinements in $P$3 also yield even lower R values. The crystal structure thus exhibits strong pseudosymmetry toward $P$6, but three nitrogen sites break

the higher symmetry. The four twin domains do not take into account inversion twinning. This was tested in a refinement assuming eight twin components; however, the refined twin fraction of the domains with inverted structure did not significantly differ from zero. Eu was neglected during refinement due to the small contribution to structure factors. Lu and Ba atoms were refined anisotropically, Si atoms isotropically, and C and O/N atoms were refined with common isotropic displacement parameters, respectively. This is required due to the weak scattering power of these atoms next to heavy Lu and Ba atoms. As O/N/C atoms cannot be distinguished due to similar atomic form factors, these atoms were assigned to the anion sites following Pauling's rules[37] and chemical plausibility. Accordingly, carbon was assigned to the fourfold bridging sites (C$^{[4]}$) in the tetrahedral network, nitrogen to threefold bridging sites (N$^{[3]}$), and oxygen to terminal sites. Twofold bridging sites were refined with mixed occupation (0.0625% O/0.9375% N) constrained to charge neutrality. This corresponds well with EDX and CHNS analyses (see above). Lattice energy (MAPLE)[38–41] and charge distribution (CHARDI)[42,43] calculations support the assignment of O/N/C (Tables S7 and S8). Electron diffraction (SAED tilt series) confirms the hexagonal metrics and gives no indication for a superstructure (Figure S7). Crystallographic data are summarized in Table 1; atomic parameters are listed in Tables S9 and S10. CSD 1860785 contains the supplementary crystallographic data for this paper. The data can be obtained free of charge from The Cambridge Crystallographic Data Centre. For RE = Y, no single-crystal X-ray diffraction data were obtained. PXRD data do not contain enough information for a significant refinement of Si, C, O, and N sites. Therefore, the structural model of $Lu_4Ba_2[Si_{12}O_2N_{16}C_3]$ was used for the Rietveld refinement of $Y_4Ba_2[Si_{12}O_2N_{16}C_3]$ (Figure S4, Table S4) and only lattice parameters and profile functions were refined. The lattice parameters are slightly larger for RE = Y compared to RE = Lu due to the larger ionic radius of Y^{3+} (Y^{3+}: 90 pm, Lu^{3+}: 86 pm, both values for CN = 6).[38] The accuracy of the Rietveld fit demonstrates that both compounds are isotypic.

5.3.3   Structure Description

The oxonitridocarbidosilicates $RE_4Ba_2[Si_{12}O_2N_{16}C_3]$:Eu^{2+} ($RE$ = Lu, Y) exhibit a highly condensed three-dimensional network of vertex-sharing SiC(O/N)$_3$ tetrahedra of Q^4- and Q^3-type (Figure 1). The degree of condensation (n(Si):n(O/N/C)) is κ = 0.57. The SiC(O/N)$_3$ tetrahedra form [C$^{[4]}$(Si(O/N)$_3$)$_4$] building blocks, in which the carbon atoms occupy the anion positions interconnecting four tetrahedra (Figure 2a). Three of these [C$^{[4]}$(Si(O/N)$_3$)$_4$] building blocks are further interconnected to build the entities shown in

Figure 2b. These entities are connected over common vertices to build up the entire anionic network. The structural motifs colored in turquoise and blue (Figure 2c) are distorted variants of the red entity. Building blocks of type $[X^{[4]}(Si(O/N)_3)_4]$ have been observed in other structure types, namely, $BaYbSi_4N_7$,[7] $CaRE[Si_9N_{17}]$ (RE = Sm, Yb),[8] $BaSm_5[Si_9Al_3N_{20}]O$,[9] $RE_4Ba_2[Si_9ON_{16}]O$:Eu^{2+} (RE = Y, Lu),[10] and $RE_2[Si_4N_6C]$ (RE = Ho, Tb).[12] In these compounds, either N or C atoms occupy the fourfold bridging anion sites X. The anionic networks of $BaYbSi_4N_7$, $RE_2[Si_4N_6C]$ (RE = Ho, Tb), and $BaSm_5[Si_9Al_3N_{20}]O$ are also exclusively built up from star-shaped units, as it is the case for $RE_4Ba_2[Si_{12}O_2N_{16}C_3]$:Eu^{2+} ($RE$ = Lu, Y). However, the linking pattern of the star-shaped units in $RE_4Ba_2[Si_{12}O_2N_{16}C_3]$:Eu^{2+} ($RE$ = Lu, Y) differs from all above named compounds, resulting in a new structure type. The unique topology exhibits the point symbol $\{3^4.6^4.7^2\}\{3^6.4.6^4.7^4\}\{3^6.4.6^5.7^3\}_4\{3^6.6^4.7^5\}\{3^7.4^3.6^4.7\}_2\{3^9.4^5.5^5.6^2\}_3$ as determined by the progam TOPOS.[44]

Table 1. Crystallographic Data of the Single-Crystal Structure Determination of $Lu_4Ba_2[Si_{12}O_2N_{16}C_3]$.

formula	$Lu_4Ba_2[Si_{12}O_2N_{16}C_3]$
formula mass / g·mol^{-1}	1603.83
space group	$P3$ (no. 143)
lattice parameters / Å	a = 16.297(4), c = 6.001(2)
cell volume / Å^3	1380.3(8)
formula units / unit cell	3
X-ray density / g·cm^{-3}	5.79
abs. coefficient / μ·mm^{-1}	4.91
absorption correction	semiempirical[32]
$F(000)$	2130
crystal dimensions / μm^3	1.6 × 0.45 × 1
wavelength / Å	0.30996 (synchrotron, ID11, ESRF)
θ range / °	1.608 ≤ θ ≤ 12.788
independent reflections	2811
independent reflections with $I \geq 2\sigma(I)$	2730
refined parameters	171
GoF	1.034
R indices ($I > 2\sigma(I)$)	R_1 = 0.0332, wR_2 = 0.0834
R indices (all data)	R_1 = 0.0340, wR_2 = 0.0838
$\Delta\rho_{max}$, $\Delta\rho_{min}$ / e·Å^{-3}	3.16, −2.12
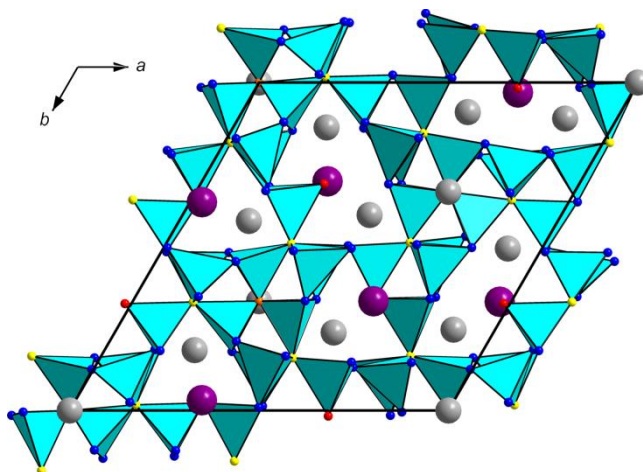
Figure 1. Crystal structure of *RE*$_4$Ba$_2$[Si$_{12}$O$_2$N$_{16}$C$_3$]:Eu^{2+} (*RE* = Lu, Y), viewed along [001]. SiC(O/N)$_3$ tetrahedra turquoise; *RE* atoms gray; Ba atoms violet; O atoms red; O/N atoms blue; N atoms orange, C atoms yellow.
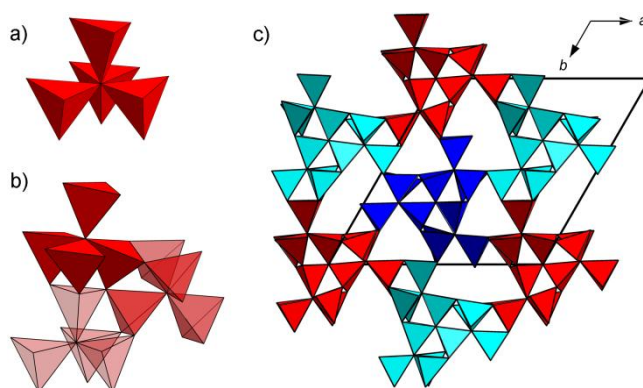
Figure 2. (a) Star-shaped [C$^{[4]}$(Si(O/N)$_3$)$_4$] unit. (b) Entity of three condensed [C$^{[4]}$(Si(O/N)$_3$)$_4$] units. (c) Anionic [Si$_{12}$O$_2$N$_{16}$C$_3$]$^{16-}$ network built up of entities from (b). The blue and turquoise entities are distorted variants of the red entity.

The interatomic distances in the anionic network are in the ranges 1.712(14) Å (Si–O), 1.61(2)–1.82(5) Å (Si–O/N), 1.755(12)–1.775(11) Å (Si–N), and 1.81(2)–2.02(3) Å (Si–C), corresponding well to comparable compounds.[12,45,46] The Si–C distances in wurtzite-type SiC, for comparison, are about 1.88 Å.[11] Lu and Ba atoms are ordered, occupying eight crystallographically independent cation sites. Such ordering is expected for cations with strongly differing ionic radii (Lu^{3+}: 98 pm, Ba^{2+}: 142 pm, both values for CN = 8).[38] Six of the heavy cation sites are occupied by Lu, two by Ba atoms (Figure 3). Three of the Lu sites are coordinated by six anions in a distorted octahedral way. The other Lu sites are

surrounded by seven anions forming distorted capped trigonal prisms. The Ba1 site exhibits a distorted anti-cuboctahedral coordination sphere; the site Ba2 is irregularly surrounded by 13 anions. The Lu–O distances are 2.379(13)–2.431(13) Å, Lu–O/N distances range from 2.18(2) to 2.650(14) Å and Lu–N distances from 2.44(3) to 2.57(3) Å. These are typical values for lutetium (oxo)nitridosilicates.[47,48] The Ba–anion distances are rather large with values of 2.95(3)–3.06(3) Å for Ba–O and 2.80(2)–3.52(3) Å in the case of Ba–O/N. However, similar distances were reported for other barium (oxo)nitridosilicates such as BaSi$_7$N$_{10}$ (2.913(3)–3.529(3) Å),[49] Ba$_2$Si$_5$N$_8$ (2.677(7)–3.171(4) Å),[25] or Y$_{26}$Ba$_6$[Si$_{22}$O$_{19}$N$_{36}$]O$_{16}$:Eu^{2+} (2.63(1)–3.59(2) Å).[50]
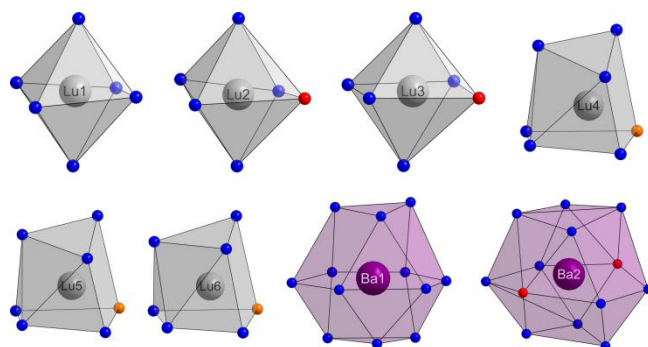
Figure 3. Coordination spheres of Lu and Ba sites in Lu$_4$Ba$_2$[Si$_{12}$O$_2$N$_{16}$C$_3$]:Eu^{2+} with O atoms red, O/N atoms blue, and N atoms orange.

5.3.4   UV/Vis Spectroscopy

The optical band gaps of *RE*$_4$Ba$_2$[Si$_{12}$O$_2$N$_{16}$C$_3$]:Eu^{2+} (*RE* = Lu, Y) were determined from diffuse reflectance UV/Vis spectra of doped samples. The measured reflectance spectra *R* (Figure S8) were transformed to pseudo-absorption spectra with the Kubelka-Munk function $F(R) = (1 - R)^2 / 2R$.[51] Subsequently, the optical band gaps were determined from Tauc plots by drawing tangents at the inflection points (Figure 4).[52] The calculations were performed assuming direct allowed transitions ($n = 1/2$) for both compounds. The optical band gap for *RE* = Y amounts to 3.9 eV; for *RE* = Lu it is significantly larger with 4.3 eV. The green (*RE* = Lu) or yellow (*RE* = Y) body colors of the doped samples are not a result of the band gaps but result from $4f^7$–$4f^6 5d^1$ transitions (absorption (Figure S8) and emission) of Eu^{2+} in the visible spectral range.
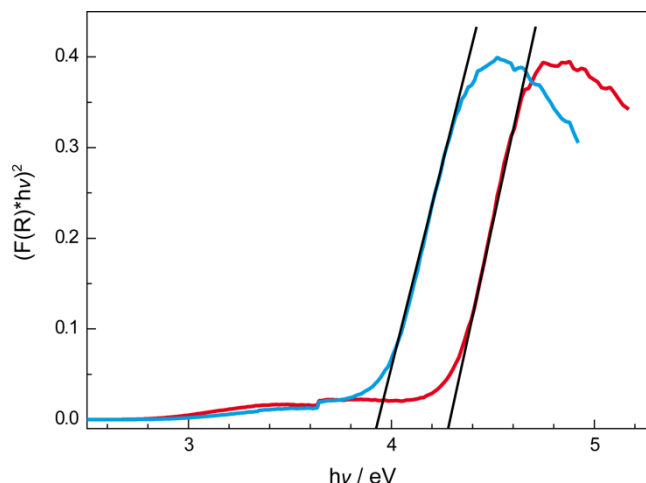
Figure 4. Tauc plots (n = 1/2) for $RE_4Ba_2[Si_{12}O_2N_{16}C_3]:Eu^{2+}$; plot for RE = Lu red, plot for RE = Y blue, tangents at the inflection points black.

5.3.5   Luminescence

$Lu_4Ba_2[Si_{12}O_2N_{16}C_3]:Eu^{2+}$ and $Y_4Ba_2[Si_{12}O_2N_{16}C_3]:Eu^{2+}$ show strong green and yellow emission, upon excitation with UV to blue light, respectively. Luminescence properties were investigated on powder samples with a nominal Eu content of 1 atom% referred to Ba. Comparing the ionic radii of Eu^{2+} (117 pm), Ba^{2+} (135 pm), and RE^{3+} (Lu^{3+}: 86 pm, Y^{3+}: 90 pm) in 6-fold coordination,[38] Eu^{2+} most likely prefers the two Ba^{2+} sites. The sample with RE = Lu shows blue-shifted and narrower emission with λ_{em} ≈ 538 nm and a full width at half-maximum (*fwhm*) ≈ 107 nm/3600 cm^{-1}. For $Y_4Ba_2[Si_{12}O_2N_{16}C_3]:Eu^{2+}$, emission with λ_{em} ≈ 556 nm and *fwhm* ≈ 130 nm/4085 cm^{-1} is observed (Figure 5). The color coordinates (CIE) are x = 0.34 and y = 0.53 for RE = Lu and x = 0.39 and y = 0.50 for RE = Y.

$Lu_4Ba_2[Si_{12}O_2N_{16}C_3]:Eu^{2+}$ exhibits a higher *IQE* of 28% compared to 15% for RE = Y (λ_{em} ≈ 440 nm). Thermal quenching data are presented in Figure 6. Both phosphors show similar, pronounced thermal quenching with a relative photoemission intensity of ca. 40% at 150 °C compared to room temperature. The rather broad emission bands most likely result from incorporation of Eu^{2+} on multiple Ba sites with different coordination spheres and a further diversification of local sites by O/N disorder. Additionally, emission band broadening could be further enhanced if Eu^{2+} atoms partially also occupy the RE^{3+} sites. The smaller distances between activator ions and anions could result in reabsorption of emitted higher-energy radiation by Eu^{2+} atoms occupying RE^{3+} sites. Furthermore, energy

transfer from high- to low-energy absorbing centers could occur in this case. This may also explain the strong thermal quenching observed for both phosphors.
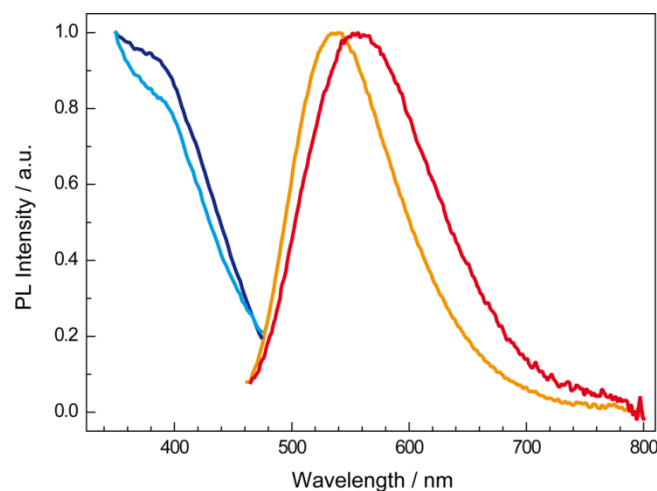
Figure 5. Lu$_4$Ba$_2$[Si$_{12}$O$_2$N$_{16}$C$_3$]:Eu^{2+}: normalized excitation spectrum (550–570 nm) dark blue, emission spectrum (λ_{exc} = 440 nm) orange; Y$_4$Ba$_2$[Si$_{12}$O$_2$N$_{16}$C$_3$]:Eu^{2+}: normalized excitation spectrum (λ_{mon} = 570–610 nm) cyan, normalized emission spectrum (λ_{exc} = 440 nm) red.
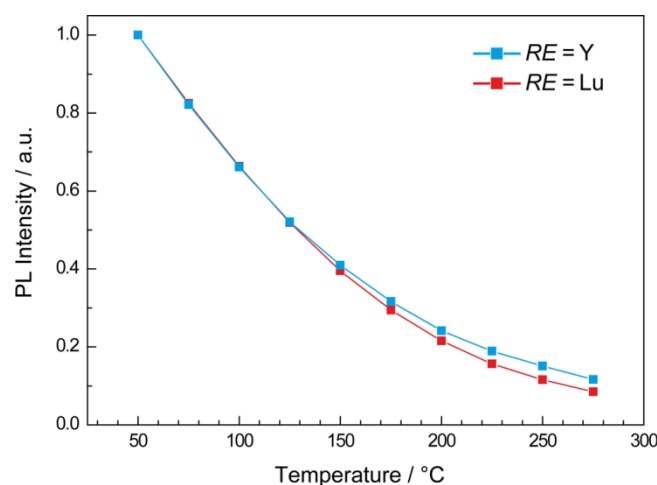
Figure 6. Thermal quenching data for *RE*$_4$Ba$_2$[Si$_{12}$O$_2$N$_{16}$C$_3$]:Eu^{2+} (*RE* = Lu, Y).

The narrower, higher-energy and higher-efficiency emission of Lu$_4$Ba$_2$[Si$_{12}$O$_2$N$_{16}$C$_3$]:Eu^{2+} compared to Y$_4$Ba$_2$[Si$_{12}$O$_2$N$_{16}$C$_3$]:Eu^{2+} is probably a result of the substantially higher atomic mass of Lu^{3+}. This can result in decreased phonon frequencies of local lattice vibrations coupled to electronic transitions of Eu^{2+}, as was explained in detail for the phosphors *RE*$_4$Ba$_2$[Si$_9$ON$_{16}$]O:Eu^{2+} (*RE* = Lu, Y) with yellow-orange (*RE* = Lu) and orange-red emission (*RE* = Y).[10,53] In this context, a detailed comparison of interatomic distances

and surroundings of the cation sites of $Lu_4Ba_2[Si_{12}O_2N_{16}C_3]$:$Eu^{2+}$ and $Y_4Ba_2[Si_{12}O_2N_{16}C_3]$:$Eu^{2+}$ would be interesting but is impeded by lacking structural data for $Y_4Ba_2[Si_{12}O_2N_{16}C_3]$:$Eu^{2+}$. However, due to the larger lattice parameters for RE = Y (Table S4), enlarged activator–ligand distances can be assumed for $Y_4Ba_2[Si_{12}O_2N_{16}C_3]$:$Eu^{2+}$. This would increase the energy of the lowest excited state of Eu^{2+} for RE = Y and therefore blue-shift the excitation spectrum, which is in accordance with the measured excitation spectra. Therefore, we conclude that the blue-shifted and narrower emission of $Lu_4Ba_2[Si_{12}O_2N_{16}C_3]$:$Eu^{2+}$ is not caused by activator-ligand geometries, but a smaller Stokes shift caused by the high atomic mass of Lu atoms. Further examples for the described effect of Lu^{3+} on luminescence properties are $RE_4Si_2O_7N_2$:Ce^{3+} and $RE_3Al_5O_{12}$:Ce^{3+} (RE = Lu, Y).[54,55]

5.4 Conclusion

In this contribution, we reported on synthesis, crystal structure, and optical properties of the oxonitridocarbidosilicates $RE_4Ba_2[Si_{12}O_2N_{16}C_3]$:$Eu^{2+}$ (RE = Lu, Y). Both materials were synthesized in high-temperature reactions using a carbothermal approach. The industrially relevant nitridosilicate $Ba_2Si_5N_8$ with a highly condensed, thermally and chemically inert network turned out to be a useful and reactive starting material in this context. The crystal structure was elucidated by a combination of TEM and diffraction of microfocused synchrotron radiation. Diffraction data collected from a submicron-sized $Lu_4Ba_2[Si_{12}O_2N_{16}C_3]$:$Eu^{2+}$ crystal (volume < 1 µm³) demonstrate the huge potential of this approach. The crystal structure exhibits an unprecedented, highly condensed 3D network composed of star-shaped units $[C^{[4]}(Si(O/N)_3)_4]$. PXRD, EDX, CHNS, and IR analyses as well as MAPLE and CHARDI calculations support the results. Eu^{2+} doped samples show intense green (RE = Lu) and yellow (RE = Y) luminescence, respectively, when excited with UV to blue light. The blue-shifted and narrower emission of $Lu_4Ba_2[Si_{12}O_2N_{16}C_3]$:$Eu^{2+}$ is ascribed to the influence of the high atomic weight of Lu on the lattice phonon structure and correspondingly on the Stokes shift. In the case of $Lu_4Ba_2[Si_{12}O_2N_{16}C_3]$:$Eu^{2+}$, a rather broad emission is nevertheless observed as the activator ions can be incorporated on multiple sites with different surroundings and O/N disorder. Consequently, screening of the system Lu/AE/Si/O/N/C (AE = alkaline earth metal) for compounds with only one, highly symmetric coordinated AE site and an ordered light-atom distribution appears promising.

5.5 References

[1]   Xie, R.-J.; Hintzen, H. T. Optical Properties of (Oxy)Nitride Materials: A Review. *J. Am. Ceram. Soc.* **2013**, *96*, 665–687.

[2]   Xia, Z.; Liu, Q. Progress in discovery and structural design of color conversion phosphors for LEDs. *Prog. Mater. Sci.* **2016**, *84*, 59–117.

[3]   Watanabe, H.; Kijima, N. Crystal structure and luminescence properties of Sr$_x$Ca$_{1-x}$AlSiN$_3$:Eu^{2+} mixed nitride phosphors. *J. Alloys Compd.* **2009**, *475*, 434–439.

[4]   Kijima, N.; Seto, T.; Hirosaki, N. A New Yellow Phosphor La$_3$Si$_6$N$_{11}$:Ce^{3+} for White LEDs. *ECS Trans.* **2009**, *25 (9)*, 247–252.

[5]   Höppe, H. A.; Lutz, H.; Morys, P.; Schnick, W.; Seilmeier, A. Luminescence in Eu^{2+}-doped Ba$_2$Si$_5$N$_8$: fluorescence, thermoluminescence, and upconversion. *J. Phys. Chem. Solids* **2000**, *61*, 2001–2006.

[6]   Schnick, W.; Huppertz, H. Nitridosilicates – A Significant Extension of Silicate Chemistry. *Chem. - Eur. J.* **1997**, *3*, 679–683.

[7]   Huppertz, H.; Schnick, W. BaYbSi$_4$N$_7$ – Unexpected Structural Possibilities in Nitridosilicates. *Angew. Chem., Int. Ed. Engl.* **1996**, *35*, 1983–1984; BaYbSi$_4$N$_7$ – überraschende strukturelle Möglichkeiten in Nitridosilicaten. *Angew. Chem.* **1996**, *108*, 2115–2116.

[8]   Huppertz, H.; Oeckler, O.; Lieb, A.; Glaum, R.; Johrendt, D.; Tegel, M.; Kaindl, R.; Schnick, W. Ca$_3$Sm$_3$[Si$_9$N$_{17}$] and Ca$_3$Yb$_3$[Si$_9$N$_{17}$] Nitridosilicates with Interpenetrating Nets that Consist of Star-Shaped [N$^{[4]}$(SiN$_3$)$_4$] Units and [Si$_5$N$_{16}$] Supertetrahedra. *Chem. - Eur. J.* **2012**, *18*, 10857–10864.

[9]   Lieb, A.; Schnick, W. BaSm$_5$[Si$_9$Al$_3$N$_{20}$]O – a nitridoaluminosilicate oxide with a new structure type composed of "star-shaped" [N$^{[4]}$((Si,Al)N$_3$)$_4$] units as secondary building units. *Solid State Sci.* **2006**, *8*, 185–191.

[10] Maak, C.; Niklaus, R.; Friedrich, F.; Mähringer, A.; Schmidt, P. J.; Schnick, W. Efficient Yellow-Orange Phosphor Lu$_4$Ba$_2$[Si$_9$ON$_{16}$]O:Eu^{2+} and Orange-Red Emitting Y$_4$Ba$_2$[Si$_9$ON$_{16}$]O:Eu^{2+}: Two Oxonitridosilicate Oxides with Outstanding Structural Variety. *Chem. Mater.* **2017**, *29*, 8377–8384.

[11] Ramsdell, L. S. The crystal structure of *α*-SiC, type IV. *Am. Mineral.* **1944**, *29*, 431–442.

[12] Höppe, H. A.; Kotzyba, G.; Pöttgen, R.; Schnick, W. High-temperature synthesis, crystal structure, optical properties, and magnetism of the carbidonitridosilicates Ho$_2$[Si$_4$N$_6$C] and Tb$_2$[Si$_4$N$_6$C]. *J. Mater. Chem.* **2001**, *11*, 3300–3306.

[13]   Zhang, H.; Horikawa, T.; Machida, K.-i. Preparation, Structure, and Luminescence Properties of Y$_2$Si$_4$N$_6$C:Ce^{3+} and Y$_2$Si$_4$N$_6$C:Tb^{3+}. *J. Electrochem. Soc.* **2006**, *153*, H151–H154.

[14]   Yan, C.; Liu, Z.; Zhuang, W.; Liu, R.; Xing, X.; Liu, Y.; Chen, G.; Li, Y.; Ma, X. YScSi$_4$N$_6$C:Ce^{3+} − A Broad Cyan-Emitting Phosphor To Weaken the Cyan Cavity in Full-Spectrum White Light-Emitting Diodes. *Inorg. Chem.* **2017**, *56*, 11087–11095.

[15]   Liddell, K.; Thompson, D. P.; Bräuniger T.; Harris, R. K. M$_2$(Si,Al)$_4$(N,C)$_7$ (M=La,Y,Ca) carbonitrides: I. Synthesis and structural characterisation by XRD and NMR. *J. Eur. Ceram. Soc.* **2005**, *25*, 37–47.

[16]   Duan, C.; Zhang, Z.; Rösler, S.; Rösler, S.; Delsing, A.; Zhao, J.; Hintzen, H. T. Preparation, Characterization, and Photoluminescence Properties of Tb^{3+}-, Ce^{3+}-, and Ce^{3+}/Tb^{3+}-Activated RE$_2$Si$_4$N$_6$C (RE = Lu, Y, and Gd) Phosphors. *Chem. Mater.* **2011**, *23*, 1851–1861.

[17]   Seibald, M.; Rosenthal, T.; Oeckler, O.; Maak, C.; Tücks, A.; Schmidt, P. J.; Wiechert, D.; Schnick, W. New Polymorph of the Highly Efficient LED-Phosphor SrSi$_2$O$_2$N$_2$:Eu^{2+} – Polytypism of a Layered Oxonitridosilicate. *Chem. Mater.* **2013**, *25*, 1852–1857.

[18]   Mitomo, M.; Izumi, F.; Horiuchi, S.; Matsui, Y. Phase relationships in the system Si$_3$N$_4$–SiO$_2$–La$_2$O$_3$. *J. Mater. Sci.* **1982**, *17*, 2359–2364.

[19]   Snigirev, A.; Kohn, V.; Snigireva, I.; Lengeler, B. A compound refractive lens for focusing high-energy X-rays. *Nature* **1996**, *384*, 49–51.

[20]   Vaughan, G. B. M.; Wright, J. P.; Bytchkov, A.; Curfs, C.; Grundlach, C.; Orlova, M.; Erra, L.; Gleyzolle, H.; Buslaps, T.; Götz, A.; Suchet, G.; Petitdemange, S.; Rossat, M.; Margulies, L.; Ludwig, W.; Snigirev, A.; Snigireva, I.; Sorensen, H. O.; Lauridsen, E. M.; Olsen, U. L.; Oddershede, J.; Poulsen, H. F. Challenges in Materials Science Possibilities in 3D and 4D Characterization Techniques. In *Proceedings of the 31st Risø International Symposium on Materials Science*; Risø National Laboratory for Sustainable Energy, Technical University of Denmark: Roskilde, Denmark, **2010**; pp 457–476.

[21]   Lengeler, B.; Schroer, C. G.; Benner, B.; Gerhardus, A.; Günzler, T. F.; Kuhlmann, M.; Meyer, J.; Zimprich, C. J. Parabolic refractive X-ray lenses. *J. Synchrotron Radiat.* **2002**, *9*, 119–124.

[22]   Fahrnbauer, F.; Rosenthal, T.; Schmutzler, T.; Wagner, G.; Vaughan, G. B. M.; Wright, J. P.; Oeckler, O. Discovery and Structure Determination of an Unusual Sulfide Telluride through an Effective Combination of TEM and Synchrotron

Microdiffraction. *Angew. Chem., Int. Ed.* **2015**, *54*, 10020–10023; *Angew. Chem.*
2015, *127*, 10158–10161.

[23]   Durach, D.; Neudert, L.; Schmidt, P. J.; Oeckler, O.; Schnick, W. La$_3$BaSi$_5$N$_9$O$_2$:Ce^{3+}
− A Yellow Phosphor with an Unprecedented Tetrahedra Network Structure
Investigated by Combination of Electron Microscopy and Synchrotron X-ray
Diffraction. *Chem. Mater.* **2015**, *27*, 4832–4838.

[24]   Paria Sena, R.; Babaryk, A. A.; Khainakov, S.; Garcia-Granda, S.; Slobodyanik, N.
S.; van Tendeloo, G.; Abakumov, A. M.; Hadermann, J. A pseudo-tetragonal
tungsten bronze superstructure: a combined solution of the crystal structure of
K$_{6.4}$(Nb,Ta)$_{36.3}$O$_{94}$ with advanced transmission electron microscopy and neutron
diffraction. *Dalton Trans.* **2016**, *45*, 973–979.

[25]   Schlieper, T.; Milius, W.; Schnick, W. Nitrido-silicate. II: Hochtemperatur-Synthesen
und Kristallstrukturen von Sr$_2$Si$_5$N$_8$ und Ba$_2$Si$_5$N$_8$. *Z. Anorg. Allg. Chem.* **1995**, *621*,
1380–1384.

[26]   Lange, H.; Wötting, G.; Winter, G. Silicon Nitride - From Powder Synthesis to
Ceramic Materials. *Angew. Chem., Int. Ed. Engl.* **1991**, *30,* 1579–1597;
Siliciumnitrid - vom Pulver zum keramischen Werkstoff. *Angew. Chem.* **1991**, *103*,
1606–1625.

[27]   *Digital Micrograph*, Gatan, Inc.: Pleasanton, CA, USA, **1999**.

[28]   Lábár, J. L. Consistent indexing of a (set of) single crystal SAED pattern(s) with the
ProcessDiffraction program. *Ultramicroscopy* **2005**, *103*, 237–249.

[29]   Stadelmann, P. A. *JEMS*; CIME-EPFL: Saas-Fee, Switzerland, **2008**.

[30]   *ES Vision*; Emispec Systems Inc.: Tempe, AZ, USA, **2002**.

[31]   *EDAX*; AMETEK GmbH: Wiesbaden, Germany, **2013**.

[32]   *SADABS*; Bruker AXS, Inc.: Madison, WI, USA, **2001**.

[33]   Sheldrick, G. M. Crystal structure refinement with SHELXL. *Acta Crystallogr., Sect.
C: Struct. Chem.* **2015**, *71*, 3–8.

[34]   *TOPAS, v. 4.1: A program for Rietveld refinement*; Coelho Software: Brisbane,
Australia, **2007**.

[35]   Bergmann, J.; Kleeberg, R.; Haase, A.; Breidenstein, B. Advanced fundamental
parameter model for improved profile analysis. *Mater. Sci. Forum* **2000**, *347–349*,
303–308.

[36]   Cheary, R. W.; Coelho, A. A.; Cline, J. P. Fundamental Parameters Line Profile
Fitting in Laboratory Diffractometers. *J. Res. Natl. Inst. Stand. Technol.* **2004**, *109*,
1–25.

[37] Morgan, P. E. D. Pauling's second crystal rule for nitrogen-substituted crystal structures. *J. Mater. Sci.* **1986**, *21*, 4305–4309.

[38] Shannon, R. D. Revised effective ionic radii and systematic studies of interatomic distances in halides and chalcogenides. *Acta Crystallogr., Sect. A: Cryst. Phys., Diffr., Theor. Gen. Crystallogr.* **1976**, *32*, 751–767.

[39] Hoppe, R. Madelung constants. *Angew. Chem., Int. Ed. Engl.* **1966**, *5*, 95–106; Über Madelungfaktoren. *Angew. Chem.* **1966**, *78*, 52–63.

[40] Hoppe, R. The Coordination Number – an "Inorganic Chameleon". *Angew. Chem., Int. Ed. Engl.* **1970**, *9*, 25–34; Die Koordinationszahl – ein „anorganisches Chamäleon". *Angew. Chem.* **1970**, *82*, 7–16.

[41] Hübenthal, R. *Maple, Program for the Calculation of MAPLE Values, version 4*; University of Gießen: Gießen, Germany, 1993.

[42] Hoppe, R.; Voigt, S.; Glaum, H.; Kissel, J.; Müller, H. P.; Bernet, K. A new route to charge distributions in ionic solids. *J. Less-Common Met.* **1989**, *156*, 105–122.

[43] Momma, K.; Izumi, F. VESTA 3 for Three-Dimensional Visualization of Crystal, Volumetric and Morphology Data. *J. Appl. Crystallogr.* **2011**, *44*, 1272–1276.

[44] Blatov, V. A.; Shevchenko, A. P.; Proserpio, D. M. Applied Topological Analysis of Crystal Structures with the Program Package ToposPro. *Cryst. Growth Des.* **2014**, *14*, 3576–3586.

[45] Liddell, K.; Thompson, D. P. The crystal structure of $Y_3Si_5N_9O$ and revision of the compositions of some high nitrogen-containing M−Si−O−N (M = Y, La) phases. *J. Mater. Chem.* **2001**, *11*, 507–512.

[46] Woike, M.; Jeitschko, W. Preparation and Crystal Structure of the Nitridosilicates $Ln_3Si_6N_{11}$ (Ln = La, Ce, Pr, Nd, Sm) and $LnSi_3N_5$ (Ln = Ce, Pr, Nd). *Inorg. Chem.* **1995**, *34*, 5105–5108.

[47] Takahashi, J.; Yamane, H.; Shimada, M.; Yamamoto, Y.; Hirosaki, N.; Mitomo, M.; Oikawa, K.; Torii, S.; Kamiyama, T. Crystal Structure of $Lu_4Si_2O_7N_2$ Analyzed by the Rietveld Method Using the Time-of-Flight Neutron Powder Diffraction Pattern. *J. Am. Ceram. Soc.* **2002**, *85*, 2072–2077.

[48] Woike, M.; Jeitschko, W. Preparation and Crystal Structures of the Rare Earth Nitrido-Oxosilicates and Nitridosilicates with the General Formula $R_{6+x/3}Si_{11}N_{20+x}O_{1-x}$ and the Ideal Compositions $R_6Si_{11}N_{20}O$ and $R_{6.33}Si_{11}N_{21}$, Respectively (R = Y and Gd–Lu). *J. Solid State Chem.* **1997**, *129*, 312–319.

[49] Huppertz, H.; Schnick, W. Edge-sharing SiN_4 Tetrahedra in the Highly Condensed Nitridosilicate $BaSi_7N_{10}$. *Chem. - Eur. J.* **1997**, *3*, 249–252.

[50]   Maak, C.; Hoch, C.; Schmidt, P. J.; Schnick, W. Oxonitridosilicate Oxides *RE*$_{26}$Ba$_6$[Si$_{22}$O$_{19}$N$_{36}$]O$_{16}$:Eu^{2+} (*RE* = Y, Tb) with a Unique Layered Structure and Orange-Red Luminescence for *RE* = Y. *Inorg. Chem.* **2018**, *57*, 2242–2248.

[51]   López, R.; Gómez, R. Band-gap energy estimation from diffuse reflectance measurements on sol-gel and commercial TiO$_2$: a comparative study. *J. Sol-Gel Sci. Technol.* **2012**, *61*, 1–7.

[52]   Tauc, J.; Grigorovici, R.; Vancu, A. Optical Properties and Electronic Structure of Amorphous Germanium. *Phys. Status Solidi B* **1966**, *15*, 627–637.

[53]   Blasse, G. Luminescence of inorganic solids: from isolated centres to concentrated systems. *Prog. Solid State Chem.* **1988**, *18*, 79–171.

[54]   Xu, X.; Cai, C.; Hao, L.; Wang, Y.; Li, Q. The photoluminescence of Ce-doped Lu$_4$Si$_2$O$_7$N$_2$ green phosphors. *Mater. Chem. Phys.* **2009**, *118*, 270–272.

[55]   Xia, Z.; Meijerink, A. Ce^{3+}-Doped garnet phosphors: composition modification, luminescence properties and applications. *Chem. Soc. Rev.* **2017**, *46*, 275–299.

6 Oxonitridosilicate Oxides $RE_{26}Ba_6[Si_{22}O_{19}N_{36}]O_{16}:Eu^{2+}$ (RE = Y, Tb) with a Unique Layered Structure and Orange-Red Luminescence for RE = Y
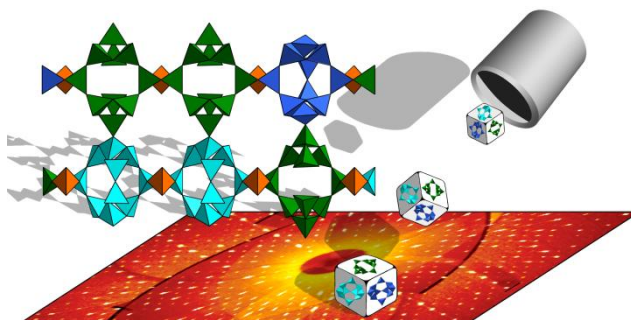
Abstract. The oxonitridosilicate oxides $RE_{26}Ba_6[Si_{22}O_{19}N_{36}]O_{16}:Eu^{2+}$ (RE = Y, Tb) were synthesized by high-temperature reaction in a radiofrequency furnace starting from REF$_3$, RE_2O_3 (RE = Y, Tb), BaH$_2$, Si(NH)$_2$, and EuF$_3$. The structure elucidation is based on single-crystal X-ray data. The isotypic materials crystallize in the monoclinic space group *Pm* (no. 6) [Z = 3, a = 16.4285(8), b = 20.8423(9), c = 16.9257(8) Å, β = 119.006(3)° for RE = Y and a = 16.5465(7), b = 20.9328(9), c = 17.0038(7) Å, β = 119.103(2)° for RE = Tb]. The unique silicate layers are made up from Q^1-, Q^2-, and Q^3-type Si(O/N)$_4$- as well as Q^4-type SiN$_4$ tetrahedra, forming three slightly differing types of cages. The corresponding 3-fold superstructure as well as pronounced hexagonal pseudosymmetry complicated the structure elucidation. Rietveld refinement on powder X-ray diffraction data, energy-dispersive X-ray spectroscopy and infrared spectroscopy support the findings from single-crystal X-ray data. When excited with UV to blue light, Y$_{26}$Ba$_6$[Si$_{22}$O$_{19}$N$_{36}$]O$_{16}$:Eu^{2+} shows broad orange-red luminescence (λ_{em} = 628 nm,

fwhm ≈ 125 nm/3130 cm^{-1}). An optical band gap of 4.2 eV was determined for the doped compound by means of UV/Vis spectroscopy.

6.1   Introduction

(Oxo)nitridosilicates are an intensively investigated and highly relevant class of compounds, combining a fascinating structural chemistry and high potential for applications.[1] Representatives of this class of materials are of considerable interest because they find broad application in phosphor-converted light emitting diodes (pcLEDs).[2–5] The covalent bonding character in highly condensed (oxo)nitridosilicate networks ($κ = n$(Si):n(N/O) ≥ 0.5) often results in high chemical and physical inertness. Next to optical transparency and high quantum efficiency, these are crucial requirements for state-of-the-art luminescent materials.[6] The higher covalency of activator–nitrogen bonds (nephelauxetic effect) leads to red-shifted Eu^{2+} and Ce^{3+} emission compared to oxosilicates.[7] Therefore, red emitting nitridosilicates or -aluminates such as (Sr,Ca)AlSiN$_3$:Eu^{2+}, (Ba,Sr)$_2$Si$_5$N$_8$:Eu^{2+}, or most recently Sr[LiAl$_3$N$_4$]:Eu^{2+} are applied in high color rendering white pcLEDs.[8–10] Furthermore, (oxo)nitridosilicates frequently exhibit intriguing crystal structures. As nitrogen can connect up to four tetrahedral centers and even allows for edge-sharing of SiN$_4$-tetrahedra, the already large structural variability of oxosilicates is substantially extended.[11] Further novel structure types have been obtained, when bivalent and trivalent cations, e.g. alkaline earth (AE) and rare earth (RE) metals, were simultaneously incorporated during synthesis. Although this approach seems quite simple, only a few representatives of respective materials have been reported so far.[12–16] Among them are for example all known silicate structure types containing 4-fold bridging N (N$^{[4]}$) atoms in so-called star-shaped units [N$^{[4]}$(SiN$_3$)$_4$]. These are BaYbSi$_4$N$_7$, Ca$_3RE_3$[Si$_9$N$_{17}$] (RE = Sm, Yb), BaSm$_5$[Si$_9$Al$_3$N$_{20}$]O, and RE_4Ba$_2$[Si$_9$ON$_{16}$]O (RE = Y, Lu).[17–20] Like most (oxo)nitridosilicates, the above named materials exhibit 3D silicate networks. Layered materials, in contrast, are rarely found in this compound class. Consequently, Sr$_{10}$Sm$_6$Si$_{30}$Al$_6$O$_7$N$_{54}$ is the only layered silicate containing alkaline earth (AE) and rare earth (RE) metals so far.[21] In order to obtain further silicates with divalent and trivalent cations, new explorative synthesis routes are desired. Recently, reactions of AE metal hydrides and RE metal halides yielded a couple of novel compounds.[16,20,22] Besides their intriguing structural chemistry, the obtained AE/RE/Si/O/N compounds are auspicious host lattices for Eu^{2+} and Ce^{3+} doping. In this context, the recently reported phosphors La$_3$BaSi$_5$N$_9$O$_2$:Ce^{3+} and Lu$_4$Ba$_2$[Si$_9$ON$_{16}$]O:Eu^{2+} stand out. La$_3$BaSi$_5$N$_9$O$_2$:Ce^{3+}, with its broad yellow emission, is a potential material for a single-phosphor approach

(1pcLED).[16] Efficiently yellow-orange emitting $Lu_4Ba_2[Si_9ON_{16}]O$:Eu^{2+} may be applied in warm white pcLEDs with low color rendering index (CRI).[20] Following on from these results, the title compounds were synthesized in an exploratory approach using the same synthesis route. The novel oxonitridosilicate oxides $Y_{26}Ba_6[Si_{22}O_{19}N_{36}]O_{16}$:$Eu^{2+}$ and $Tb_{26}Ba_6[Si_{22}O_{19}N_{36}]O_{16}$:$Eu^{2+}$ represent a new structure type with unique silicate layers. Additionally, the compound with RE = Y is a suitable host lattice for Eu^{2+} ions and exhibits luminescence in the orange-red spectral range.

6.2   Experimental Section

6.2.1   Synthesis

Due to the sensitivity of some starting materials to air and moisture, all synthesis steps were carried out in an argon-filled glovebox (Unilab, MBraun, Garching; O_2 < 1 ppm; H_2O < 1 ppm) or in flame-dried glass ware. $Y_{26}Ba_6[Si_{22}O_{19}N_{36}]O_{16}$:$Eu^{2+}$ was synthesized from YF_3 (1.80 mmol, 262.7 mg; Chempur, 99.999%), Y_2O_3 (0.18 mmol, 40.7 mg; Sigma-Aldrich, 99.999%), BaH_2 (3.42 mmol, 476.7 mg; Chemco, 99.7%), $Si(NH)_2$ (1.80 mmol, 104.6 mg),[23] and EuF_3 (0.014 mmol, 3.0 mg; Sigma-Aldrich, 99.99%). $Tb_{26}Ba_6[Si_{22}O_{19}N_{36}]O_{16}$:$Eu^{2+}$ was synthesized from TbF_3 (1.80 mmol, 388.8 mg; Chempur, 99.9%), Tb_2O_3 (0.18 mmol, 3.42 mg; Sigma-Aldrich, 99.99%), BaH_2 (3.42 mmol, 476.7 mg), $Si(NH)_2$ (1.80 mmol, 104.6 mg),[23] and EuF_3 (0.014 mmol, 3.0 mg). Starting materials were ground in an agate mortar, filled into a tungsten crucible and then transferred into a water-cooled silica glass reactor of a radiofrequency furnace (type IG 10/600; Hüttinger Elektronik Freiburg). Under N_2-atmosphere the crucibles were heated to 1600 °C for 1 h, maintained at 1600 °C for 9 h, cooled down to 900 °C within 50 h and finally quenched to room temperature. The reactions yielded inhomogeneous reddish samples containing orange crystals of the title compounds. Crystals of $Y_{26}Ba_6[Si_{22}O_{19}N_{36}]O_{16}$:$Eu^{2+}$ show orange-red luminescence when excited with blue light. Both compounds are stable toward air and water. In an optimized synthesis procedure for $Y_{26}Ba_6[Si_{22}O_{19}N_{36}]O_{16}$:$Eu^{2+}$ crucibles were heated to 1500 °C for 1 h, maintained at 1500 °C for 60 h, and finally quenched to room temperature. Washing of the product with water and subsequent treatment with a 1:1 mixture of isopropanol/glacial acetic acid gave $Y_{26}Ba_6[Si_{22}O_{19}N_{36}]O_{16}$:$Eu^{2+}$ as main phase with ≈ 15% yield. The powders also show orange-red luminescence but significantly weaker than single crystals from the synthesis procedure with a final cooling ramp.

6.2.2   Electron Microscopy

Scanning electron microscopy (SEM) was carried out with a JSM 6500F microscope (JEOL). Energy-dispersive X-ray spectroscopy EDX was performed using a Si/Li EDX detector (Oxford instruments, model 7418) at an acceleration voltage of 30 kV.

6.2.3   FTIR Spectroscopy

Fourier transform infrared (FTIR) analysis of $Y_{26}Ba_6[Si_{22}O_{19}N_{36}]O_{16}$:Eu^{2+} was carried out with a Jasco FT/IR-4100 spectrometer using the ATR method.

6.2.4   Single-Crystal X-ray Diffraction

Single crystals of both phases were isolated and mounted on MicroMounts (MiTeGen) with an aperture size of 20 µm. Measurements were carried out on a Bruker D8 Venture diffractometer with rotating anode (Bruker AXS, Karlsruhe, Germany, Mo Kα radiation, Goebel mirror optics). Absorption effects were corrected with the program SADABS.[24] The crystal structures were solved using Direct Methods (SHELXS)[25] and refined by full-matrix least-squares method (SHELXL).[26,27] Details on crystal structure investigations can be obtained from the Cambridge Crystallographic Data Centre (CCDC) upon quoting the CCDC codes 1812427 for $Y_{26}Ba_6[Si_{22}O_{19}N_{36}]O_{16}$:Eu^{2+} and 1812428 for $Tb_{26}Ba_6[Si_{22}O_{19}N_{36}]O_{16}$:Eu^{2+}.

6.2.5   Powder X-ray Diffraction

Powder X-ray diffraction (PXRD) was performed for $Y_{26}Ba_6[Si_{22}O_{19}N_{36}]O_{16}$:Eu^{2+} with a STOE STADI P diffractometer (Stoe&Cie, Darmstadt, Germany, Cu Kα_1 radiation, Ge(111) monochromator; Mythen1K detector, DECTRIS Ltd., Baden-Daettwil, Switzerland) in parafocusing Debye-Scherrer geometry. Rietveld refinement was performed with TOPAS Academic V4.1 software applying the fundamental parameters approach (direct convolution of source emission profiles, axial instrument contributions, crystallite size and microstrain effects).[28–31]

6.2.6   UV/Vis Spectroscopy

For UV/Vis spectroscopy on $Y_{26}Ba_6[Si_{22}O_{19}N_{36}]O_{16}$:$Eu^{2+}$ a Jasco V-650 UV/Vis spectrophotometer with a deuterium and a halogen lamp was used (JASCO, Pfungstadt, Germany, Czerny-Turner monochromator with 1200 lines/mm, concave grating, photomultiplier tube detector).

6.2.7   Luminescence

Luminescence of $Y_{26}Ba_6[Si_{22}O_{19}N_{36}]O_{16}$:$Eu^{2+}$ was measured on single crystals in glass capillaries using a HORIBA Fluoromax4 spectrofluorimeter system, attached via optical fibers to an Olympus BX51 microscope. The excitation wavelength was λ_{exc} = 440 nm. The spectral width of the excitation wavelength at 440 nm was 10 nm. Emission spectra were captured with 2 nm step size in a wavelength range between 400 and 800 nm. Excitation spectra were obtained with monitoring wavelength of 628 nm.

6.3   Results and Discussion

6.3.1   Synthesis and Chemical Analysis

The title compounds were synthesized at high temperatures in an exploratory approach starting from REF_3, RE_2O_3 (RE = Y, Tb), BaH_2, $Si(NH)_2$, and EuF_3. The driving force of the reactions is probably the decomposition of BaH_2 (at 675 °C)[32] and the following formation of BaF_2 with F^- ions from REF_3. The synthesis procedure with a final cooling ramp (see chapter 6.2.1 Synthesis) yielded single crystals of both phases sufficient for single-crystal X-ray diffraction measurements. The chemical composition of such crystals was determined using EDX (six point measurements for each phase). The results of the EDX measurements (Table 1) are in good agreement with the crystal structure refinements from single-crystal X-ray data. No other elements were detected. The absence of O–H and N–H bonds was checked with FTIR spectroscopy (Figure S1). Eu was not detected with EDX but is unequivocally proven by luminescence measurements, as nondoped samples do not show luminescence.

$Y_{26}Ba_6[Si_{22}O_{19}N_{36}]O_{16}$:$Eu^{2+}$ was obtained as main phase by washing the heterogeneous products of the optimized synthesis with H_2O and then in a mixture of isopropanol/glacial acetic acid (ratio 1:1). Rietveld refinements of washed samples support the results from

single-crystal X-ray data (Figure 1). Data of the refinement are summarized in the Supporting Information (Table S1). For comparison, PXRD data of a sample before washing with BaF_2 as main phase are shown in the Supporting Information (Figure S2, Table S1).

Table 1. EDX Results for $RE_{26}Ba_6[Si_{22}O_{19}N_{36}]O_{16}$:$Eu^{2+}$ (RE = Y, Tb).

	Theoretical atom%	Experimental atom%	
		RE = Y	RE = Tb
RE	20.8	17.4(12)	24.3(11)
Ba	4.8	4.0(7)	6(2)
Si	17.6	16(2)	17(2)
O	28.0	33(4)	26(2)
N	28.8	30(2)	27(3)
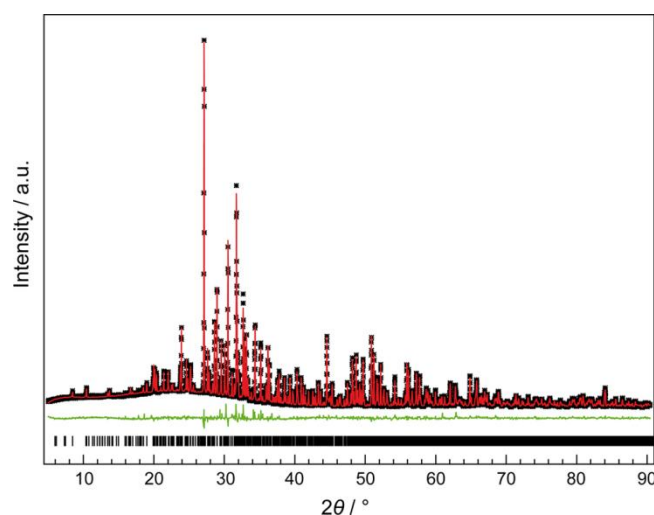
Figure 1. Rietveld refinement for washed $Y_{26}Ba_6[Si_{22}O_{19}N_{36}]O_{16}$:$Eu^{2+}$ (Cu Kα_1, λ = 1.54056 Å).

6.3.2   Structure Determination and Description

The crystal structures of $Y_{26}Ba_6[Si_{22}O_{19}N_{36}]O_{16}$:$Eu^{2+}$ and $Tb_{26}Ba_6[Si_{22}O_{19}N_{36}]O_{16}$:$Eu^{2+}$ were solved (SHELXS-97) and refined (SHELXL-97) from single-crystal X-ray data in monoclinic space group Pm (no. 6).[25,26] Inversion twinning had to be taken into account for both refinements, yielding twin ratios of approximately 1:1. The small amounts of Eu (0.4 mol% referred to Ba) were neglected due to insignificant contribution to the structure factor. As O and N atoms can hardly be distinguished by X-rays due to similar atomic form

factors, assignment of N/O was performed according to Pauling's rules.[33] Accordingly, 2-fold bridging anion sites were occupied with N, noncondensed anion sites were occupied with O, and terminal anion sites were mixed occupied with a fixed ratio of 86.4% O/13.6% N in order to obtain charge neutrality. The heavy atoms (Y/Tb and Ba) were refined with anisotropic displacement parameters, whereas Si, N, and O atoms were refined with isotropic thermal displacement parameters. Additionally, isotropic displacement parameters of chemically equivalent Si (differentiation between Si atoms in Q^1, Q^2, Q^3, and Q^4 type tetrahedra) and N/O (differentiation between, bridging, terminal, and oxidic) atoms were constrained to be of the same values in order to keep the number of parameters reasonably small (Tables 2 and S2). Crystallographic data are summarized in Table 2. Fractional atomic coordinates and isotropic displacement parameters (Tables S3 and S4) as well as anisotropic displacement parameters (Tables S5 and S6) are summarized in the Supporting Information.

Characteristic for the crystal structure are the $[Si_{22}O_{19}N_{36}]^{58-}$ layers stacked along [100]. Between each layer there is an additional shift along [102] (Figure 2). The silicate layers are made up from vertex-sharing Q^1-, Q^2-, and Q^3-type Si(O/N)$_4$ and Q^4-type SiN$_4$ tetrahedra in a molar ratio of 1:5:4:10, leading to a degree of condensation of κ = 0.4. The layers exhibit a hierarchical buildup with three different types of cages (Figure 3), each containing ten tetrahedra. All cages have an identical *sechser* ring in common but differ in the arrangement of the residual four tetrahedra. Cages of type 1 (Figure 3a, green) contain two tetrahedra of Q^1-type and can therefore be considered as open cages. In cages of type 2 (Figure 3a, turquoise) and type 3 (Figure 3a, blue) tetrahedra of Q^1-type are replaced by Q^2-type tetrahedra, resulting in closed cages. Cages of type 2 and 3 are crystallographically not identical but could be transformed into each other by inversion. The cages are directly connected via common corners. Additional Q^2-type tetrahedra (Figure 3b, orange) are present, leading to connecting *dreier* rings. Figure 3b shows the repeating unit within the layers. The cage sequence –1*–1*–3– over –2–2–1– (*: rotation of 180° around [010]) apparently impedes centrosymmetry.

The presence of three different cage types leads to a 3-fold superstructure, as is highlighted in the *h*0*l* reciprocal lattice section (Figure 4b). Furthermore, the diffraction patterns show strongly pronounced hexagonal pseudosymmetry. Indeed, Ba and Y/Tb are close to hexagonal symmetry. This is exemplarily shown for Ba atoms, which form Kagomé nets in the *ac*-plane. One third of the Ba atoms is located within silicate cages (Figure 4a, turquoise), two-thirds are located between them (Figure 4a, violet). The metric of the Kagomé nets can be described by a smaller pseudohexagonal unit cell (Figure 4a,

green), which would also hold if only one type of silicate cages was present. Accordingly, strong reflections in the reciprocal lattice section can be described by a larger pseudohexagonal reciprocal cell (Figure 4b, green). However, the presence of three slightly differing cages in the crystal structure as well as the sequence of these cages require the larger monoclinic unit cell (Figure 4a, black), which can be interpreted as a distorted ($\sqrt{3} \times \sqrt{3}$)$R$30° supercell.

Table 2. Crystallographic Data for $Y_{26}Ba_6[Si_{22}O_{19}N_{36}]O_{16}$:$Eu^{2+}$ and $Tb_{26}Ba_6[Si_{22}O_{19}N_{36}]O_{16}$:$Eu^{2+}$.

	$Y_{26}Ba_6[Si_{22}O_{19}N_{36}]O_{16}$:$Eu^{2+}$	$Tb_{26}Ba_6[Si_{22}O_{19}N_{36}]O_{16}$:$Eu^{2+}$
formula mass / g·mol^{-1}	4818.04	6638.30
crystal system	monoclinic	
space group	Pm (no. 6)	
lattice parameters / Å, °	a = 16.4285(8), b = 20.8423(9) c = 16.9257(8), β = 119.006(3)	a = 16.5465(7), b = 20.9328(9) c = 17.0038(7), β = 119.103(2)
volume / Å^3	5068.6(4)	5145.9(4)
formula units/cell	3	
X-ray density / g·cm^{-3}	4.735	6.426
abs. coefficient / μ·mm^{-1}	25.946	30.255
F(000)	6570	8598
crystal dimensions / mm^3	0.03 × 0.03 × 0.01	0.03 × 0.03 × 0.01
diffractometer	D8 Venture, Bruker AXS	
radiation	Mo Kα (λ = 0.71073 Å)	
temperature / K	298(2)	296(2)
absorption correction	multiscan[24]	
θ range / °	2.390–25.999	2.380–25.000
observed reflections	45751	128700
independent reflections	18335	18635
independent reflections with I ≥ 2σ(I)	15385	12836
min./max. transmission	0.5740/0.7470	0.6175/0.7498
refined parameters	908	908
GoF	1.041	1.174
R_{int}/R_σ	0.0219/0.0324	0.0443/0.0265
R values (I ≥ 2σ(I))	R_1 = 0.0388/wR_2 = 0.0955	R_1 = 0.0342/wR_2 = 0.0871
R values (all data)	R_1 = 0.0493/wR_2 = 0.1002	R_1 = 0.0578/wR_2 = 0.0941
min./max. residual electron density / e·Å^{-3}	−2.607/2.973	−4.443/4.376
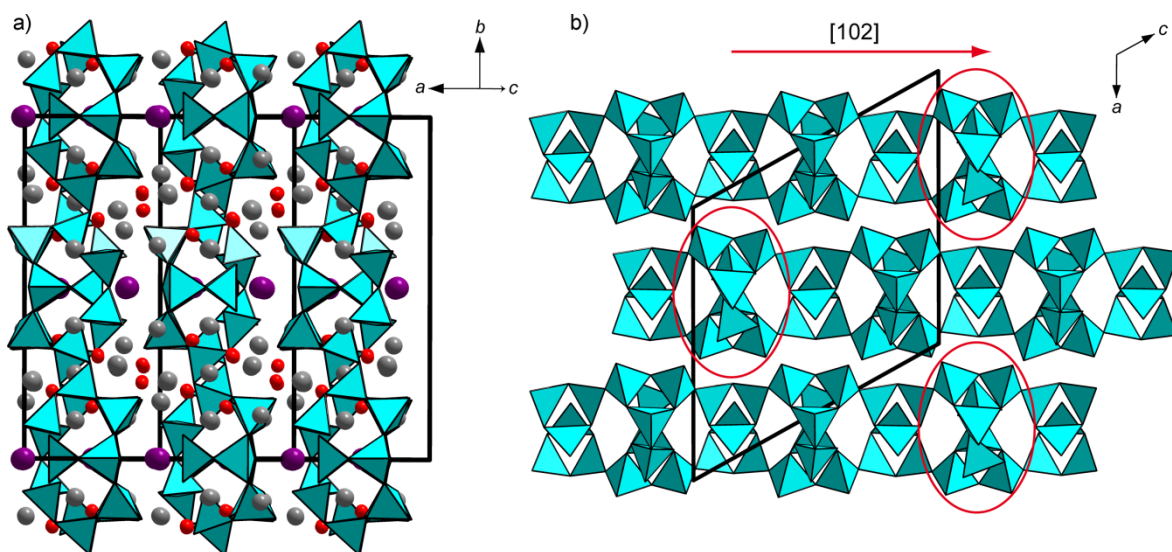
Figure 2. (a) Crystal structure of $RE_{26}Ba_6[Si_{22}O_{19}N_{36}]O_{16}$:Eu^{2+} ($RE$ = Y, Tb), viewing direction [102]. (b) $[Si_{22}O_{19}N_{36}]^{58-}$ layers, viewed along [010] with shift along [102] indicated by red arrow. SiN$_4$/Si(O/N)$_4$ tetrahedra, turquoise; Y/Tb atoms, gray; Ba atoms, violet; and noncondensed O atoms, red.
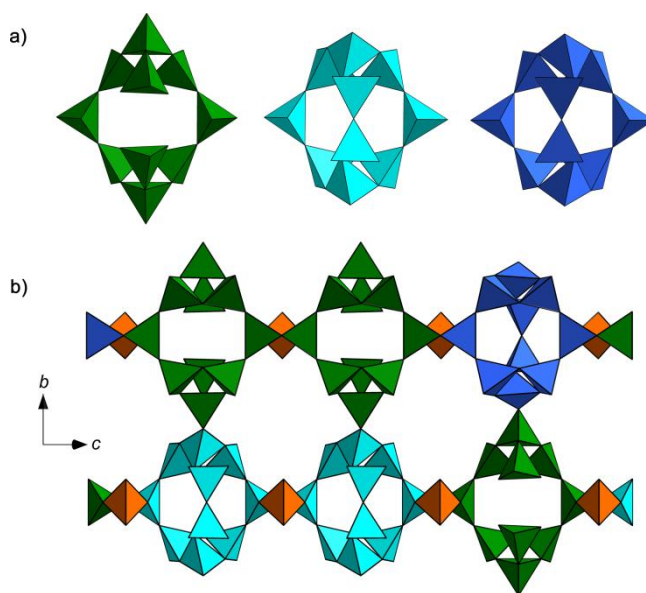
Figure 3. (a) Cages of type 1 (green), type 2 (turquoise), and type 3 (blue). (b) Repeating unit in $[Si_{22}O_{19}N_{36}]^{58-}$ layers, viewing direction [100].
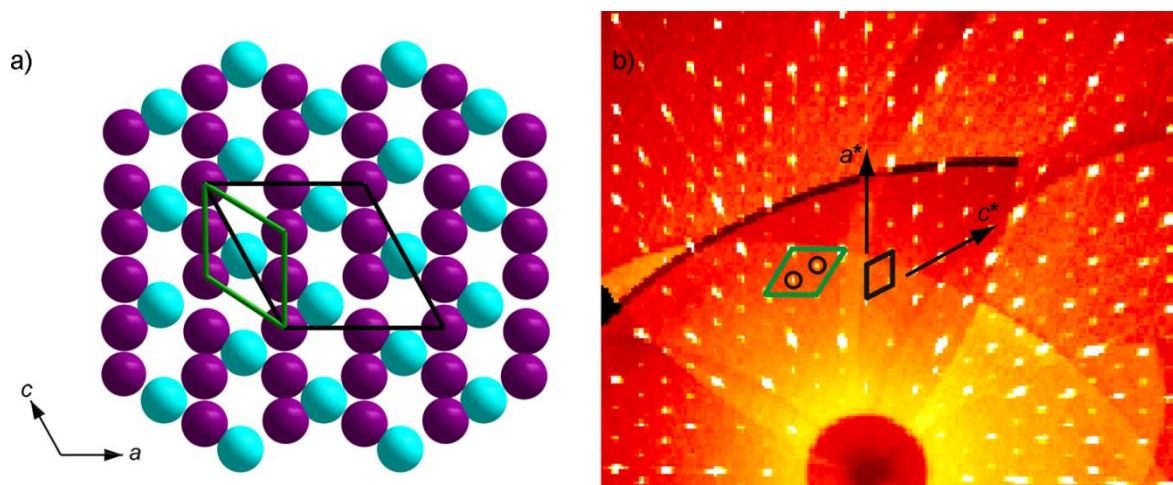
Figure 4. (a) Layer of Ba atoms forming Kagomé nets in the *ac*-plane. Ba atoms located in silicate cages, turquoise; Ba atoms outside cages, violet. Small pseudohexagonal unit cell, green; actual unit cell including the superstructure, black. Radius of Ba atoms ≈ 2.4 Å. (b) *h*0*l* reciprocal lattice section with corresponding green and black reciprocal cells. Superstructure reflections marked by black circles only described by black reciprocal cell.

The Si–N[2] distances range between 1.63(2)–1.80(2) Å for RE = Y and 1.60(2)–1.82(3) Å for RE = Tb. The Si–N/O[1] distances are 1.58(2)–1.71(2) Å for RE = Y and 1.55(2)–1.73(2) Å for RE = Tb. Therefore, all distances are in the typical ranges compared to other (oxo)nitridosilicates.[34,35] The heavy atoms Ba and Y/Tb are ordered and occupy 57 crystallographically independent sites, 18 for Ba and 39 for Y/Tb. The 18 Ba sites are coordinated by 8 to 11 N/O and N atoms. Ba–N/O distances range from 2.63(1) to 3.59(2) Å for the Y containing compound and 2.56(2) to 3.59(2) Å for RE = Tb. The Ba−N/O distances are rather large with an average value of 3.1 Å for both compounds. However, they correspond to those in other Ba-nitridosilicates such as $Ba_2Si_5N_8$ (2.677(7)–3.171(4) Å) or $BaSi_7N_{10}$ (2.913(3)–3.529(3) Å).[36,37] Y/Tb sites are coordinated either 6- or 7-fold by N/O and N atoms. The atom distances range from 2.07(1) to 2.73(1) Å for Y–N/O and from 2.11(2) to 2.76(2) Å in the case of Tb–N/O. These are typical values compared to other yttrium/terbium silicates.[38,39]

The coordination geometry around six Y/Tb (Y/Tb 1, 4, 7, 31, 35, 39, see Tables S3 and S4) sites with similar surroundings requires closer consideration. Each of these sites is coordinated by three O and N/O atoms with rather short interatomic distances (Figure 5, yellow), whereas the distances to the three coordinating N atoms are significantly larger (Figure 5, green). This is exemplarily shown for atom Y39, as the anisotropic displacement parameters (ADP) of Y39/Tb39 have the largest ADP max/min ratios. An

explanation for the strongly anisotropic ellipsoids can be derived from the calculated Fourier map ($F_{obs} - F_{calc}$, calculated with *VESTA*[40]). The large differences in interatomic distances result in a bean-shaped electron density distribution, which cannot be described properly by anisotropic refinement of the displacement parameters. Anharmonic refinement using JANA2006 was carried out but was not successful.[41] Convergence of the refinements was not achieved, probably because of the large amount of parameters (939 parameters, isotropic displacement parameters of chemically similar Si, O, and N atoms already constrained).
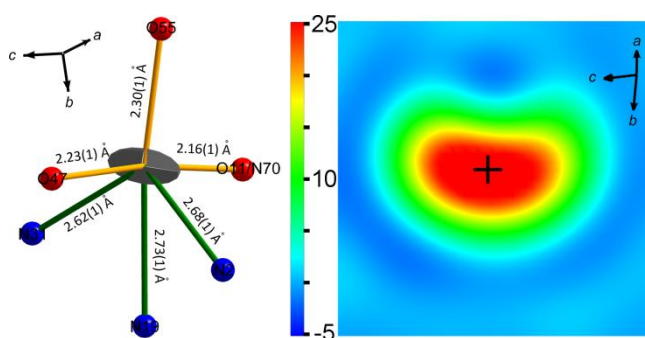
Figure 5. Left: Coordination sphere around Y39 with long green and significantly shorter yellow distances. Right: Resulting electron density distribution ($F_{obs} - F_{calc}$) with viewing direction along the Y39–O47 bond (scale bar in e$^-$/a$_0^3$ with a$_0$: Bohr radius).[40]

6.3.3   UV/Vis Spectroscopy

In order to determine the optical band gap of the title compounds, solid-state UV/Vis spectroscopy was representatively performed with a sample of $Y_{26}Ba_6[Si_{22}O_{19}N_{36}]O_{16}$:Eu^{2+}. Samples of $Tb_{26}Ba_6[Si_{22}O_{19}N_{36}]O_{16}$:Eu^{2+} with sufficient purity for significant UV/Vis data were not obtained. The reflectance spectrum (Figure S3) of $Y_{26}Ba_6[Si_{22}O_{19}N_{36}]O_{16}$:Eu^{2+} shows a broad absorption band in the UV region around 265 nm. For the determination of the optical band gap, the reflectance (R) spectrum was converted to pseudoabsorption by the Kubelka-Munk function $F(R) = (1 - R)^2/2R$.[42] Then, the band gap was determined in a Tauc plot by drawing a line tangent at the inflection point (Figure 6).[43] The evaluated band gap is approximately 4.2 eV. Thereby, a direct allowed transition was assumed (n = 1/2).
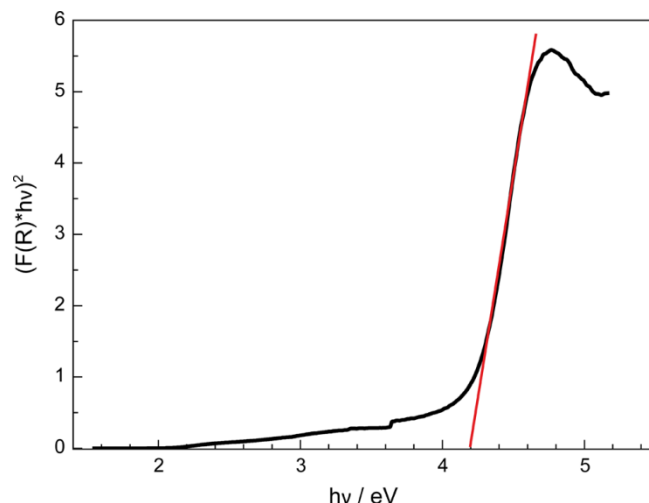
Figure 6. Tauc plot (n = 1/2) for $Y_{26}Ba_6[Si_{22}O_{19}N_{36}]O_{16}$:Eu^{2+}.

6.3.4   Luminescence

Single crystals of $Y_{26}Ba_6[Si_{22}O_{19}N_{36}]O_{16}$:Eu^{2+} show strong orange-red emission when excited by UV to blue light of an (In,Ga)N-LED. In contrast, $Tb_{26}Ba_6[Si_{22}O_{19}N_{36}]O_{16}$:Eu^{2+} single crystals as well as the bulk samples of $Y_{26}Ba_6[Si_{22}O_{19}N_{36}]O_{16}$:Eu^{2+}, obtained from washing with water and isopropanol/glacial acetic acid, show significantly weaker orange-red emission, and consequently, no meaningful luminescence data were obtained. Therefore, luminescence measurements were only performed on single crystals of $Y_{26}Ba_6[Si_{22}O_{19}N_{36}]O_{16}$:Eu^{2+}. The excitation spectrum indicates a maximum at ≈ 400 nm (Figure 7). The emission has a maximum at 628 nm; color coordinates (CIE) are x = 0.51 and y = 0.47. $Y_{26}Ba_6[Si_{22}O_{19}N_{36}]O_{16}$:Eu^{2+} exhibits a broad emission band with a full width at half-maximum (*fwhm*) of ≈ 125 nm/3130 cm^{-1}. The Stokes shift was roughly estimated to be ≈ 6100 cm^{-1} (as twice the energy difference between the peak energy of the emission band and the zero phonon line. The zero phonon line was empirically determined as the intersection point of excitation and emission spectra).[44,45] The broad emission and large Stokes shift probably result from incorporation of Eu^{2+} on a large number of sites with different surroundings. The crystal structure exhibits 57 crystallographically independent cation sites, 18 for Ba (CN 8–11) and 39 for Y (CN 6/7). Regarding the ionic radius of Eu^{2+} compared to Ba^{2+} and Y^{3+} (Eu^{2+}: 117 pm, Ba^{2+}: 149 pm, Y^3: 90 pm; coordination number CN = 6, respectively),[46] we assume that Eu^{2+} prefers the Ba^{2+} sites but partially also occupies Y^{3+} sites. This may give rise to strong reabsorption of shorter wavelength emission light by lower absorption energy centers and/or to energy transfer from higher energy absorbing centers to lower energy

absorbing centers, resulting in the observed broad emission. The emission of $Y_{26}Ba_6[Si_{22}O_{19}N_{36}]O_{16}$:Eu^{2+} is comparable to that of recently reported $Y_4Ba_2[Si_9ON_{16}]O$:Eu^{2+}, a phosphor that was obtained from an analogous synthesis approach. $Y_4Ba_2[Si_9ON_{16}]O$:Eu^{2+} also shows orange-red luminescence, with $\lambda_{em} \approx 622$ nm and $fwhm \approx 111$ nm.[20]
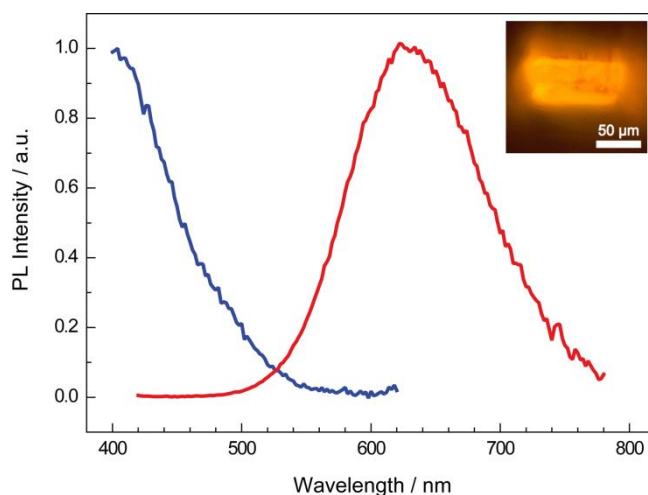
Figure 7. Excitation (blue) and emission spectra (red) for crystals of $Y_{26}Ba_6[Si_{22}O_{19}N_{36}]O_{16}$:Eu^{2+}.

6.4   Conclusion

The oxonitridosilicate oxides $RE_{26}Ba_6[Si_{22}O_{19}N_{36}]O_{16}$:Eu^{2+} ($RE$ = Y, Tb) were synthesized in a radiofrequency furnace and characterized by means of X-ray diffraction (single-crystal and PXRD), EDX, FTIR, and UV/Vis spectroscopy. The isotypic materials crystallize in a novel structure type containing unique $[Si_{22}O_{19}N_{36}]^{58-}$ layers. Observed superstructure and pseudosymmetry phenomena are discussed in detail. The applied reaction route starting from REF$_3$, RE_2O_3 (RE = Y, Tb), BaH$_2$, and Si(NH)$_2$ is probably promoted by the decomposition of the alkaline earth metal hydrides and subsequent formation of highly stable fluorides AEF$_2$. Since a couple of new materials synthesized in this way have been reported recently, this route seems auspicious in order to explore the system AE/RE/Si/O/N.[16,20] Besides a fascinating structural chemistry, such materials are promising host lattices for Eu^{2+} and Ce^{3+} and, hence, for application in pcLEDs. The orange-red luminescence of $Y_{26}Ba_6[Si_{22}O_{19}N_{36}]O_{16}$:Eu^{2+} reported in this contribution exhibits a broad emission band and a large Stokes shift. This is probably caused by incorporation of Eu^{2+} on a large number of different sites, resulting in strong reabsorption

effects. Therefore, novel highly symmetric AE/RE/Si/O/N (AE = Ca–Ba) host lattices with a small number of cation sites are of interest. Such phosphors may exhibit more narrow Eu^{2+} emission suitable for state-of-the-art pcLEDs.

6.5   References

[1]   Zeuner, M.; Pagano, S.; Schnick, W. Nitridosilicates and Oxonitridosilicates: From Ceramic Materials to Structural and Functional Diversity. *Angew. Chem., Int. Ed.* **2011**, *50*, 7754–7775; Nitridosilicate und Oxonitridosilicate: von keramischen Materialien zu struktureller und funktioneller Diversität. *Angew. Chem.* **2011**, *123*, 7898–7920.

[2]   Xie, R.-J.; Hirosaki, N.; Takeda, T. Rare-Earth Activated Nitride Phosphors: Synthesis, Luminescence and Applications. *Materials* **2010**, *3*, 3777–3793.

[3]   Höppe, H. A. Recent developments in the field of inorganic phosphors. *Angew. Chem., Int. Ed.* **2009**, *48*, 3572–3582; Aktuelle Entwicklungen auf dem Gebiet der anorganischen Leuchtstoffe. *Angew. Chem.* **2009**, *121*, 3626–3636.

[4]   Pust, P.; Schmidt, P. J.; Schnick, W. A revolution in lighting. *Nat. Mater.* **2015**, *14*, 454–458.

[5]   Xia, Z.; Xu, Z.; Chen, M.; Liu, Q. Recent developments in the new inorganic solid-state LED phosphors. *Dalton. Trans.* **2016**, *45*, 11214–11232.

[6]   Mueller-Mach, R.; Mueller, G.; Krames, M. R.; Höppe, H. A.; Stadler, F.; Schnick, W.; Juestel, T.; Schmidt, P. Highly efficient all-nitride phosphor-converted white light emitting diode. *Phys. Status Solidi A* **2005**, *202*, 1727–1732.

[7]   Feldmann, C. Technical Revolution Underway − Nitride-based Phosphors for LED Application. *Z. Anorg. Allg. Chem.* **2012**, *638*, 2169–2171.

[8]   Watanabe, H.; Kijima, N. Crystal structure and luminescence properties of Sr$_x$Ca$_{1-x}$AlSiN$_3$:Eu^{2+} mixed nitride phosphors. *J. Alloys Compd.* **2009**, *475*, 434–439.

[9]   Höppe, H. A.; Lutz, H.; Morys, P.; Schnick, W.; Seilmeier, A. Luminescence in Eu^{2+}-doped Ba$_2$Si$_5$N$_8$: fluorescence, thermoluminescence, and upconversion. *J. Phys. Chem. Solids* **2000**, *61*, 2001–2006.

[10] Pust, P.; Weiler, V.; Hecht, C.; Tücks, A.; Wochnik, A. S.; Henß, A.-K.; Wiechert, D.; Scheu, C.; Schmidt, P. J.; Schnick, W. Narrow-band red-emitting Sr[LiAl$_3$N$_4$]:Eu^{2+} as a next-generation LED-phosphor material. *Nat. Mater.* **2014**, *13*, 891–896.

[11] Schnick, W.; Huppertz, H. Nitridosilicates – A Significant Extension of Silicate Chemistry. *Chem. - Eur. J.* **1997**, *3*, 679–683.

[12]   Huppertz, H.; Schnick W. $Ba_2Nd_7Si_{11}N_{23}$ – A Nitridosilicate with a Zeolite-Analogous Si–N Structure. *Angew. Chem., Int. Ed. Engl.* **1997**, *36*, 2651–2652; $Ba_2Nd_7Si_{11}N_{23}$ – ein Nitridosilicat mit zeolithartiger Si-N-Gerüststruktur. *Angew. Chem.* **1997**, *109*, 2765–2767.

[13]   Huppertz, H.; Schnick, W. Synthese und Kristallstruktur von $BaEu(Ba_{0.5}Eu_{0.5})YbSi_6N_{11}$. *Z. Anorg. Allg. Chem.* **1998**, *624*, 371–374.

[14]   Lauterbach, R.; Irran, E.; Henry, P. F.; Weller, M. T.; Schnick, W. High-temperature synthesis, single-crystal X-ray and neutron powder diffraction, and materials properties of $Sr_3Ln_{10}Si_{18}Al_{12}O_{18}N_{36}$ (Ln = Ce, Pr, Nd) – novel sialons with an ordered distribution of Si, Al, O, and N. *J. Mater. Chem.* **2000**, *10*, 1357–1364.

[15]   Neudert, L.; Durach, D.; Fahrnbauer, F.; Vaughan, G. B. M.; Schnick, W.; Oeckler, O. Highly Symmetric AB$_2$ Framework Related to Tridymite in the Disordered Nitridosilicate $La_{24}Sr_{14-7x}[Si_{36}N_{72}](O_{1-x}F_x)_{14}$ (x = 0.489). *Inorg. Chem.* **2017**, *56*, 13070–13077.

[16]   Durach, D.; Neudert, L.; Schmidt, P. J.; Oeckler, O.; Schnick, W. $La_3BaSi_5N_9O_2$:Ce^{3+} – A Yellow Phosphor with an Unprecedented Tetrahedra Network Structure Investigated by Combination of Electron Microscopy and Synchrotron X-ray Diffraction. *Chem. Mater.* **2015**, *27*, 4832–4838.

[17]   Huppertz, H.; Schnick, W. $BaYbSi_4N_7$ – Unexpected Structural Possibilities in Nitridosilicates. *Angew. Chem., Int. Ed. Engl.* **1996**, *35*, 1983–1984; $BaYbSi_4N_7$ – überraschende strukturelle Möglichkeiten in Nitridosilicaten. *Angew. Chem.* **1996**, *108*, 2115–2116.

[18]   Huppertz, H.; Oeckler, O.; Lieb, A.; Glaum, R.; Johrendt, D.; Tegel, M.; Kaindl, R.; Schnick, W. $Ca_3Sm_3[Si_9N_{17}]$ and $Ca_3Yb_3[Si_9N_{17}]$ Nitridosilicates with Interpenetrating Nets that Consist of Star-Shaped $[N^{[4]}(SiN_3)_4]$ Units and $[Si_5N_{16}]$ Supertetrahedra. *Chem. - Eur. J.* **2012**, *18*, 10857–10864.

[19]   Lieb, A.; Schnick, W. $BaSm_5[Si_9Al_3N_{20}]O$ – a nitridoaluminosilicate oxide with a new structure type composed of "star-shaped" $[N^{[4]}((Si,Al)N_3)_4]$ units as secondary building units. *Solid State Sci.* **2006**, *8*, 185–191.

[20]   Maak, C.; Niklaus, R.; Friedrich, F.; Mähringer, A.; Schmidt, P. J.; Schnick, W. Efficient Yellow-Orange Phosphor $Lu_4Ba_2[Si_9ON_{16}]O$:Eu^{2+} and Orange-Red Emitting $Y_4Ba_2[Si_9ON_{16}]O$:Eu^{2+}: Two Oxonitridosilicate Oxides with Outstanding Structural Variety. *Chem. Mater.* **2017**, *29*, 8377–8384.

[21]   Lauterbach, R.; Schnick, W. High-temperature synthesis and single-crystal X-ray structure determination of $Sr_{10}Sm_6Si_{30}Al_6O_7N_{54}$ – a layered sialon with an ordered distribution of Si, Al, O, and N. *Solid State Sci.* **2000**, *2*, 463–472.

[22] Durach, D.; Fahrnbauer, F.; Oeckler, O.; Schnick, W. $La_6Ba_3[Si_{17}N_{29}O_2]Cl$ – An
Oxonitridosilicate Chloride with Exceptional Structural Motifs. *Inorg. Chem.* **2015**,
54, 8727–8732.

[23] Lange, H.; Wötting, G.; Winter, G. Silicon Nitride - From Powder Synthesis to
Ceramic Materials. *Angew. Chem., Int. Ed. Engl.* **1991***, 30,* 1579–1597;
Siliciumnitrid - vom Pulver zum keramischen Werkstoff. *Angew. Chem.* **1991**, *103*,
1606–1625.

[24] Sheldrick, G. M. *SADABS, v. 2: Multi-Scan Absorption Correction*; Bruker-AXS:
Billerica, MA, 2012.

[25] Sheldrick, G. M. *SHELXS-97: A Program for Crystal Structure Solution*; University of
Göttingen: Göttingen, Germany, 1997.

[26] Sheldrick, G. M. *SHELXL-97: A Program for Crystal Structure Refinement*;
University of Göttingen: Göttingen, Germany, 1997.

[27] Sheldrick, G. M. A short history of SHELX. *Acta Crystallogr., Sect A: Found.
Crystallogr.* **2008**, *64*, 112–122.

[28] Rietveld, H. M. A profile refinement method for nuclear and magnetic structures. *J.
Appl. Crystallogr.* **1969**, *2*, 65–71.

[29] Coelho, A. A. *TOPAS, v. 4.1: A program for Rietveld refinement*, Coelho Software
2007.

[30] Bergmann, J.; Kleeberg, R.; Haase, A.; Breidenstein, B. Advanced fundamental
parameter model for improved profile analysis. *Mater. Sci. Forum* **2000**, *347–349*,
303–308.

[31] Cheary, R. W.; Coelho, A. A.; Cline, J. P. Fundamental Parameters Line Profile
Fitting in Laboratory Diffractometers. *J. Res. Natl. Inst. Stand. Technol.* **2004**, *109*,
1–25.

[32] Grochala, W.; Edwards, P. Thermal Decomposition of the Non- Interstitial Hydrides
for the Storage and Production of Hydrogen. *Chem. Rev.* **2004**, *104*, 1283–1316.

[33] Morgan, P. E. D. Pauling's second crystal rule for nitrogen-substituted crystal
structures. *J. Mater. Sci.* **1986**, *21*, 4305–4309.

[34] MacKenzie, K. J. D.; Gainsford, G. J.; Ryan, M. J. Rietveld refinement of the crystal
structures of the yttrium silicon oxynitrides $Y_2Si_3N_4O_3$ (N-melilite) and $Y_4Si_2O_7N_2$
(J-phase). *J. Eur. Ceram. Soc.* **1996**, *16*, 553–560.

[35] Hick, S. M.; Miller, M. I.; Kaner, R. B.; Blair, R. G. Synthesis and Crystal Structure of
Cubic $Ca_{16}Si_{17}N_{34}$. *Inorg. Chem.* **2012**, *51*, 12626–12629.

[36] Schlieper, T.; Milius, W.; Schnick, W. Nitrido-silicate. II: Hochtemperatur-Synthesen und Kristallstrukturen von $Sr_2Si_5N_8$ und $Ba_2Si_5N_8$. *Z. Anorg. Allg. Chem.* **1995**, *621*, 1380–1384.

[37] Huppertz, H.; Schnick, W. Edge-sharing SiN_4 Tetrahedra in the Highly Condensed Nitridosilicate $BaSi_7N_{10}$. *Chem. - Eur. J.* **1997**, *3*, 249–252.

[38] Liddell, K.; Thompson, D. P. The crystal structure of $Y_3Si_5N_9O$ and revision of the compositions of some high nitrogen-containing M–Si–O–N (M = Y, La) phases. *J. Mater. Chem.* **2001**, *11*, 507–512.

[39] Fleet, M. E.; Liu, X. Rare earth disilicates $R_2Si_2O_7$ (R = Gd, Tb, Dy, Ho): type B. *Z. Kristallogr. - Cryst. Mater.* **2003**, *218*, 795–801.

[40] Momma, K.; Izumi F. *VESTA 3* for three-dimensional visualization of crystal, volumetric and morphology data. *J. Appl. Crystallogr.* **2011**, *44*, 1272–1276.

[41] Petrícek, V.; Dušek, M.; Palatinus, L. Crystallographic Computing System JANA2006: General features. *Z. Kristallogr. - Cryst. Mater.* **2014**, *229*, 345–352.

[42] López, R.; Gómez, R. Band-gap energy estimation from diffuse reflectance measurements on sol-gel and commercial TiO_2: a comparative study. *J. Sol-Gel Sci. Technol.* **2012**, *61*, 1–7.

[43] Tauc, J.; Grigorovici, R.; Vancu, A. Optical Properties and Electronic Structure of Amorphous Germanium. *Phys. Status Solidi B* **1966**, *15*, 627–637.

[44] Meijerink, A.; Blasse, G. Luminescence properties of Eu^{2+}-activated alkaline earth haloborates. *J. Lumin.* **1989**, *43*, 283–289.

[45] Li, X.; Budai, J. D.; Liu, F.; Howe, J. Y.; Zhang, J.; Wang, X.-J.; Gu, Z.; Sun, C.; Meltzer, R. S.; Pan, Z. New yellow $Ba_{0.93}Eu_{0.07}Al_2O_4$ phosphor for warm-white light-emitting diodes through single-emitting-center conversion. *Light: Sci. Appl.* **2013**, *2*, e50.

[46] Shannon, R. D. Revised effective ionic radii and systematic studies of interatomic distances in halides and chalcogenides. *Acta Crystallogr., Sect. A: Cryst. Phys. Diffr., Theor. Gen. Crystallogr.* **1976**, *32*, 751–767.

7 $Y_{23}Sr_{17}[Si_{38}O_{18}N_{67}]O_9$ – An Oxonitridosilicate Oxide with a Unique Layered Structure
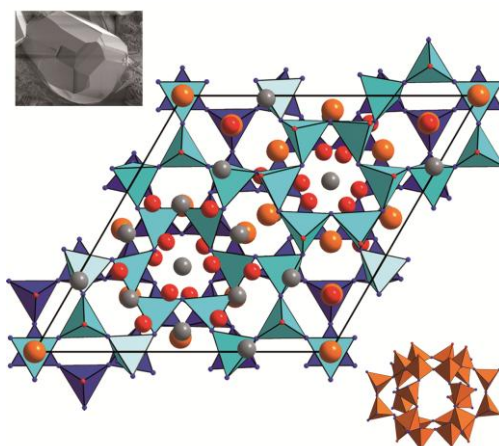
Abstract. The oxonitridosilicate oxide $Y_{23}Sr_{17}[Si_{38}O_{18}N_{67}]O_9$ was synthesized in a radiofrequency furnace at 1450 °C starting from YF_3, Y_2O_3, SrH_2 and silicon diimide. The driving force of the metathesis reaction is probably the simultaneous formation of SrF_2 and H_2. The crystal structure was solved and refined from single-crystal X-ray diffraction data in space group $P6_3/m$ (no. 176) with $a = 16.5764(4)$, $c = 18.6177(5)$ Å, and $Z = 2$ ($R_1 = 0.0196$, $wR_2 = 0.0377$). The results are supported by Rietveld refinement on X-ray powder data, X-ray spectroscopy, and IR spectroscopy. The crystal structure contains $[Si_{38}O_{18}N_{67}]^{85-}$ layers built up of vertex-sharing SiN_4 and $SiON_3$ tetrahedra. Lattice energy (MAPLE) and charge distribution (CHARDI) calculations indicate anion and cation ordering, with the exception of one mixed occupied Y/Sr site. UV/Vis spectroscopy and DFT calculations yield an optical optical bandgap of 3.8 eV and an electronic bandgap of 3.6 eV, respectively.

7.1   Introduction

(Oxo)nitridosilicates have been of great interest over the last two decades as they unite an intriguing structural chemistry and high potential for applications. Lithium ion conductors such as Li$_8$SiN$_4$ or Li$_{14}$$Ln$$_5$[Si$_{11}N_{19}O_5$]O$_2F_2$ (Ln = Ce, Nd), for example, may be applied in lithium batteries.[1,2] Compounds such as (Ba,Sr)$_2$Si$_5$N$_8$ or (Sr,Ca)SiAlN$_3$ are suitable host materials for activator ions such as Eu^{2+} and find broad application in phosphor-converted light-emitting diodes (pcLEDs).[3,4] Recently, some (oxo)nitridosilicates have been synthesized in metathesis reactions starting from rare earth metal fluorides (REF$_3$, RE = La–Lu, Y), alkaline earth metal hydrides (AEH$_2$, AE = Mg–Ba) and reactive precursors such as Si(NH)$_2$ or Si$_2$(NH)$_3$·6NH$_4$Cl.[5] Presumably, the driving force of these reactions is the formation of stable binary compounds AEF$_2$ as well as H$_2$, leading to the desired (oxo)nitridosilicates. If an excess of AEH$_2$ is provided during synthesis, RE/AE/Si/O/N compounds with fascinating crystal structures and luminescence properties, such as La$_3$BaSi$_5$N$_9$O$_2$:Ce^{3+}, Lu$_4$Ba$_2$[Si$_9$ON$_{16}$]O:Eu^{2+} or La$_{3-x}$Ca$_{1.5x}$Si$_6$N$_{11}$:Eu^{2+} ($x \approx 0.77$) are obtained.[6–8]

Like most (oxo)nitridosilicates, all above mentioned materials exhibit three-dimensional anionic networks built up of Si(O/N)$_4$ tetrahedra. In contrast, layered materials are rather rare in this compound class. The formation of network structures is favored compared to layered structures due to the high connectivity of nitrogen in (oxo)nitridosilicates. Whereas oxygen usually connects only two tetrahedral centers or acts as terminal atom, nitrogen can connect up to four tetrahedral centers and even enables edge-sharing of tetrahedra.[9,10] Nitridosilicates with layered structures are represented by Li$_2$Sr$_4$[Si$_2$N$_5$]N and AESiN$_2$ (AE = Sr, Ba),[11,12] layered oxonitridosilicates by e.g. Ce$_4$[Si$_4$O$_4$N$_6$]O and Nd$_{10}$[Si$_{10}$O$_9$N$_{17}$]Br.[13,14] Further layered compounds include MSi$_2$O$_2$N$_2$ (AE = Ca–Ba), $M$$_3Si_6O_9N_4$ (M = Ba, Eu), Ba$_3$Si$_6$O$_{12}$N$_2$, BaSi$_4$O$_6$N$_2$, and Y$_2$Si$_3$O$_3$N$_4$.[15–21] In the system RE/AE/Si/O/N, which was investigated in this contribution, Sr$_{10}$Sm$_6$Si$_{30}$Al$_6$O$_7$N$_{54}$ and $RE$$_{26}Ba_6$[Si$_{22}O_{19}N_{36}$] ($RE$ = Y, Tb) are the only two compounds with layered structures so far.[22,23]

Herein we employed a synthesis route starting from REF$_3$ and AEH$_2$ and obtained the oxonitridosilicate oxide Y$_{23}$Sr$_{17}$[Si$_{38}$O$_{18}$N$_{67}$]O$_9$, which exhibits an unprecedented crystal structure with intriguing [Si$_{38}$O$_{18}$N$_{67}$]$^{85-}$ layers.

7.2   Experimental Section

7.2.1   Synthesis

The starting materials were handled under exclusion of air and moisture in an argon-filled glovebox (Unilab, MBraun, Garching; $O_2 < 1$ ppm; $H_2O < 1$ ppm) or in argon-filled glass ware. YF_3 (0.38 mmol, 55.0 mg; Chempur, 99.999 %), Y_2O_3 (0.38 mmol, 85.1 mg; Sigma-Aldrich, 99.999 %), SrH_2 (1.51 mmol, 135.1 mg; Chemco, 99.7%), and $Si(NH)_2$ (1.13 mmol, 65.7 mg)[24] were mixed in an agate mortar and filled into a tungsten crucible. The crucible was placed into the water-cooled silica glass reactor of a radiofrequency furnace (type IG 10/600; Hüttinger Elektronik Freiburg) and heated to 1450 °C for 3 h in a purified N_2 atmosphere, maintained at that temperature for 15 h, and quenched to room temperature by switching off the furnace. The synthesis yields heterogeneous products with colorless single crystals of $Y_{23}Sr_{17}[Si_{38}O_{18}N_{67}]O_9$. Some crystals exhibit reddish to dark-red body color, possibly due to defects. Homogeneous, colorless samples were obtained by washing the products in hot water and subsequently annealing in air at 450 °C for 100 h.

7.2.2   Single-Crystal X-ray Diffraction

The single-crystal X-ray diffraction data of $Y_{23}Sr_{17}[Si_{38}O_{18}N_{67}]O_9$ were collected with a Bruker D8 Venture diffractometer with rotating anode (Mo Kα radiation, $\lambda = 0.71073$ Å). Semiempirical absorption correction was executed using SADABS.[25] The crystal structure was solved by direct methods and refined by least-squares methods with SHELX-2014, respectively.[26] Further details of the crystal structure investigations may be obtained from the Fachinformationszentrum Karlsruhe, 76344 Eggenstein-Leopoldshafen, Germany (Fax: +49-7247-808-666; E-Mail:crysdata@fiz-karlsruhe.de) on quoting the depository number CSD-434652.

7.2.3   Electron Microscopy and X-ray Spectroscopy

The chemical composition and the morphology were investigated with a Helios NanoLab G3 scanning electron microscope (SEM). The samples were carbon-coated (BAL-TEC MED 020, Bal Tec AG) in order to prevent electrostatic charging. Energy dispersive X-ray (EDX) measurements were performed with an acceleration voltage of 20 kV using an X-Max 80 SDD detector (Oxford Instruments).

7.2.4   Infrared Spectroscopy

The Fourier transformed infrared (FT-IR) spectrum was measured on a bulk sample of $Y_{23}Sr_{17}[Si_{38}O_{18}N_{67}]O_9$ with a Jasco FT/IR-4100 spectrometer using the ATR method.

7.2.5   Powder X-ray Diffraction

Powder X-ray diffraction data of samples in glass capillaries (0.1 mm diameter, Hilgenberg GmbH) were collected with a STOE STADI P diffractometer [Cu Kα_1 radiation, $\lambda = 1.540596$ Å, Ge(111) monochromator, Mythen1K detector] in modified Debye-Scherrer setup. Rietveld refinement was carried out with the TOPAS-Academic V4.1 software.[27,28]

7.2.6   UV/Vis Spectroscopy

Diffuse reflectance UV/Vis spectroscopy was performed with a Jasco V-650 UV/Vis spectrophotometer in the range of 240 to 800 nm with 1 nm step size. The device was equipped with a deuterium and a halogen lamp (Czerny-Turner monochromator with 1200 lines/mm concave grating, photomultiplier tube detector).

7.2.7   DFT Calculations

A DFT calculation with structural relaxation for $Y_{23}Sr_{17}[Si_{38}O_{18}N_{67}]O_9$ was carried out with the Vienna ab initio simulation package (VASP)[29–31] with regard to convergence criteria of 10^{-7} eV per atom for the lattice parameters and 4×10^{-3} eV·Å^{-1} for all individual residual atomic forces (2×10^{-2} eV·Å^{-1} total). In order to treat the exchange correlation the generalized gradient approximation (GGA) of *Perdew, Burke*, and *Ernzerhof* (PBE)[32,33] was used with the projector-augmented-wave (PAW) method.[34,35] A further correction for an accurate bandgap estimate was applied by utilization of the modified Becke-Johnson formalism.[36,37] A plane-wave cut-off of 535 eV was chosen for all calculations. The Brillouin zone was sampled on a Γ-centered *k*-mesh ($3 \times 3 \times 3$) produced from the method of *Monkhorst* and *Pack*.[38]

7.3   Results and Discussion

7.3.1   Synthesis and Sample Characterization

Y$_{23}$Sr$_{17}$[Si$_{38}$O$_{18}$N$_{67}$]O$_9$ was synthesized starting from YF$_3$, SrH$_2$, Y$_2$O$_3$, and Si(NH)$_2$. The driving force of the reaction is probably the formation of hydrogen from hydride ions and protons as well as SrF$_2$ according to Equation 1.

$$5\ YF_3 + 9\ Y_2O_3 + 38\ Si(NH)_2 + 24.5\ SrH_2 \rightarrow Y_{23}Sr_{17}[Si_{38}O_{18}N_{67}]O_9 + 7.5\ SrF_2 + 9\ NH_3 + 49\ H_2 \qquad (1)$$
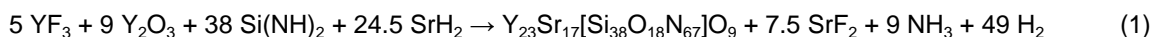
Y$_{23}$Sr$_{17}$[Si$_{38}$O$_{18}$N$_{67}$]O$_9$ was obtained by reacting non-stoichiometric amounts of the starting materials. Detailed information on the synthesis is given in the Experimental Section. The chemical composition was determined by EDX spectroscopy. Results from 15 point measurements on 15 different crystals are summarized in Table 1 (see also Table S1 and Figure S1, Supporting Information). The results are in good agreement with the sum formula. Infrared spectroscopy confirms the absence of O–H and N–H groups (Figure S2). The bulk phase composition of washed and annealed samples was determined by Rietveld refinement of powder X-ray diffraction data (Table S2). The refinement shows that Y$_{23}$Sr$_{17}$[Si$_{38}$O$_{18}$N$_{67}$]O$_9$ was obtained as the main phase (Figure 1). In addition, the sample contains small amounts of SrF$_2$, YN, and Y$_2$O$_3$.

Table 1. EDX results (average of 15 point measurements). Standard deviations in parentheses.

	Theoretical atom%	Experimental atom%
Y	13.4	14(2)
Sr	9.9	9(1)
Si	22.1	23(3)
O	15.7	18(2)
N	38.9	36(4)

7.3.2   Crystal Structure Determination

The crystal structure of Y$_{23}$Sr$_{17}$[Si$_{38}$O$_{18}$N$_{67}$]O$_9$ was solved and refined from single-crystal X-ray diffraction data in space group $P6_3/m$ (no. 176). Crystallographic data are summarized in Table 2. Merohedral twinning (twin law: 010 100 001) was taken into account, yielding a twin ratio of 1:1. The crystal structure exhibits pseudosymmetry towards $P6_3/mmc$ (no. 194) but has no additional symmetry. Due to similar atomic form

factors of O/N and Y/Sr atoms, these atoms usually cannot be distinguished by conventional X-ray diffraction. Lattice energy calculations using the MAPLE[39–42] concept and charge distribution (CHARDI)[43] calculations (with VESTA)[44] were performed to obtain information on the distribution of anions and cations. Results of these calculations are summarized in Table 3 and Table 4. They indicate anion and cation ordering with the exception of one mixed-occupied Y/Sr site. Accordingly, nitrogen atoms occupy twofold bridging sites (N2), oxygen atoms occupy terminal (O1) and discrete O sites. These findings are in agreement with Pauling's rules for ionic crystals.[45] The site Y/Sr6 was refined with mixed occupation assuming charge neutrality, which also matches the smaller CHARDI value for this site in contrast to sites solely occupied by Y atoms. The obtained sum formula is in good agreement with the EDX analysis (Table 1). Fractional atomic coordinates, Wyckoff positions, and isotropic displacement parameters are listed in Table S3. Anisotropic displacement parameters are shown in Table S4.
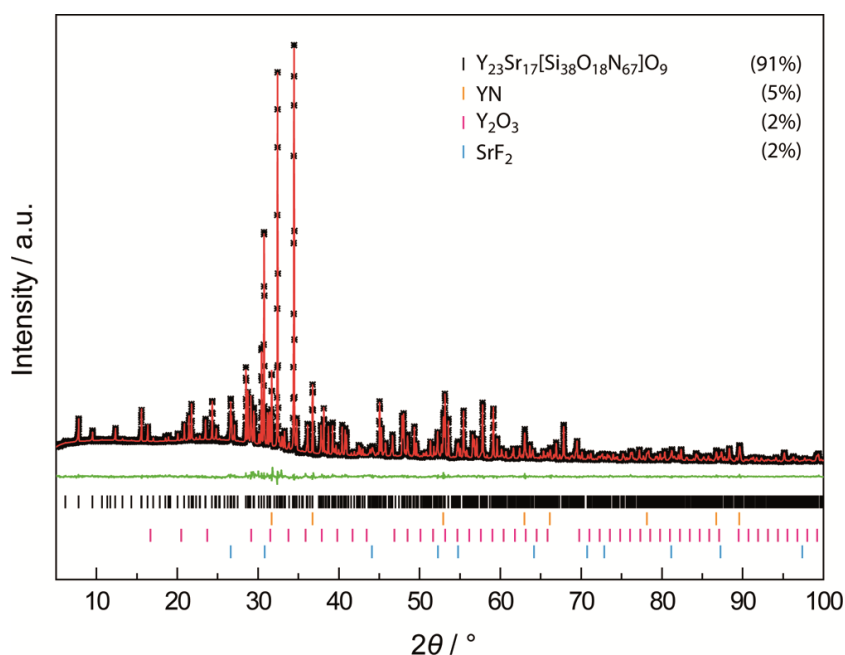
Figure 1. Rietveld refinement based on the XRD pattern of a washed and annealed $Y_{23}Sr_{17}[Si_{38}O_{18}N_{67}]O_9$ sample with measured histogram (black stars), Rietveld fit (red line), difference plot (green line), and positions of reflections (bars): $Y_{23}Sr_{17}[Si_{38}O_{18}N_{67}]O_9$ (black), YN (orange), Y_2O_3 (magenta), SrF_2 (cyan); phase proportions in wt %.

Table 2. Crystallographic data of the single-crystal structure determination of $Y_{23}Sr_{17}[Si_{38}O_{18}N_{67}]O_9$.

formula	$Y_{23}Sr_{17}[Si_{38}O_{18}N_{67}]O_9$
molar mass / g·mol^{-1}	5972.56
crystal system	hexagonal
space group	$P6_3/m$ (no. 176)
lattice parameters / Å	a = 16.5764(4), c = 18.6177(5)
cell volume / Å^3	4430.3(2)
formula units per unit cell	2
density / g·cm^{-3}	4.48
μ / mm^{-1}	25.6
temperature / K	297(2)
diffractometer	Bruker D8 Venture
absorption correction	multiscan[25]
radiation / Å	Mo Kα (λ = 0.71073)
$F(000)$	5520
θ range / °	2.608 ≤ θ ≤ 27.497
total no. of reflections	78857
independent refl. [$I ≥ 2\sigma(I)$ / all]	3208 / 3502
R_σ, R_{int}	0.0184, 0.0588
refined parameters	277
GoF	1.247
R indices [$I ≥ 2\sigma(I)$]	R_1 = 0.0196, wR_2 = 0.0377
R indices (all data)	R_1 = 0.0253, wR_2 = 0.0394
$\Delta\rho_{max}, \Delta\rho_{min}$ / e·Å^{-3}	0.98, −0.79

Table 3. Results of MAPLE calculations / kJ·mol^{-1} for $Y_{23}Sr_{17}[Si_{38}O_{18}N_{67}]O_9$. Partial MAPLE values, total MAPLE sum, and difference to theoretical MAPLE value corresponding to the reference equation in the right column.[a]

Y	4174–4481	5 YN
Sr	1743–2031	+ 9 Y2O3
Y/Sr6	3774	+ 7 α-Si3N4
Si	9817–10253	+ 17 SrSiN2
N[2]	5115–5613	
O[1]	2465–2484	
O[0]	1933–2170	
	$\sum$ = 936221	$\sum$ = 932325
		Δ = 0.41 %

a) Typical partial MAPLE Values /kJ·mol^{-1}: Y^{3+}: 3500–5100; Sr^{2+}:1500–2100; Si^{4+}: 9000–10200; N$^{[2]\,3-}$: 4600–6000; O$^{[1]\,2-}$: 2000–2800; O$^{[0]\,2-}$: 1800–2200.[46]

Table 4. Results of CHARDI calculations for $Y_{23}Sr_{17}[Si_{38}O_{18}N_{67}]O_9$.

Y1	2.86	Sr5	2.09
Y2	2.73	Si1	3.98
Y3	2.86	Si2	4.24
Y4	2.74	Si3	4.09
Y5	2.80	Si4	4.26
Y/Sr6	2.54	Si5	4.21
Sr1	2.06	Si6	4.25
Sr2	2.01	Si7	4.31
Sr3	2.02	Si8	4.19
Sr4	1.86		

7.3.3   Structure Description

The crystal structure (Figure 2) of $Y_{23}Sr_{17}[Si_{38}O_{18}N_{67}]O_9$ exhibits unique silicate layers of vertex-sharing Q4-type SiN_4 and Q3-type $SiON_3$ tetrahedra. The degree of condensation within the layers is $\kappa = 0.45$. The anionic substructure (Figure 3d/e) can be built up from three structural motifs, which are connected through common vertices. The first motif is a cage (Figure 3a) consisting of two *sechser* rings ($SiON_3$ tetrahedra) and six *achter* rings (four $SiON_3$ and four SiN_4 tetrahedra).[47] The cages are interconnected via further *sechser* rings (Figure 3b) and an entity consisting of eight tetrahedra (Figure 3c). The unit cell contains two layers, which are rotated 180° according to the 6_3 screw axis. Atom N10 in the third structural motif (Figure 3c) exhibits anion disorder around the special position 0,0,3/4 (Wyckoff position 2*b*), probably in order to avoid a linear Si–N–Si arrangement. The site was refined as split position with a site occupancy factor of 1/3. The corresponding difference Fourier map of data reduced in *P*1 is illustrated in Figure 4. Similar anion disorder was reported e.g. for dodecasil 3C.[48] Additional refinements were conducted in the subgroup $P2_1/m$ (taking into account further threefold twinning) to exclude ordering which would be possible if three independent N atom sites are refined. However, the difference Fourier map for the refinement in $P2_1/m$ (Figure S3) does not indicate ordering of the respective N site. Thus, $P6_3/m$ was chosen to describe the crystal structure of $Y_{23}Sr_{17}[Si_{38}O_{18}N_{67}]O_9$.
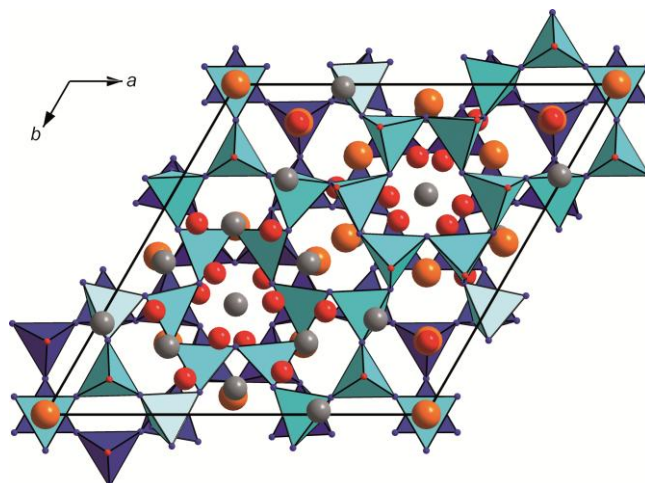
Figure 2. Crystal structure of Y$_{23}$Sr$_{17}$[Si$_{38}$O$_{18}$N$_{67}$]O$_9$ along [001] with upper [Si$_{38}$O$_{18}$N$_{67}$]$^{85-}$ layer turquoise, lower layer blue. Y and the Y/Sr site gray, Sr atoms orange, O atoms red, and N atoms blue; unit cell outlined in black.
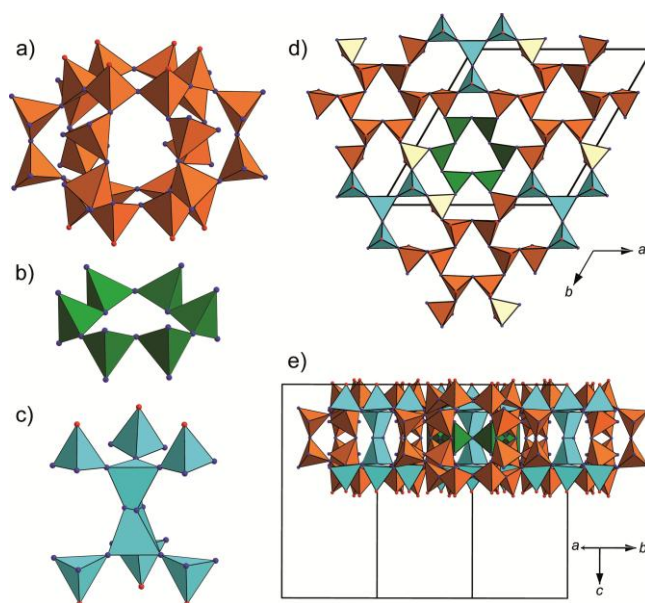
Figure 3. (a) Cage. (b) *Sechser* ring. (c) Entity of eight tetrahedra. (d) [Si$_{38}$O$_{18}$N$_{67}$]$^{85-}$ layer along [001]. (e) [Si$_{38}$O$_{18}$N$_{67}$]$^{85-}$ layer along [210]; unit cells outlined in black.

The crystal structure exhibits eleven crystallographically independent sites for Y and Sr atoms. Five sites are occupied by Y atoms and five sites solely by Sr atoms. The site Y/Sr6, which has the smallest CHARDI and partial MAPLE value compared to the other Y sites requires mixed occupancy (Y: 0.8333 %, Sr: 0.1667 %) in order to obtain charge neutrality. The distribution of Y^{3+} and Sr^{2+} atoms also corresponds to the significantly

differing ionic radii (Y^{3+}: 96 pm; Sr^{2+}: 121 pm, both for CN = 7).[39] Surroundings of Y and Sr atoms are shown in Figure S4. The Y sites are coordinated by six or seven ligand atoms, respectively. The coordination numbers (CN) of the Sr atoms range from 7–12. The mixed occupied site Y/Sr has CN = 8 (Figure S4). The Y–O distances range from 2.216(3) to 2.583(4) Å, Y–N distances from 2.337(4) to 2.739(4) Å. The Sr–ligand distances are significantly larger with Sr–O ranging from 2.405(4) to 3.325(4) and Sr–N from 2.559(5) to 3.186(4) Å. Bond lengths of the mixed-occupied site are between 2.302(3)–2.463(3) Å (Y/Sr–O) and 2.438(4)–2.720(4) Å (Y/Sr–N). The Y, Y/Sr, and Sr−ligand distances are listed in Table S5. The Si–O bond lengths lie between 1.680(3) and 1.709(3) Å, the Si–N distances between 1.663(4) and 1.759(5) Å. All interatomic distances correspond to typical values reported for other yttrium- and strontium-containing (oxo)nitridosilicates, such as $Y_2Si_3O_3N_4$, $SrYSi_4N_7$, $Y_3Si_5N_9O$, or $Sr_2Si_5N_8$.[21,49–51]
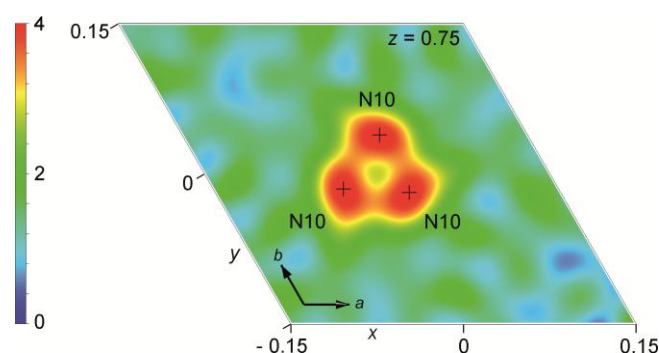
Figure 4. Residual electron density (F_{obs} − F_{calc}) around special position 0,0,3/4 plotted with VESTA (scale bar in e⁻ per a_0^3 with a_0 = Bohr radius).[44]

7.3.4   Band Gap Determination

The optical bandgap of $Y_{23}Sr_{17}[Si_{38}O_{18}N_{67}]O_9$ was determined using UV/Vis spectroscopy. The reflectance spectrum exhibits a broad absorption band around 280 nm owing to the absorption of the host structure (Figure 5a). The absorption band in the UV range corresponds to the colorless sample obtained after annealing. The optical bandgap was determined by converting the reflectance (R) spectrum to pseudoabsorption using the Kubelka-Munk function $F(R) = (1 − R)^2/2R$.[52] Subsequently, a tangent was drawn at the inflection point of a Tauc plot (Figure 5b),[53] indicating an optical bandgap of approximately 3.8 eV. A Kubelka-Munk exponent $n = 1/2$ was chosen, assuming a direct allowed transition. DFT calculations using the modified Becke-Johnson potential support the experimental data as optical and calculated electrical (3.6 eV) bandgaps are expected

to be similar in a highly ionic insulator. Figure 6 shows the total and atom resolved density of states (DOS).
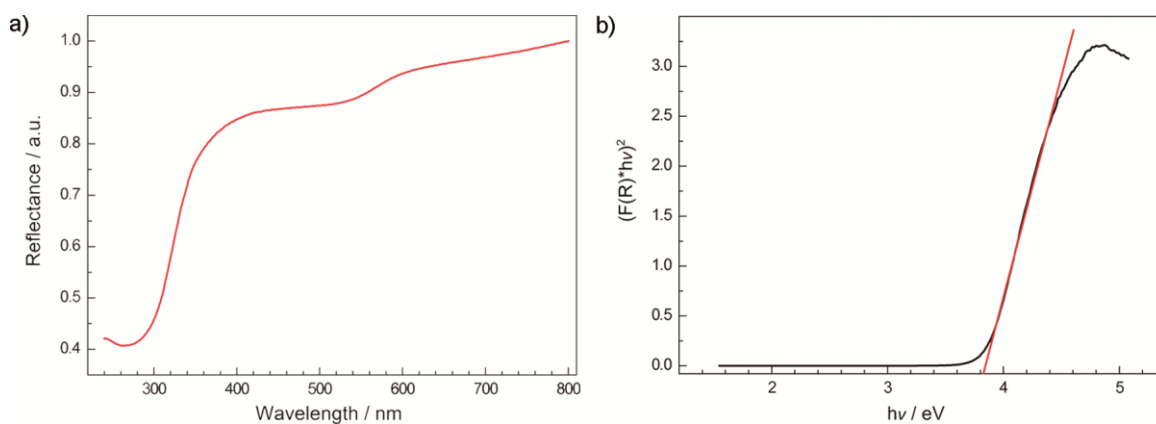
Figure 5. (a) Diffuse reflectance UV/Vis spectrum of Y$_{23}$Sr$_{17}$[Si$_{38}$O$_{18}$N$_{67}$]O$_9$ after washing and annealing. (b) Tauc plot (black, $n = 1/2$) with tangent (red) at the inflection point.
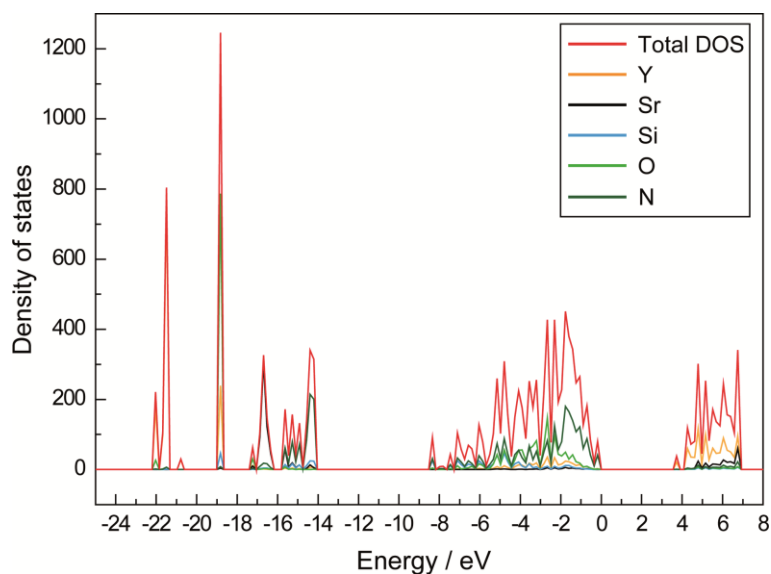
Figure 6. Total and atom resolved DOS of Y$_{23}$Sr$_{17}$[Si$_{38}$O$_{18}$N$_{67}$]O$_9$ calculated with DFT using the modified Becke-Johnson potential.

7.4   Conclusion

The oxonitridosilicate oxide Y$_{23}$Sr$_{17}$[Si$_{38}$O$_{18}$N$_{67}$]O$_9$ crystallizes in a new structure type with [Si$_{38}$O$_{18}$N$_{67}$]$^{85-}$ layers. The optical bandgap of 3.8 eV corresponds to that obtained by DFT calculations. The compound is stable toward air and moisture even at temperatures of up to 450 °C. Y$_{23}$Sr$_{17}$[Si$_{38}$O$_{18}$N$_{67}$]O$_9$ was synthesized in a high-temperature reaction starting

from reactive starting materials such as YF_3, SrH_2, and $Si(NH)_2$. The driving force for its formation is probably the formation of the binary compounds SrF_2 and H_2. The described synthesis route has brought up a couple of RE/AE/Si/O/N (RE = La–Lu, Y; AE = Ca–Ba) compounds with new structure types in recent years. Therefore, this approach seems promising for further exploration. Attempts to synthesize a possibly isotypic compound with smaller alkaline earth cations such as Ca or Mg instead of Sr have not been successful so far. In this context, ion exchange experiments as demonstrated for $Mg_2Si_5N_8$ and β-$Ca_2Si_5N_8$[54] may be promising due to the layered structure of $Y_{23}Sr_{17}[Si_{38}O_{18}N_{67}]O_9$ and channels within the layers.

7.5   References

[1]   Yamane, H.; Kikkawa, S.; Koizumi, M. Preparation of lithium silicon nitrides and their lithium ion conductivity. *Solid State Ionics* **1987**, *25*, 183–191.

[2]   Lupart, S.; Gregori, G.; Maier, J.; Schnick, W. $Li_{14}Ln_5[Si_{11}N_{19}O_5]O_2F_2$ with Ln = Ce, Nd – Representatives of a Family of Potential Lithium Ion Conductors. *J. Am. Chem. Soc.* **2012**, *134*, 10132–10137.

[3]   Höppe, H. A.; Lutz, H.; Morys, P.; Schnick, W.; Seilmeier, A. Luminescence in Eu^{2+}-doped $Ba_2Si_5N_8$: fluorescence, thermoluminescence, and upconversion. *J. Phys. Chem. Solids* **2000**, *61*, 2001–2006.

[4]   Watanabe, H.; Kijima, N. Crystal structure and luminescence properties of $Sr_xCa_{1-x}AlSiN_3$:Eu^{2+} mixed nitride phosphors. *J. Alloys Compd.* **2009**, *475*, 434–439.

[5]   Durach, D.; Fahrnbauer, F.; Oeckler, O.; Schnick, W. $La_6Ba_3[Si_{17}N_{29}O_2]Cl$ – An Oxonitridosilicate Chloride with Exceptional Structural Motifs. *Inorg. Chem.* **2015**, *54*, 8727–8732.

[6]   Durach, D.; Neudert, L.; Schmidt, P. J.; Oeckler, O.; Schnick, W. $La_3BaSi_5N_9O_2$:Ce^{3+} – A Yellow Phosphor with an Unprecedented Tetrahedra Network Structure Investigated by Combination of Electron Microscopy and Synchrotron X-ray Diffraction. *Chem. Mater.* **2015**, *27*, 4832–4838.

[7]   Maak, C.; Niklaus, R.; Friedrich, F.; Mähringer, A.; Schmidt, P. J.; Schnick, W. Efficient Yellow-Orange Phosphor $Lu_4Ba_2[Si_9ON_{16}]O$:Eu^{2+} and Orange-Red Emitting $Y_4Ba_2[Si_9ON_{16}]O$:Eu^{2+}: Two Oxonitridosilicate Oxides with Outstanding Structural Variety. *Chem. Mater.* **2017**, *29*, 8377–8384.

[8]   Maak, C.; Durach, D.; Martiny, C.; Schmidt, P. J.; Schnick, W. Narrow-Band Yellow-Orange Emitting $La_{3-x}Ca_{1.5x}Si_6N_{11}$:$Eu^{2+}$ ($x ≈ 0.77$): A Promising Phosphor for Next-Generation Amber pcLEDs. *Chem. Mater.* **2018**, *30*, 3552–3558.

[9]   Schnick, W.; Huppertz, H. Nitridosilicates – A Significant Extension of Silicate Chemistry. *Chem. - Eur. J.* **1997**, *3*, 679–683.

[10] Huppertz, H.; Schnick, W. BaYbSi$_4$N$_7$ – Unexpected Structural Possibilities in Nitridosilicates. *Angew. Chem., Int. Ed. Engl.* **1996**, *35*, 1983–1984; BaYbSi$_4$N$_7$ – überraschende strukturelle Möglichkeiten in Nitridosilicaten. *Angew. Chem.* **1996**, *108*, 2115–2116.

[11] Lupart, S.; Pagano, S.; Oeckler, O.; Schnick, W. Li$_2$Sr$_4$[Si$_2$N$_5$]N – A Layered Lithium Nitridosilicate Nitride. *Eur. J. Inorg. Chem.* **2011**, 2118–2123.

[12] Gál, Z. A.; Mallinson, P. M.; Orchard, H. J.; Clarke, S. J. Synthesis and Structure of Alkaline Earth Silicon Nitrides: BaSiN$_2$, SrSiN$_2$, and CaSiN$_2$. *Inorg. Chem.* **2004**, *43*, 3998–4006.

[13] Irran, E.; Köllisch, K.; Leoni, S.; Nesper, R.; Henry, P. F.; Weller, M. T.; Schnick, W. Ce$_4$[Si$_4$O$_4$N$_6$]O – A Hyperbolically Layered Oxonitridosilicate Oxide with an Ordered Distribution of Oxygen and Nitrogen. *Chem. - Eur. J.* **2000**, *6*, 2714–2720.

[14] Lieb, A.; Schnick, W. Ce$_{10}$[Si$_{10}$O$_9$N$_{17}$]Br, Nd$_{10}$[Si$_{10}$O$_9$N$_{17}$]Br and Nd$_{10}$[Si$_{10}$O$_9$N$_{17}$]Cl oxonitridosilicate halides with a new layered structure type. *J. Solid State Chem.* **2005**, *178*, 3323–3335.

[15] Höppe, H. A.; Stadler, F.; Oeckler, O.; Schnick, W. Ca[Si$_2$O$_2$N$_2$] – A Novel Layer Silicate. *Angew. Chem., Int. Ed.* **2004**, *43*, 5540–5542; Ca[Si$_2$O$_2$N$_2$] – ein neuartiges Schichtsilicat. *Angew. Chem.* **2004**, *116*, 5656–5659.

[16] Kechele, J. A.; Oeckler, O.; Stadler, F.; Schnick, W. Structure elucidation of BaSi$_2$O$_2$N$_2$ – A host lattice for rare-earth doped luminescent materials in phosphor-converted (pc)-LEDs. *Solid State Sci.* **2009**, *11*, 537–543.

[17] Oeckler, O.; Stadler, F.; Rosenthal, T.; Schnick, W. Real structure of SrSi$_2$O$_2$N$_2$. *Solid State Sci.* **2007**, *9*, 205–212.

[18] Stadler, F.; Schnick, W. Die neuen Schichtsilicate Ba$_3$Si$_6$O$_9$N$_4$ und Eu$_3$Si$_6$O$_9$N$_4$. *Z. Anorg. Allg. Chem.* **2006**, *632*, 949–954.

[19] Braun, C.; Seibald, M.; Börger, S. L.; Oeckler, O.; Boyko, T. D.; Moewes, A.; Miehe, G.; Tücks, A.; Schnick, W. Material Properties and Structural Characterization of M$_3$Si$_6$O$_{12}$N$_2$:Eu^{2+} (M = Ba, Sr) - A Comprehensive Study on a Promising Green Phosphor for pc-LEDs. *Chem. - Eur. J.* **2010**, *16*, 9646–9657.

[20] Braun, C.; Ehrenberg, H.; Schnick, W. BaSi$_4$O$_6$N$_2$ – A Hexacelsian-Type Layered Oxonitridosilicate. *Eur. J. Inorg. Chem.* **2012**, 3923–3928.

[21] Wills, R. R.; Stewart, R. W.; Cunningham, J. A.; Wimmer, J. M. The silicon lanthanide oxynitrides. *J. Mater. Sci.* **1976**, *11*, 749–759.

[22]   Lauterbach, R.; Schnick, W. High-temperature synthesis and single-crystal X-ray structure determination of Sr$_{10}$Sm$_6$Si$_{30}$Al$_6$O$_7$N$_{54}$ – a layered sialon with an ordered distribution of Si, Al, O, and N. *Solid State Sci.* **2000**, *2*, 463–472.

[23]   Maak, C.; Hoch, C.; Schmidt, P. J.; Schnick, W. Oxonitridosilicate Oxides *RE*$_{26}$Ba$_6$[Si$_{22}$O$_{19}$N$_{36}$]O$_{16}$:Eu^{2+} (*RE* = Y, Tb) with a Unique Layered Structure and Orange-Red Luminescence for *RE* = Y. *Inorg. Chem.* **2018**, *57*, 2242–2248.

[24]   Lange, H.; Wötting, G.; Winter, G. Silicon Nitride - From Powder Synthesis to Ceramic Materials. *Angew. Chem., Int. Ed. Engl.* **1991***, 30,* 1579–1597; Siliciumnitrid - vom Pulver zum keramischen Werkstoff. *Angew. Chem.* **1991**, *103*, 1606–1625.

[25]   Sheldrick, G. M. *SADABS, v. 2: Multi-Scan Absorption Correction*; Bruker-AXS: Billerica, MA, 2012.

[26]   Sheldrick, G. M. Crystal structure refinement with SHELXL. *Acta Crystallogr., Sect. C* **2015**, *71*, 3–8.

[27]   Rietveld, H. M. A profile refinement method for nuclear and magnetic structures. *J. Appl. Crystallogr.* **1969**, *2*, 65–71.

[28]   Coelho, A. A. *TOPAS, v. 4.1: A program for Rietveld refinement*; Coelho Software: Brisbane, Australia, 2007.

[29]   Kresse, G.; Hafner, J. *Ab initio* molecular dynamics for liquid metals. *Phys. Rev. B: Condens. Matter Mater. Phys.* **1993**, *47*, 558–561.

[30]   Kresse, G.; Hafner, J. *Ab initio* molecular-dynamics simulation of the liquid-metal–amorphous-semiconductor transition in germanium. *Phys. Rev. B: Condens. Matter Mater. Phys.* **1994**, *49*, 14251–14269.

[31]   Kresse, G.; Furthmüller, J. Efficiency of ab-initio total energy calculations for metals and semiconductors using a plane-wave basis set. *Comput. Mater. Sci.* **1996**, *6*, 15–50.

[32]   Perdew, J. P.; Burke, K.; Ernzerhof, M. Generalized Gradient Approximation Made Simple. *Phys. Rev. Lett.* **1996**, *77*, 3865–3868.

[33]   Perdew, J. P.; Burke, K.; Ernzerhof, M. Generalized Gradient Approximation Made Simple. *Phys. Rev. Lett.* **1997**, *78*, 1396–1396.

[34]   Blöchl, P. E. Projector augmented-wave method. *Phys. Rev. B: Condens. Matter Mater. Phys.* **1994**, *50*, 17953–17979.

[35]   Kresse, G.; Joubert, D. From ultrasoft pseudopotentials to the projector augmented-wave method. *Phys. Rev. B: Condens. Matter Mater. Phys.* **1999**, *59*, 1758−1775.

[36]   Becke, A. D.; Johnson, E. R. A simple effective potential for exchange. *J. Chem. Phys.* **2006**, *124*, 221101.

[37] Camargo-Martínez, J. A.; Baquero, R. Performance of the modified Becke-Johnson potential for semiconductors. *Phys. Rev. B: Condens. Matter Mater. Phys.* **2012**, *86*, 195106.

[38] Monkhorst, H. J.; Pack, J. D. Special points for Brillouin-zone integrations. *Phys. Rev. B* **1976**, *13*, 5188–5192.

[39] Shannon, R. D. Revised effective ionic radii and systematic studies of interatomic distances in halides and chalcogenides. *Acta Crystallogr., Sect. A: Cryst. Phys., Diffr., Theor. Gen. Crystallogr.* **1976**, *32*, 751–767.

[40] Hoppe, R. Madelung constants. *Angew. Chem., Int. Ed. Engl.* **1966**, *5*, 95–106; Über Madelungfaktoren. *Angew. Chem.* **1966**, *78*, 52–63.

[41] Hoppe, R. The Coordination Number – an "Inorganic Chameleon". *Angew. Chem., Int. Ed. Engl.* **1970**, *9*, 25–34; Die Koordinationszahl – ein „anorganisches Chamäleon". *Angew. Chem.* **1970**, *82*, 7–16.

[42] Hübenthal, R. *Maple, Program for the Calculation of MAPLE values, version 4*; University of Gießen: Gießen, Germany, 1993.

[43] Hoppe, R.; Voigt, S.; Glaum, H.; Kissel, J.; Müller, H. P.; Bernet, K. A new route to charge distributions in ionic solids. *J. Less-Common Met.* **1989**, *156*, 105–122.

[44] Momma, K.; Izumi F. *VESTA 3* for three-dimensional visualization of crystal, volumetric and morphology data. *J. Appl. Crystallogr.* **2011**, *44*, 1272–1276.

[45] Morgan, P. E. D. Pauling's second crystal rule for nitrogen-substituted crystal structures. *J. Mater. Sci.* **1986**, *21*, 4305–4309.

[46] Zeuner, M.; Pagano, S.; Schnick, W. Nitridosilicates and Oxonitridosilicates: From Ceramic Materials to Structural and Functional Diversity. *Angew. Chem., Int. Ed.* **2011**, *50*, 7754–7775; Nitridosilicate und Oxonitridosilicate: von keramischen Materialien zu struktureller und funktioneller Diversität. *Angew. Chem.* **2011**, *123*, 7898–7920.

[47] The term *sechser* (*achter*)ring was coined by *Liebau* and is derived from the German word "sechser" ("achter"); a *sechser* (*achter*) ring comprises six (eight) tetrahedra centers.

[48] Könnecke, M.; Miehe, G.; Fuess, H. Static disorder of dodecasil 3C. A single-crystal study with synchrotron radiation. *Z. Kristallogr.* **1992**, *201*, 147–155.

[49] Fang, C. M.; Li, Y. Q.; Hintzen, H. T.; de With, G. Crystal and electronic structure of the novel nitrides MYSi$_4$N$_7$(M = Sr, Ba) with peculiar NSi$_4$ coordination. *J. Mater. Chem.* **2003**, *13*, 1480–1483.

[50]   Liddell, K.; Thompson, D. P. The crystal structure of Y$_3$Si$_5$N$_9$O and revision of the compositions of some high nitrogen-containing M–Si–O–N (M = Y, La) phases. *J. Mater. Chem.* **2001**, *11*, 507–512.

[51]   Schlieper, T.; Milius, W.; Schnick, W. Nitrido-silicate. II: Hochtemperatur-Synthesen und Kristallstrukturen von Sr$_2$Si$_5$N$_8$ und Ba$_2$Si$_5$N$_8$. *Z. Anorg. Allg. Chem.* **1995**, *621*, 1380–1384.

[52]   López, R.; Gómez, R. Band-gap energy estimation from diffuse reflectance measurements on sol-gel and commercial TiO$_2$: a comparative study. *J. Sol-Gel Sci. Technol.* **2012**, *61*, 1–7.

[53]   Tauc, J.; Grigorovici, R.; Vancu, A. Optical Properties and Electronic Structure of Amorphous Germanium. *Phys. Status Solidi B* **1966**, *15*, 627–637.

[54]   Bielec, P.; Schnick, W. Increased Synthetic Control - Gaining Access to Predicted Mg$_2$Si$_5$N$_8$ and β-Ca$_2$Si$_5$N$_8$. *Angew. Chem., Int. Ed.* **2017**, *56*, 4810–4813; *Angew. Chem.* **2017**, *129*, 4888–4891.

8   Luminescent Oxoberyllates

8.1   Introduction

Beside the incorporation of different counter ions as demonstrated in the last chapters for RE^{3+} and AE^{2+} containing (oxo)nitridosilicates, the compositional and structural range can also be significantly increased by substitution of Si^{4+} on the tetrahedrally coordinated sites. In the context of luminescence, the most relevant atoms which can also occupy these sites are Al^{3+}, Mg^{2+}, and Li^{+}. In the last years, the partial or complete substitution of Si^{4+} by these atoms lead to luminescent materials with intriguing emission characteristics. Prominent examples are the nitridolithoalumosilicate $Ba[Li_2(Al_2Si_2)N_6]:Eu^{2+}$ with narrow-band green emission as well as the nitridomagnesosilicate $Sr[Mg_3SiN_4]:Eu^{2+}$ and the nitridolithoaluminate $Sr[LiAl_3N_4]:Eu^{2+}$ with narrow-band red emissions.[1–3] In addition to symmetric environments for the activator atoms, the emission properties of all these materials benefit from highly condensed, rigid structures. The degree of condensation in these materials of $\kappa = 1.0$ is significantly higher than the maximum value of $\kappa = 0.75$ which can be obtained in nitridosilicates. Another element that comes to mind in this context is beryllium. Be^{2+} atoms have an almost identical ionic radius compared to Si^{4+} (Be^{2+}: 27 pm, Si^{4+}: 26 pm, both values for 4-fold coordination)[4] and also occur in tetrahedral coordination, e.g. in the highly condensed binary phases BeO ($\kappa = 1$) and Be_3N_2 ($\kappa = 1.5$).[5,6] Furthermore, Be^{2+} also occurs in trigonal planar coordination, as e.g. in $AEBe_2N_2$ (AE = Ca–Ba), which enables an exceptionally large structural variety in beryllates.[7]

So far, only a few beryllate compounds have been synthesized, possibly because of the high toxicity of beryllium dusts. Most recently our group came up with a couple of luminescent beryllates which demonstrated the large potential of this substance class for solid-state lighting.[8] The most promising materials are the oxoberyllate β-$SrBeO_2:Eu^{2+}$ and the oxonitridoberyllate $Sr[Be_6ON_4]:Eu^{2+}$. β-$SrBeO_2:Eu^{2+}$ exhibits narrow-band emission in the yellow spectral range ($\lambda_{em} = 564$ nm, $fwhm = 55$ nm/1680 cm^{-1}). The oxonitridoberyllate $Sr[Be_6ON_4]:Eu^{2+}$ shows narrow-band cyan emission ($\lambda_{em} = 495$ nm; $fwhm = 35$ nm/1400 cm^{-1}) with an excellent thermal quenching behavior. Additionally, both materials exhibit further important properties for state-of-the-art phosphors such as large band gaps and high chemical stability.[9,10]

The following chapter describes the synthesis, crystal structure and luminescence properties of the oxoberyllates $AELi_2[Be_4O_6]:Eu^{2+}$ (AE = Sr, Ba). These materials can be

derived from the isotypic, narrow-band green emitting $Ba[Li_2(Al_2Si_2)N_6]:Eu^{2+}$ by isoelectronic substitution of $(Al_2Si_2N_6)^{4-}$ through $(Be_4O_6)^{4-}$. The resulting ultra-narrow band blue emissions of the reported phosphors fulfill all requirements for highly efficient RGB pcLEDs.

References

[1] Strobel, P.; Schmiechen, S.; Siegert, M.; Tücks, A.; Schmidt, P. J.; Schnick, W. Narrow-Band Green Emitting Nitridolithoalumosilicate $Ba[Li_2(Al_2Si_2)N_6]:Eu^{2+}$ with Framework Topology *whj* for LED/LCD-Backlighting Applications. *Chem. Mater.* **2015**, *27*, 6109–6115.

[2] Schmiechen, S.; Schneider, H.; Wagatha, P.; Hecht, C.; Schmidt, P. J.; Schnick, W. Toward New Phosphors for Application in Illumination-Grade White pc-LEDs: The Nitridomagnesosilicates $Ca[Mg_3SiN_4]:Ce^{3+}$, $Sr[Mg_3SiN_4]:Eu^{2+}$, and $Eu[Mg_3SiN_4]$. *Chem. Mater.* **2014**, *26*, 2712–2719.

[3] Pust, P.; Weiler, V.; Hecht, C.; Tücks, A.; Wochnik, A. S.; Henß, A.-K.; Wiechert, D.; Scheu, C.; Schmidt, P. J.; Schnick, W. Narrow-band red-emitting $Sr[LiAl_3N_4]:Eu^{2+}$ as a next-generation LED-phosphor material. *Nat. Mater.* **2014**, *13*, 891–896.

[4] Shannon, R. D. Revised effective ionic radii and systematic studies of interatomic distances in halides and chalcogenides. *Acta Crystallogr., Sect A: Found. Crystallogr.* **1976**, *32*, 751–767.

[5] Zachariasen, W. Über die Kristallstruktur von BeO. *Norsk. Geol. Tidssk* **1925**, *8*, 189–200.

[6] von Stackelberg, M.; Paulus, R. Untersuchungen über die Kristallstruktur der Nitride und Phosphide zweiwertiger Metalle. *Z. Phys. Chem.* **1933**, *22B*, 305–322.

[7] Somer, M.; Yarasik, A.; Akselrud, L.; Leoni, S.; Rosner, H.; Schnelle, W.; Kniep, R. $Ae[Be_2N_2]$: Nitridoberyllates of the Heavier Alkaline-Earth Metals. *Angew. Chem., Int. Ed.* **2004**, *43*, 1088–1092; $EA[Be_2N_2]$: Nitridoberyllate der schwereren Erdalkalimetalle. *Angew. Chem.* **2004**, *116*, 1108–1112.

[8] Strobel, P. Dissertation, LMU Munich **2018**.

[9] Strobel, P.; Niklaus, R.; Schmidt, P. J.; Schnick, W. Oxoberyllates $SrBeO_2$ and $Sr_{12}Be_{17}O_{29}$ as Novel Host Materials for Eu^{2+} Luminescence. *Chem. - Eur. J.* **2018**, *24*, 12678–12685.

[10] Strobel, P.; de Boer, T.; Weiler, V.; Schmidt, P. J.; Moewes, A.; Schnick, W. Luminescence of an Oxonitridoberyllate: A Study of Narrow-Band Cyan-Emitting $Sr[Be_6ON_4]:Eu^{2+}$. *Chem. Mater.* **2018**, *30*, 3122–3130.

8.2 Ultra-Narrow-Band Blue-Emitting Oxoberyllates AELi$_2$[Be$_4$O$_6$]:Eu^{2+} (AE = Sr, Ba) Paving the Way to Efficient RGB pc-LEDs

Abstract. Highly efficient phosphor-converted light-emitting diodes (pcLEDs) are popular in lighting and high-tech electronics applications. The main goals of present LED research are increasing light quality, preserving color point stability and reducing energy consumption. For those purposes excellent phosphors in all spectral regions are required. Here, we report on ultra-narrow band blue emitting oxoberyllates AELi$_2$[Be$_4$O$_6$]:Eu^{2+} (AE = Sr, Ba) exhibiting a rigid covalent network isotypic to the nitridoalumosilicate BaLi$_2$[(Al$_2$Si$_2$)N$_6$]:Eu^{2+}. The oxoberyllates' extremely small Stokes shift and unprecedented ultra-narrow band blue emission with *fwhm* ≈ 25 nm (≈ 1200 cm^{-1}) at λ_{em} = 454–456 nm result from its rigid, highly condensed tetrahedra network. AELi$_2$[Be$_4$O$_6$]:Eu^{2+} allows for using short-wavelength blue LEDs (λ_{em} < 440 nm) for efficient excitation of the ultra-narrow band blue phosphor, for application in violet pumped white RGB phosphor LEDs with improved color point stability, excellent color rendering, and high energy efficiency.
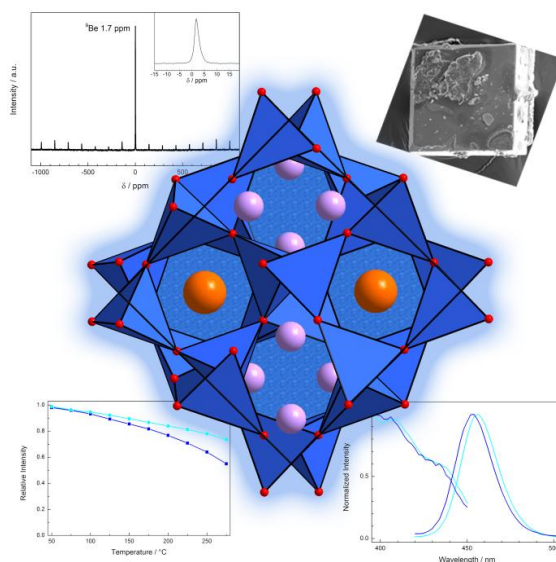
8.2.1 Article

Cost-effective and energy-efficient illumination-grade white phosphor converted (pc-)LEDs have nowadays been well established at the global lighting market.[1] The rapid distribution of LEDs has evolved from mass production of warm-white LEDs with innovative red phosphors, offering CRI (color rendering index) values beyond 80.[2] To gain increased luminous efficacy, exploration of narrow-band red emitting phosphors was in the focus of recent LED phosphor development reducing IR-spillover of white light emitting pcLEDs.[2–7] With the discovery of highly efficient red emitting BSSNE ((Ba,Sr)$_2$Si$_5$N$_8$:Eu^{2+}) and SCASN ((Sr,Ca)AlSiN$_3$:Eu^{2+}) as well as narrow-band red emitting SLA (Sr[LiAl$_3$N$_4$]:Eu^{2+}), the base for highly efficient, high CRI pcLEDs was established.[2,8,9] As was shown with application of SLA in high-power LEDs, an increase of 14% in luminous efficacy was achieved, when compared to standard red phosphors, such as BSSNE and SCASN, with a CRI > 90.[2]

Understanding structure-property relations allows creating phosphors with efficient narrow-band emission to further improve emission characteristics of state-of-the-art pcLEDs. A highly condensed network with a large degree of condensation (e.g., molar ratio of (Be,Al,Si):(O,N)) of $\kappa \geq 0.5$, cation ordering and only one crystallographic dopant site are prerequisites for narrow-band emission. Suitable compounds have been found in the materials classes of nitridosilicates as well as -aluminates, and recently, exploring (oxo)nitridoberyllate compounds.[2,7,10–14] Upon doping with Eu^{2+} highly efficient narrow-band phosphors for application in pcLEDs have been developed in these compound classes.

An approach to further improve emission characteristics of pcLEDs is the development of violet pumped white RGB (red-green-blue) phosphor converted LEDs. In RGB pcLEDs, near ultraviolet emitting (nUV-)LEDs ($\lambda_{em} < 420$ nm) are combined with highly efficient phosphors covering the blue to red spectral region to obtain high quality illumination grade white light with high color point stability under varying application conditions and for example, reduced glare.[15,16] Essential phosphors in the red spectral region are BSSNE, SCASN and SLA as well as K$_2$SiF$_6$:Mn^{4+}.[2,8,9,17] The main part of the visible spectrum is typically covered by broad-band yellow-green emitting phosphors, such as (Y,Lu)$_3$Al$_5$O$_{12}$:Ce^{3+} (YAG:Ce, LuAG:Ce).[16] Further suitable phosphors in the cyan-yellow spectral region are, e.g., Sr[Be$_6$ON$_4$]:Eu^{2+}, (Ba,Sr)$_2$SiO$_4$:Eu^{2+}, SrSi$_2$O$_2$N$_2$:Eu^{2+}, β-SiAlON:Eu^{2+}, Ba$_2$LiSi$_7$AlN$_{12}$:Eu^{2+}, and BaLi$_2$[(Al$_2$Si$_2$)N$_6$]:Eu^{2+} (BLSA).[10,12,18–22]

To minimize the intrinsic down-conversion energy loss of a white pcLED with an RGB phosphor mix a very small Stokes shift for the blue phosphor is needed. The small Stokes shift ideally allows shifting the emission of a nUV primary pump LED in the blue spectral range, very close to the emission of the blue phosphor. Yet, in the blue spectral region no commercial small Stokes shift narrow-band phosphors are known. Conventional blue phosphors for RGB pcLEDs with high quantum efficiency are $(\text{Sr,Ba,Ca})_{10}(\text{PO}_4)_6\text{Cl}_2$:$\text{Eu}^{2+}$ (SCAP), $\text{BaMgAl}_{10}\text{O}_{17}$:$\text{Eu}^{2+}$ (BAM), LiCaPO_4:Eu^{2+} (LCP), $\text{Sr}_3\text{MgSi}_2\text{O}_8$:$\text{Eu}^{2+}$ (SMSO), and $\text{Ba}_3\text{MgSi}_2\text{O}_8$:$\text{Eu}^{2+}$ (BMSO), all of them showing a relatively large Stokes shift compared to ultra-narrow red emitters like SLA.[23–26] To further improve the overall efficiency of white emitting RGB pcLEDs a blue phosphor that can be efficiently excited by pump LEDs with only inconsiderably higher emission energies is thus required.

This goal was accomplished by the synthesis of the novel oxoberyllate compounds $AE\text{Li}_2[\text{Be}_4\text{O}_6]$:$\text{Eu}^{2+}$ with AE = Sr and Ba exhibiting all postulated structural characteristics for efficient, ultra-narrow band emission. These extremely narrow-band blue emitting phosphors with an emission band width of only 25 nm ($\approx 1200 \text{ cm}^{-1}$) and a maximum at 454–456 nm show comparable material properties as narrow-band red emitting SLA ($fwhm \approx 1180 \text{ cm}^{-1}$).[2]

$AE\text{Li}_2[\text{Be}_4\text{O}_6]$:$\text{Eu}^{2+}$ (AE = Sr, Ba) is one of the first beryllate phosphors discussed for application in LEDs. Be compounds, such as metal alloys are widely spread in industrial applications, e.g., ceramics, automotive, and electronics. It is known that Be-containing dusts can cause diseases such as berylliosis, cancer, and chronic beryllium disease (CBD).[27] As a result, beryllate compounds have not been investigated in great detail so far. Be dusts and soluble salts are hazardous. Small beryllium particles can be inhaled, and dissolved Be can accumulate in the human body. Working in closed systems, such as Schlenk lines and glove boxes is suitable and required to reduce risk of exposure. Insoluble, coarsely grained Be containing solid-state phosphors are therefore less dangerous, while handling with appropriate safety measures is practicable.[7,27] We therefore assess insoluble, coarse-grained Be containing solid-state compounds to be less dangerous. Natural examples are Be-containing gem stones, e.g., beryl, aquamarine, and emerald. Therefore, application of beryllate phosphors, such as $AE\text{Li}_2[\text{Be}_4\text{O}_6]$:$\text{Eu}^{2+}$ with a particle size of up to $0.2 \times 0.2 \times 0.2 \text{ mm}^3$ (Figure S1) in pcLEDs is conceivable.

The highly condensed beryllates $AE\text{Li}_2[\text{Be}_4\text{O}_6]$:$\text{Eu}^{2+}$ (AE = Sr, Ba) were successfully synthesized by applying high-temperature routes. Due to its highly condensed network structure, $AE\text{Li}_2[\text{Be}_4\text{O}_6]$:$\text{Eu}^{2+}$ (AE = Sr, Ba) meets requirements for narrow-band emitting phosphors: chemical and thermal stability, a large band gap as well as high quantum

efficiency (QE) and color point stability at elevated temperatures. Its rigid network is the base for the narrow-band emission, as it limits the local structural relaxation of the dopant (Eu^{2+}) site in its excited state and allows a small Stokes shift.[2,28] Introduction of tetrahedrally coordinated Be into the crystal structures results in improved, targeted properties like a large band gap and a rigid network, due to the strong covalent character of Be−ligand bonds, when comparing to compounds with Li or Mg in tetrahedral coordination. This was also shown for the luminescent (oxo)nitridoberyllates Sr[Be$_6$ON$_4$]:Eu^{2+} and Sr[BeSi$_2$N$_4$]:Eu^{2+}.[7,10]

AELi$_2$[Be$_4$O$_6$]:Eu^{2+} (AE = Sr, Ba) crystallizes isotypically with the green emitting phosphor BaLi$_2$[(Al$_2$Si$_2$)N$_6$]:Eu^{2+} (BLSA).[12] Exchange of N in BLSA by O in AELi$_2$[Be$_4$O$_6$]:Eu^{2+} results in a decreased nephelauxetic effect leading to a larger energy difference between the Eu $4f^75d^0$ ground state and the excited Eu $4f^65d^1$ state. Accordingly, emission in the blue spectral region is observed for AELi$_2$[Be$_4$O$_6$]:Eu^{2+} in contrast to the green emission of BaLi$_2$[(Al$_2$Si$_2$)N$_6$]:Eu^{2+}.[1,2,6,12,29] Excitation and emission spectra of BLBO (BaLi$_2$[Be$_4$O$_6$]:Eu^{2+}) and SLBO (SrLi$_2$[Be$_4$O$_6$]:Eu^{2+}) are compared in Figure 1a. The nominal doping concentration is 1%. While SLBO exhibits maximum emission at 456 nm, BLBO emits blue light at 454 nm. Due to a small Stokes shift of only ≈ 1200 cm^{-1} both compounds show remarkably narrow emission with *fwhm* of ≈ 1200 cm^{-1}. Both compounds show a broad absorption band, extending into the UV and reaching towards the blue spectral area. Like the emission spectrum, the excitation spectrum of BLBO is also slightly blue-shifted compared to the Sr compound. The phosphors are highly excitable up to ≈ 440 nm and therefore are suitable for excitation with violet to short wavelength blue InGaN-LEDs. The narrow emission band width of only 1200 cm^{-1} of AELi$_2$[Be$_4$O$_6$]:Eu^{2+} is comparable to the most narrow-band Eu^{2+} phosphors, namely Sr[LiAl$_3$N$_4$]:Eu^{2+} (*fwhm* = 1180 cm^{-1}) and Sr[Mg$_3$SiN$_4$]:Eu^{2+} (1150 cm^{-1}). Compared to SCAP, BAM, LCP, and BMSO, the two novel blue emitting phosphors BLBO and SLBO show an even narrower, unprecedented emission signal, resulting from the extremely small Stokes shift. Powder layers of non-optimized BLBO exhibit proficient internal (external) quantum efficiency of 64% (47%), when excited at 410 nm (SLBO: 47%/16%). Temperature-dependent emission (Figure 1b) shows improved thermal quenching (TQ) behavior for BLBO. At 200 °C the relative emission intensity of BLBO is still 83%, while SLBO exhibits 76%. The low TQ is related to the sufficient band gap that was estimated to 3.8 eV for BLBO from undoped samples from diffuse reflectance spectra and analysis corresponding to the Tauc method.[30] An indirect band gap was assumed, due to the structural analogy of AELi$_2$[Be$_4$O$_6$]:Eu^{2+} and BaLi$_2$[(Al$_2$Si$_2$)N$_6$]:Eu^{2+}.[31]
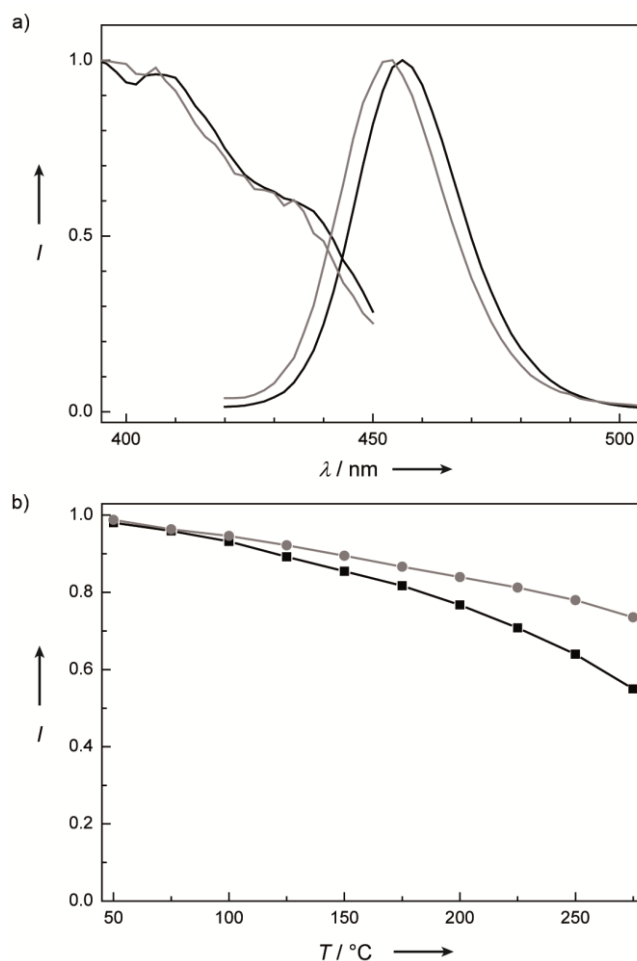
Figure 1. Photoluminescence properties of ultra-narrow band blue emitting AELi$_2$[Be$_4$O$_6$]:Eu^{2+} (AE = Sr, Ba). (a) Excitation and emission spectra of BaLi$_2$[Be$_4$O$_6$]:Eu^{2+} (gray) and SrLi$_2$[Be$_4$O$_6$]:Eu^{2+} (black) for λ_{exc} = 400 nm. (b) Temperature dependence of the relative integrated photoluminescence intensity for BLBO (gray) and SLBO (black), revealing a decrease at 200 °C of only 17 and 24%, respectively, compared to room-temperature QE.

Samples of SrLi$_2$[Be$_4$O$_6$]:Eu^{2+} and BaLi$_2$[Be$_4$O$_6$]:Eu^{2+} were investigated by single-crystal and powder X-ray diffraction (PXRD).[32] Both compounds crystallize in space group $P4/ncc$ (no. 130), isotypic with the nitridoalumosilicate BaLi$_2$[(Al$_2$Si$_2$)N$_6$].[12] Rietveld refinement on PXRD data confirms the structural model. The calculated pattern and the experimental data are compared in Figure 2. The calculated data disregards the Eu-content, due to its insignificant contribution to the structure factor. The crystallographic details are summarized in the Supporting Information.

The title compounds' morphology and elemental composition were investigated by electron microscopy, associated by EDS (energy-dispersive X-ray spectroscopy; Sr,Ba,O)

on single crystals and powder samples as well as complementary ICP-OES investigations (inductively coupled plasma optical emission spectrometry; Sr,Eu,Be) on powder samples. Results of EDS and ICP analysis are compared in Table S1. The obtained results are in good accordance with the sum formula. Solid-state magic angle spinning nuclear magnetic resonance (MAS-NMR) investigations were conducted for ^{6}Li, ^{7}Li as well as ^{9}Be on an undoped sample of BLBO to confirm the incorporation of both elements as well as the high symmetry and ordering of each crystallographic position. The NMR spectra are displayed in Figure S1. All MAS-NMR spectra give one single isotropic signal, indicating the ordering of Li and Be in the network. For the ^{7}Li spectrum, a chemical shift of δ = 1.3 ppm is found which is comparable to Li in highly condensed solid-state nitride structures (SLA: 2.6 ppm, Li$_2$SrSi$_2$N$_4$: 2.0 ppm).[2,33] For the ^{9}Be spectrum, a shift of 1.7 ppm is obtained.
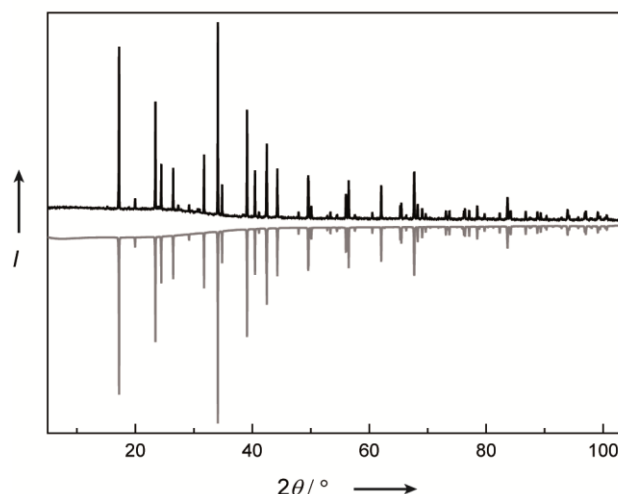
Figure 2. Crystal structure characterization of ultra-narrow band blue emitting AELi$_2$[Be$_4$O$_6$]:Eu^{2+} (AE = Sr, Ba). X-ray powder pattern of BLBO with the measured data (black line) and calculated pattern based on Rietveld refinement data (gray line).

The network structure of SLBO and BLBO is displayed in Figure 3. Corner- and edge-sharing BeO$_4$ tetrahedra form two different types of *vierer* ring channels that run along [001] and are filled with either Li or AE (Sr,Ba) atoms.[34] As was shown recently, Li atoms, which are in 4+1 coordination by anions, are better described as counter ions.[31] The strong ionic character of Li−N bonds was shown with DFT methods, accompanied by XAS/XES investigations, in BaLi$_2$[(Al$_2$Si$_2$)N$_6$].[31] The highly symmetric crystal structure offers one crystallographic site each for AE^{2+} (AE = Sr, Ba) and Li$^+$ in the highly

condensed network. The *AE* site is in eight-fold coordination that is best described as square pyramid trunk.

Therefore, the title compounds structure shows striking similarities to SLA. Both structures contain two types of channels. One of these channels in each structure provides the regular symmetric eightfold coordination sphere for the *AE* site. While the second channel is unoccupied in SLA, in the title compounds structure type the second channel offers space for Li atoms that form a tetragonal bisphenoidal arrangement.[12] The regular eight-fold coordination of the *AE* site is essential for narrow-band emission. Eu^{2+} is expected to replace the *AE* ions, due to their similar chemical behavior.[2]

Lattice parameters of SrLi$_2$[Be$_4$O$_6$] and BaLi$_2$[Be$_4$O$_6$] show only little differences, despite different ionic radii of *AE*. Compared to BaLi$_2$[(Al$_2$Si$_2$)N$_6$] lattice parameters are significantly shorter. Parameters *a* and *b* are decreased by approximately 0.6 Å, *c* by ≈ 1.1 Å, leading to a reduced unit cell volume (*AE* = Ba: 77%, *AE* = Sr: 75%) compared to BLSA. This is caused by the decreased inter-atomic metal to ligand distances resulting from the replacement of N by O. Ba−O (2.77–2.84 Å), Be–O (1.6–1.7 Å), and Li–O distances (2.0–2.4 Å) are decreased compared to BLSA (Ba–N: 2.9–3.1 Å, (Al,Si)–N: 1.7–1.8 Å, Li–N: 2.1–2.5 Å), due to the reduced ionic radius of O.[35,36] Comparing both beryllates, Sr−O distances are decreased to 2.6 Å, while Be–O and Li–O distances are similar. The metal–ligand distances are in good accordance with literature: Be–O (1.65 Å)[37] and Li–O (2.0 Å).[38]

Oxoberyllate compounds with tetrahedrally coordinated Be show close relations to highly condensed nitridosilicate structures, and notably less similarity to oxosilicates. Even fourfold coordinated O4 atoms are found in BeO crystallizing in the wurtzite structure type, or in ternary Ca$_{12}$Be$_{17}$O$_{29}$.[37,39] In particular, this structural relation is also shown in *AE*Li$_2$[Be$_4$O$_6$] (*AE* = Sr, Ba). In nitridosilicates, a highly condensed network structure with edge-sharing tetrahedra is achieved due to the large ionic radius of the nitride ligand. In oxide structures, the introduction of Be^{2+} with the same ionic radius, and decreased formal charge, compared to Si^{4+}, results in a higher degree of condensation.

When compared to BaLi$_2$[(Al$_2$Si$_2$)N$_6$]:Eu^{2+}, luminescence properties of SrLi$_2$[Be$_4$O$_6$]:Eu^{2+} and BaLi$_2$[Be$_4$O$_6$]:Eu^{2+} are significantly improved. Especially, the reduction of the emission band width from 1960 cm^{-1} (57 nm, green) in BLSA to ≈ 1200 cm^{-1} (25 nm, blue) is remarkable. This feature is strongly related to the chemical composition. While in BLSA the tetrahedra network is built up of statistically distributed AlN$_4$- and SiN$_4$-tetrahedra in an atomic 1:1 ratio, in SLBO and BLBO tetrahedra centers are solely occupied by Be. This has significant influence on the spectral shape. In general, the emission band width in

Eu^{2+}-doped compounds is broadened due to electron-phonon coupling of the emission centers as well as fluctuations in the local Eu^{2+}-coordination sphere. A mixed occupied (Al,Si) site leads to a range of chemically differing second coordination spheres around Eu^{2+} resulting in inhomogeneous line broadening of the emission band. This effect, also observed for, e.g., MLiAl$_3$N$_4$:Eu^{2+} (M = Ca, Sr) and the higher symmetric UCr$_4$C$_4$ structure type compounds MMg$_2$Al$_2$N$_4$:Eu^{2+} (M = Ca, Sr), is avoided by the substitution of Al and Si by Be in AELi$_2$[Be$_4$O$_6$]:Eu^{2+} phosphors.
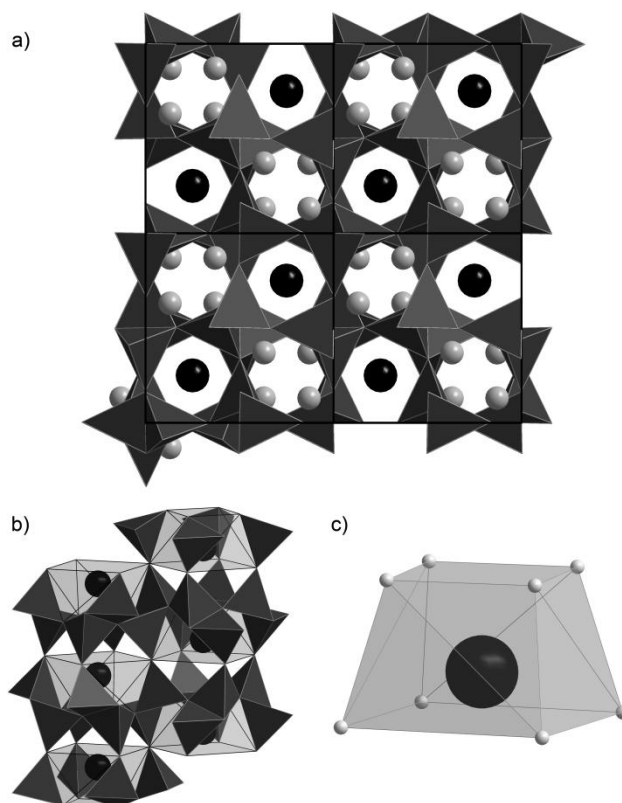
Figure 3. Structural overview of ultra-narrow band blue emitting AELi$_2$[Be$_4$O$_6$]:Eu^{2+} (AE = Sr, Ba). (a) 2 × 2 × 1 type supercell, view with two types of channels of *vierer* rings along [001]. (b) Strands of corner-sharing (Sr,Ba)O$_8$ polyhedra coordinated by BeO$_4$ tetrahedra. (c) (Sr,Ba)O$_8$ polyhedron. Black spheres are (Sr,Ba); gray spheres are Li; dark gray tetrahedra are BeO$_4$; light gray polyhedra are (Sr,Ba)O$_4$, white spheres are O.

The narrow-band emission is additionally supported by a rigid network structure, offering a highly symmetric Eu^{2+}-coordination. The strong covalent bonding between Be and its ligands, comparable to Al– and Si–ligand bonds, leads to an extremely rigid network. As a result, weak electron-phonon coupling and low local phonon frequencies lead to a small Stokes shift. The rigid nature of the network is emphasized by the crystallographic data.

Due to the larger ionic radius of Ba, when compared to Sr, the lattice parameters are expected to increase significantly. However, only little increase of the a-axis is observed, while the c-axis even decreases. This again is in accordance with the results from luminescence measurements, where only a small shift of the emission band of 2 nm is detected. Nevertheless, the exchange of Sr by Ba leads to a slightly blue-shifted emission, as expected. This can be explained by the larger ligand distances of Eu^{2+} on the Ba site, leading to a reduced ligand-field splitting and therefore higher energetic emission. This extraordinary small shift underlines the rigidity of the network, as emission shift due to substitutions on the AE site can reach values of about 50 nm, e.g., in (Sr$_{1-x}$Ca$_x$)Si$_5$N$_8$:Eu^{2+}. or (Sr$_{2-x}$Ba$_x$)Ga$_2$SiO$_7$:Eu^{2+}.[40]

Summarizing, we present ultra-narrow band blue emitting oxoberyllate phosphors, synthesized at 1100 °C with remarkably short reaction time of only 2 h. AELi$_2$[Be$_4$O$_6$]:Eu^{2+} (AE = Sr, Ba) phosphors show narrow-band emission with λ_{em} = 454–456 nm and $fwhm$ of only 1200 cm^{-1}. Because of a very small Stokes shift the phosphors are highly excitable up to ≈ 440 nm by for example, InGaN LEDs. This difference to conventional blue phosphors with larger Stokes shifts, such as SCAP, BAM, LCP, and BMSO allows the substitution of violet LEDs emitting at ≈ 410 nm by primaries with longer wavelength emission. Hence, RGB phosphor converted light sources with an increased luminous efficacy and an increased overall conversion efficiency can be achieved, applying AELi$_2$[Be$_4$O$_6$]:Eu^{2+} phosphors. The total amount of blue emitting phosphor in short wavelength blue pumped RGB light sources can also be lowered using, e.g., common green to yellow emitting Ce^{3+} doped garnet phosphors with a rather narrow excitation band centered in the blue spectral range. Excitation from both, the blue emitting phosphor and the pump LED is possible if AELi$_2$[Be$_4$O$_6$]:Eu^{2+} (AE = Sr, Ba) is being applied as blue emitting phosphor component. Therefore, application of AELi$_2$[Be$_4$O$_6$]:Eu^{2+} (AE = Sr, Ba) in illumination-grade white LEDs seems highly promising, solving a number of recent problems in solid-state lighting.

8.2.2 References

[1]   Pust, P.; Schmidt, P. J.; Schnick, W. A revolution in lighting. *Nat. Mater.* **2015**, *14*, 454–458.

[2]   Pust, P.; Weiler, V.; Hecht, C.; Tücks, A.; Wochnik, A. S.; Henß, A. K.; Wiechert, D.; Scheu, C.; Schmidt, P. J.; Schnick, W. Narrow-band red-emitting Sr[LiAl$_3$N$_4$]:Eu^{2+} as a next-generation LED-phosphor material. *Nat. Mater.* **2014**, *13*, 891–896.

[3]   Wilhelm, D.; Baumann, D.; Seibald, M.; Wurst, K.; Heymann, G.; Huppertz, H. Narrow-Band Red Emission in the Nitridolithoaluminate Sr$_4$[LiAl$_{11}$N$_{14}$]:Eu^{2+}. *Chem. Mater.* **2017**, *29*, 1204–1209.

[4]   Wagatha, P.; Pust, P.; Weiler, V.; Wochnik, A. S.; Schmidt, P. J.; Scheu, C.; Schnick, W. Ca$_{18.75}$Li$_{10.5}$[Al$_{39}$N$_{55}$]:Eu^{2+} – Supertetrahedron Phosphor for Solid-State Lighting. *Chem. Mater.* **2016**, *28*, 1220–1226.

[5]   Wagatha, P.; Weiler, V.; Schmidt, P. J.; Schnick, W. Tunable Red Luminescence in Nitridomagnesoaluminates α-Sr$_2$[MgAl$_5$N$_7$]:Eu^{2+}, β-Sr$_2$[MgAl$_5$N$_7$]:Eu^{2+} and Sr$_8$[LiMg$_2$Al$_{21}$N$_{28}$]:Eu^{2+}. *Chem. Mater.* **2018**, *30*, 1755–1761.

[6]   Strobel, P.; Weiler, V.; Hecht, C.; Schmidt, P. J.; Schnick, W. Luminescence of the Narrow-Band Red Emitting Nitridomagnesosilicate Li$_2$(Ca$_{1-x}$Sr$_x$)$_2$[Mg$_2$Si$_2$N$_6$]:Eu^{2+} (x = 0–0.06). *Chem. Mater.* **2017**, *29*, 1377–1383.

[7]   Strobel, P.; Weiler, V.; Schmidt, P. J.; Schnick, W. Sr[BeSi$_2$N$_4$]:Eu^{2+}/Ce^{3+} and Eu[BeSi$_2$N$_4$]: Nontypical Luminescence in Highly Condensed Nitridoberyllosilicates. *Chem. - Eur. J.* **2018**, *24*, 7243–7249.

[8]   Höppe, H. A.; Lutz, H.; Morys, P.; Schnick, W.; Seilmeier, A. Luminescence in Eu^{2+}-doped Ba$_2$Si$_5$N$_8$: fluorescence, thermoluminescence, and upconversion. *J. Phys. Chem. Solids* **2000**, *61*, 2001–2006.

[9]   Watanabe, H.; Kijima, N. Crystal structure and luminescence properties of Sr$_x$Ca$_{1-x}$AlSiN$_3$:Eu^{2+} mixed nitride phosphors. *J. Alloys Compd.* **2009**, *475*, 434–439.

[10]   Strobel, P.; de Boer, T.; Weiler, V.; Schmidt, P. J.; Moewes, A.; Schnick, W. Luminescence of an Oxonitridoberyllate: A Study of Narrow-Band Cyan Emitting Sr[Be$_6$ON$_4$]:Eu^{2+}. *Chem. Mater.* **2018**, *30*, 3122–3130.

[11]   Pust, P.; Hintze, F.; Hecht, C.; Weiler, V.; Locher, A.; Zitnanska, D.; Harm, S.; Wiechert, D.; Schmidt, P. J.; Schnick, W. Group (III) Nitrides M[Mg$_2$Al$_2$N$_4$] (M = Ca, Sr, Ba, Eu) and Ba[Mg$_2$Ga$_2$N$_4$] – Structural Relation and Nontypical Luminescence Properties of Eu^{2+} Doped Samples. *Chem. Mater.* **2014**, *26*, 6113–6119.

[12]   Strobel, P.; Schmiechen, S.; Siegert, M.; Tücks, A.; Schmidt, P. J.; Schnick, W. Narrow-Band Green Emitting Nitridolithoalumosilicate Ba[Li$_2$(Al$_2$Si$_2$)N$_6$]:Eu^{2+} with

Framework Topology *whj* for LED/LCD-Backlighting Applications. *Chem. Mater.* **2015**, *27*, 6109–6115.

[13] Tolhurst, T. M.; Schmiechen, S.; Pust, P.; Schmidt, P. J.; Schnick, W.; Moewes, A. Electronic Structure, Bandgap, and Thermal Quenching of Sr[Mg$_3$SiN$_4$]:Eu^{2+} in Comparison to Sr[LiAl$_3$N$_4$]:Eu^{2+}. *Adv. Opt. Mater.* **2016**, *4*, 584–591.

[14] Uheda, K.; Hirosaki, N.; Yamamoto, Y.; Naita, A.; Nakajima, T.; Yamamoto, H. Luminescence Properties of a Red Phosphor, CaAlSiN$_3$:Eu^{2+}, for White Light-Emitting Diodes *Electrochem. Solid State Lett.* **2006**, *9*, H22–H25.

[15] U.S. Department of Energy, Solid-State Lighting - R&D Plan, 2016.

[16] Kitai, A., *Materials for Solid State Lighting and Displays*, John Wiley and Sons: West Sussex, U.K., 2017.

[17] Takahashi, T.; Adachi, S. Mn^{4+}-Activated Red Photoluminescence in K$_2$SiF$_6$ Phosphor. *J. Electrochem. Soc.* **2008**, *155*, E183–E188.

[18] Seibald, M.; Rosenthal, T.; Oeckler, O.; Schnick, W. Highly Efficient pc-LED Phosphors Sr$_{1-x}$Ba$_x$Si$_2$O$_2$N$_2$:Eu^{2+} (0<x<1) - Crystal Structures and Luminescence Properties Revisited. *Crit. Rev. Solid State Mater. Sci.* **2014**, *39*, 215–229.

[19] Zhang, M.; Wang, J.; Zhang, Q.; Ding, W.; Su, Q. Optical properties of Ba$_2$SiO$_4$:Eu^{2+} phosphor for green light-emitting diode (LED). *Mater. Res. Bull.* **2007**, *42*, 33–39.

[20] Hirosaki, N.; Xie, R.-J.; Kimoto, K.; Sekiguchi, T.; Yamamoto, Y.; Suehiro, T.; Mitomo, M. Characterization and properties of green-emitting *β*-SiAlON:Eu^{2+} powder phosphors for white light-emitting diodes. *Appl. Phys. Lett.* **2005**, *86*, 211905.

[21] Seong, T.-Y.; Han, J.; Amano, H.; Morkoc, H., *III-Nitride Based Light Emitting Diodes and Applications*, Springer: Dordrecht, Germany, 2013.

[22] Takeda, T.; Hirosaki, N.; Funahshi, S.; Xie, R.-J. Narrow-Band Green-Emitting Phosphor Ba$_2$LiSi$_7$AlN$_{12}$:Eu^{2+} with High Thermal Stability Discovered by a Single Particle Diagnosis Approach. *Chem. Mater.* **2015**, *27*, 5892–5898.

[23] McKittrick, J.; Hannah, M. E.; Piquette, A.; Han, J. K.; Choi, J. I.; Anc, M.; Galvez, M.; Lugauer, H.; Talbot, J. B.; Mishra, K. C. Phosphor Selection Considerations for Near-UV LED Solid State Lighting. *ECS J. Solid State Sci. Technol.* **2013**, *2*, R3119–R3131.

[24] Piquette, A.; Bergbauer, W.; Galler, B.; Mishra, K. C. On Choosing Phosphors for Near-UV and Blue LEDs for White Light. *ECS J. Solid State Sci. Technol.* **2016**, *5*, R3146–R3159.

[25] Wang, Y.-F.; Liu, L.; Xie, R.-J.; Huang, Q. Microwave Assisted Sintering of Thermally Stable BaMgAl$_{10}$O$_{17}$:Eu^{2+} Phosphors. *ECS J. Solid State Sci. Technol.* **2013**, *2*, R196–R200.

[26] Morimoto, K.; Kasugai, H.; Takizawa, T.; Yoshida, S.; Yamanaka, K.; Katayama, T.; Okuyama, K.; Shiraishi, S.; Mizuyama, Y. 60.2: *Distinguished Paper*: A 30 W Pure Blue Emission with NUV Laser-Diode-Pumped Phosphor for High-Brightness Projectors. *SID Symp. Dig. Tech. Pap.* **2013**, *44*, 832–835.

[27] Agency for Toxic Substances and Disease Registry (ATSDR) – Case Studies in Environmental Medicine - Beryllium Toxicity, 2018.

[28] Blasse, G.; Bril, A. Characteristic luminescence. *Philips Tech. Rev.* **1970**, *31*, 304–314.

[29] Schmiechen, S.; Pust, P.; Schmidt, P. J.; Schnick, W. Weißes Licht aus Nitriden. *Nachr. Chem.* **2014**, *62*, 847–851.

[30] Tauc, J.; Grigorovici, R.; Vancu, A. Optical Properties and Electronic Structure of Amorphous Germanium. *Phys. Status Solidi B* **1966**, *15*, 627–637.

[31] Tolhurst, T. M.; Strobel, P.; Schmidt, P. J.; Schnick, W.; Moewes, A. Designing Luminescent Materials and Band Gaps: A Soft X-ray Spectroscopy and Density Functional Theory Study of Li$_2$Ca$_2$[Mg$_2$Si$_2$N$_6$]:Eu^{2+} and Ba[Li$_2$(Al$_2$Si$_2$)N$_6$]:Eu^{2+}. *J. Phys. Chem. C* **2017**, *121*, 14296–14301.

[32] Crystal data for SrLi$_2$[Be$_4$O$_6$]: crystal size: 0.246 × 0.150 × 0.059 mm^3, space group *P*4/*ncc* (no. 130), a = 7.1659(2), c = 8.9085(6) Å, V = 457.45(4) Å^3, Z = 4, ρ_{diff} = 3.391 g·cm^{-3}, Bruker D8 Venture, Mo Kα radiation (71.073 pm), multi-scan absorption correction, 8810 reflections, 339 independent reflections, R_{int} = 0.0365, least-squares refinement on F^2, R values (all data/ $F_{obs}^2 \geq 2\sigma(F_{obs}^2)$): $R$1 = 0.0193/0.0174, wR2 = 0.0487/0.0473, GooF = 1.194 for 306 observed reflections ($F_{obs}^2 \geq 2\sigma(F_{obs}^2)$) and 33 parameters. Crystal data for BaLi$_2$[Be$_4$O$_6$]: crystal size: 0.080 × 0.030 × 0.020 mm^3, space group *P*4/*ncc* (no. 130), a = 7.2770(4), c = 8.8872(5) Å, V = 470.62(5) Å^3, Z = 4, ρ_{diff} = 3.998 g·cm^{-3}, Bruker D8 Venture, Mo Kα radiation(71.073 pm), multi-scan absorption correction, 8043 reflections, 349 independent reflections, R_{int} = 0.0347, least-squares refinement on F^2, R values (all data/ $F_{obs}^2 \geq 2\sigma(F_{obs}^2)$): $R$1 = 0.0137/0.0121, wR2 = 0.0374/0.0365, GooF = 1.098 for 310 observed reflections($F_{obs}^2 \geq 2\sigma(F_{obs}^2)$) and 33 parameters. Further details on the crystal structure investigation may be obtained from the Fachinformationszentrum Karlsruhe, 76344 Eggenstein-Leopoldshafen, Germany (fax:(+ 49) 7247-808-666;e-mail:crysdata@fiz-karlsruhe.de), on quoting the depository numbers CSD-434376 and -434377.

[33] Zeuner, M.; Pagano, S.; Hug, S.; Pust, P.; Schmiechen, S.; Scheu, C.; Schnick, W. Li$_2$CaSi$_2$N$_4$ and Li$_2$SrSi$_2$N$_4$ – a Synthetic Approach to Three-Dimensional Lithium Nitridosilicates. *Eur. J. Inorg. Chem.* **2010**, 4945–4951.

[34] Liebau, F. *Structural Chemistry of Silicates*; Springer: Berlin, 1985.

[35] Shannon, R. D. Revised effective ionic radii and systematic studies of interatomic distances in halides and chalcogenides. *Acta Crystallogr., Sect A: Found. Crystallogr.* **1976**, *32*, 751–767.

[36] Baur, W. H. Effective ionic radii in nitrides. *Crystallogr. Rev.* **1987**, *1*, 59–83.

[37] Zachariasen, W. Über die Kristallstruktur von BeO. *Norsk. Geol. Tidssk* **1925**, *8*, 189–200.

[38] Zintl, E.; Harder, A.; Dauth, B. Gitterstruktur der Oxyde, Sulfide, Selenide und Telluride des Lithiums, Natriums und Kaliums. *Z. Elektrochem. Angew. Phys. Chem.* **1934**, *40*, 588–593.

[39] Harris, L. A.; Yakel, H. L. The crystal structure of calcium beryllate, Ca$_{12}$Be$_{17}$O$_{29}$. *Acta Crystallogr.* **1966**, *20*, 295–301.

[40] Li, G.; Tian, Y.; Zhao, Y.; Lin, J. Recent progress in luminescence tuning of Ce^{3+} and Eu^{2+}-activated phosphors for pc-WLEDs. *Chem. Soc. Rev.* **2015**, *44*, 8688–8713.

9   Discussion and Outlook

Novel luminescent materials with specific absorption and emission characteristics are required to improve phosphor-converted light-emitting diodes (pcLEDs) and to open up new fields of application for phosphors. In the case of Ce^{3+} activated phosphors, e.g. materials covering the red to infrared spectral range are desired. Prior to this thesis, the accessible region was limited to the range from blue to orange-red. Current research on Eu^{2+} doped materials especially focuses on narrow-band emitting phosphors. Although large progress has been made in recent years,[1] there were still some unachieved goals such as narrow-band yellow-orange phosphors or narrow-band blue phosphors with a very small Stokes shift.

The aim of this thesis was the synthesis of luminescent materials addressing the above named needs of the lighting industry as well as the identification of systems promising for further exploration. Herein, the work focused on complex systems with multiple cations and/or anions with different valences, which led to numerous novel nitrido-, oxonitrido-, and oxonitridocarbidosilicates containing both trivalent rare earth and bivalent alkaline earth atoms.

The multiple cation and anion approach paved the way to seven novel oxonitrido- and oxonitridocarbidosilicates crystallizing in four new structure types. In-depth structural investigations using powder and single-crystal X-ray diffraction were performed to master crystallographic challenges such as superstructure and pseudosymmetry phenomena in the yellow-orange phosphors $RE_{26}Ba_6[Si_{22}O_{19}N_{36}]O_{16}:Eu^{2+}$ (RE = Y, Tb) or anion disorder and merohedral twinning in $Y_{23}Sr_{17}[Si_{38}O_{18}N_{67}]O_9$.[2,3] The powerful combination of transmission electron microscopy and synchrotron microdiffraction enabled the crystal structure elucidation of green-yellow emitting $RE_4Ba_2[Si_{12}O_2N_{16}C_3]:Eu^{2+}$ (RE = Lu, Y) from data of a submicron-sized single-crystal.[4] Due to the similar atomic form factors of the incorporated anions O/N/C or cations Y/Sr, lattice energy, bond valence sum, and charge distribution calculations were applied for the assignment of the respective atom sites. These methods proved to be useful tools to support X-ray diffraction and spectroscopic data such as EDX and CHNS for multinary compounds. The electronic and optical properties were analyzed by means of DFT calculations, UV/Vis spectroscopy, and luminescence measurements. All materials exhibit large optical band gaps (≥ 4 eV) and high chemical stability, which are key prerequisites for industrial phosphors. The high potential of the investigated multinary compounds is best illustrated by the example of

oxonitridosilicate oxides $RE_4Ba_2[Si_9ON_{16}]O:Eu^{2+}$ (RE = Lu, Y), which stand out from both a structural and an application point of view.[5] These materials are the first (oxo)nitridosilicates featuring N or O atoms in connecting types ranging from $X^{[0]}$ to $X^{[4]}$. Accordingly, they are prime examples for the large structural variety in (oxo)nitridosilicates. In addition, $Lu_4Ba_2[Si_9ON_{16}]:Eu^{2+}$ shows highly efficient yellow-orange emission for application in low color rendering index warm-white pcLEDs.

The simultaneous incorporation of trivalent and bivalent cations resulted in some remarkable phosphors homeotypic to known rare earth metal nitridosilicates. The results demonstrate the high potential of the multiple cation and anion approach to obtain desired properties by modifying known materials. The first system in this context is represented by the nitridolithosilicates $Li_{38.7}RE_{3.3}Ca_{5.7}[Li_2Si_{30}N_{59}]O_2F$ (RE = La, Ce, Y), which are homeotypic to known $Li_{33}RE_9[Li_2Si_{30}N_{59}]O_2F$ (RE = Ce, Pr).[6] These modified materials significantly extended the spectral range accessible with the activator Ce^{3+}. The phosphors exhibit unrivaled long-wavelength Ce^{3+} emission covering the deep-red to infrared range with λ_{em} = 638–651 nm and $fwhm \approx 3600$ cm^{-1}.[7] The strong red-shifts of excitation and emission compared to known phosphors presumably result from the high covalency of activator-nitrogen bonds, short activator-ligand distances and low site symmetries of the activator sites. First follow-up investigations have shown that the emission is also tunable by incorporation of Lu and Sr. Further optimization with respect to phase-purity, particle morphology, and luminescence engineering by substitution on the RE/AE sites (RE = Y, La–Lu; AE = Mg–Ba) will be necessary to bring these materials into application. With their deep-red to infrared emission $Li_{38.7}RE_{3.3}AE_{5.7}[Li_2Si_{30}N_{59}]O_2F:Ce^{3+}$ are auspicious luminescent materials for horticultural lighting.[8] This fast-growing business segment in solid-state lighting has the potential to replace conventional agriculture and may guarantee safe harvests independent of location and weather.[9]

The second material is $La_{3-x}Ca_{1.5x}Si_6N_{11}:Eu^{2+}$ (x = 0.77), which crystallizes homeotypically to the industrially relevant yellow phosphor $La_3Si_6N_{11}:Ce^{3+}$.[10] *Xie* et al. reported on improved Ce^{3+} luminescence properties for incorporation of AE metals (AE = Ca–Ba), but no sufficient structural and spectroscopic investigations were performed to explain this effect.[11,12] Our investigations clarified the charge balance mechanism and will allow for a more detailed understanding of structure-property relationships. This might help to bring the $La_{3-x}AE_{1.5x}Si_6N_{11}:Ce^{3+}$ phosphors into application. More importantly, $La_{3-x}Ca_{1.5x}Si_6N_{11}:Eu^{2+}$ (x = 0.77) exhibits narrow-band yellow-orange emission with λ_{em} = 587 nm and $fwhm$ = 60 nm/1700 cm^{-1}, which enables amber-LEDs with high color purity and luminous efficacy.[13] The crucial point to bring $La_{3-x}AE_{1.5x}Si_6N_{11}:Eu^{2+}$ into application will be to increase the internal quantum efficiency, which is limited by

reabsorption of the target emission. The incorporation of Mg^{2+} instead of Ca^{2+} appears promising as the smaller ionic radius of Mg^{2+} may prevent Eu^{2+} from occupying the unfavorable sites. First syntheses aiming for $La_{3-x}Mg_xSi_6N_{11}$:Eu^{2+} were not successful in analogous high-temperature syntheses due to the low evaporation temperature of magnesium. Future investigations should therefore focus on syntheses in hot isostatic presses, which allow for nitrogen pressures up to about 200 MPa and proved to be useful for the synthesis of luminescent nitridometalates.[14–16] If the internal quantum efficiency can be improved significantly, application of $La_{3-x}AE_{1.5x}Si_6N_{11}$:$Eu^{2+}$ in next-generation amber pcLEDs e.g. for outdoor lighting is conceivable.

Most recently, *Strobel* et al. demonstrated the high potential of Eu^{2+}/Ce^{3+} doped beryllates for application in solid-state lighting. In a joint work, the novel ultra narrow-band blue-emitting oxoberyllates AELi$_2$[Be$_4$O$_6$]:Eu^{2+} (AE = Sr, Ba) were synthesized and investigated. In addition to the narrow-band emission (λ_{em} = 454–456 nm, *fwhm* ≈ 1200 cm^{-1}) AELi$_2$[Be$_4$O$_6$]:Eu^{2+} exhibit a very small Stokes shift enabling efficient RGB pcLEDs excited by short-wavelength blue LEDs (λ_{em} < 440 nm).[17] The crystal structures are isotypic to the narrow-band green-emitting nitridoalumosilicate Ba[Li$_2$(Al$_2$Si$_2$)N$_6$]:Eu^{2+}, therefore demonstrating the large structural similarities between silicates and beryllates.[18] A main reason for the small Stokes shift is the highly condensed, rigid tetrahedra network. In general, beryllates allow for significantly higher degrees of condensation compared to silicates. Increased structural variety additionally arises from the possibility of trigonal planar coordination of beryllium.[19] However, a challenge that occurs when considering highly condensed beryllates for application in pcLEDs are strict guidelines regarding the allowed maximum beryllium content. This issue could be solved by compounds with multiple tetrahedrally coordinated cations, e.g. nitridoberyllosilicates. With such materials the Be content could be reduced but the maximum degree of condensation and structural variety can nevertheless be increased compared to silicates. With the exception of the ternary double nitride BeSiN$_2$, Sr[BeSi$_2$N$_4$]:Eu^{2+} is the only known (oxo)nitridoberyllosilicate.[20,21] Further investigations on this almost unexplored class of compounds could be very fruitful in terms of both fundamental research and applications.

An important conclusion from this thesis is the beneficial impact of heavy atoms on the luminescence characteristics. Heavy atoms can reduce phonon frequencies of local lattice vibrations that are coupled to the electronic transitions in the activator ions. This results in a reduced Stokes shift and consequently more narrow and efficient emission. The increased efficiency can be put down to a smaller parabola offset in the excited state and

hence a higher energy barrier for nonradiative decay already at room temperature.[22] Additionally, improved quenching behavior at the increased operating temperatures of a pcLED can be expected. The described effects can be observed if e.g. Y^{3+} is substituted by Lu^{3+} with an almost identical ionic radius but twice the atomic weight. Consequently, the phosphors $RE_4Ba_2[Si_{12}O_2N_{16}C_3]:Eu^{2+}$ and $RE_4Ba_2[Si_9ON_{16}]:Eu^{2+}$ (RE = Lu, Y) presented in this thesis exhibit a significantly smaller Stokes shift, more narrow emission and higher efficiency in the case of the Lu compound, respectively.[4,5] Especially the highly efficient yellow-orange phosphor $Lu_4Ba_2[Si_9ON_{16}]:Eu^{2+}$ has potential for application. The effects can be observed independently of the activator, degree of condensation, or the chemical system as indicated by further examples such as the sorosilicates $RE_4Si_2O_7N_2:Ce^{3+}$ or the industrially important garnets $RE_3Al_5O_{12}:Ce^{3+}$ (RE = Lu, Y).[23,24] However, despite the beneficial effects on the luminescence properties, only a handful of Lu-(oxo)nitridosilicates have been published so far, including the two phosphors presented in this thesis.

Future studies on Lu-silicates could be based on two different synthesis strategies. The first strategy is based on explorative syntheses, which have once again proved fruitful in this work. It is expected that these will lead to an immeasurable number of new compounds in the future, especially if multinary systems, which have hardly been investigated so far, are examined more closely. The second strategy is more target-oriented and utilizes computational screening for crystal structures with favorable structural motifs. On the search for narrow-band emitting materials *Sohn* et al. screened the ICSD database for structures with a single activator site with 8-fold cuboidal coordination, as it is the case for other narrow-band emitting phosphors such as $Sr[LiAl_3N_4]:Eu^{2+}$.[25] They finally came up with a promising narrow-band red-emitting $(Sr,Ca)_2[MgAl_5N_7]:Eu^{2+}$ as a substitutional variant of the $K_2Zn_6O_7$ structure type.[26] Although this material had already been published shortly before by *Wagatha* et al. the approach appears to be very promising.[27] A first database screening without the limitation of only one activator site and solely focused on nitrides bore $Ca_3RE_3Si_9N_{17}$ (RE = Sm, Yb)[28] as an auspicious candidate for substitution experiments and Ce^{3+}/Eu^{2+} doping. The crystal structure exhibits an 8-fold cuboidal coordinated site preferably occupied by the larger Ca^{2+} atoms. Additionally, there is an irregularly 6-fold coordinated site mostly occupied by RE^{3+}. Due to the nearly identical ionic radii of Yb^{3+} and Lu^{3+} in 6-fold coordination (Yb^{3+}: 87 pm, Lu^{3+}: 86 pm)[29] there is a high probability for successful substitution. The substitution of Ca^{2+} by larger Sr^{2+} also appears feasible, as the metal–N distances on the 8-fold coordinated site ($\approx$ 262 pm) resemble that in other Sr-nitridometalates such as $SrAlSiN_7:Eu^{2+}$ or $Li_2SrSi_2N_4$.[30,31] The substitution of Ca^{2+} by

Sr^{2+} would be exciting if cation ordering would occur due to the larger difference in ionic radii of Sr^{2+} and Lu^{3+} compared to Ca^{2+} and Yb/Sm^{3+}. A hypothetical compound $Sr_3Lu_3Si_9N_{17}$:Eu^{2+} with cation ordering would comprise important criteria for narrow-band Eu^{2+} emission, namely a highly condensed rigid network and a single activator site with highly symmetric cuboidal coordination. The high atomic weight of Lu^{3+} would further contribute to narrow-band and efficient emission.

References

[1]   Leaño Jr., J. L.; Fang, M.-H.; Liu, R.-S. Review—Narrow-Band Emission of Nitride Phosphors for Light-Emitting Diodes: Perspectives and Opportunities. *ECS J. Solid State Sci. Technol.* **2018**, *7*, R3111–R3133.

[2]   Maak, C.; Hoch, C.; Schmidt, P. J.; Schnick, W. Oxonitridosilicate Oxides $RE_{26}Ba_6[Si_{22}O_{19}N_{36}]O_{16}$:$Eu^{2+}$ (RE = Y, Tb) with a Unique Layered Structure and Orange-Red Luminescence for RE = Y. *Inorg. Chem.* **2018**, *57*, 2242–2248.

[3]   Maak, C.; Niklaus, R.; Oeckler, O.; Schnick, W. $Y_{23}Sr_{17}[Si_{38}O_{18}N_{67}]O_9$ – An Oxonitridosilicate Oxide with a Unique Layered Structure. *Z. Anorg. Allg. Chem.* **2019**, *645*, 182–187.

[4]   Maak, C.; Eisenburger, L.; Wright, J. P.; Nentwig, M.; Schmidt, P. J.; Oeckler, O.; Schnick, W. $RE_4Ba_2[Si_{12}O_2N_{16}C_3]$:$Eu^{2+}$ (RE = Lu, Y): Green-Yellow Emitting Oxonitridocarbidosilicates with a Highly Condensed Network Structure Unraveled through Synchrotron Microdiffraction. *Inorg. Chem.* **2018**, *57*, 13840–13846.

[5]   Maak, C.; Niklaus, R.; Friedrich, F.; Mähringer, A.; Schmidt, P. J.; Schnick, W. Efficient Yellow-Orange Phosphor $Lu_4Ba_2[Si_9ON_{16}]O$:Eu^{2+} and Orange-Red Emitting $Y_4Ba_2[Si_9ON_{16}]O$:Eu^{2+}: Two Oxonitridosilicate Oxides with Outstanding Structural Variety. *Chem. Mater.* **2017**, *29*, 8377–8384.

[6]   Lupart, S.; Durach, D.; Schnick, W. $Li_{35}Ln_9Si_{30}N_{59}O_2F$ with Ln = Ce, Pr – Highly Condensed Nitridosilicates. *Z. Anorg. Allg. Chem.* **2011**, *637*, 1841–1844.

[7]   Maak, C.; Strobel, P.; Weiler, V.; Schmidt, P. J.; Schnick, W. Unprecedented Deep-Red Ce^{3+} Luminescence of the Nitridolithosilicates $Li_{38.7}RE_{3.3}Ca_{5.7}[Li_2Si_{30}N_{59}]O_2F$ (RE = La, Ce, Y). *Chem. Mater.* **2018**, *30*, 5500–5506.

[8]   https://cen.acs.org/materials/inorganic-chemistry/chemical-search-better-white-light/96/i46, visited on February 14th, 2019.

[9]   https://www.sueddeutsche.de/wirtschaft/landwirtschaft-im-labor-wo-die-erdbeeren-ohne-sonne-wachsen-1.4177054, visited on December 11th, 2018.

[10] Kijima, N.; Seto, T.; Hirosaki, N. A New Yellow Phosphor $La_3Si_6N_{11}$:Ce^{3+} for White LEDs. *ECS Trans.* **2009**, *25(9)*, 247–252.

[11] Suehiro, T.; Hirosaki, N.; Xie, R.-J. Synthesis and Photoluminescent Properties of $(La,Ca)_3Si_6N_{11}$:Ce^{3+} Fine Powder Phosphors for Solid-State Lighting. *Appl. Mater. Interfaces*, **2011**, *3*, 811–816.

[12] Chen, Z.; Zhang, Q.; Li, Y.; Wang, H.; Xie, R.-J. A promising orange-yellow-emitting phosphor for high power warm-light white LEDs: Pure-phase synthesis and photoluminescence properties. *J. Alloys Compd.* **2017**, *715*, 184–191.

[13] Maak, C.; Durach, D.; Martiny, C.; Schmidt, P. J.; Schnick, W. Narrow-Band Yellow-Orange Emitting $La_{3-x}Ca_{1.5x}Si_6N_{11}$:$Eu^{2+}$ ($x \approx 0.77$): A Promising Phosphor for Next-Generation Amber pcLEDs. *Chem. Mater.* **2018**, *30*, 3552–3558.

[14] Atkinson, H. V.; Davies, S. Fundamental Aspects of Hot Isostatic Pressing: An Overview. *Metall. and Mat. Trans. A* **2000**, *31*, 2981–3000.

[15] Wagatha, P.; Pust, P.; Weiler, V.; Wochnik, A. S.; Schmidt, P. J.; Scheu, C.; Schnick, W. $Ca_{18.75}Li_{10.5}[Al_{39}N_{55}]$:$Eu^{2+}$ – Supertetrahedron Phosphor for Solid-State Lighting. *Chem. Mater.* **2016**, *28*, 1220–1226.

[16] Watanabe, H.; Kijima, N. Crystal structure and luminescence properties of $Sr_xCa_{1-x}AlSiN_3$:Eu^{2+} mixed nitride phosphors. *J. Alloys Compd.* **2009**, *475*, 434–439.

[17] Strobel, P.; Maak, C.; Weiler, V.; Schmidt, P. J.; Schnick, W. Ultra-Narrow-Band Blue-Emitting Oxoberyllates $AELi_2[Be_4O_6]$:Eu^{2+} (AE = Sr,Ba) Paving the Way to Efficient RGB pc-LEDs. *Angew. Chem., Int. Ed.* **2018**, *57*, 8739–8743; *Angew. Chem.* **2018**, *130*, 8875–8879.

[18] Strobel, P.; Schmiechen, S.; Siegert, M.; Tücks, A.; Schmidt, P. J.; Schnick, W. Narrow-Band Green Emitting Nitridolithoalumosilicate $Ba[Li_2(Al_2Si_2)N_6]$:Eu^{2+} with Framework Topology *whj* for LED/LCD-Backlighting Applications. *Chem. Mater.* **2015**, *27*, 6109–6115.

[19] Somer, M.; Carrillo-Cabrera, W.; Peters, E.-M.; Peters, K.; von Schnering, H. G. Crystal structure of lithium beryllium nitride, LiBeN. *Z. Kristallogr.* **1996**, *211*, 635.

[20] Eckerlin, P. Zur Kenntnis des Systems Be_3N_2-Si_3N_4, IV. Die Kristallstruktur von $BeSiN_2$. *Z. Anorg. Allg. Chem.* **1967**, *353*, 225–235.

[21] Strobel, P.; Weiler, V.; Schmidt, P. J.; Schnick, W. $Sr[BeSi_2N_4]$:Eu^{2+}/Ce^{3+} and $Eu[BeSi_2N_4]$: Nontypical Luminescence in Highly Condensed Nitridoberyllosilicates. *Chem. - Eur. J.* **2018**, *24*, 7243–7249.

[22] Blasse, G. Luminescence of inorganic solids: from isolated centres to concentrated systems. *Prog. Solid State Chem.* **1988**, *18*, 79–171.

[23] Xu, X.; Cai, C.; Hao, L.; Wang, Y.; Li, Q. The photoluminescence of Ce-doped $Lu_4Si_2O_7N_2$ green phosphors. *Mater. Chem. Phys.* **2009**, *118*, 270–272.

[24] Xia, Z.; Meijerink, A. Ce^{3+}-Doped garnet phosphors: composition modification, luminescence properties and applications. *Chem. Soc. Rev.* **2017**, *46*, 275–299.

[25] Pust, P.; Weiler, V.; Hecht, C.; Tücks, A.; Wochnik, A. S.; Henß, A.-K.; Wiechert, D.; Scheu, C.; Schmidt, P. J.; Schnick, W. Narrow-band red-emitting $Sr[LiAl_3N_4]:Eu^{2+}$ as a next-generation LED-phosphor material. *Nat. Mater.* **2014**, *13*, 891–896.

[26] Kim, M.; Singh, S. P.; Lee, J.-W.; Izawa, T.; Kim, D.; Yun, B.; Yoon, C.; Park, W. B.; Sohn, K.-S. Identification of a narrow band red light-emitting phosphor using computational screening of ICSD: Its synthesis and optical characterization. *J. Alloys Compd.* **2019**, *774*, 338–346.

[27] Wagatha, P.; Weiler, V.; Schmidt, P. J.; Schnick, W. Tunable Red Luminescence in Nitridomagnesoaluminates α-$Sr_2[MgAl_5N_7]:Eu^{2+}$, β-$Sr_2[MgAl_5N_7]:Eu^{2+}$, and $Sr_8[LiMg_2Al_{21}N_{28}]:Eu^{2+}$. *Chem. Mater.* **2018**, *30*, 1755–1761.

[28] Huppertz, H.; Oeckler, O.; Lieb, A.; Glaum, R.; Johrendt, D.; Tegel, M.; Kaindl, R.; Schnick, W. $Ca_3Sm_3[Si_9N_{17}]$ and $Ca_3Yb_3[Si_9N_{17}]$ Nitridosilicates with Interpenetrating Nets that Consist of Star-Shaped $[N^{[4]}(SiN_3)_4]$ Units and $[Si_5N_{16}]$ Supertetrahedra. *Chem. - Eur. J.* **2012**, *18*, 10857–10864.

[29] Shannon, R. D. Revised effective ionic radii and systematic studies of interatomic distances in halides and chalcogenides. *Acta Crystallogr., Sect. A: Cryst. Phys., Diffr., Theor. Gen. Crystallogr.* **1976**, *32*, 751–767.

[30] Hecht, C.; Stadler, F.; Schmidt, P. J.; Schmedt auf der Günne, J.; Baumann, V.; Schnick, W. $SrAlSi_4N_7:Eu^{2+}$ – A Nitridoalumosilicate Phosphor for Warm White Light (pc)LEDs with Edge-Sharing Tetrahedra. *Chem. Mater.* **2009**, *21*, 1595–1601.

[31] Zeuner, M.; Pagano, S.; Hug, S.; Pust, P.; Schmiechen, S.; Scheu, C.; Schnick, W. $Li_2CaSi_2N_4$ and $Li_2SrSi_2N_4$ – a Synthetic Approach to Three-Dimensional Lithium Nitridosilicates. *Eur. J. Inorg. Chem.* **2010**, 4945–4951.

150

10 Summary

1. Unprecedented Deep-Red Ce^{3+} Luminescence of the Nitridolithosilicates Li$_{38.7}$RE$_{3.3}$Ca$_{5.7}$[Li$_2$Si$_{30}$N$_{59}$]O$_2$F (RE = La, Ce, Y)

Christian Maak, Philipp Strobel, Volker Weiler, Peter J. Schmidt, and Wolfgang Schnick
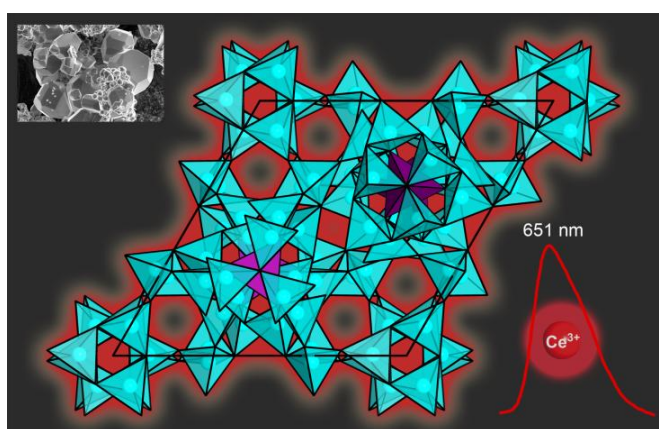
Ce^{3+} doped phosphors, which exhibit emission spectra from the blue to the orange-red spectral range, find broad application on the LED market. The red to infrared spectral range was not yet accessible with Ce^{3+} as activator. In this chapter, the nitridolithosilicates Li$_{38.7}$RE$_{3.3}$Ca$_{5.7}$[Li$_2$Si$_{30}$N$_{59}$]O$_2$F (RE = La, Ce, Y) with an unprecedented red-shifted Ce^{3+} emission are presented. These luminescent materials absorb light from the UV to green-yellow spectral range with excitation maxima at λ_{exc} = 540 nm. The emission peaks are in the deep-red to infrared range with λ_{em} = 638–651 nm. Due to this remarkable luminescence properties with unrivaled long-wavelength Ce^{3+} excitation and emission, application in horticultural lighting or as luminescent solar concentrators appears promising. The materials were synthesized in tantalum ampules in high-temperature metathesis reactions. The isotypic crystal structures exhibit a highly condensed three-dimensional network made up by SiN$_4$ and LiN$_4$ tetrahedra. The structure elucidation is based on single-crystal and powder X-ray diffraction data. X-ray spectroscopy as well as lattice energy, charge distribution, and bond valence sum calculations support the results from X-ray diffraction data.

2. Narrow-Band Yellow-Orange Emitting $La_{3-x}Ca_{1.5x}Si_6N_{11}:Eu^{2+}$ ($x \approx 0.77$): A Promising Phosphor for Next-Generation Amber pcLEDs

Christian Maak, Dajana Durach, Christoph Martiny, Peter J. Schmidt, and Wolfgang Schnick

Chem. Mater. **2018**, *30*, 3552–3558
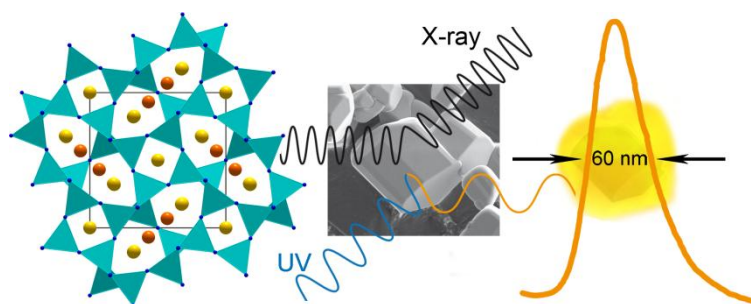
The nitridosilicate $La_{3-x}Ca_{1.5x}Si_6N_{11}:Eu^{2+}$ ($x \approx 0.77$) exhibits a large optical band gap, high chemical stability, and a remarkably narrow yellow-orange emission with $\lambda_{em} \approx 587$ nm and *fwhm* ≈ 60 nm/1700 cm^{-1}. Phosphors with such a narrow yellow-orange emission allow to increase the color purity and luminous efficacy compared to state-of-the-art amber pcLEDs. Accordingly, application in next-generation amber pcLEDs, which could be used for example as warning signs, automotive turn signals or for outdoor lighting, appears promising. The phosphor was synthesized in a high-temperature reaction using LaF_3, $La(NH_2)_3$, CaH_2, $Si(NH)_2$, and EuF_3. The compound crystallizes in the tetragonal space group *P*4*bm* (no. 100) with $a = 10.1142(6)$, $c = 4.8988(3)$ Å, and $Z = 2$. The crystal structure is homeotypic to that of commercially applied $La_3Si_6N_{11}:Ce^{3+}$. Our results provide evidence for the charge balance mechanism in "$(La,AE)_3Si_6N_{11}:Ce^{3+}$" materials for the first time. According to single-crystal X-ray diffraction data, charge balance is obtained through incorporation of La and Ca atoms on three cation sites in $La_{3-x}Ca_{1.5x}Si_6N_{11}:Eu^{2+}$ ($x \approx 0.77$) in contrast to only two sites in the $La_3Si_6N_{11}$ structure type. The results are supported by powder X-ray diffraction data, infrared and energy-dispersive X-ray spectroscopy.

3. **Efficient Yellow-Orange Phosphor $Lu_4Ba_2[Si_9ON_{16}]O:Eu^{2+}$ and Orange-Red Emitting $Y_4Ba_2[Si_9ON_{16}]O:Eu^{2+}$: Two Oxonitridosilicate Oxides with Outstanding Structural Variety**

Christian Maak, Robin Niklaus, Franziska Friedrich, Andre Mähringer, Peter J. Schmidt, and Wolfgang Schnick

Chem. Mater. **2017**, *29*, 8377–8384
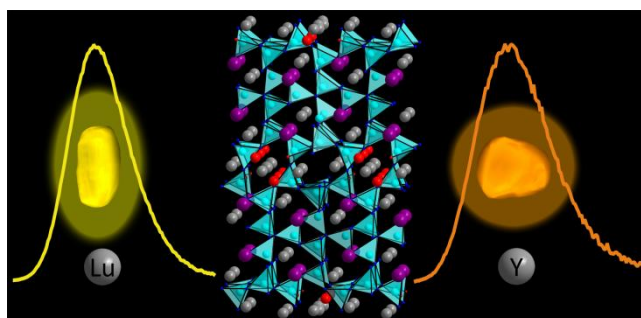
The oxonitridosilicate oxides $Lu_4Ba_2[Si_9ON_{16}]O:Eu^{2+}$ and $Y_4Ba_2[Si_9ON_{16}]O:Eu^{2+}$ exhibit a highly condensed 3D-network containing 4-fold bridging $N^{[4]}$ atoms next to $N^{[3]}$, $N^{[2]}$, $O^{[1]}$, and noncondensed oxide ions. Accordingly, this new structure type demonstrates the vast structural variety in the compound class of oxonitridosilicates. Both materials were synthesized in high-temperature reactions using REF_3, RE_2O_3 (RE = Y, Lu), BaH_2, $Si(NH)_2$, and EuF_3 as starting materials. The compounds crystallize isotypic in the monoclinic space group $P2_1/c$ (no. 14) with Z = 4 and a = 6.0756(2), b = 27.0606(9), c = 9.9471(3) Å, and β = 91.0008(8)° for RE = Y and a = 6.0290(3), b = 26.7385(12), c = 9.8503(5) Å, and β = 90.7270(30)° for RE = Lu. Upon excitation with an (In,Ga)N-LED, $Y_4Ba_2[Si_9ON_{16}]O:Eu^{2+}$ shows orange-red emission (λ_{max} = 622 nm, *fwhm* $\approx$ 2875 cm^{-1}). $Lu_4Ba_2[Si_9ON_{16}]O:Eu^{2+}$ shows more narrow and highly efficient emission with λ_{max} = 586 nm / *fwhm* $\approx$ 2530 cm^{-1} and an internal quantum efficiency *IQE* $\approx$ 85%. The beneficial effects of the high atomic weight of Lu atoms on the luminescence characteristics are discussed in detail. Due to the efficient emission in the yellow-orange spectral range, $Lu_4Ba_2[Si_9ON_{16}]O:Eu^{2+}$ is a promising phosphor for application in low color rendering index warm-white light emitting diodes, which are required e.g. for outdoor illumination.

4. **$RE_4Ba_2[Si_{12}O_2N_{16}C_3]:Eu^{2+}$** **($RE$ = Lu, Y): Green-Yellow Emitting Oxonitridocarbidosilicates with a Highly Condensed Network Structure Unraveled through Synchrotron Microdiffraction**

Christian Maak, Lucien Eisenburger, Jonathan P. Wright, Markus Nentwig, Peter J. Schmidt, Oliver Oeckler, and Wolfgang Schnick
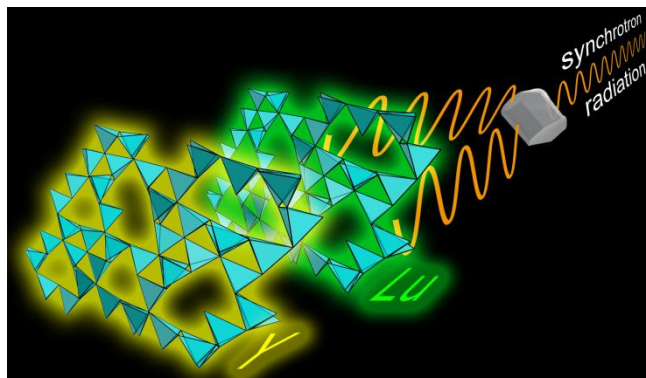
The oxonitridocarbidosilicates $RE_4Ba_2[Si_{12}O_2N_{16}C_3]:Eu^{2+}$ (RE = Lu, Y) were obtained from a carbothermal reaction starting from $Ba_2Si_5N_8$, RE_2O_3, graphite, $Si(NH)_2$, and Eu_2O_3. The crystal structure elucidation is based on a combination of transmission electron microscopy and synchrotron microdiffraction on a submicron sized single crystal for RE = Lu [$P3$ (no. 143), a = 16.297(4), c = 6.001(2) Å, Z = 3]. The unique silicate network is made up by star-shaped units $[C^{[4]}(Si(O/N)_3)_4]$ with carbon in fourfold bridging positions. The results are supported by Rietveld refinements, CHNS analysis, EDX spectroscopy and lattice energy calculations. Upon excitation with UV to blue light, the materials exhibit green luminescence for RE = Lu ($\lambda_{em} \approx 538$ nm, $fwhm \approx 3600$ cm^{-1}) and yellow emission in the case of RE = Y ($\lambda_{em} \approx 556$ nm, $fwhm \approx 4085$ cm^{-1}). The large atomic weight of Lu atoms results in blue-shifted and more narrow emission as well as higher efficiency for $Lu_4Ba_2[Si_{12}O_2N_{16}C_3]:Eu^{2+}$. The results demonstrate the huge potential of the combination of TEM and synchrotron microdiffraction for structure analysis. Further exploration of novel (oxo)nitridocarbidosilicates appears promising, as the presented materials fulfill a couple of prerequisites for state-of-the-art phosphors, such as large optical band gaps and high chemical stability.

5. **Oxonitridosilicate Oxides *RE*$_{26}$Ba$_6$[Si$_{22}$O$_{19}$N$_{36}$]O$_{16}$:Eu^{2+} (*RE* = Y, Tb) with a Unique Layered Structure and Orange-Red Luminescence for *RE* = Y**

Christian Maak, Constantin Hoch, Peter J. Schmidt, and Wolfgang Schnick

Inorg. Chem. **2018**, *57*, 2242–2248
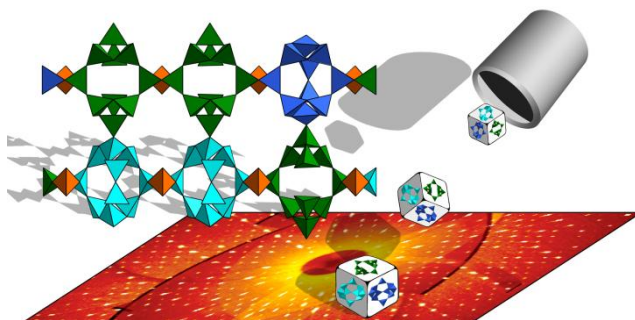
The oxonitridosilicate oxides *RE*$_{26}$Ba$_6$[Si$_{22}$O$_{19}$N$_{36}$]O$_{16}$:Eu^{2+} (*RE* = Y, Tb) were synthesized by reacting *RE*F$_3$, *RE*$_2$O$_3$, BaH$_2$, Si(NH)$_2$, and EuF$_3$. The reactions are probably promoted by the formation of highly stable fluorides *AE*F$_2$ as well as H$_2$. The crystal structures were solved and refined from single-crystal X-ray diffraction data in the monoclinic space group *Pm* (no. 6) [*Z* = 3, *a* = 16.4285(8), *b* = 20.8423(9), *c* = 16.9257(8) Å, *β* = 119.006(3)° for *RE* = Y; *a* = 16.5465(7), *b* = 20.9328(9), *c* = 17.0038(7) Å, *β* = 119.103(2)° for *RE* = Tb]. The crystal structure exhibits unique silicate layers made up by three slightly differing types of cages. The resulting threefold superstructure together with pronounced hexagonal pseudosymmetry complicated the structure elucidation. The results are supported by powder X-ray diffraction as well as infrared and EDX spectroscopy. Y$_{26}$Ba$_6$[Si$_{22}$O$_{19}$N$_{36}$]O$_{16}$:Eu^{2+} exhibits a large optical band gap of 4.2 eV and shows broad orange-red luminescence (*λ*$_{em}$ = 628 nm, *fwhm* ≈ 125 nm/3130 cm^{-1}) when excited by an (In,Ga)N-LED. The broad emission results from incorporation of Eu^{2+} on a large number of sites with different coordination spheres. Novel highly symmetric *AE*/*RE*/Si/O/N (*AE* = Ca–Ba) host lattices with a small number of cation sites may be promising to obtain more narrow Eu^{2+} emission for state-of-the-art pcLEDs.

6. Y₂₃Sr₁₇[Si₃₈O₁₈N₆₇]O₉ – An Oxonitridosilicate Oxide with a Unique Layered Structure

Christian Maak, Robin Niklaus, Oliver Oeckler, and Wolfgang Schnick

Z. Anorg. Allg. Chem. **2019**, *645*, 182–187
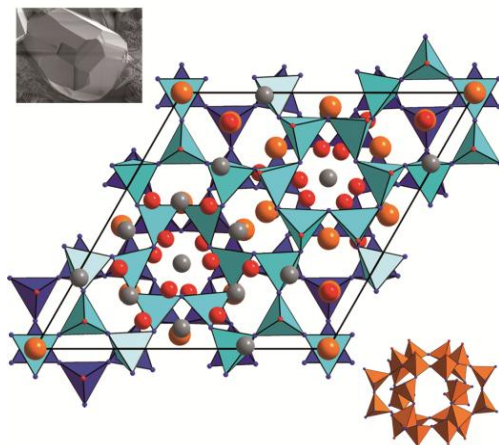
$Y_{23}Sr_{17}[Si_{38}O_{18}N_{67}]O_9$ was obtained in a high-temperature synthesis starting from YF_3, Y_2O_3, SrH_2, and $Si(NH)_2$. The driving force of the reaction is probably the formation of the binary compounds SrF_2 and H_2. The oxonitridosilicate oxide $Y_{23}Sr_{17}[Si_{38}O_{18}N_{67}]O_9$ represents a new structure type with unique $[Si_{38}O_{18}N_{67}]^{85-}$ layers, built up of vertex-sharing SiN_4 and $SiON_3$ tetrahedra. The crystal structure elucidation is based on single-crystal X-ray diffraction data [$P6_3/m$ (no. 176) with a = 16.5764(4), c = 18.6177(5) Å, and Z = 2]. Rietveld refinements on powder X-ray diffraction data as well as infrared and X-ray spectroscopy support the results. Lattice energy (MAPLE) and charge distribution (CHARDI) calculations were performed to assign Y/Sr and O/N, indicating ordering for both anions and cations. The compound is stable toward air and moisture and exhibits large optical and electronic (DFT) band gaps ≈ 3.8 eV. These are important properties of host materials for application in pcLEDs. Although the title compound exhibits no luminescence when doped with Eu^{2+} or Ce^{3+}, *RE*/*AE*/Si/O/N (*RE* = La–Lu, Y; *AE* = Ca–Ba) materials should be further explored as potential host materials for solid-state lighting. The reaction route starting from rare earth element fluorides, alkaline earth element hydrides, and reactive silicon containing precursors appears promising to further explore the system *RE*/*AE*/Si/O/N.

7. Ultra-Narrow-Band Blue-Emitting Oxoberyllates *AE*Li$_2$[Be$_4$O$_6$]:Eu^{2+} (*AE* = Sr, Ba) Paving the Way to Efficient RGB pc-LEDs

Philipp Strobel, Christian Maak, Volker Weiler, Peter J. Schmidt, and Wolfgang Schnick

Angew. Chem., Int. Ed. **2018**, *57*, 8739–8743; *Angew. Chem.* **2018**, *130*, 8875–8879
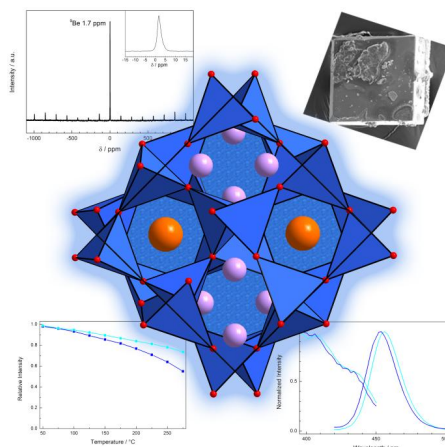
The oxoberyllates *AE*Li$_2$[Be$_4$O$_6$]:Eu^{2+} (*AE* = Sr, Ba) were synthesized at 1100 °C in a radiofrequency furnace starting from the binary oxides. The crystal structures were solved and refined from single-crystal X-ray diffraction data in space group *P*4/*ncc* (no. 130; SrLi$_2$[Be$_4$O$_6$]: *a* = 7.1659(2), *c* = 8.9085(6) Å; BaLi$_2$[Be$_4$O$_6$]: *a* = 7.2770(4), *c* = 8.8872(5) Å; *Z* = 4). Structural and elemental analysis was supported by ^{6}Li, ^{7}Li and ^{9}Be NMR-spectroscopic investigations. *AE*Li$_2$[Be$_4$O$_6$]:Eu^{2+} (*AE* = Sr, Ba) crystallize isotypic to the narrow-band green emitting nitridoalumosilicate BaLi$_2$[(Al$_2$Si$_2$)N$_6$]:Eu^{2+}. The title compounds exhibit an extremely small Stokes shift, resulting from the highly condensed rigid tetrahedral network. The small Stokes shift, the replacement of N by O atoms, and the prevention of inhomogeneous line broadening in contrast to Ba[Li$_2$(Al$_2$Si$_2$)N$_6$]:Eu^{2+} lead to an unprecedented ultra-narrow band blue emission (λ_{em} = 454–456 nm, *fwhm* ≈ 25 nm/1200 cm^{-1}). The decreased Stokes shift of *AE*Li$_2$[Be$_4$O$_6$]:Eu^{2+} compared to conventional blue emitting phosphors allows for using blue primary LEDs with λ_{em} < 440 nm in white RGB (red, green, blue) phosphor-converted LEDs. This new type of LED will have improved color point stability, enhanced color rendering, and excellent energy efficiency.

11 Appendix

11.1 Supporting Information for Chapter 2

Unprecedented Deep-Red Ce^{3+} Luminescence of the Nitridolithosilicates $Li_{38.7}RE_{3.3}Ca_{5.7}[Li_2Si_{30}N_{59}]O_2F$ (RE = La, Ce, Y)

Christian Maak, Philipp Strobel, Volker Weiler, Peter J. Schmidt, and Wolfgang Schnick

Chem. Mater. **2018**, *30,* 5500–5506

Table S1. Amounts of starting materials for the syntheses of $Li_{38.7}RE_{3.3}Ca_{5.7}[Li_2Si_{30}N_{59}]O_2F$ (RE = La, Ce, Y).

$Li_{38.7}La_{3.3}Ca_{5.7}[Li_2Si_{30}N_{59}]O_2F$	
LaF$_3$ (Sigma-Aldrich, 99.99%)	13.8 mg / 0.07 mmol
La$_2$O$_3$ (Chempur, 99.999%)	9.6 mg / 0.029 mmol
CaF$_2$ (Alfa Aesar, 99.99%)	17.4 mg / 0.223 mmol
Si$_3$N$_4$ (Ube Industries, amorphous, > 99%)	54.9 mg / 0.391 mmol
Li$_3$N (Alfa Aesar, 99.4%)	25.9 mg / 0.743 mmol
$Li_{38.7}Ce_{3.3}Ca_{5.7}[Li_2Si_{30}N_{59}]O_2F$	
CeF$_3$ (Sigma-Aldrich, 99.99%)	13.9 mg / 0.07 mmol
CeO$_2$ (Auer-Remy, 99.9%)	10.1 mg / 0.059 mmol
CaF$_2$ (Alfa Aesar, 99.99%)	17.4 mg / 0.223 mmol
Si$_3$N$_4$ (Ube Industries, amorphous, > 99%)	54.9 mg / 0.391 mmol
Li$_3$N (Alfa Aesar, 99.4%)	25.9 mg / 0.743 mmol
$Li_{38.7}Y_{3.3}Ca_{5.7}[Li_2Si_{30}N_{59}]O_2F$	
YF$_3$ (Chempur, 99.999%)	10.3 mg / 0.07 mmol
Y$_2$O$_3$ (Sigma-Aldrich, 99.999%)	6.6 mg / 0.029 mmol
CaF$_2$ (Alfa Aesar, 99.99%)	17.4 mg / 0.223 mmol
Si$_3$N$_4$ (Ube Industries, amorphous, > 99%)	54.9 mg / 0.391 mmol
Li$_3$N (Alfa Aesar, 99.4%)	25.9 mg / 0.743 mmol

Substitution of Ce^{3+} as activator into the host compounds $Li_{38.7}RE_{3.3}Ca_{5.7}[Li_2Si_{30}N_{59}]O_2F$ (RE = La, Y) was done by adding CeF$_3$ and simultaneously reducing the corresponding amounts of YF$_3$ and LaF$_3$, respectively.
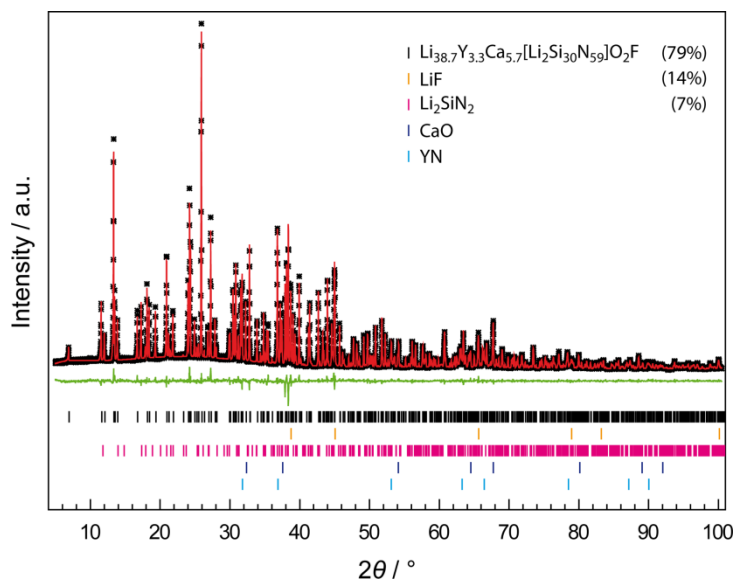
Figure S1. Rietveld refinement of data collected from a $Li_{38.7}Y_{3.3}Ca_{5.7}[Li_2Si_{30}N_{59}]O_2F$ sample (λ = 1.54056 Å). Experimental PXRD data as black stars, Rietveld fit red, difference plot green. Reflection positions of $Li_{38.7}Y_{3.3}Ca_{5.7}[Li_2Si_{30}N_{59}]O_2F$ as black bars. The sample contains LiF formed during the metathesis reaction (orange bars, 14 wt%), small amounts of Li_2SiN_2 (magenta bars, 7 wt%), and traces of CaO (blue bars) and YN (cyan bars).
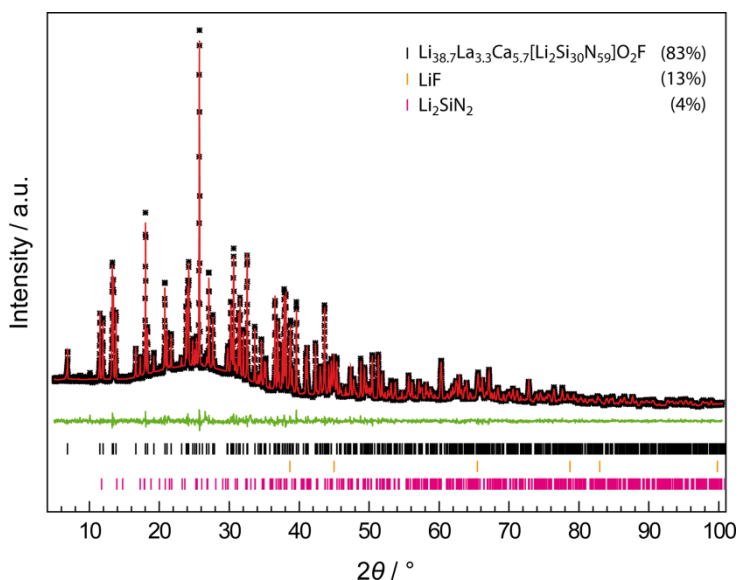
Figure S2. Rietveld refinement of data collected from a $Li_{38.7}La_{3.3}Ca_{5.7}[Li_2Si_{30}N_{59}]O_2F$ sample (λ = 1.54056 Å). Experimental PXRD data as black stars, Rietveld fit red, difference plot green. Reflection positions of $Li_{38.7}La_{3.3}Ca_{5.7}[Li_2Si_{30}N_{59}]O_2F$ as black bars. The sample contains LiF formed during the metathesis reaction (orange bars, 13 wt%), and small amounts of Li_2SiN_2 (magenta bars, 4 wt%).
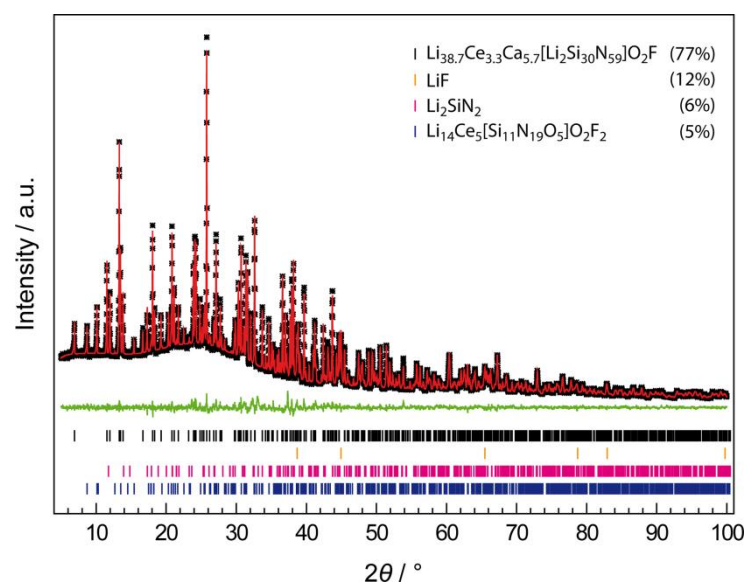
Figure S3. Rietveld refinement of data collected from a $Li_{38.7}Ce_{3.3}Ca_{5.7}[Li_2Si_{30}N_{59}]O_2F$ sample ($\lambda = 1.54056$ Å). Experimental PXRD data as black stars, Rietveld fit red, difference plot green. Reflection positions of $Li_{38.7}Ce_{3.3}Ca_{5.7}[Li_2Si_{30}N_{59}]O_2F$ as black bars. The sample contains LiF formed during the metathesis reaction (orange bars, 12 wt%), and small amounts of Li_2SiN_2 (magenta bars, 6 wt%), and $Li_{14}Ce_5[Si_{11}N_{19}O_5]O_2F_2$ (blue bars, 5 wt%).

Table S2. Data for Rietveld refinements of $Li_{38.7}RE_{3.3}Ca_{5.7}[Li_2Si_{30}N_{59}]O_2F$ (RE = La, Ce, Y) samples (least squares standard deviations in parentheses).

formula	RE = La	RE = Ce	RE = Y
formula mass / g·mol^{-1}	2691.98	2696.30	2524.61
crystal system		trigonal	
space group		$P3c1$ (no. 165)	
lattice parameters / Å	a = 14.7789(3), c = 15.3370(3)	a = 14.75380(11), c = 15.3132(2)	a = 14.64513(5), c = 15.21393(8)
volume / Å^3	2901.07(13)	2886.72(5)	2825.91(3)
formula units/cell		2	
X-ray density / g·cm^{-3}	3.082(2)	3.102(3)	2.9670(1)
diffractometer		Stoe StadiP	
radiation		Cu Kα_1 (λ = 1.54056 Å)	
monochromator		Ge(111)	
detector		MYTHEN 1K	
$F(000)$	2564	2575	2446
2θ range / °		5–100	
data points		6335	
observed reflections	1002	1000	978
number of parameters	97	108	40
constraints	4	4	0
restraints	3	3	0
software		TOPAS Academic V4.1	
structure refinement		Rietveld-Method	
background function		Shifted Chebyshev	
	24 polynomials	18 polynomials	12 polynomials
R_{wp}	0.0353	0.0361	0.0592
R_{exp}	0.0310	0.0282	0.0514
R_p	0.0277	0.0267	0.0458
R_{Bragg}	0.0108	0.0159	0.0305
χ^2	1.137	1.280	1.153

The refinements are based on the structure model of $Li_{38.7}Y_{3.3}Ca_{5.7}[Li_2Si_{30}N_{59}]O_2F$ obtained from single-crystal X-ray data. In the case of RE = Y, only lattice parameters were refined. In the case of RE = La, Ce also fractional atomic coordinates, site occupancy factors and isotropic displacement parameters for the sites $RE$1/Ca1 and $RE$2/Ca2 as well as fractional atomic coordinates of Si, N, and O/F sites were refined. Li sites were not refined. Isotropic displacement parameters for Si, N, O/F, and Li sites were taken from the single-crystal structure refinement of $Li_{38.7}Y_{3.3}Ca_{5.7}[Li_2Si_{30}N_{59}]O_2F$ (U_{eq} values from the single-crystal were converted to B_{iso} values according to $B = U\cdot8\pi^2$). Rietveld refinements for RE = La, Ce were performed with constrained isotropic displacement parameters for the sites $RE$1/Ca1 and $RE$2/Ca2, respectively. The site occupancy factors of the sites $RE$1/Ca1 and $RE$2/Ca2 were refined using the constraints occCa1 = 1−occ$RE$1 and occCa2 = 1−occ$RE$2.

Table S3. Results in atom% for 10 EDX point-measurements of 10 different $Li_{38.7}Y_{3.3}Ca_{5.7}[Li_2Si_{30}N_{59}]O_2F$ crystals.

	Y	Ca	Si	N	O	F
1	3.9	5.1	29.5	56.5	3.3	1.7
2	3.6	4.8	26.6	59.2	4.0	1.9
3	4.0	5.5	29.3	55.8	3.7	1.8
4	3.6	5.7	30.1	55.6	3.3	1.6
5	3.5	5.2	28.1	57.1	4.1	2.0
6	3.2	4.9	26.8	58.5	4.7	1.8
7	3.3	5.1	28.0	58.1	3.5	1.9
8	3.1	5.0	27.7	58.3	3.8	2.0
9	2.9	5.3	26.7	57.8	4.7	2.5
10	3.0	6.1	28.6	55.2	5.2	1.9
Average	3.4	5.3	28.1	57.2	4.0	1.9
Deviation	0.4	0.4	1.2	1.4	0.6	0.3
Theory	3.3	5.6	29.7	58.4	2.0	1.0
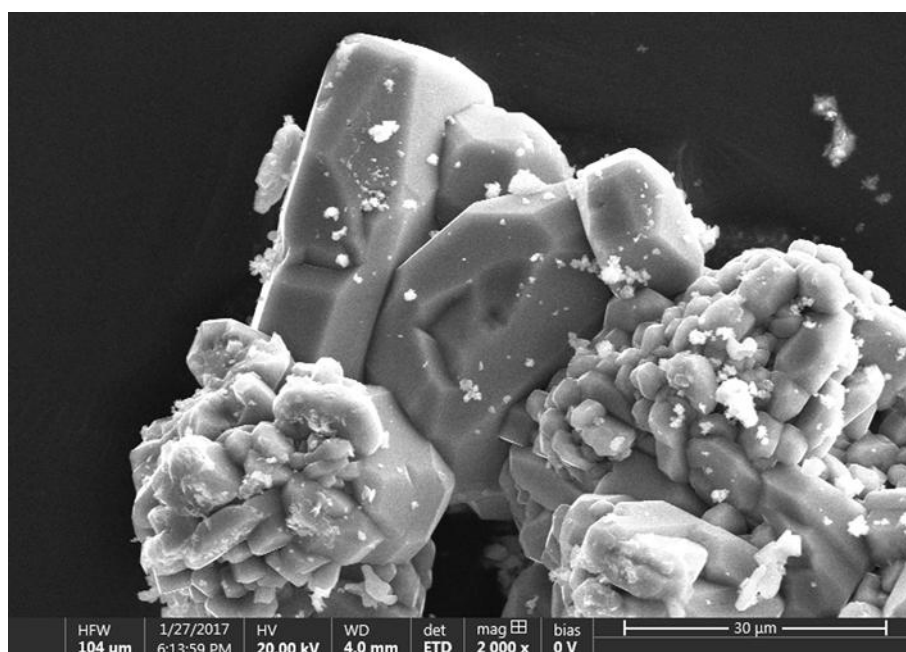
Figure S4. SEM image of $Li_{38.7}Y_{3.3}Ca_{5.7}[Li_2Si_{30}N_{59}]O_2F$ crystals.

Table S4. Results in atom% for 10 EDX point-measurements of 10 different $Li_{38.7}La_{3.3}Ca_{5.7}[Li_2Si_{30}N_{59}]O_2F$ crystals.

	La	Ca	Si	N	O	F
1	3.2	5.0	23.3	62.9	4.1	1.6
2	3.1	5.2	24.4	59.9	5.2	2.3
3	3.5	5.7	24.9	59.1	5.0	1.8
4	3.3	5.3	23.8	59.8	5.6	2.2
5	2.9	5.1	26.0	56.9	5.9	3.2
6	2.9	5.3	26.8	56.2	6.0	2.8
7	2.6	5.3	25.2	59.0	5.8	2.1
8	3.3	6.5	29.8	54.4	3.9	2.1
9	3.3	6.6	30.0	53.9	4.2	2.1
10	2.4	4.4	23.8	61.0	6.2	2.3
Average	3.1	5.4	25.8	58.3	5.2	2.2
Deviation	0.4	0.7	2.4	2.9	0.9	0.5
Theory	3.3	5.6	29.7	58.4	2.0	1.0
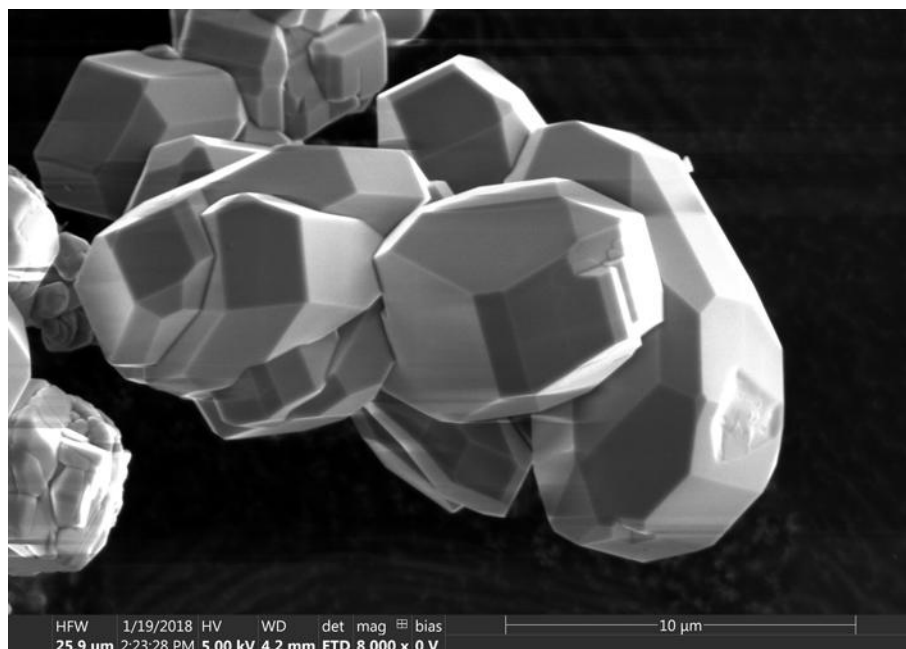
Figure S5. SEM image of $Li_{38.7}La_{3.3}Ca_{5.7}[Li_2Si_{30}N_{59}]O_2F$ crystals.

Table S5.   Results   in   atom%   for   10   EDX   point-measurements   of   10   different $Li_{38.7}Ce_{3.3}Ca_{5.7}[Li_2Si_{30}N_{59}]O_2F$ crystals.

	Ce	Ca	Si	N	O	F
1	2.35	4.5	23.66	61.64	7.07	0.78
2	2.63	4.52	23.75	63	5.21	0.9
3	2.66	4.54	24.24	62.13	5.7	0.75
4	2.65	4.6	24.07	62.15	5.78	0.74
5	3.32	5.46	28.08	57.17	4.68	1.29
6	3.27	5.51	27.93	56.6	5.03	1.66
7	1.97	4.08	21.89	65.14	6.01	0.91
8	3.29	5.49	28.08	56.02	5.47	1.66
9	4.01	5.7	29.99	54.1	4.15	2.05
10	4.27	6.18	29.85	53.24	4.59	1.88
Average	3.0	5.1	26.2	59.1	5.4	1.3
Deviation	0.7	0.7	2.9	4.2	0.8	0.5
Theory	3.3	5.6	29.7	58.4	2.0	1.0
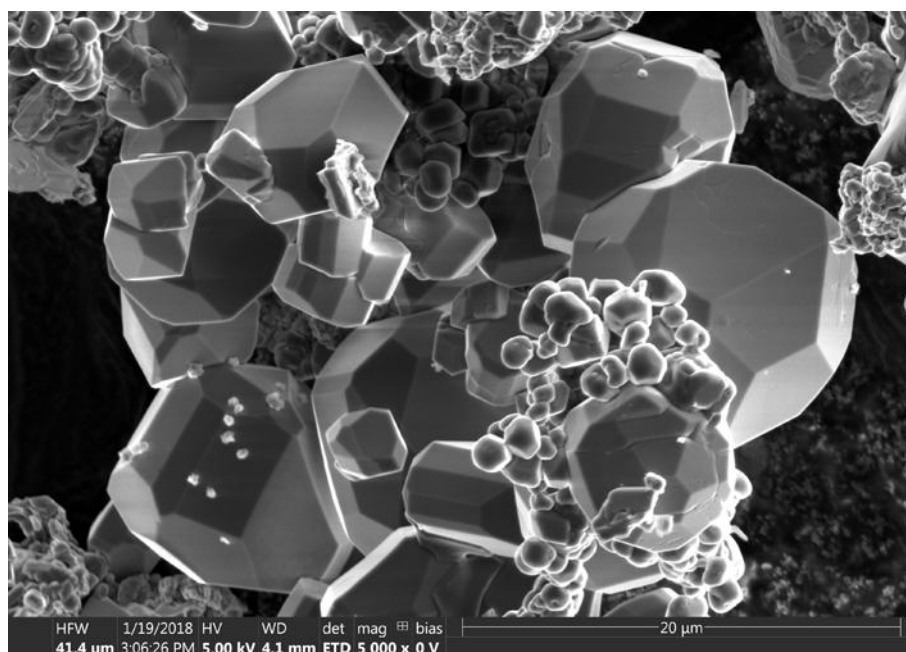
Figure S6. SEM image of $Li_{38.7}Ce_{3.3}Ca_{5.7}[Li_2Si_{30}N_{59}]O_2F$ crystals.

Table S6. Wyckoff positions, fractional atomic coordinates, isotropic displacement parameters [Å^2], and site occupancy factors of Li$_{38.7}$Y$_{3.3}$Ca$_{5.7}$[Li$_2$Si$_{30}$N$_{59}$]O$_2$F from single-crystal X-ray data (standard deviations in parentheses). Y1/Ca1, Y2/Ca2, and O1/F1 occupy the same site, respectively.

Atom	Wyckoff	x	y	z	U_{eq}	s.o.f
Y1	6f	0.30237(3)	x	1/4	0.00590(12)	0.846(5)
Ca1	6f	0.30237(3)	x	1/4	0.00590(12)	0.154(5)
Y2	12g	0.10966(4)	0.33444(4)	0.13334(3)	0.00894(15)	0.128(3)
Ca2	12g	0.10966(4)	0.33444(4)	0.13334(3)	0.00894(15)	0.872(3)
Si1	12g	0.46452(6)	0.69466(5)	0.25154(5)	0.00428(14)	1
Si2	12g	0.37885(6)	0.50419(5)	0.14510(5)	0.00453(14)	1
Si3	12g	0.33695(5)	0.31096(5)	0.05012(5)	0.00422(14)	1
Si4	12g	0.11504(6)	0.11899(6)	0.13898(5)	0.00485(14)	1
Si5	12g	0.29096(6)	0.45834(5)	0.95735(5)	0.00424(14)	1
Li1	4d	2/3	1/3	0.1011(7)	0.0182(19)	1
Li2	12g	0.4596(5)	0.0345(4)	0.1678(4)	0.0232(12)	1
Li3	12g	0.5040(4)	0.3464(4)	0.1407(4)	0.0140(10)	1
Li4	12g	0.1903(4)	0.5201(4)	0.0507(3)	0.0131(10)	1
Li5	4d	1/3	2/3	0.0942(6)	0.0110(16)	1
Li6	2b	0	0	0	0.015(2)	1
Li7	6e	1/2	0	0	0.0250(18)	1
Li8	6f	0.1433(5)	0	1/4	0.0119(13)	1
Li9	12g	0.2371(6)	0.0893(5)	0.0236(5)	0.040(2)	1
Li10	12g	0.328(2)	0.1127(12)	0.1611(11)	0.118(7)	0.95
N1	12g	0.3305(2)	0.36504(18)	0.95076(14)	0.0071(4)	1
N2	12g	0.3440(2)	0.54028(17)	0.04718(14)	0.0068(4)	1
N3	12g	0.4148(2)	0.41048(17)	0.12418(15)	0.0055(4)	1
N4	12g	0.2140(2)	0.23495(18)	0.09656(15)	0.0088(4)	1
N5	6f	0.1398(2)	x	1/4	0.0078(6)	1
N6	12g	0.4897(2)	0.61625(17)	0.18389(14)	0.0065(4)	1
N7	12g	0.5506(2)	0.82632(18)	0.22404(15)	0.0069(4)	1
N8	12g	0.1567(2)	0.39424(19)	0.97283(16)	0.0097(4)	1
N9	12g	0.1157(2)	0.00421(17)	0.10879(15)	0.0071(4)	1
N10	12g	0.4702(2)	0.67209(18)	0.36123(15)	0.0073(4)	1
N11	4d	1/3	2/3	0.2299(2)	0.0049(7)	1
O1	6f	0.2696(2)	0	1/4	0.0351(10)	2/3
F1	6f	0.2696(2)	0	1/4	0.0351(10)	1/3

Table S7. Anisotropic displacement parameters (U_{ij} in Å^2) of Li$_{38.7}$Y$_{3.3}$Ca$_{5.7}$[Li$_2$Si$_{30}$N$_{59}$]O$_2$F with standard deviations in parentheses. Y1/Ca1, Y2/Ca2, and O1/F1 were refined with equal atomic displacement parameters, respectively.

Atom	U_{11}	U_{22}	U_{33}	U_{23}	U_{13}	U_{12}
Y1	0.0052(2)	U_{11}	0.0057(2)	0.00065(7)	−0.00065(7)	0.0014(2)
Ca1	0.0052(2)	U_{11}	0.0057(2)	0.00065(7)	−0.00065(7)	0.0014(2)
Y2	0.0097(2)	0.0108(2)	0.0076(2)	−0.0000(2)	−0.0013(2)	0.0061(2)
Ca2	0.0097(2)	0.0108(2)	0.0076(2)	−0.0000(2)	−0.0013(2)	0.0061(2)
Si1	0.0046(3)	0.0039(3)	0.0045(3)	0.0003(2)	0.0001(2)	0.0022(3)
Si2	0.0045(3)	0.0042(3)	0.0053(3)	−0.0005(2)	0.0000(2)	0.0025(3)
Si3	0.0042(3)	0.0038(3)	0.0047(3)	0.0000(2)	0.0002(2)	0.0020(2)
Si4	0.0048(3)	0.0045(3)	0.0046(3)	−0.0003(2)	0.0005(2)	0.0018(3)
Si5	0.0046(3)	0.0040(3)	0.0045(3)	0.0003(2)	−0.0001(2)	0.0025(2)
Li1	0.013(3)	U_{11}	0.028(5)	0	0	0.0067(13)
Li2	0.026(3)	0.004(2)	0.036(3)	0.001(2)	−0.004(3)	0.006(2)
Li3	0.011(2)	0.017(2)	0.018(3)	0.003(2)	0.001(2)	0.010(2)
Li4	0.014(2)	0.013(2)	0.014(2)	−0.003(2)	−0.001(2)	0.008(2)
Li5	0.009(2)	U_{11}	0.014(4)	0	0	0.0047(12)
Li6	0.018(4)	U_{11}	0.007(5)	0	0	0.009(2)
Li7	0.019(4)	0.031(5)	0.026(4)	0.002(4)	−0.005(3)	0.013(4)
Li8	0.009(2)	0.012(3)	0.015(3)	−0.003(3)	−0.0016(13)	0.006(2)
Li9	0.041(4)	0.018(3)	0.047(4)	−0.006(3)	0.032(3)	0.003(3)
Li10	0.16(2)	0.081(9)	0.128(13)	0.038(9)	0.112(12)	0.075(10)
N1	0.0095(10)	0.0079(10)	0.0061(9)	0.0001(8)	0.0008(8)	0.0060(9)
N2	0.0091(10)	0.0059(10)	0.0068(10)	−0.0004(8)	−0.0018(8)	0.0048(8)
N3	0.0047(9)	0.0037(9)	0.0073(9)	−0.0007(8)	0.0001(8)	0.0015(8)
N4	0.0064(10)	0.0087(10)	0.0073(10)	0.0009(8)	0.0010(8)	0.0008(8)
N5	0.0081(10)	U_{11}	0.0056(14)	−0.0003(6)	0.0003(6)	0.0029(12)
N6	0.0047(9)	0.0058(10)	0.0079(10)	−0.0033(8)	−0.0001(8)	0.0018(8)
N7	0.0069(10)	0.0070(10)	0.0065(10)	0.0008(8)	0.0004(8)	0.0034(8)
N8	0.0039(10)	0.0114(11)	0.0132(11)	0.0019(9)	−0.0003(8)	0.0035(9)
N9	0.0072(10)	0.0065(10)	0.0078(10)	0.0003(8)	0.0014(8)	0.0035(8)
N10	0.0072(10)	0.0086(10)	0.0066(10)	−0.0017(8)	−0.0022(8)	0.0043(8)
N11	0.0051(10)	U_{11}	0.005(2)	0	0	0.0025(5)
O1	0.0213(11)	U_{11}	0.035(2)	−0.039(2)	−0.0197(9)	0.0313(13)
F1	0.0213(11)	U_{11}	0.035(2)	−0.039(2)	−0.0197(9)	0.0313(13)

Table S8. Wyckoff positions, fractional atomic coordinates, isotropic displacement parameters [Å^2], and site occupancy factors of Li$_{38.7}$La$_{3.3}$Ca$_{5.7}$[Li$_2$Si$_{30}$N$_{59}$]O$_2$F from Rietveld refinement on X-ray powder data (standard deviations in parentheses). La1/Ca1, La2/Ca2, and O1/F1 occupy the same site, respectively.

Atom	Wyckoff	x	y	z	U_{iso}	s.o.f
La1	6f	0.3018(2)	x	1/4	0.0065(9)	0.494(8)
Ca1	6f	0.3018(2)	x	1/4	0.0065(9)	0.506(8)
La2	12g	0.1103(2)	0.3336(2)	0.13441(14)	0.0089(8)	0.307(3)
Ca2	12g	0.1103(2)	0.3336(2)	0.13441(14)	0.0089(8)	0.693(3)
Si1	12g	0.4629(3)	0.6939(3)	0.2489(4)	0.0043	1
Si2	12g	0.3785(4)	0.5049(4)	0.1424(3)	0.0045	1
Si3	12g	0.3375(4)	0.3133(4)	0.0496(3)	0.0042	1
Si4	12g	0.1136(4)	0.1187(4)	0.1396(3)	0.0049	1
Si5	12g	0.2910(4)	0.4576(4)	0.9569(3)	0.0042	1
Li1	4d	2/3	1/3	0.1011	0.0182	1
Li2	12g	0.4596	0.0345	0.1678	0.0232	1
Li3	12g	0.504	0.3464	0.1407	0.014	1
Li4	12g	0.1903	0.5201	0.0507	0.0131	1
Li5	4d	1/3	2/3	0.0942	0.011	1
Li6	2b	0	0	0	0.015	1
Li7	6e	1/2	0	0	0.025	1
Li8	6f	0.1433	0	1/4	0.0119	1
Li9	12g	0.2371	0.0893	0.0236	0.04	1
Li10	12g	0.328	0.1127	0.1611	0.118	0.95
N1	12g	0.3293(9)	0.3630(9)	0.9506(7)	0.0071	1
N2	12g	0.3417(10)	0.5393(9)	0.0457(8)	0.0068	1
N3	12g	0.4129(8)	0.4135(8)	0.1208(7)	0.0055	1
N4	12g	0.2132(9)	0.2311(8)	0.0946(7)	0.0088	1
N5	6f	0.1425(10)	x	1/4	0.0078	1
N6	12g	0.4860(10)	0.6137(10)	0.1789(7)	0.0065	1
N7	12g	0.5477(9)	0.8232(9)	0.2246(8)	0.0069	1
N8	12g	0.1555(10)	0.3998(9)	0.9703(8)	0.0097	1
N9	12g	0.1135(9)	0.0048(13)	0.1105(8)	0.0071	1
N10	12g	0.4697(9)	0.6672(9)	0.3611(10)	0.0073	1
N11	4d	1/3	2/3	0.2362(14)	0.0049	1
O1	6f	0.2710(8)	0	1/4	0.0351	2/3
F1	6f	0.2710(8)	0	1/4	0.0351	1/3

Table S9. Wyckoff positions, fractional atomic coordinates, isotropic displacement parameters [Å^2], and site occupancy factors of $Li_{38.7}Ce_{3.3}Ca_{5.7}[Li_2Si_{30}N_{59}]O_2F$ from Rietveld refinement on X-ray powder data (standard deviations in parentheses). Ce1/Ca1, Ce2/Ca2, and O1/F1 occupy the same site, respectively.

Atom	Wyckoff	x	y	z	U_{iso}	s.o.f
Ce1	6f	0.30214(15)	x	1/4	0.0179(9)	0.668(10)
Ca1	6f	0.30214(15)	x	1/4	0.0179(9)	0.334(10)
Ce2	12g	0.1095(2)	0.3329(2)	0.13436(19)	0.0175(11)	0.221(3)
Ca2	12g	0.1095(2)	0.3329(2)	0.13436(19)	0.0175(11)	0.779(3)
Si1	12g	0.4620(3)	0.6937(4)	0.2491(5)	0.0043	1
Si2	12g	0.3784(4)	0.5060(4)	0.1417(4)	0.0045	1
Si3	12g	0.3366(4)	0.3116(4)	0.0496(3)	0.0042	1
Si4	12g	0.1114(5)	0.1164(4)	0.1391(3)	0.0049	1
Si5	12g	0.2917(5)	0.4569(4)	0.9569(4)	0.0042	1
Li1	4d	2/3	1/3	0.1011	0.0182	1
Li2	12g	0.4596	0.0345	0.1678	0.0232	1
Li3	12g	0.504	0.3464	0.1407	0.014	1
Li4	12g	0.1903	0.5201	0.0507	0.0131	1
Li5	4d	1/3	2/3	0.0942	0.011	1
Li6	2b	0	0	0	0.015	1
Li7	6e	1/2	0	0	0.025	1
Li8	6f	0.1433	0	1/4	0.0119	1
Li9	12g	0.2371	0.0893	0.0236	0.04	1
Li10	12g	0.328	0.1127	0.1611	0.118	0.95
N1	12g	0.3291(10)	0.3653(10)	0.9530(8)	0.0071	1
N2	12g	0.3423(12)	0.5382(10)	0.0437(9)	0.0068	1
N3	12g	0.4115(9)	0.4156(10)	0.1219(8)	0.0055	1
N4	12g	0.2102(10)	0.2282(9)	0.0964(8)	0.0088	1
N5	6f	0.1464(12)	x	1/4	0.0078	1
N6	12g	0.4890(12)	0.6173(11)	0.1790(8)	0.0065	1
N7	12g	0.5430(10)	0.8209(10)	0.2263(9)	0.0069	1
N8	12g	0.1556(11)	0.3966(10)	0.9760(10)	0.0097	1
N9	12g	0.1149(11)	0.0050(16)	0.1067(9)	0.0071	1
N10	12g	0.4728(10)	0.6707(11)	0.3597(11)	0.0073	1
N11	4d	1/3	2/3	0.2395(18)	0.0049	1
O1	6f	0.2718(9)	0	1/4	0.0351	2/3
F1	6f	0.2718(9)	0	1/4	0.0351	1/3

Table S10. *RE*/Ca−ligand distances in Li$_{38.7}$*RE*$_{3.3}$Ca$_{5.7}$[Li$_2$Si$_{30}$N$_{59}$]O$_2$F (*RE* = La, Ce, Y) in Å.

	RE = La	*RE* = Ce	*RE* = Y
RE/Ca1−N5	2.354(14)	2.30(2)	2.386(3)
RE/Ca1−N7	2.47(2)	2.51(2)	2.410(2)
RE/Ca1−N7	2.47(2)	2.51(2)	2.410(2)
RE/Ca1−N3	2.576(11)	2.560(13)	2.511(2)
RE/Ca1−N3	2.576(11)	2.560(13)	2.511(2)
RE/Ca1−N4	2.668(11)	2.661(12)	2.618(2)
RE/Ca1−N4	2.668(11)	2.661(12)	2.618(2)
RE/Ca2−O1/F1	2.270(7)	2.259(8)	2.265(1)
RE/Ca2−N1	2.47(2)	2.51(2)	2.451(2)
RE/Ca2−N7	2.58(2)	2.64(2)	2.567(2)
RE/Ca2−N8	2.662(12)	2.57(2)	2.576(2)
RE/Ca2−N6	2.64(2)	2.59(2)	2.584(2)
RE/Ca2−N4	2.698(14)	2.69(2)	2.651(2)
RE/Ca2−N9	2.90(2)	2.88(2)	2.858(2)
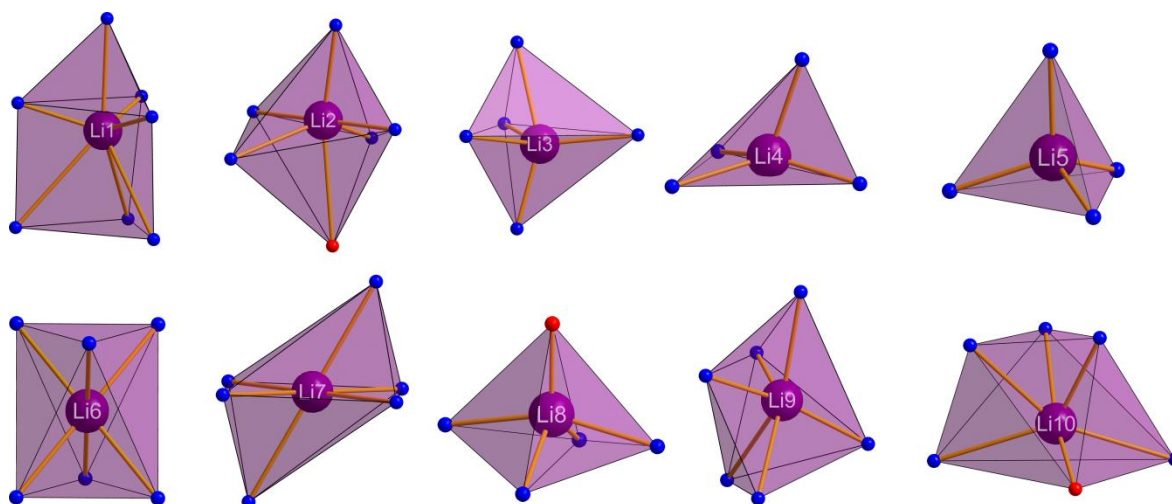
Figure S7. Coordination spheres of the Li sites in Li$_{38.7}$*RE*$_{3.3}$Ca$_{5.7}$[Li$_2$Si$_{30}$N$_{59}$]O$_2$F (*RE* = La, Ce, Y). Due to its regular tetrahedral coordination, Li5 is listed as cation with contribution to the network structure.

Table S11. Results of charge distribution (CHARDI) calculations for cation sites in $Li_{38.7}RE_{3.3}Ca_{5.7}[Li_2Si_{30}N_{59}]O_2F$ (RE = La, Ce, Y). CHARDI calculations were performed with VESTA according to the theory of Hoppe et al.[1,2]

Atom	RE = La	RE = Ce	RE = Y
RE/Ca1	2.58	2.75	2.87
RE/Ca2	2.11	1.97	1.92
Si1	4.09	4.17	4.14
Si2	4.03	4.03	4.05
Si3	3.96	3.91	3.94
Si4	4.34	4.35	4.31
Si5	4.07	4.02	4.01
Li1	0.94	1.05	0.99
Li2	0.99	1.01	0.99
Li3	1.01	1.02	0.98
Li4	1.03	1.04	1.03
Li5	1.02	1.01	1.05
Li6	1.12	1.11	1.15
Li7	0.94	0.92	0.96
Li8	0.93	0.88	0.88
Li9	1.07	1.06	1.06
Li10	0.71	0.63	0.67

Table S12. Results of MAPLE calculations (all values in kJ/mol) for $Li_{38.7}RE_{3.3}Ca_{5.7}[Li_2Si_{30}N_{59}]O_2F$ (RE = La, Ce, Y). Partial MAPLE values, total MAPLE values and deviation to sums of total MAPLE values of binary ionic compounds, forming $Li_{38.7}RE_{3.3}Ca_{5.7}[Li_2Si_{30}N_{59}]O_2F$ (RE = La, Ce, Y) in hypothetical reactions (structural data from references 3–8).

$Li_{38.7}La_{3.3}Ca_{5.7}[Li_2Si_{30}N_{59}]O_2F$

$La1^{3+}/Ca1^{2+}$ (49.4%/50.6%)	$La2^{3+}/Ca2^{2+}$ (30.7%/69.3%)	Si^{4+}	Li^+	$O^{2-}/F^{-[0]}$ (2/3 / 1/3)	$N^{[2]3-}$	$N^{[3]3-}$	**total MAPLE**
2944	2489	9448– 9834	470– 752	1523	5371– 5768	6079	**670360**

3.3 $LaN^{[3]}$ + 2 $CaO^{[4]}$ + 10 α-$Si_3N_4^{[5]}$ + 3.7 $CaF_2^{[6]}$ + 15.7 $Li_3N^{[7]}$ − 6.4 $LiF^{[8]}$

3.3·8244 + 2·4064 + 10·53023 + 3.7·2959 + 15.7·6346 − 6.4·1199	**668470**
	Δ = 0.28%

$Li_{38.7}Ce_{3.3}Ca_{5.7}[Li_2Si_{30}N_{59}]O_2F$

$Ce1^{3+}/Ca1^{2+}$ (66.8%/33.4%)	$Ce2^{3+}/Ca2^{2+}$ (22.1%/77.9%)	Si^{4+}	Li^+	$O^{2-}/F^{-[0]}$ (2/3 / 1/3)	$N^{[2]3-}$	$N^{[3]3-}$	**total MAPLE**
3238	2359	9444– 9865	472– 777	1508	5360– 5815	6084	**671594**

3.3 $CeN^{[3]}$ + 2 $CaO^{[4]}$ + 10 α-$Si_3N_4^{[5]}$ + 3.7 $CaF_2^{[6]}$ + 15.7 $Li_3N^{[7]}$ − 6.4 $LiF^{[8]}$

3.3·8703 + 2·4064 + 10·53023 + 3.7·2959 + 15.7·6346 − 6.4·1199	**669982**
	Δ = 0.24%

$Li_{38.7}Y_{3.3}Ca_{5.7}[Li_2Si_{30}N_{59}]O_2F$

$Y1^{3+}/Ca1^{2+}$ (84.6%/15.4%)	$Y2^{3+}/Ca2^{2+}$ (12.8%/87.2%)	Si^{4+}	Li^+	$O^{2-}/F^{-[0]}$ (2/3 / 1/3)	$N^{[2]3-}$	$N^{[3]3-}$	**total MAPLE**
3650	2211	9610– 9912	480– 780	1472	5386– 5861	6128	**675163**

3.3 $YN^{[3]}$ + 2 $CaO^{[4]}$ + 10 α-$Si_3N_4^{[5]}$ + 3.7 $CaF_2^{[6]}$ + 15.7 $Li_3N^{[7]}$ − 6.4 $LiF^{[8]}$

3.3·8990 + 2·4064 + 10·53023 + 3.7·2959 + 15.7·6346 − 6.4·1199	**670932**
	Δ = 0.63%

Typical MAPLE values in nitridosilicates (in kJ/mol):[9,10]
RE^{3+}: 3500–5100; Ca^{2+}: 1700–2200; Si^{4+}: 9000–10200; Li^+: 500–800; $O^{[1]2-}$: 2000–2800;
$N^{[2]3-}$: 4600–6000; $N^{[3]3-}$: 5000–6200

Lattice energy calculations using the MAPLE concept were carried out to support the experimental data and the assignment of Li, N and O/F atoms.[9–14] Partial MAPLE values were calculated for each site and compared to typical (empirical) partial MAPLE values.[9,10] All partial MAPLE values (Table S12) are in the reported typical ranges (below Table S12).[9,10] Furthermore, total MAPLE values for the whole crystal structures were compared to sums of total MAPLE values of binary ionic compounds, forming $Li_{38.7}RE_{3.3}Ca_{5.7}[Li_2Si_{30}N_{59}]O_2F$ (RE = Y, La, Ce) in hypothetical reactions (Table S12). These total MAPLE values should be equal or within a deviation of < 1%.[9] Therefore, the small deviations between 0.24% (RE = Ce) and 0.63% (RE = Y) demonstrate the electrostatic consistency of the structure models refined from X-ray diffraction data.

Table S13. Results of bond valence sum (BVS) calculations for $Li_{38.7}RE_{3.3}Ca_{5.7}[Li_2Si_{30}N_{59}]O_2F$ (RE = La, Ce, Y). Calculations were performed with VaList.[15]

Atom	RE = La	RE = Ce	RE = Y
RE/Ca1	2.96	2.73	2.98
RE/Ca2	2.30	2.14	2.29
Si1	3.75	4.02	3.87
Si2	3.92	3.94	3.81
Si3	3.99	3.83	4.00
Si4	3.92	3.91	3.89
Si5	3.83	4.037	3.97
Li1	1.00	0.97	1.08
Li2	0.92	0.92	0.96
Li3	1.00	0.94	1.06
Li4	1.24	1.25	1.21
Li5	1.14	1.06	1.25
Li6	0.82	0.89	0.83
Li7	0.72	0.72	0.70
Li8	1.24	1.15	1.32
Li9	0.92	0.99	1.00
Li10	0.63	0.63	0.67
N1	−2.97	−3.07	−2.98
N2	−2.98	−3.05	−3.00
N3	−3.10	−3.07	−3.05
N4	−2.87	−2.82	−2.95
N5	−3.19	−3.06	−3.18
N6	−2.92	−2.86	−2.90
N7	−2.84	−2.83	−2.88
N8	−2.97	−2.97	−3.11
N9	−2.75	−2.76	−2.72
N10	−2.75	−2.80	−2.97
N11	−3.16	−3.31	−3.03
O1/F1	−1.76	−1.67	−1.67
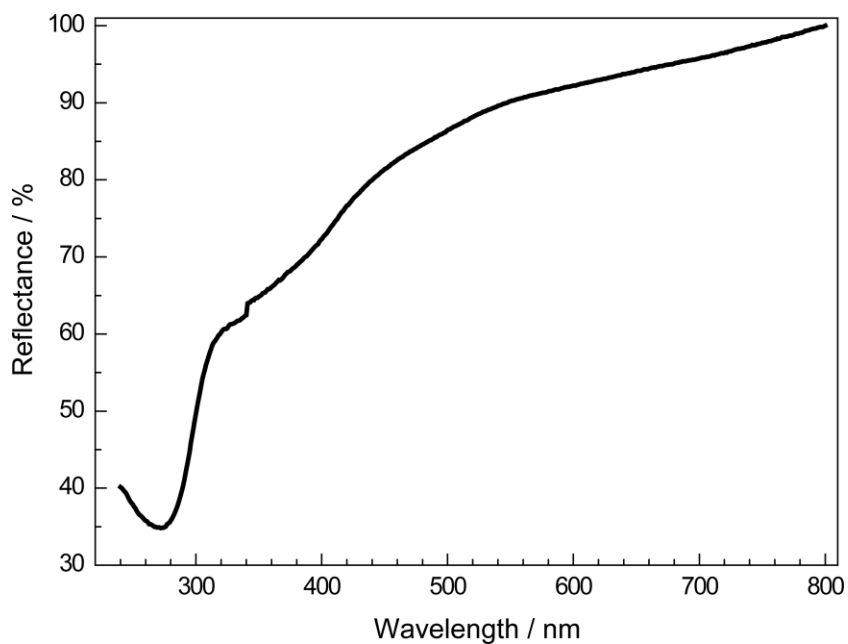
Figure S8. Diffuse reflectance UV/Vis spectrum of a nondoped $Li_{38.7}La_{3.3}Ca_{5.7}[Li_2Si_{30}N_{59}]O_2F$ powder sample. The artifact around 340 nm corresponds to the lamp switch.
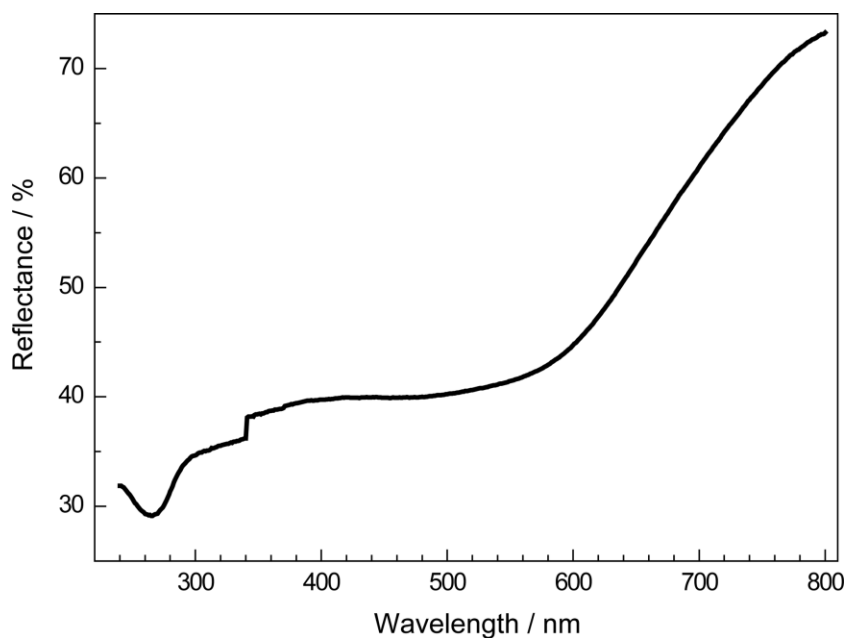
Figure S9. Diffuse reflectance UV/Vis spectrum of a nondoped $Li_{38.7}Y_{3.3}Ca_{5.7}[Li_2Si_{30}N_{59}]O_2F$ powder sample. The artifact around 340 nm corresponds to the lamp switch.
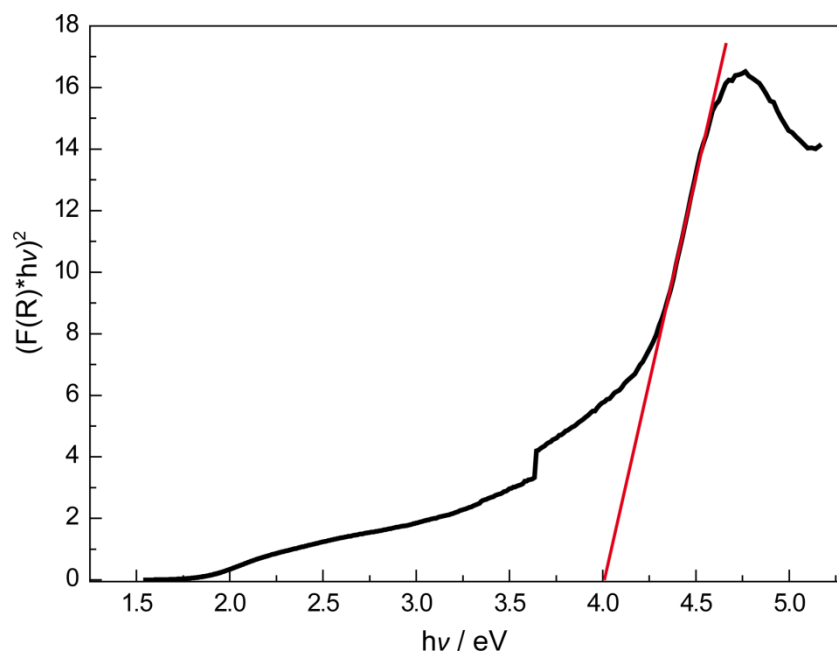
Figure S10. Tauc plot ($n = 1/2$) for the nondoped $Li_{38.7}Y_{3.3}Ca_{5.7}[Li_2Si_{30}N_{59}]O_2F$ powder sample.
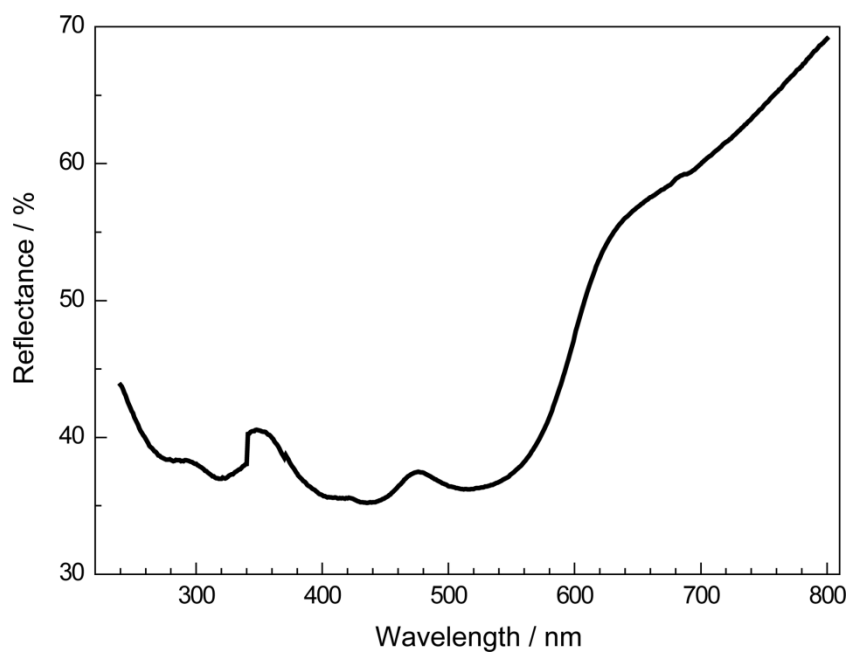
Figure S11. Diffuse reflectance UV/Vis spectrum of a $Li_{38.7}Ce_{3.3}Ca_{5.7}[Li_2Si_{30}N_{59}]O_2F$ powder sample. The compound shows strong absorption in the visible to blue range with absorption bands around 530 nm and 420 nm. The artifact around 340 nm corresponds to the lamp switch.
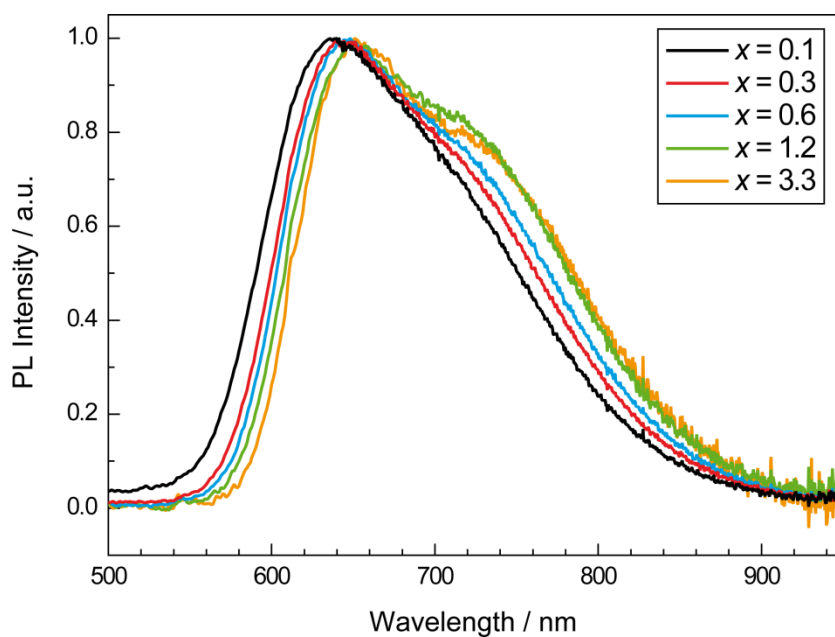
Figure S12. Emission spectra of $Li_{38.7}La_{3.3−x}Ce_xCa_{5.7}[Li_2Si_{30}N_{59}]O_2F$ (x = 0.1–3.3).

Table S14. Emission wavelength (λ_{em}), full width at half-maximum (*fwhm*) and color coordinates (CIE) of $Li_{38.7}La_{3.3−x}Ce_xCa_{5.7}[Li_2Si_{30}N_{59}]O_2F$ (x = 0.1–3.3).

x	λ_{em} [nm]	*fwhm* [nm / cm^{-1}]	color coordinates (CIE)
0.1	638	156 / 3540	x = 0.62, y = 0.37
0.3	643	162 / 3543	x = 0.65, y = 0.35
0.6	647	167 / 3600	x = 0.66, y = 0.34
1.2	650	173 / 3642	x = 0.66, y = 0.33
3.3	651	175 / 3650	x = 0.67, y = 0.32
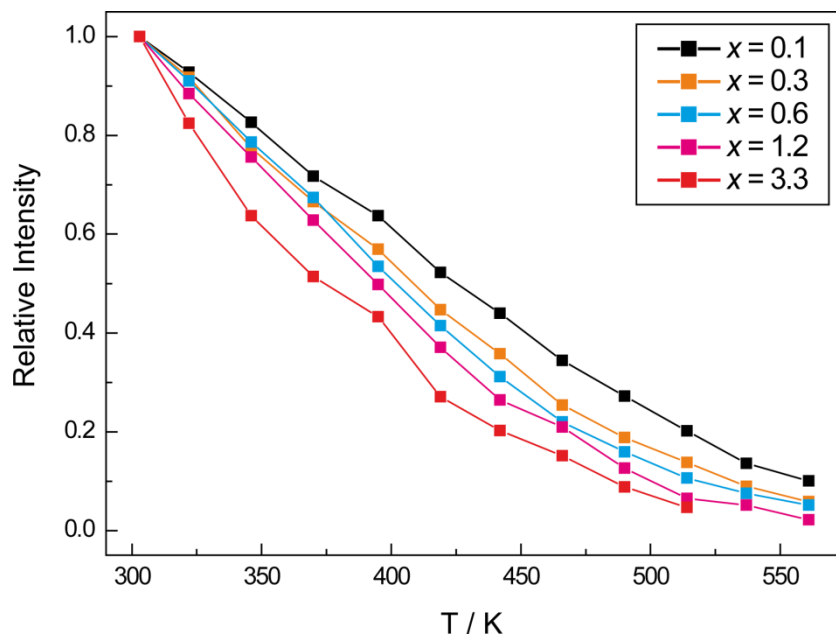
Figure S13.   Temperature   dependent   integrated   luminescence   intensities   of $Li_{38.7}La_{3.3-x}Ce_xCa_{5.7}[Li_2Si_{30}N_{59}]O_2F$.

Table S15. Amounts of starting materials for the syntheses of $Li_{38.7}Y_{3.3}Sr_{5.7}[Li_2Si_{30}N_{59}]O_2F:Ce^{3+}$ and $Li_{38.7}Lu_{3.3}Ca_{5.7}[Li_2Si_{30}N_{59}]O_2F:Ce^{3+}$ (nominal stoichiometries).

$Li_{38.7}Y_{3.3}Sr_{5.7}[Li_2Si_{30}N_{59}]O_2F:Ce^{3+}$	
YF_3 (Chempur, 99.999%)	10.3 mg / 0.070 mmol
Y_2O_3 (Sigma-Aldrich, 99.999%)	6.6 mg / 0.029 mmol
SrF_2 (Alfa Aesar, 99.99%)	30.0 mg / 0.223 mmol
Si_3N_4 (Ube Industries, amorphous, > 99%)	54.9 mg / 0.391 mmol
Li_3N (Alfa Aesar, 99.4%)	25.9 mg / 0.743 mmol
CeF_3 (Sigma-Aldrich, 99.99%)	0.8 mg / 0.004 mmol
$Li_{38.7}Lu_{3.3}Ca_{5.7}[Li_2Si_{30}N_{59}]O_2F:Ce^{3+}$	
LuF_3 (Chempur, 99.9%)	16.3 mg / 0.070 mmol
Lu_2O_3 (Chempur, 99.99%)	11.7 mg / 0.029 mmol
CaF_2 (Alfa Aesar, 99.99%)	17.4 mg / 0.223 mmol
Si_3N_4 (Ube Industries, amorphous, > 99%)	54.9 mg / 0.391 mmol
Li_3N (Alfa Aesar, 99.4%)	25.9 mg / 0.743 mmol
CeF_3 (Sigma-Aldrich, 99.99%)	0.8 mg / 0.004 mmol

Figure S14. Rietveld refinement of data collected from a $Li_{38.7}Y_{3.3}Sr_{5.7}[Li_2Si_{30}N_{59}]O_2F$ sample (λ = 1.54056 Å). Experimental PXRD data as black stars, Rietveld fit red, difference plot green. Reflection positions of $Li_{38.7}Y_{3.3}Sr_{5.7}[Li_2Si_{30}N_{59}]O_2F$ as black bars. The sample also contains Li_2SiN_2 (orange bars, 15 wt%), LiF (magenta bars, 14 wt%), $Li_2SrSi_2N_4$ (blue bars, 8 wt%), and YN (green bars, 2 wt%).
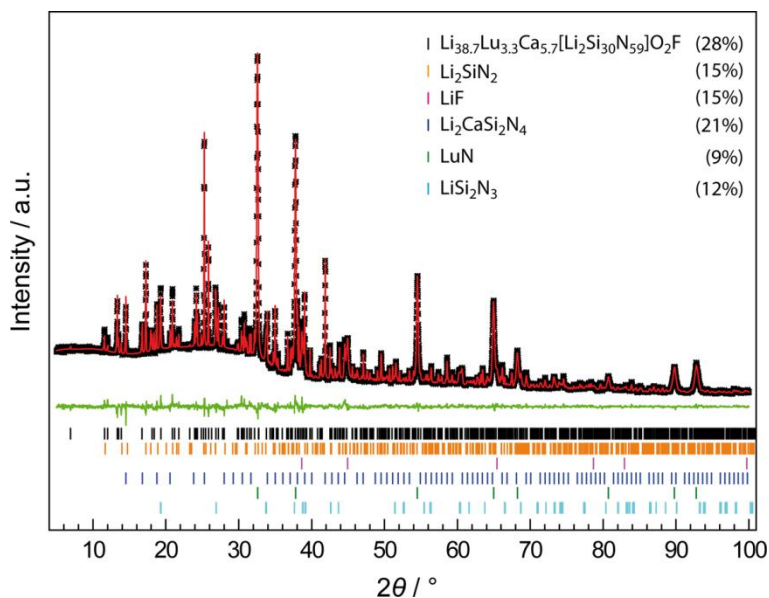
Figure S15. Rietveld refinement of data collected from a $Li_{38.7}Lu_{3.3}Ca_{5.7}[Li_2Si_{30}N_{59}]O_2F$ sample (λ = 1.54056 Å). Experimental PXRD data as black stars, Rietveld fit red, difference plot green. Reflection positions of $Li_{38.7}Lu_{3.3}Ca_{5.7}[Li_2Si_{30}N_{59}]O_2F$ as black bars. The sample also contains Li_2SiN_2 (orange bars, 15 wt%), LiF (magenta bars, 15 wt%), $Li_2CaSi_2N_4$ (blue bars, 21 wt%), LuN (green bars, 9 wt%), and $LiSi_2N_3$ (cyan bars, 12 wt%).

Table S16. Data of Rietveld refinements for $Li_{38.7}Y_{3.3}Sr_{5.7}[Li_2Si_{30}N_{59}]O_2F$ and $Li_{38.7}Lu_{3.3}Ca_{5.7}[Li_2Si_{30}N_{59}]O_2F$ with least squares standard deviations in parentheses. The structure model obtained from single-crystal X-ray data of $Li_{38.7}Y_{3.3}Ca_{5.7}[Li_2Si_{30}N_{59}]O_2F$ was used for both refinements. Only lattice parameters were refined.

	RE = Y, AE = Sr	RE = Lu, AE = Ca
crystal system	trigonal	
space group	$P3c1$ (no. 165)	
lattice parameters / Å	a = 14.75557(11) c = 15.3370(2)	a = 14.71626(14) c = 15.2684(3)
volume / Å^3	2891.90(5)	2863.64(7)
formula units / cell	2	
X-ray density / g·cm^{-3}	3.21012(6)	3.25772(13)
diffractometer, detector	Stoe StadiP, MYTHEN 1K	
radiation	Cu Kα_1 (λ = 1.54056 Å)	
monochromator	Ge(111)	
2θ range / °	5–75	5–100
data points	4690	6334
observed reflections	516	1008
number of parameters	50	66
software	TOPAS Academic V4.1	
structure refinement	Rietveld-Method	
background function	Shifted Chebyshev	
	18 polynomials	
R_{wp}	0.0793	0.0333
R_{exp}	0.0600	0.0251
R_p	0.0562	0.0251
R_{Bragg}	0.0294	0.0245
χ^2	1.322	1.329

Table S17. Results of EDX point-measurements in atom% for the $Li_{38.7}Y_{3.3}Sr_{5.7}[Li_2Si_{30}N_{59}]O_2F:Ce^{3+}$ and $Li_{38.7}Lu_{3.3}Ca_{5.7}[Li_2Si_{30}N_{59}]O_2F:Ce^{3+}$ particles used for luminescence measurements. The small amounts of the dopant Ce^{3+} were not detected.

	RE	*AE*	Si	N	O	F

	RE	*AE*	Si	N	O	F
$Li_{38.7}Y_{3.3}Sr_{5.7}[Li_2Si_{30}N_{59}]O_2F$						
1	4.2	5.0	27.2	54.6	6.5	1.9
2	3.9	5.1	26.0	55.8	6.9	2.3
3	4.0	5.3	26.0	54.6	7.9	2.3
Average	4.0	5.2	26.4	55.0	7.1	2.1
Theory	3.3	5.6	29.7	58.4	2.0	1.0
$Li_{38.7}Lu_{3.3}Ca_{5.7}[Li_2Si_{30}N_{59}]O_2F$						
1	4.23	4.29	20.41	62.35	6.82	1.45
2	2.45	6.38	24.02	49.73	15.41	1.98
3	1.86	4.91	20.22	63.39	7.81	1.82
Average	2.8	5.2	21.6	58.5	10.0	1.8
Theory	3.3	5.6	29.7	58.4	2.0	1.0

References

[1]   Momma, K.; Izumi, F. VESTA 3 for Three-Dimensional Visualization of Crystal, Volumetric and Morphology Data. *J. Appl. Crystallogr.* **2011**, *44*, 1272–1276.

[2]   Hoppe, R.; Voigt, S.; Glaum, H.; Kissel, J.; Müller, H. P.; Bernet, K. A new route to charge distributions in ionic solids. *J. Less-Common Met.* **1989**, *156*, 105–122.

[3]   Brown, R. C.; Clark, N. J. Composition limits and vaporization of rare earth nitrides. *J. Inorg. Nucl. Chem.* **1974**, *36*, 2507–2514.

[4]   Ghebouli, M. A.; Ghebouli, B.; Bouhemadou, A.; Fatmi, M.; Bouamama, K. Structural, electronic, optical and thermodynamic properties of $Sr_xCa_{1-x}O$, $Ba_xSr_{1-x}O$ and $Ba_xCa_{1-x}O$ alloys. *J. Alloys Compd.* **2011**, *509*, 1440–1447.

[5]   Yang, P.; Fun, H.-K.; Rahman, I. A.; Saleh, M. I. Two phase refinements of the structures of $α$-Si_3N_4 and $β$-Si_3N_4 made from rice husk by Rietveld analysis. *Ceram. Int.* **1995**, *21*, 137–142.

[6]   Batchelder, D. N.; Simmons, R. O. Lattice Constants and Thermal Expansivities of Silicon and of Calcium Fluoride between 6° and 322°K. *J. Chem. Phys.* **1964**, *41*, 2324–2329.

[7]   Huq, A.; Richardson, J. W.; Maxey, E. R.; Chandra, D.; Chien, W.-W. Structural studies of Li_3N using neutron powder diffraction. *J. Alloys Compd.* **2007**, *436*, 256–260.

[8]   Debye, P.; Scherrer, P. Crystal structure of lithium halides. *Phys. Z.* **1916**, *17*, 277–283.

[9]   Zeuner, M.; Pagano, S.; Schnick, W. Nitridosilicates and Oxonitridosilicates: From Ceramic Materials to Structural and Functional Diversity. *Angew. Chem., Int. Ed.* **2011**, *50*, 7754–7775; Nitridosilicate und Oxonitridosilicate: von keramischen Materialien zu struktureller und funktioneller Diversität. *Angew. Chem.* **2011**, *123*, 7898–7920.

[10]   Zeuner, M.; Pagano, S.; Schnick, W. Single-Crystal Structure Determination and Solid-State NMR Investigations of Lithium Nitridosilicate Li_2SiN_2 Synthesized by a Precursor Approach Employing Amorphous "$Si(CN_2)_2$". *Eur. J. Inorg. Chem.* **2009**, 1579–1584.

[11]   Shannon, R. D. Revised effective ionic radii and systematic studies of interatomic distances in halides and chalcogenides. *Acta Crystallogr., Sect A: Found. Crystallogr.* **1976**, *32*, 751–767.

[12]   Hoppe, R. Madelung constants. *Angew. Chem., Int. Ed. Engl.* **1966**, *5*, 95–106; Über Madelungfaktoren. *Angew. Chem.* **1966**, *78*, 52–63.

[13]   Hoppe, R. The Coordination Number – an "Inorganic Chameleon". *Angew. Chem., Int. Ed. Engl.* **1970**, *9*, 25–34; Die Koordinationszahl – ein „anorganisches Chamäleon". *Angew. Chem.* **1970**, *82*, 7–16.

[14]   Hübenthal, R. *Maple, Program for the Calculation of MAPLE values, version 4*; University of Gießen: Gießen, Germany, 1993.

[15]   Wills, A. S. *VaList*, Program available from www.ccp14.ac.uk, 2011.

11.2 Supporting Information for Chapter 3

Narrow-Band Yellow-Orange Emitting La$_{3-x}$Ca$_{1.5x}$Si$_6$N$_{11}$:Eu^{2+} ($x \approx 0.77$): A Promising Phosphor for Next-Generation Amber pcLEDs

Christian Maak, Dajana Durach, Christoph Martiny, Peter J. Schmidt, and Wolfgang Schnick

Chem. Mater. **2018**, *30*, 3552–3558
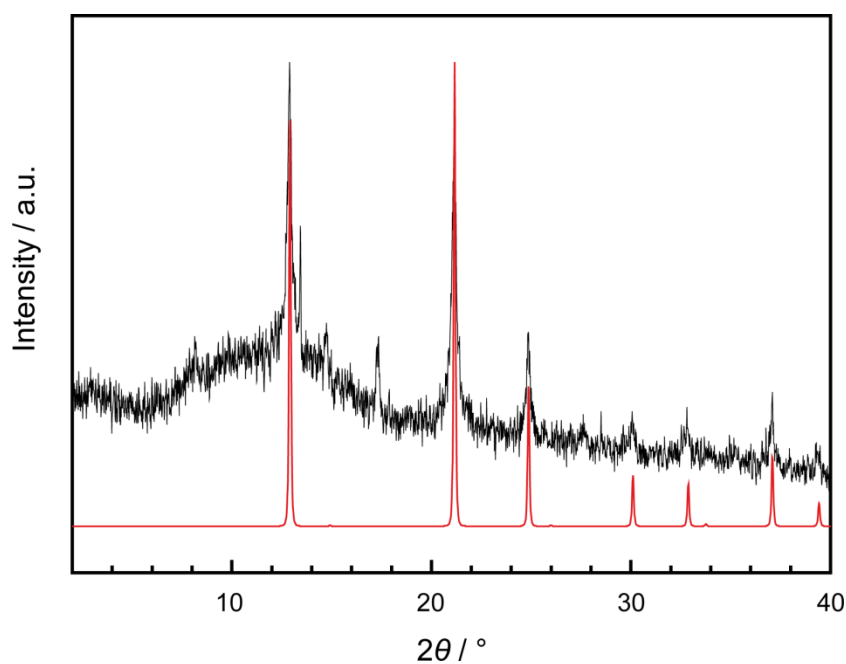
Figure S1. Experimental PXRD data (black, Mo Kα_1 radiation, Ge(111) monochromator, Mythen1K detector) of colorless powder deposited on the silica glass reactor wall during the reaction and simulated PXRD pattern of CaF$_2$ (red).

Table S1. Results in atom% from 15 EDX point-measurements of 15 different crystals.

	La	Ca	Si	N	La/Ca
1	9.2	4.8	27.2	58.6	1.9
2	12.4	7.0	30.5	50.0	1.8
3	14.2	7.1	32.3	46.4	2.0
4	10.4	5.3	29.6	54.7	2.0
5	11.6	5.6	30.9	51.8	2.1
6	10.5	5.2	29.2	55.1	2.0
7	8.6	4.4	25.7	61.3	2.0
8	10.2	5.5	29.0	55.3	1.9
9	9.1	5.2	27.6	58.1	1.8
10	12.3	7.2	31.5	49.1	1.7
11	12.2	6.5	30.4	50.9	1.9
12	11.9	5.4	30.1	52.5	2.2
13	12.1	5.5	30.2	52.3	2.2
14	12.9	6.0	31.2	49.9	2.2
15	9.4	5.3	26.8	58.6	1.8
Average	11.1	5.7	29.5	53.6	
Deviation	1.6	0.8	1.9	4.2	
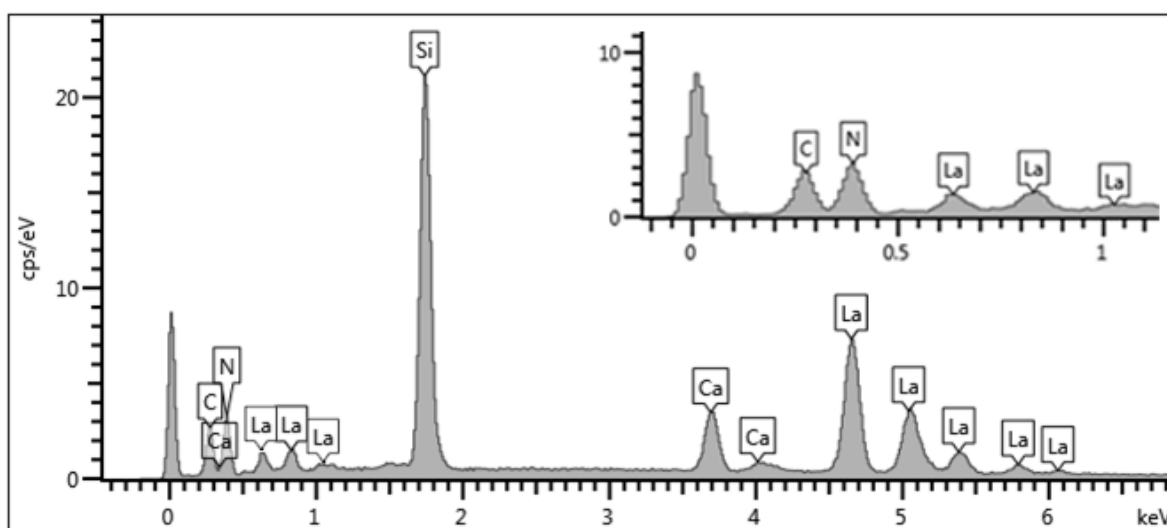
Figure S2. Exemplary EDX spectrum measured on a $La_{3-x}Ca_{1.5x}Si_6N_{11}$:$Eu^{2+}$ ($x \approx 0.77$) crystal. The carbon peak originates from the carbon coating as well as the carbon pad on which the crystals were mounted. The magnified region from 0–1 keV illustrates that no significant amounts of O (0.525 keV) and no F (0.677 keV) were detected.
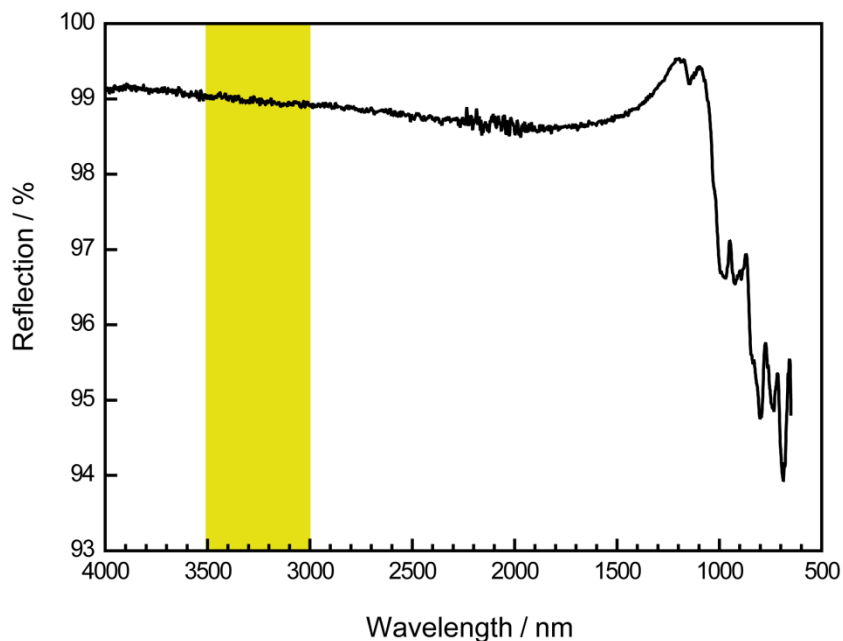
Figure S3. ATR-FTIR spectrum of a $La_{3-x}Ca_{1.5x}Si_6N_{11}$:Eu^{2+} ($x \approx 0.77$) powder sample. Typical region for N–H vibrations colored yellow.

Table S2. Atomic coordinates, isotropic displacement parameters [Å^2], and site occupancy factors of $La_{2.23}Ca_{1.16}Si_6N_{11}$ with standard deviations in parentheses. La1A/Ca1A, La1B/Ca1B, and La2/Ca2 occupy the same site, respectively.

Atom	Wyckoff	x	y	z	U_{eq}	s.o.f
La1A	4c	0.17982(2)	x + 1/2	0.97421(11)	0.01044(12)	0.585(3)
Ca1A	4c	0.17982(2)	x + 1/2	0.97421(11)	0.01044(12)	0.268(5)
La1B	4c	0.1746(3)	x + 1/2	0.8006(11)	0.01044(12)	0.035(2)
Ca1B	4c	0.1746(3)	x + 1/2	0.8006(11)	0.01044(12)	0.113(5)
La2	2a	0	0	0.00000(8)	0.00487(10)	0.974(4)
Ca2	2a	0	0	0.00000(8)	0.00487(10)	0.026(4)
Ca3	4c	0.0709(3)	x + 1/2	0.4331(9)	0.0064(9)	0.196(2)
Si1	8d	0.07979(8)	0.20816(8)	0.4637(2)	0.0050(2)	1
Si2	4c	0.61880(8)	x − 1/2	0.9546(3)	0.0044(2)	1
N1	8d	0.0751(3)	0.2318(3)	0.8128(6)	0.0064(5)	1
N2	8d	0.1805(3)	0.0800(3)	0.3570(6)	0.0073(5)	1
N3	4c	0.6505(3)	x − 1/2	0.3043(8)	0.0042(6)	1
N4	2b	1/2	0	0.928(2)	0.0179(14)	1

Table S3. Anisotropic displacement parameters (U_{iy} in Å^2) of La$_{2.23}$Ca$_{1.16}$Si$_6$N$_{11}$ with standard deviations in parentheses. La1A/Ca1A and La1B/Ca1B were refined with equal atomic displacement parameters. La2/Ca2 were refined with equal atomic displacement parameters.

Atom	U_{11}	U_{22}	U_{33}	U_{23}	U_{13}	U_{12}
La1A	0.00492(12)	U_{11}	0.0215(2)	0.00103(13)	U_{23}	−0.00069(9)
Ca1A	0.00492(12)	U_{11}	0.0215(2)	0.00103(13)	U_{23}	−0.00069(9)
La1B	0.00492(12)	U_{11}	0.0215(2)	0.00103(13)	U_{23}	−0.00069(9)
Ca1B	0.00492(12)	U_{11}	0.0215(2)	0.00103(13)	U_{23}	−0.00069(9)
La2	0.00484(11)	U_{11}	0.00493(14)	0	U_{23}	0
Ca2	0.00484(11)	U_{11}	0.00493(14)	0	U_{23}	0
Ca3	0.0075(11)	U_{11}	0.004(2)	−0.0003(9)	U_{23}	0.0012(14)
Si1	0.0056(3)	0.0056(3)	0.0037(4)	−0.0002(3)	0.0002(3)	−0.0031(2)
Si2	0.0048(3)	U_{11}	0.0035(5)	0.0003(3)	U_{23}	0.0001(3)
N1	0.0077(12)	0.0061(11)	0.0053(12)	−0.0003(9)	0.0005(9)	−0.0024(9)
N2	0.0091(12)	0.0050(11)	0.0080(12)	0.0005(9)	−0.0029(10)	0.0008(9)
N3	0.0036(9)	U_{11}	0.006(2)	0.0000(8)	U_{23}	0.0003(11)
N4	0.012(2)	U_{11}	0.030(4)	0	U_{23}	−0.009(2)

Table S4. Selected atomic distances from single-crystal X-ray diffraction data of $La_{2.23}Ca_{1.16}Si_6N_{11}$ in Å.

La,Ca1A–La,Ca1B	0.854(6)
La,Ca1A–N2	2.556(3)
La,Ca1A–N2	2.556(3)
La,Ca1A–N4	2.5820(8)
La,Ca1A–N1	2.655(3)
La,Ca1A–N1	2.655(3)
La,Ca1A–Ca3	2.735(5)
La,Ca1A–N1	2.841(3)
La,Ca1A–N1	2.841(3)
La,Ca1A–N3	2.917(4)
La,Ca1B–Ca3	2.332(7)
La,Ca1B–N4	2.574(5)
La,Ca1B–N1	2.598(5)
La,Ca1B–N1	2.598(5)
La,Ca1B–N1	2.698(3)
La,Ca1B–N1	2.698(3)
La,Ca1B–N2	2.790(5)
La,Ca1B–N2	2.790(5)
La,Ca2–N1	2.629(3)
La,Ca2–N1	2.629(3)
La,Ca2–N1	2.629(3)
La,Ca2–N1	2.629(3)
La,Ca2–N2	2.654(3)
La,Ca2–N2	2.654(3)
La,Ca2–N2	2.654(3)
La,Ca2–N2	2.654(3)
Ca3–Ca3	2.029(9)
Ca3–N3	2.462(4)
Ca3–N3	2.462(4)
Ca3–N2	2.543(5)
Ca3–N2	2.543(5)
Ca3–N4	2.629(9)
Ca3–N4	2.674(9)
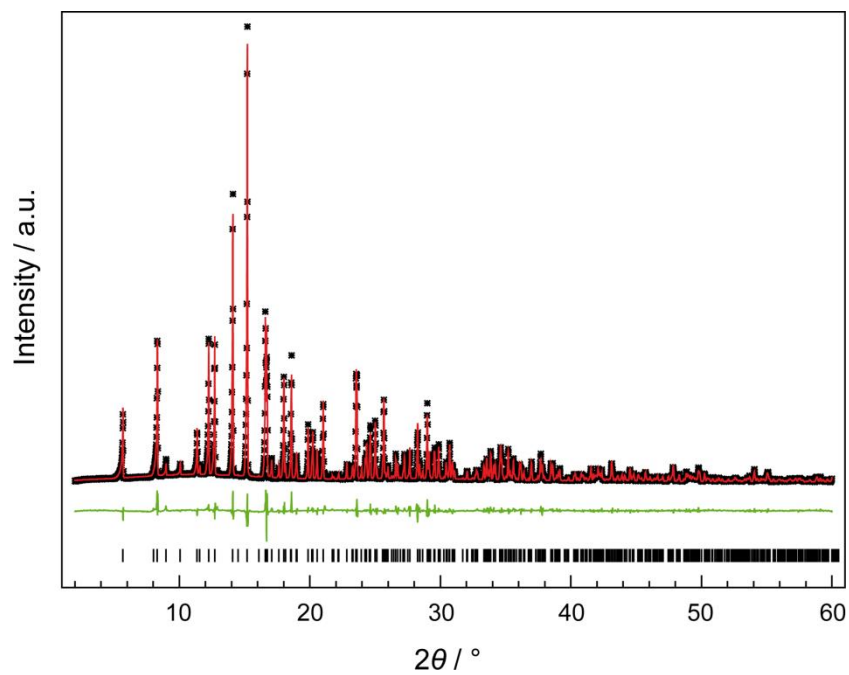
Figure S4. Rietveld refinement of data collected from a $La_{3-x}Ca_{1.5x}Si_6N_{11}:Eu^{2+}$ ($x \approx 0.77$) sample. Experimental PXRD data as black stars, Rietveld fit red, difference plot green, reflection positions of $La_{3-x}Ca_{1.5x}Si_6N_{11}:Eu^{2+}$ ($x \approx 0.77$) as black bars.

Table S5. Data for the Rietveld refinement of a $La_{3-x}Ca_{1.5x}Si_6N_{11}:Eu^{2+}$ ($x \approx 0.77$) sample.

formula	$La_{2.23}Ca_{1.16}Si_6N_{11}:Eu^{2+}$
formula mass / g·mol^{-1}	678.42
crystal system	tetragonal
space group	*P4bm* (no. 100)
lattice parameters / Å	a = 10.13720(9), c = 4.89183(6)
volume / Å^3	502.698(11)
formula units/cell	2
X-ray density / g·cm^{-3}	4.4752(1)
diffractometer	Stoe StadiP
radiation	Mo Kα_1 (λ = 0.709300 Å)
monochromator	Ge(111)
detector	MYTHEN 1K
$F(000)$	622
2θ range / °	2–60
data points	3868
number of observed reflections	449
number of parameters	32
constraints	0
program used	TOPAS Academic V4.1
structure refinement	Rietveld-Method
background function	Shifted Chebyshev (12 polynomials)
R_{wp}	0.0844
R_{exp}	0.0328
R_p	0.0634
R_{Bragg}	0.0291
χ^2	2.576
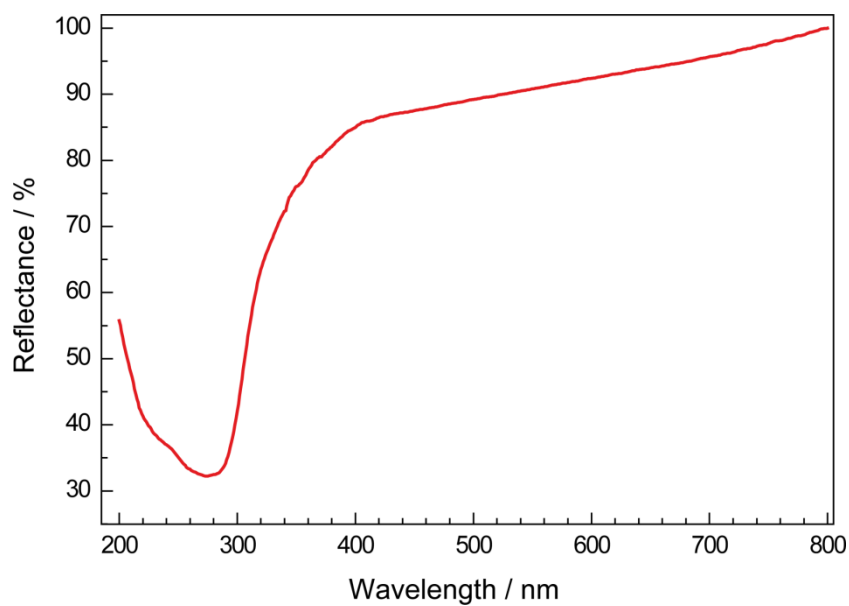
Figure S5. Diffuse reflectance UV/Vis spectrum of a nondoped $La_{3-x}Ca_{1.5x}Si_6N_{11}$ ($x \approx 0.77$) powder sample.
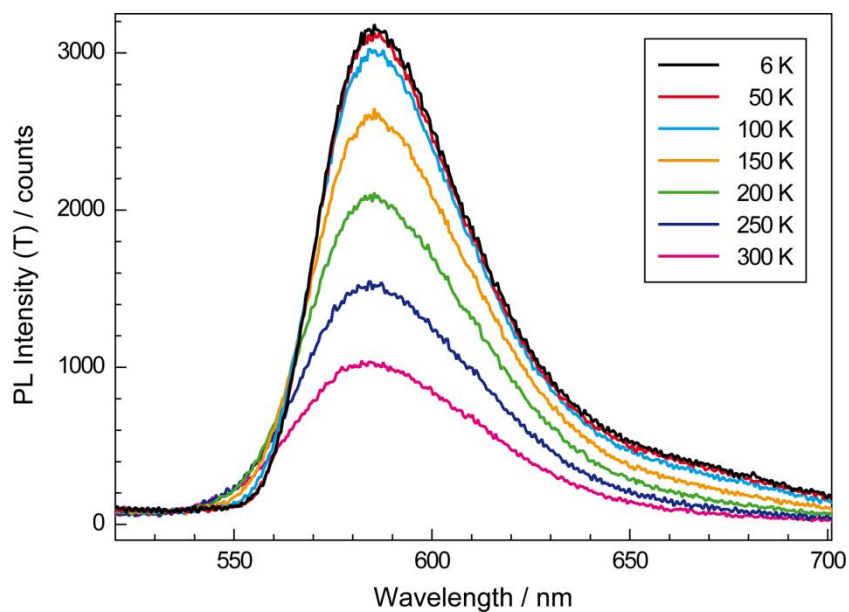
Figure S6. Temperature dependent emission spectra of $La_{3-x}Ca_{1.5x}Si_6N_{11}$:$Eu^{2+}$ ($x \approx 0.77$) with a nominal dopant concentration of 1 mol%.

189
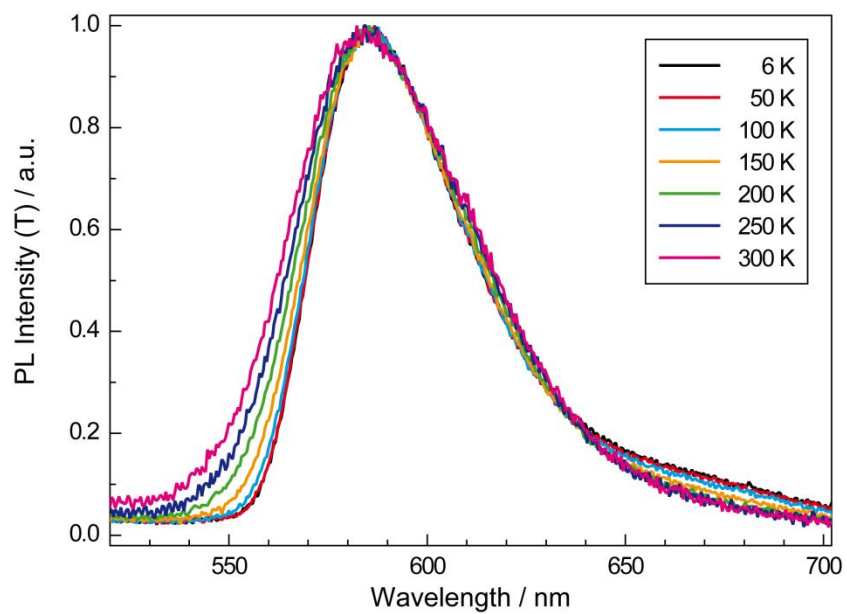
Figure S7. Normalized temperature dependent emission spectra of $La_{3-x}Ca_{1.5x}Si_6N_{11}:Eu^{2+}$ ($x \approx 0.77$) with a nominal dopant concentration of 1 mol%.

11.3 Supporting Information for Chapter 4

Efficient Yellow-Orange Phosphor $Lu_4Ba_2[Si_9ON_{16}]O:Eu^{2+}$ and Orange-Red Emitting $Y_4Ba_2[Si_9ON_{16}]O:Eu^{2+}$: Two Oxonitridosilicate Oxides with Outstanding Structural Variety

Christian Maak, Robin Niklaus, Franziska Friedrich, Andre Mähringer, Peter J. Schmidt, and Wolfgang Schnick
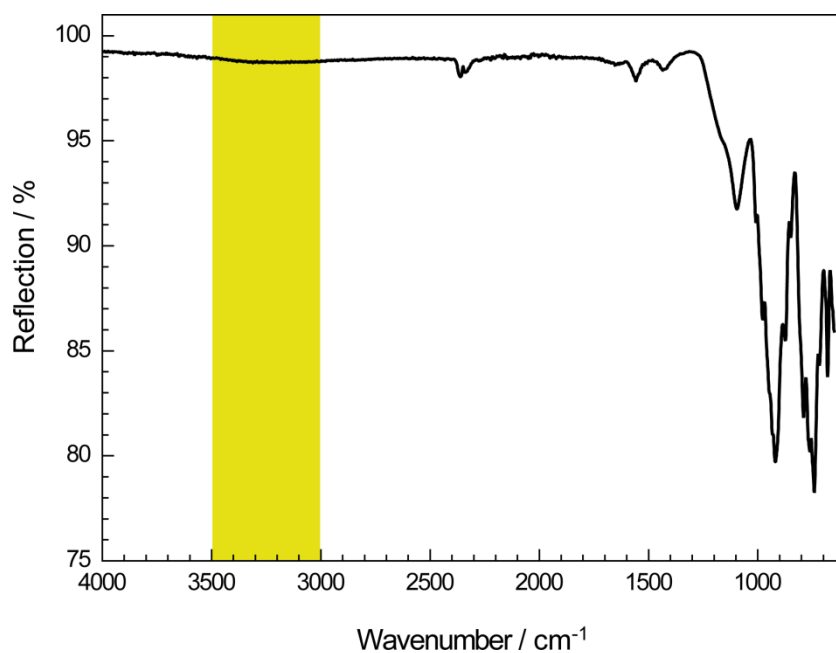
Figure S1. ATR-FTIR spectrum of a $Y_4Ba_2[Si_9ON_{16}]O$ powder sample. Typical region for N–H and O–H vibrations colored yellow.

Table S1. Atomic coordinates and isotropic displacement parameters of $Y_4Ba_2[Si_9ON_{16}]O:Eu^{2+}$. All atoms on Wyckoff position 4*e*.

Atom	*x*	*y*	*z*	$U_{eq}/Å^3$	*s.o.f*
Y1	0.02078(5)	0.18268(2)	0.16246(3)	0.00326(6)	1
Y2	0.23855(5)	0.00256(2)	0.48648(3)	0.00442(6)	1
Y3	0.48757(5)	0.48897(2)	0.32114(3)	0.00332(6)	1
Y4	0.52598(5)	0.38039(2)	0.16267(3)	0.00381(6)	1
Ba1	0.02861(3)	0.31369(2)	0.28899(2)	0.00584(4)	1
Ba2	0.52403(3)	0.12560(2)	0.29186(2)	0.00652(4)	1
Si1	0.01062(15)	0.12354(3)	0.48282(9)	0.00273(15)	1
Si2	0.03504(15)	0.44473(3)	0.23590(9)	0.00249(15)	1
Si3	0.03853(15)	0.05821(3)	0.23504(9)	0.00287(15)	1
Si4	0.21602(15)	0.71841(3)	0.02643(9)	0.00279(15)	1
Si5	0.22111(14)	0.58741(3)	0.51724(9)	0.00255(15)	1
Si6	0.26344(15)	0.21696(3)	0.47211(9)	0.00331(16)	1
Si7	0.28013(14)	0.40840(3)	0.48809(9)	0.00254(15)	1
Si8	0.52312(15)	0.25035(3)	0.23860(9)	0.00252(15)	1
Si9	0.52753(15)	0.31701(3)	0.47053(9)	0.00288(15)	1
N1	0.0036(5)	0.43220(10)	0.0652(3)	0.0039(5)	1
N2	0.0148(5)	0.61336(10)	0.1890(3)	0.0051(5)	1
N3	0.0266(4)	0.25286(10)	0.0238(3)	0.0047(5)	1
N4	0.0350(4)	0.06890(10)	0.0624(3)	0.0040(5)	1
N5	0.1198(5)	0.50816(10)	0.2189(3)	0.0055(5)	1
N6	0.2076(5)	0.57127(10)	0.6854(3)	0.0058(5)	1
N7	0.2461(5)	0.72171(10)	0.2001(3)	0.0052(5)	1
N8	0.2551(5)	0.41590(10)	0.3154(3)	0.0041(5)	1
N9	0.2552(4)	0.34423(10)	0.0249(3)	0.0039(5)	1
N10	0.2957(4)	0.22007(10)	0.2992(3)	0.0050(5)	1
N11	0.3043(5)	0.15275(10)	0.0328(3)	0.0044(5)	1
N12	0.5172(5)	0.30991(10)	0.2983(3)	0.0055(5)	1
N13	0.5264(5)	0.24885(10)	0.0481(3)	0.0043(5)	1
N14	0.5276(4)	0.05896(10)	0.0340(3)	0.0036(5)	1
N15	0.7580(5)	0.15052(10)	0.0163(3)	0.0053(5)	1
N16	0.7837(4)	0.34143(10)	0.0313(3)	0.0042(5)	1
O1	0.2920(4)	0.04173(9)	0.2861(2)	0.0065(4)	1
O2	0.4991(4)	0.45817(9)	0.0889(2)	0.0064(4)	1

Table S2. Atomic coordinates and isotropic displacement parameters of $Lu_4Ba_2[Si_9ON_{16}]O:Eu^{2+}$. Lu, Ba and Si atoms were refined anisotropic, N and O atoms were refined isotropic. All atoms on Wyckoff position 4e.

Atom	x	y	z	$U_{eq}, U_{iso}/Å^3$	s.o.f
Lu1	0.02198(3)	0.18310(2)	0.16543(2)	0.00471(4)	1
Lu2	0.24294(4)	0.00182(2)	0.49165(2)	0.00538(5)	1
Lu3	0.49200(3)	0.48831(2)	0.32121(2)	0.00492(5)	1
Lu4	0.52671(4)	0.38008(2)	0.16547(2)	0.00495(5)	1
Ba1	0.03022(5)	0.31373(2)	0.29204(3)	0.00776(6)	1
Ba2	0.52369(5)	0.12412(2)	0.29575(3)	0.00824(6)	1
Si1	0.0131(2)	0.12253(5)	0.48402(14)	0.0041(2)	1
Si2	0.0394(2)	0.44555(5)	0.23581(14)	0.0041(2)	1
Si3	0.0356(2)	0.05759(5)	0.23555(14)	0.0040(2)	1
Si4	0.2152(2)	0.71784(5)	0.02311(14)	0.0043(2)	1
Si5	0.2193(2)	0.58672(5)	0.51585(14)	0.0039(2)	1
Si6	0.2648(2)	0.21656(6)	0.47545(15)	0.0060(2)	1
Si7	0.2818(2)	0.40884(5)	0.48890(14)	0.0037(2)	1
Si8	0.5247(2)	0.25017(5)	0.24101(14)	0.0043(2)	1
Si9	0.5293(2)	0.31713(5)	0.47455(14)	0.0040(2)	1
N1	0.0055(7)	0.43497(16)	0.0632(4)	0.0042(7)	1
N2	0.0068(7)	0.61366(16)	0.1899(4)	0.0057(7)	1
N3	0.0272(8)	0.25284(18)	0.0284(5)	0.0086(8)	1
N4	0.0363(7)	0.06726(17)	0.0616(4)	0.0062(7)	1
N5	0.1372(7)	0.50907(17)	0.2220(4)	0.0058(7)	1
N6	0.2060(7)	0.57119(17)	0.6859(4)	0.0056(7)	1
N7	0.2432(7)	0.72065(16)	0.1972(4)	0.0058(7)	1
N8	0.2602(7)	0.41548(16)	0.3148(4)	0.0045(7)	1
N9	0.2574(7)	0.34557(16)	0.0296(4)	0.0049(7)	1
N10	0.2955(7)	0.21973(17)	0.3005(5)	0.0064(8)	1
N11	0.3032(7)	0.15253(17)	0.0365(4)	0.0058(7)	1
N12	0.5204(7)	0.31050(16)	0.3010(4)	0.0054(7)	1
N13	0.5278(7)	0.24921(17)	0.0499(4)	0.0059(7)	1
N14	0.5292(7)	0.05787(16)	0.0349(4)	0.0053(7)	1
N15	0.7621(7)	0.15007(17)	0.0207(4)	0.0062(7)	1
N16	0.7839(7)	0.34270(16)	0.0356(4)	0.0048(7)	1
O1	0.2858(6)	0.03872(14)	0.2894(4)	0.0069(7)	1
O2	0.5019(6)	0.45600(15)	0.0842(4)	0.0085(7)	1

Table S3. Anisotropic displacement parameters (U_{iy} in Å^2) for $Y_4Ba_2[Si_9ON_{16}]O:Eu^{2+}$.

Atom	U_{11}	U_{22}	U_{33}	U_{23}	U_{13}	U_{12}
Y1	0.00330(14)	0.00371(13)	0.00275(13)	0.00015(10)	0.00002(10)	0.00007(10)
Y2	0.00424(14)	0.00437(13)	0.00467(13)	−0.00110(10)	0.00054(10)	0.00004(11)
Y3	0.00430(14)	0.00280(13)	0.00285(12)	0.00000(10)	0.00027(10)	−0.00052(10)
Y4	0.00565(14)	0.00281(13)	0.00297(13)	−0.00016(10)	0.00049(10)	0.00044(10)
Ba1	0.00619(9)	0.00639(8)	0.00495(8)	0.00007(6)	0.00007(6)	−0.00037(7)
Ba2	0.00653(9)	0.00645(8)	0.00654(8)	−0.00064(6)	−0.00059(6)	−0.00059(7)
Si1	0.0040(4)	0.0023(4)	0.0019(4)	−0.0001(3)	0.0003(3)	0.0005(3)
Si2	0.0034(4)	0.0026(4)	0.0015(3)	0.0006(3)	0.0001(3)	0.0001(3)
Si3	0.0037(4)	0.0022(4)	0.0027(4)	0.0003(3)	0.0004(3)	−0.0002(3)
Si4	0.0033(4)	0.0022(4)	0.0029(4)	0.0001(3)	−0.0002(3)	−0.0001(3)
Si5	0.0029(4)	0.0030(4)	0.0018(4)	0.0003(3)	0.0000(3)	0.0003(3)
Si6	0.0037(4)	0.0030(4)	0.0033(4)	−0.0001(3)	0.0002(3)	0.0002(3)
Si7	0.0026(4)	0.0025(4)	0.0026(4)	−0.0001(3)	0.0002(3)	0.0000(3)
Si8	0.0037(4)	0.0025(4)	0.0014(4)	0.0001(3)	0.0003(3)	−0.0001(3)
Si9	0.0031(4)	0.0026(4)	0.0030(4)	−0.0001(3)	0.0001(3)	0.0003(3)
N1	0.0066(12)	0.0024(11)	0.0025(11)	0.0000(9)	−0.0005(9)	0.0012(9)
N2	0.0100(13)	0.0028(11)	0.0024(11)	−0.0011(9)	0.0009(9)	−0.0010(10)
N3	0.0030(12)	0.0063(12)	0.0046(12)	0.0023(9)	−0.0011(9)	0.0001(9)
N4	0.0048(12)	0.0044(11)	0.0027(11)	0.0021(9)	0.0000(9)	0.0001(10)
N5	0.0066(13)	0.0054(12)	0.0045(12)	−0.0001(9)	−0.0003(9)	−0.0008(10)
N6	0.0073(13)	0.0038(12)	0.0063(12)	0.0007(9)	0.0001(10)	−0.0006(10)
N7	0.0044(12)	0.0067(12)	0.0045(11)	−0.0005(9)	−0.0008(9)	−0.0012(10)
N8	0.0055(12)	0.0050(11)	0.0017(11)	−0.0003(9)	−0.0013(9)	0.0002(10)
N9	0.0041(12)	0.0033(11)	0.0041(11)	0.0003(9)	−0.0012(9)	0.0004(9)
N10	0.0029(12)	0.0073(12)	0.0049(12)	0.0004(9)	0.0003(9)	−0.0016(10)
N11	0.0044(12)	0.0034(11)	0.0053(12)	−0.0011(9)	0.0016(9)	−0.0008(9)
N12	0.0090(13)	0.0045(11)	0.0031(11)	0.0008(9)	0.0002(9)	0.0005(10)
N13	0.0074(12)	0.0036(11)	0.0017(11)	−0.0005(9)	−0.0006(9)	−0.0006(9)
N14	0.0024(12)	0.0038(12)	0.0047(11)	−0.0004(9)	0.0004(9)	−0.0002(9)
N15	0.0035(12)	0.0054(12)	0.0068(12)	−0.0010(9)	−0.0015(9)	−0.0003(10)
N16	0.0024(12)	0.0039(11)	0.0064(12)	−0.0008(9)	0.0007(9)	−0.0005(9)
O1	0.0066(11)	0.0079(11)	0.0049(10)	−0.0001(8)	0.0008(8)	0.0018(9)
O2	0.0067(11)	0.0057(10)	0.0067(10)	0.0019(8)	−0.0007(8)	0.0004(9)

Table S4. Anisotropic displacement parameters (U_{ij} in Å^2) for Lu$_4$Ba$_2$[Si$_9$ON$_{16}$]O:Eu^{2+}.

Atom	U_{11}	U_{22}	U_{33}	U_{23}	U_{13}	U_{12}
Lu1	0.00457(9)	0.00485(9)	0.00472(9)	0.00000(6)	0.00017(6)	−0.00002(6)
Lu2	0.00488(8)	0.00535(9)	0.00592(9)	−0.00069(7)	0.00062(7)	−0.00006(7)
Lu3	0.00519(9)	0.00441(9)	0.00518(9)	0.00013(6)	0.00024(6)	−0.00049(7)
Lu4	0.00598(9)	0.00416(9)	0.00474(9)	−0.00016(6)	0.00066(7)	0.00060(7)
Ba1	0.00724(13)	0.00839(14)	0.00765(13)	−0.00028(10)	0.00019(10)	−0.00082(10)
Ba2	0.00755(13)	0.00872(14)	0.00843(13)	−0.00036(10)	−0.00055(10)	−0.00096(10)
Si1	0.0043(6)	0.0040(6)	0.0040(6)	0.0003(4)	0.0002(4)	−0.0001(4)
Si2	0.0045(6)	0.0031(6)	0.0048(6)	0.0001(4)	0.0000(4)	−0.0002(4)
Si3	0.0042(6)	0.0038(6)	0.0040(6)	0.0006(4)	0.0004(4)	0.0007(4)
Si4	0.0048(6)	0.0044(6)	0.0038(6)	−0.0002(4)	0.0000(4)	0.0001(4)
Si5	0.0039(6)	0.0044(6)	0.0035(6)	−0.0004(4)	0.0007(4)	0.0000(4)
Si6	0.0059(6)	0.0066(6)	0.0055(6)	−0.0001(5)	−0.0001(5)	−0.0007(5)
Si7	0.0030(6)	0.0042(6)	0.0039(6)	−0.0002(4)	0.0008(4)	0.0001(4)
Si8	0.0050(6)	0.0038(6)	0.0040(6)	0.0001(4)	0.0013(4)	0.0000(4)
Si9	0.0051(6)	0.0029(6)	0.0041(6)	−0.0007(4)	0.0007(4)	−0.0002(4)

Table S5. Results of MAPLE Calculations (all values in kJ/mol) for Y$_4$Ba$_2$[Si$_9$ON$_{16}$]O and Lu$_4$Ba$_2$[Si$_9$ON$_{16}$]O. Partial MAPLE values, total MAPLE values, and deviation to sums of total MAPLE values of binary ionic compounds forming Y$_4$Ba$_2$[Si$_9$ON$_{16}$]O and Lu$_4$Ba$_2$[Si$_9$ON$_{16}$]O in hypothetical reactions (structural data from references 1–4).

Y$_4$Ba$_2$[Si$_9$ON$_{16}$]O								
Y^{3+}	Ba^{2+}	Si^{4+}	O^{2-}	O$^{[1]2-}$	N$^{[2]3-}$	N$^{[3]3-}$	N$^{[4]3-}$	**total MAPLE**
4373–4930	1741–1761	9516–10123	2132	2585	5277–5513	5846	5793	**201680**
4 YN$^{[1]}$ + 2 BaO$^{[2]}$ + 3 α-Si$_3$N$_4$$^{[3]}$								
4·8990 + 2·3479 + 3·53023								**201987**
								Δ = 0.15 %
Lu$_4$Ba$_2$[Si$_9$ON$_{16}$]O								
Lu^{3+}	Ba^{2+}	Si^{4+}	O^{2-}	O$^{[1]2-}$	N$^{[2]3-}$	N$^{[3]3-}$	N$^{[4]3-}$	**total MAPLE**
4485–5023	1741–1744	9411–9975	2108	2601	5299–5497	5810	5885	**202528**
4 LuN$^{[4]}$ + 2 BaO$^{[2]}$ + 3 α-Si$_3$N$_4$$^{[3]}$								
4·9167 + 2·3479 + 3·53023								**202695**
								Δ = 0.08 %

Typical MAPLE values:[5] RE^{3+}: 3500–5100; Ba^{2+}: 1500–2000; Si^{4+}: 9000–10200; O$^{[1]2-}$: 2000–2800; N$^{[2]3-}$: 4600–6000; N$^{[3]3-}$: 5000–6200

As stated in the main text, ordering of O and N atoms is strongly indicated by the refinement of single-crystal X-ray data. Terminal and non-bridging anion sites could only be refined as O atoms for both $Y_4Ba_2[Si_9ON_{16}]O:Eu^{2+}$ and $Lu_4Ba_2[Si_9ON_{16}]O:Eu^{2+}$ (N atoms would have negative displacement parameters for $Y_4Ba_2[Si_9ON_{16}]O:Eu^{2+}$ and are close to zero for $Lu_4Ba_2[Si_9ON_{16}]O:Eu^{2+}$). However, additional lattice energy calculations using the MAPLE concept were carried out to support the assignment of O and N atoms.[6–9] Partial MAPLE values were calculated for each site and compared to typical (empirical) partial MAPLE values.[5] All partial MAPLE values for O and N atoms as well as for cations Y/Lu and Ba (Table S5) are in the reported typical ranges (below Table S5).[5] Furthermore, total MAPLE values for the whole crystal structures were compared to sums of total MAPLE values of binary ionic compounds forming $Y_4Ba_2[Si_9ON_{16}]O$ and $Lu_4Ba_2[Si_9ON_{16}]O$ in hypothetical reactions (Table S5). These total MAPLE values should be equal or within a deviation of < 1%.[5] Therefore, the very small deviations of 0.15% for $Y_4Ba_2[Si_9ON_{16}]O$ and 0.08% for $Lu_4Ba_2[Si_9ON_{16}]O$ support the crystal structure models refined from single-crystal X-ray diffraction data.

Table S6. Selected atomic distances in $Y_4Ba_2[Si_9ON_{16}]O:Eu^{2+}$ and $Lu_4Ba_2[Si_9ON_{16}]O:Eu^{2+}$ in pm.

	$Y_4Ba_2[Si_9ON_{16}]O$	$Lu_4Ba_2[Si_9ON_{16}]O$
*RE*1–N15	231.1(3)	228.3(5)
*RE*1–N11	231.6(3)	228.3(4)
*RE*1–N3	234.8(3)	230.2(5)
*RE*1–N10	236.3(3)	232.2(5)
*RE*1–N7	238.5(3)	233.5(4)
*RE*1–N2	240.0(3)	234.8(4)
*RE*2–O2	214.2(2)	211.1(4)
*RE*2–O2	214.9(2)	212.2(4)
*RE*2–O1	228.5(2)	224.1(4)
*RE*2–N1	240.9(3)	233.0(4)
*RE*2–N5	245.1(3)	238.3(4)
*RE*2–N1	245.5(3)	239.0(4)
*RE*3–O1	224.1(2)	219.9(4)
*RE*3–N14	238.3(3)	234.3(4)
*RE*3–N8	243.0(3)	239.7(4)
*RE*3–O2	245.8(2)	249.1(4)
*RE*3–N6	246.9(3)	241.9(4)
*RE*3–N14	249.1(3)	244.8(4)
*RE*3–N5	249.3(3)	240.5(4)
*RE*4–O2	223.4(2)	218.7(4)
*RE*4–N16	231.1(3)	225.6(4)
*RE*4–N9	233.7(3)	228.6(4)
*RE*4–N12	233.7(3)	229.0(4)
*RE*4–N8	245.5(3)	238.8(4)
*RE*4–N6	255.5(3)	252.5(4)
Ba1–N3	295.0(3)	293.1(5)
Ba1–N12	297.0(3)	295.7(4)
Ba1–N15	298.1(3)	295.2(4)
Ba1–N7	300.0(3)	298.8(4)
Ba1–N10	300.9(3)	298.0(4)
Ba1–N16	303.5(3)	301.5(4)
Ba1–N11	306.1(3)	303.7(4)
Ba1–N8	309.8(3)	306.1(4)
Ba1–N9	309.9(3)	306.2(4)
Ba1–N3	310.9(3)	306.5(5)
Ba1–N12	311.2(3)	307.7(4)
Ba1–N6	344.0(3)	340.0(5)
Ba2–O1	267.2(2)	269.7(4)
Ba2–N2	282.5(3)	284.6(4)
Ba2–N10	291.0(3)	290.4(4)
Ba2–N7	295.3(3)	293.9(4)
Ba2–N16	297.1(3)	295.6(4)
Ba2–N11	297.4(3)	296.3(4)
Ba2–N9	297.3(3)	293.8(4)
Ba2–N14	313.6(3)	312.2(4)
Ba2–N15	318.2(3)	316.0(4)
Ba2–N2	329.9(3)	321.6(4)
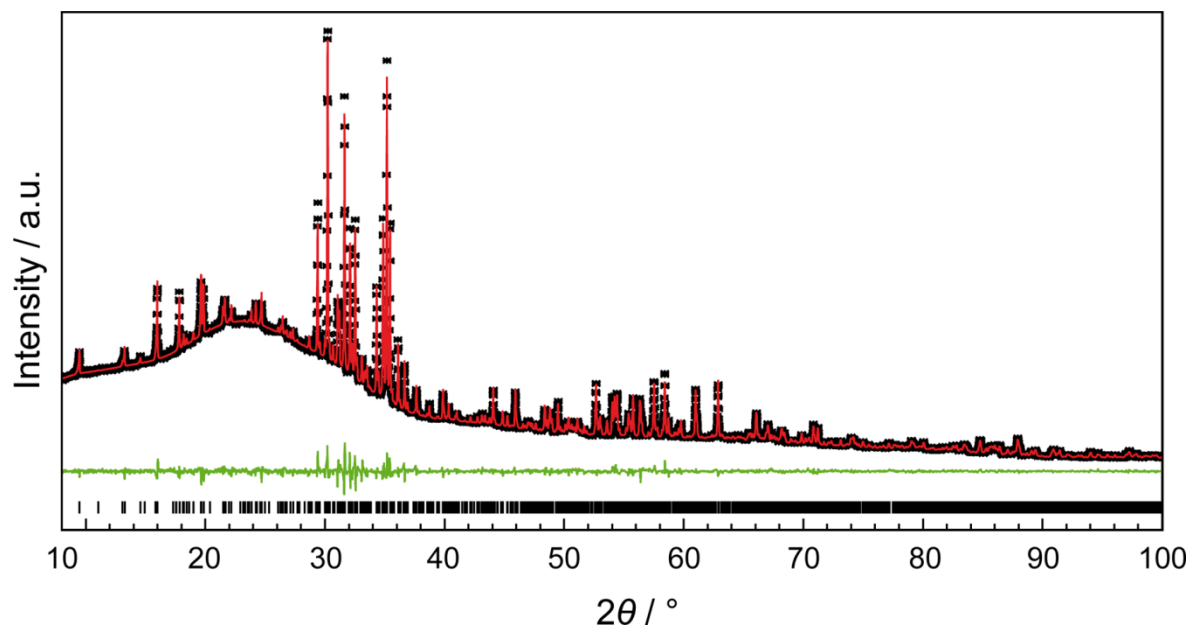
Figure S2. Rietveld refinement of data collected from a $Y_4Ba_2[Si_9ON_{16}]O:Eu^{2+}$ sample. Reflection positions for $Y_4Ba_2[Si_9ON_{16}]O:Eu^{2+}$ as black bars.
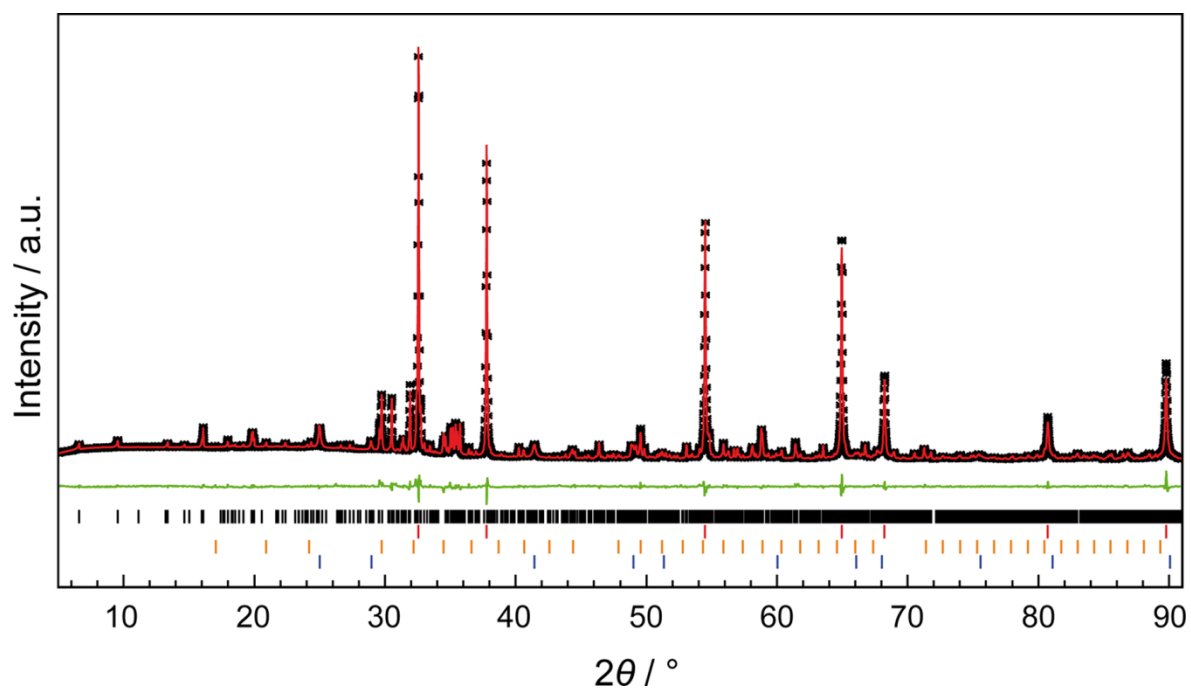
Figure S3. Rietveld refinement of data collected from a $Lu_4Ba_2[Si_9ON_{16}]O:Eu^{2+}$ sample. Reflection positions for $Lu_4Ba_2[Si_9ON_{16}]O:Eu^{2+}$ black (43 wt%), LuN red (43 wt%), Lu_2O_3 orange (6 wt%), BaF_2 blue bars (8 wt%), respectively.

Table S7. Data for Rietveld refinements of a $Y_4Ba_2[Si_9ON_{16}]O:Eu^{2+}$ and a $Lu_4Ba_2[Si_9ON_{16}]O:Eu^{2+}$ sample.

formula	$Y_4Ba_2[Si_9ON_{16}]O:Eu^{2+}$	$Lu_4Ba_2[Si_9ON_{16}]O:Eu^{2+}$
formula mass / $g \cdot mol^{-1}$	1139.29	1483.53
crystal system	monoclinic	
space group	$P2_1/c$ (no. 14)	
lattice parameters / Å, °	$a = 6.07285(5)$, $b = 27.0493(2)$ $c = 9.94099(9)$, $\beta = 90.9724(7)$	$a = 6.03566(6)$, $b = 26.7725(3)$ $c = 9.86209(11)$, $\beta = 90.7295(9)$
volume / $Å^3$	1632.73(2)	1593.49(3)
formula units/cell	4	
X-ray density / $g \cdot cm^{-3}$	4.63419(7)	6.18327(12)
diffractometer	Stoe StadiP	
radiation	Cu $K\alpha_1$ ($\lambda = 1.54056$ Å)	
monochromator	Ge(111)	
detector	MYTHEN 1K	
$F(000)$	2088	2600
2θ range / °	5–100	5–90
data points	6334	5667
number of observed reflections	1673	1294
number of parameters	72	57
constraints	0	
program used	TOPAS Academic V4.1	
structure refinement	Rietveld-Method	
background function	Shifted Chebyshev	
	30 polynomials	12 polynomials
R_{wp}	0.0219	0.0445
R_{exp}	0.0121	0.0250
R_p	0.0153	0.0335
R_{Bragg}	0.0132	0.0227
χ^2	1.805	1.783
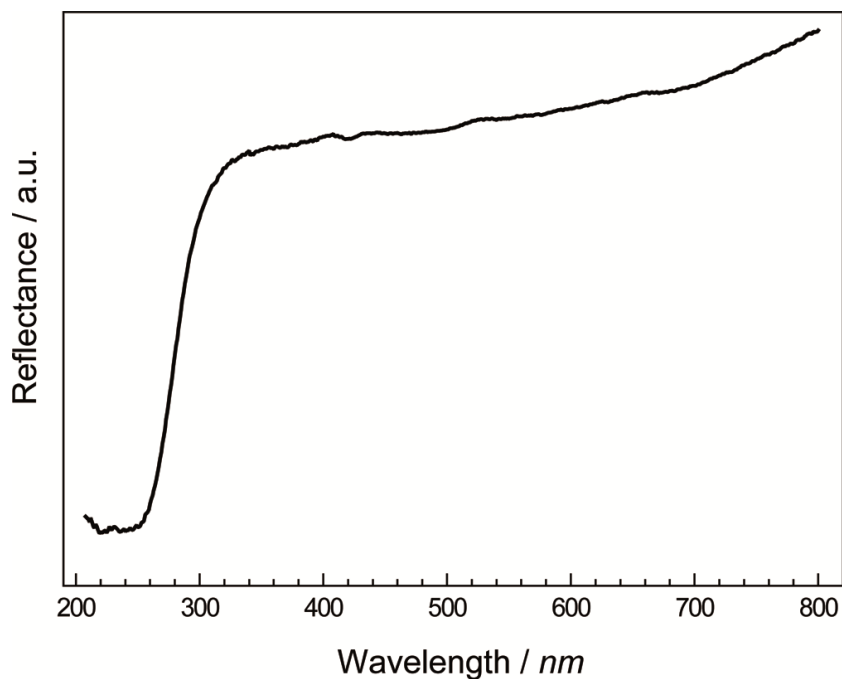
Figure S4. UV/Vis spectrum of nondoped $Y_4Ba_2[Si_9ON_{16}]O$.
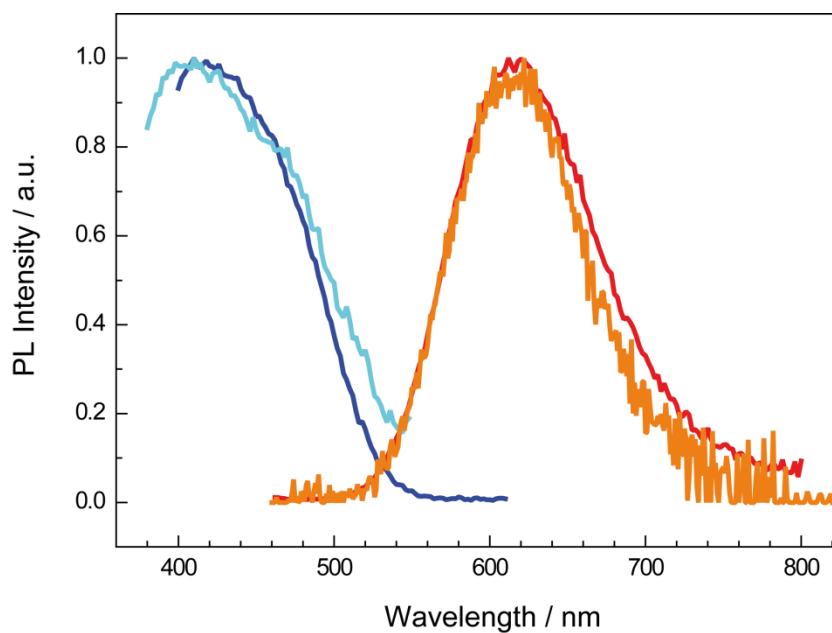
Figure S5. $Y_4Ba_2[Si_9ON_{16}]O:Eu^{2+}$ single crystal: normalized excitation spectrum (λ_{mon} = 636 nm) dark blue, normalized emission spectrum (λ_{exc} = 440 nm) red; $Y_4Ba_2[Si_9ON_{16}]O:Eu^{2+}$ powder: normalized excitation spectrum (λ_{mon} = 636 nm) cyan, normalized emission spectrum (λ_{exc} = 440 nm) orange.
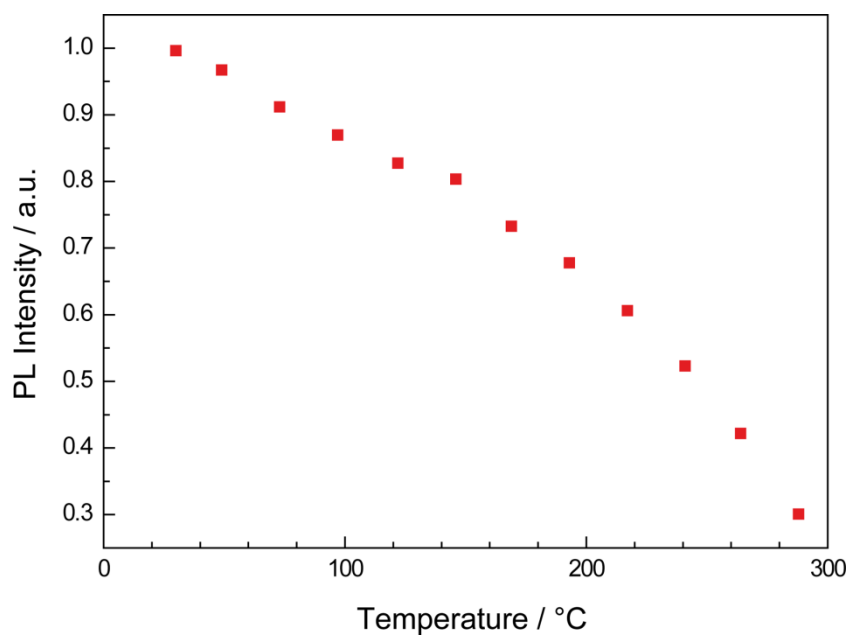
Figure S6. Thermal quenching data for $Y_4Ba_2[Si_9ON_{16}]O:Eu^{2+}$.
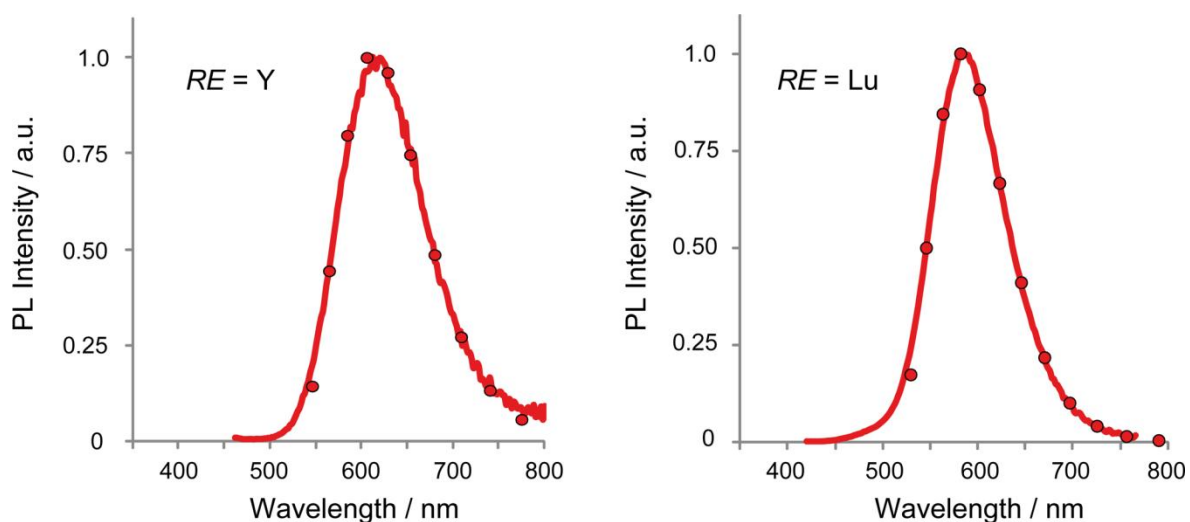
Figure S7. Experimental (lines) and calculated (circles) emission spectra of $Y_4Ba_2[Si_9ON_{16}]O:Eu^{2+}$ (left) and $Lu_4Ba_2[Si_9ON_{16}]O:Eu^{2+}$ (right). Best fits were obtained for $S \approx 4$, $\hbar\omega \approx 601$ cm^{-1} in the case of $Y_4Ba_2[Si_9ON_{16}]O:Eu^{2+}$ and $S \approx 3.8$, $\hbar\omega \approx 567$ cm^{-1} in the case of $Lu_4Ba_2[Si_9ON_{16}]O:Eu^{2+}$. Using the formula $E_{Stokes} = (2S - 1)\cdot\hbar\omega$, values of $E_{Stokes} \approx 4200$ cm^{-1} for $Y_4Ba_2[Si_9ON_{16}]O:Eu^{2+}$ and $E_{Stokes} \approx 3700$ cm^{-1} for $Lu_4Ba_2[Si_9ON_{16}]O:Eu^{2+}$ were obtained.
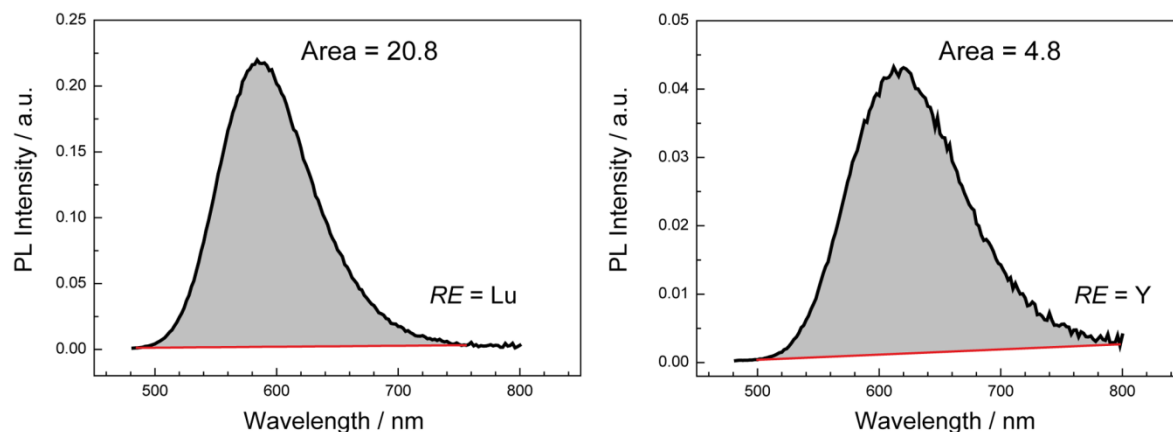
Figure S8. Integrated emission spectra of $Lu_4Ba_2[Si_9ON_{16}]O:Eu^{2+}$ (left) and $Y_4Ba_2[Si_9ON_{16}]O:Eu^{2+}$ (right) single crystals with similar light propagation properties. The excitation peak at 440 nm was normalized to 1 to allow comparison between the two spectra (Figure 9 in the manuscript). The ratio R between the areas under the two emission spectra (R = 20.8/4.8 = 4.3) was multiplied with the IQE of $Y_4Ba_2[Si_9ON_{16}]O:Eu^{2+}$ (IQE = 20 %) powder samples to estimate the IQE of $Lu_4Ba_2[Si_9ON_{16}]O:Eu^{2+}$. This results in $IQE \approx 85$ % for $Lu_4Ba_2[Si_9ON_{16}]O:Eu^{2+}$.

References

[1]   Brown, R. C.; Clark, N. J. Composition limits and vaporization of rare earth nitrides. *J. Inorg. Nucl. Chem.* **1974**, *36*, 2507–2514.

[2]   Ghebouli, M. A.; Ghebouli, B.; Bouhemadou, A.; Fatmi, M.; Bouamama, K. Structural, electronic, optical and thermodynamic properties of $Sr_xCa_{1-x}O$, $Ba_xSr_{1-x}O$ and $Ba_xCa_{1-x}O$ alloys. *J. Alloys Compd.* **2011**, *509*, 1440–1447.

[3]   Yang, P.; Fun, H.-K.; Rahman, I. A.; Saleh, M. I. Two phase refinements of the structures of α-Si_3N_4 and β-Si_3N_4 made from rice husk by Rietveld analysis. *Ceram. Int.* **1995**, *21*, 137–142.

[4]   Klemm, W.; Winkelmann, G. Zur Kenntnis der Nitride der Seltenen Erden. *Z. Anorg. Allg. Chem.* **1956**, *288*, 87–90.

[5]   Zeuner, M.; Pagano, S.; Schnick, W. Nitridosilicates and Oxonitridosilicates: From Ceramic Materials to Structural and Functional Diversity. *Angew. Chem., Int. Ed.* **2011**, *50*, 7754–7775; Nitridosilicate und Oxonitridosilicate: von keramischen Materialien zu struktureller und funktioneller Diversität. *Angew. Chem.* **2011**, *123*, 7898–7920.

[6]   Shannon, R. D. Revised effective ionic radii and systematic studies of interatomic distances in halides and chalcogenides. *Acta Crystallogr., Sect A: Found. Crystallogr.* **1976**, *32*, 751–767.

[7]   Hoppe, R. Madelung constants. *Angew. Chem., Int. Ed. Engl.* **1966**, *5*, 95–106; Über Madelungfaktoren. *Angew. Chem.* **1966**, *78*, 52–63.

[8]   Hoppe, R. The Coordination Number – an "Inorganic Chameleon". *Angew. Chem., Int. Ed. Engl.* **1970**, *9*, 25–34; Die Koordinationszahl – ein „anorganisches Chamäleon". *Angew. Chem.* **1970**, *82*, 7–16.

[9]   Hübenthal, R. *Maple, Program for the Calculation of MAPLE values, version 4*; University of Gießen: Gießen, Germany, 1993.

11.4 Supporting Information for Chapter 5

RE$_4$Ba$_2$[Si$_{12}$O$_2$N$_{16}$C$_3$]:Eu^{2+} (*RE* = Lu, Y): Green-Yellow Emitting Oxonitridocarbidosilicates with a Highly Condensed Network Structure Unraveled through Synchrotron Microdiffraction

Christian Maak, Lucien Eisenburger, Jonathan P. Wright, Markus Nentwig, Peter J. Schmidt, Oliver Oeckler, and Wolfgang Schnick

Inorg. Chem. **2018**, *57*, 13840–13846

Table S1. Amounts of starting materials for the synthesis of Ba$_2$Si$_5$N$_8$.

BaH$_2$ (ABCR, 99.5%)	152.7 mg / 1.096 mmol
Si$_3$N$_4$ (Ube Industries, amorphous, > 99%)	128.1 mg / 0.913 mmol

Table S2. Temperature program of the radiofrequency furnace for the synthesis of Ba$_2$Si$_5$N$_8$.

Step	Starting T / °C	Target T / °C	t / h	ΔT / °C·h^{-1}
1	25	1600	3	525
2	1600	1600	3	0
3	1600	500	5	−367
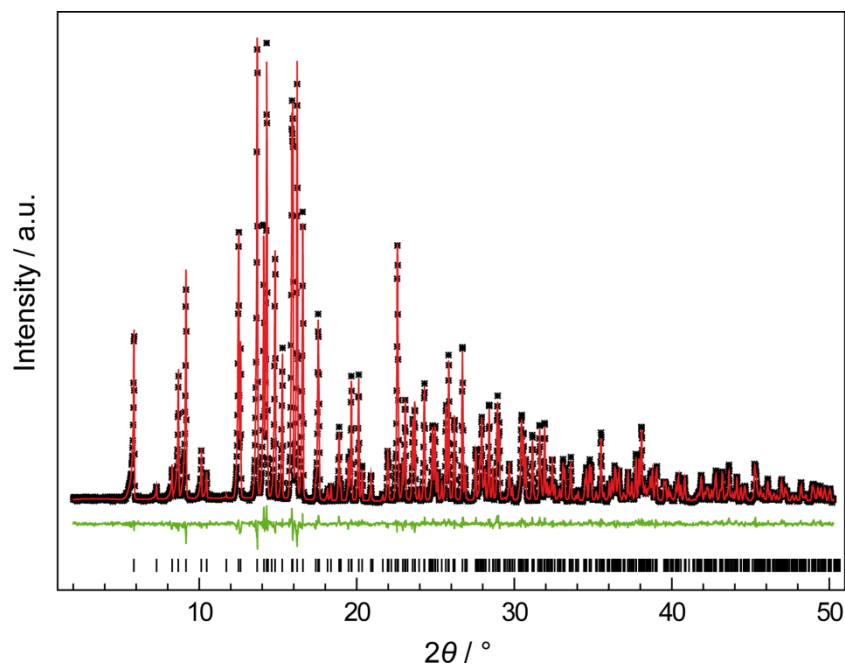
Figure S1. Rietveld refinement based on the XRD pattern of $Ba_2Si_5N_8$ which was used as starting material (Mo $K\alpha_1$, $\lambda = 0.7093$ Å).[1] Measured histogram (black stars), Rietveld fit (red line), difference plot (green line). Only lattice parameters and profile functions were refined.
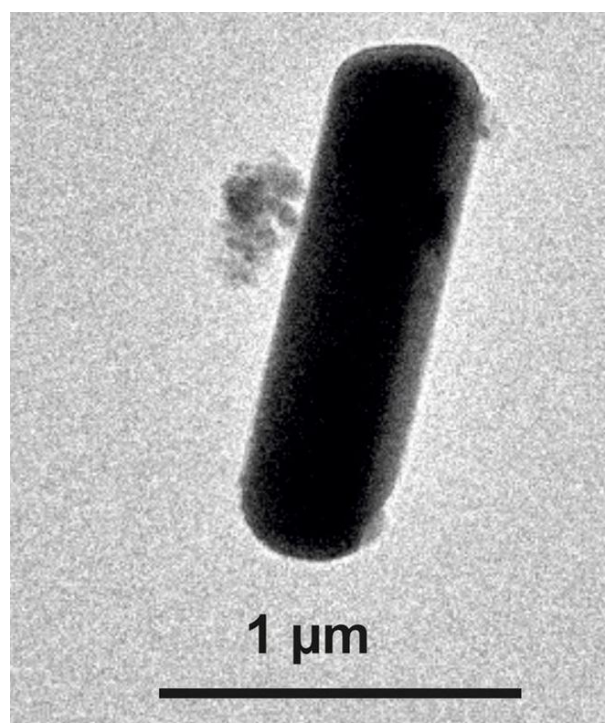
Figure S2. TEM image of the $Lu_4Ba_2[Si_{12}O_2N_{16}C_3]$ crystallite used for the collection of single-crystal X-ray diffraction data.

Table S3. Results of EDX analyses (eleven point measurements for RE = Lu, eight for RE = Y; standard deviations in parentheses).

	Calculated atom%	Experimental atom%	
		RE = Lu	RE = Y
RE	10.2	12(2)	9(2)
Ba	5.1	5(1)	5(1)
Si	30.7	33(2)	38(4)
O	5.1	8(3)	7(1)
N	41	35(3)	35(4)
C	7.6	7(1)	6(2)
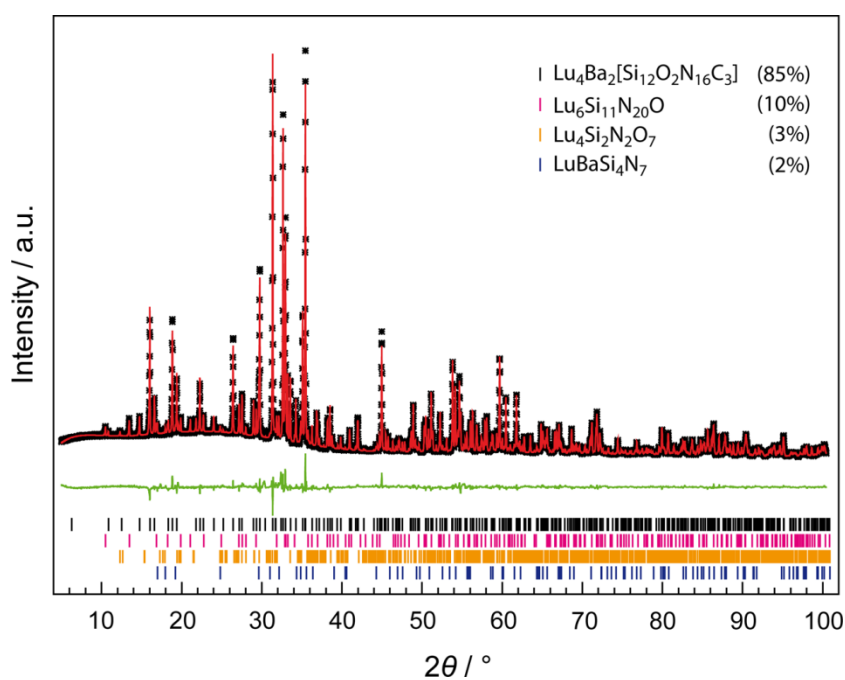
Legend:
- $Lu_4Ba_2[Si_{12}O_2N_{16}C_3]$ (85%)
- $Lu_6Si_{11}N_{20}O$ (10%)
- $Lu_4Si_2N_2O_7$ (3%)
- $LuBaSi_4N_7$ (2%)

Figure S3. Rietveld refinement based on the XRD pattern (Cu Kα_1, λ = 1.54056 Å) of a $Lu_4Ba_2[Si_{12}O_2N_{16}C_3]$ sample with measured histogram (black stars), Rietveld fit (red line), difference plot (green line), and positions of reflections (bars).
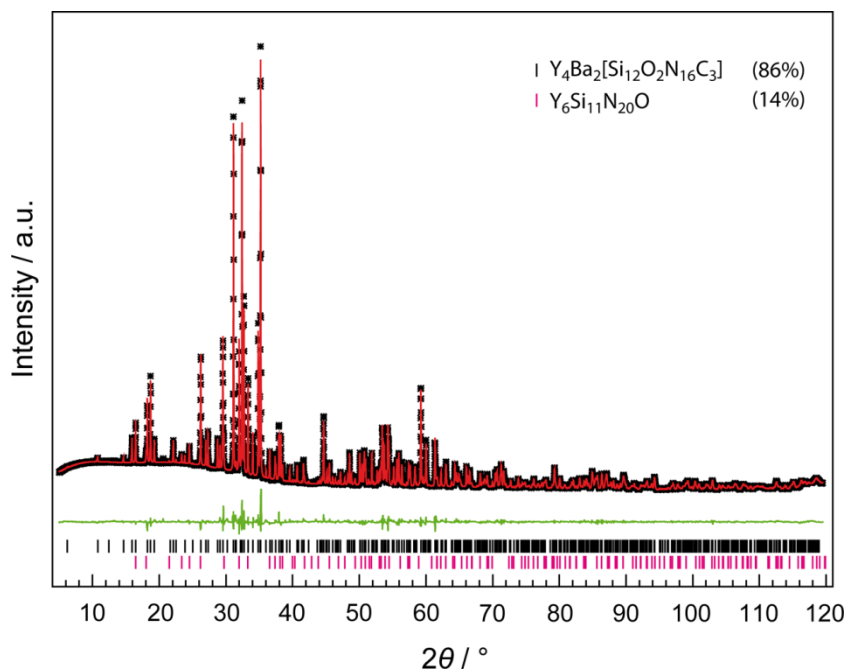
Figure S4. Rietveld refinement based on the XRD pattern (Cu Kα_1, $\lambda = 1.54056$ Å) of a $Y_4Ba_2[Si_{12}O_2N_{16}C_3]$ sample with measured histogram (black stars), Rietveld fit (red line), difference plot (green line), and positions of reflections (bars).

Table S4. Data of Rietveld refinements for $RE_4Ba_2[Si_{12}O_2N_{16}C_3]:Eu^{2+}$ (RE = Lu, Y) with least squares standard deviations in parentheses. The structure model obtained from single-crystal X-ray diffraction data for RE = Lu was used for both refinements. Only lattice parameters were refined.

	RE = Lu	RE = Y
formula mass / $g \cdot mol^{-1}$	1603.83	1259.59
crystal system	trigonal	
space group	$P3$ (no. 143)	
lattice parameters / Å	a = 16.29588(9), c = 6.00121(4)	a = 16.41190(6), c = 6.03909(3)
volume / $Å^3$	1380.15(2)	1408.70(2)
formula units / cell	3	
X-ray density / $g \cdot cm^{-3}$	5.78847(7)	4.45378(4)
diffractometer, detector	Stoe StadiP, MYTHEN 1K	
radiation	Cu Kα_1 (λ = 1.54056 Å)	
monochromator	Ge(111)	
F(000)	2130	1746
2θ range / °	5–100	5–119.5
data points	6365	7634
observed reflections	970	1398
number of parameters	50	38
software	TOPAS Academic V4.1	
structure refinement	Rietveld-Method	
background function	Shifted Chebyshev	
	18 polynomials	
R_{wp}	0.0444	0.0427
R_{exp}	0.0205	0.0111
R_p	0.0317	0.0292
R_{Bragg}	0.0266	0.0205
χ^2	2.164	3.841

Table S5. Results of CHNS analyses; expected values were calculated from the sum formula, taking into account the side phases as obtained from Rietveld refinements (all values in wt%).

RE	C expected	C measured	N expected	N measured
Lu	1.9	2.2	14.0	14.0
Y	2.5	2.9	18.7	17.8

Table S6. Details on the calculation of the expected wt% values for C and N in the CHNS analyses (M(N): 14.007 g/mol , M(C): 12.011 g/mol).

Compound	molar mass / g/mol	M% N	M% C	wt % Rietveld
$Lu_4Ba_2[Si_{12}O_2N_{16}C_3]$	1603.83	13.97	2.25	85
$Lu_6Si_{11}N_{20}O$	1654.89	16.93	0	10
$Lu_4Si_2N_2O_7$	896.09	3.13	0	3
$LuBaSi_4N_7$	522.70	18.76	0	2
$Y_4Ba_2[Si_{12}O_2N_{16}C_3]$	1259.59	17.79	2.86	86
$Y_6Si_{11}N_{20}O$	1138.50	24.61	0	14

$Lu_4Ba_2[Si_{12}O_2N_{16}C_3]$

C expected $= 0.85 \cdot 0.0225 =$ **0.019**

N expected $= 0.85 \cdot 0.1397 + 0.1 \cdot 0.1693 + 0.03 \cdot 0.0313 + 0.02 \cdot 0.1876 =$ **0.140**

$Y_4Ba_2[Si_{12}O_2N_{16}C_3]$

C expected $= 0.86 \cdot 0.0286 =$ **0.025**

N expected $= 0.86 \cdot 0.1779 + 0.14 \cdot 0.2461 =$ **0.187**
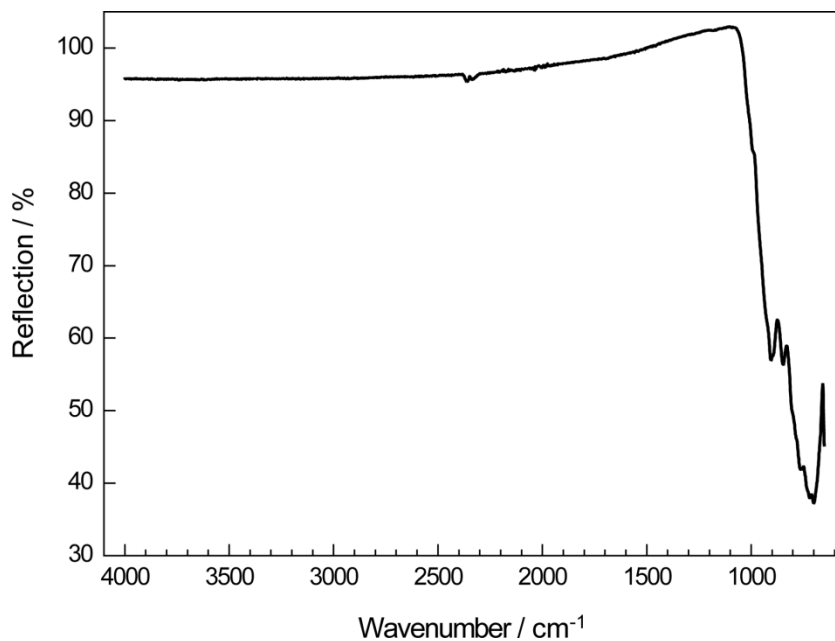
Figure S5. ATR-FTIR spectrum of a $Lu_4Ba_2[Si_{12}O_2N_{16}C_3]:Eu^{2+}$ powder sample. Bands at 2345 cm^{-1} belong to the asymmetric stretching vibration of CO_2. No O–H and N–H bands are observed in the typical region.
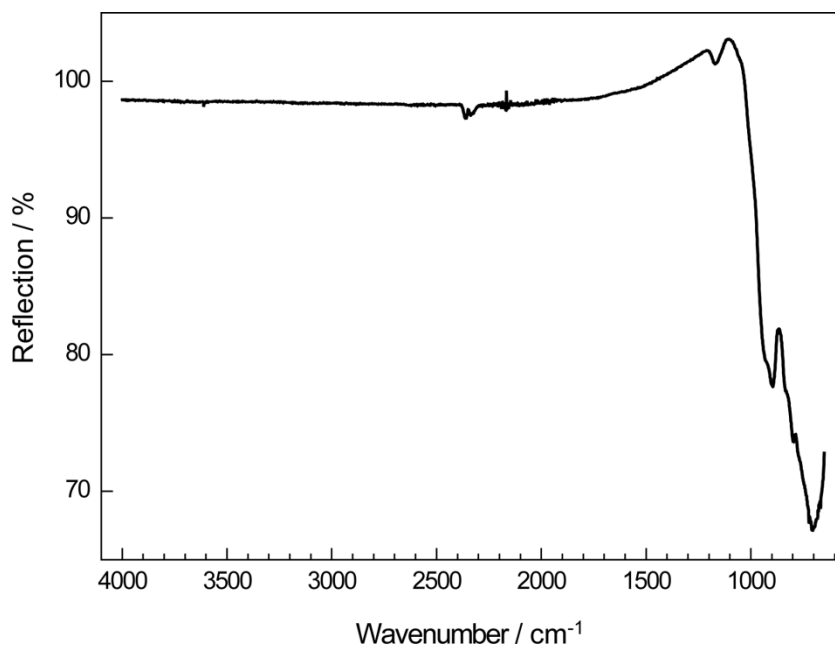
Figure S6. ATR-FTIR spectrum of a $Y_4Ba_2[Si_{12}O_2N_{16}C_3]:Eu^{2+}$ powder sample. Bands at 2345 cm^{-1} belong to the asymmetric stretching vibration of CO_2. No O–H and N–H bands are observed in the typical region.

Table S7. Results of MAPLE calculations for $Lu_4Ba_2[Si_{12}O_2N_{16}C_3]$ (all values in kJ/mol).[2–4] Partial MAPLE values, total MAPLE value and deviation to sum of total MAPLE values of binary ionic compounds, forming $Lu_4Ba_2[Si_{12}O_2N_{16}C_3]$ in a hypothetical reaction (structural data from references 5–8).

Lu^{3+}	Ba^{2+}	Si^{4+}	$C^{[4]4-}$	$N^{[3]3-}$	$N^{[2]3-}/O^{[2]2-}$	$O^{[1]2-}$
3840–5036	1690–1714	9210–10036	9471–9885	5931–6544	5084–5610	2345

					Total MAPLE
					260455

4 LuN + 2 BaO + 3 SiC (wurtzite) + 3 Si_3N_4	
4 · 9167 + 2 · 3479 + 3 · 19217 + 3 · 53023	260346
Deviation	**0.04%**

Typical MAPLE values in nitridosilicates (in kJ/mol):[9,10]

RE^{3+}: 3500–5100, Ba^{2+}: 1500–2000, Si^{4+}: 9000–10200, $(C^{[4]})^{4-}$: 8700–9700,

$(N^{[3]})^{3-}$: 5000–6200, $(N^{[2]})^{3-}$: 4600–6000, $(O^{[1]})^{2-}$: 2000–2800

Table S8. Results of charge distribution (CHARDI) calculations for the cations in $Lu_4Ba_2[Si_{12}O_2N_{16}C_3]$. CHARDI calculations were performed with VESTA according to the theory of Hoppe et al.[11,12]

Lu1	2.82	Si3	4.02
Lu2	2.75	Si4	4.01
Lu3	2.75	Si5	4.19
Lu4	2.71	Si6	4.08
Lu5	2.65	Si7	4.22
Lu6	2.73	Si8	4.14
Ba1	1.88	Si9	4.08
Ba2	1.82	Si10	3.77
Si1	4.07	Si11	4.30
Si2	3.21	Si12	4.24
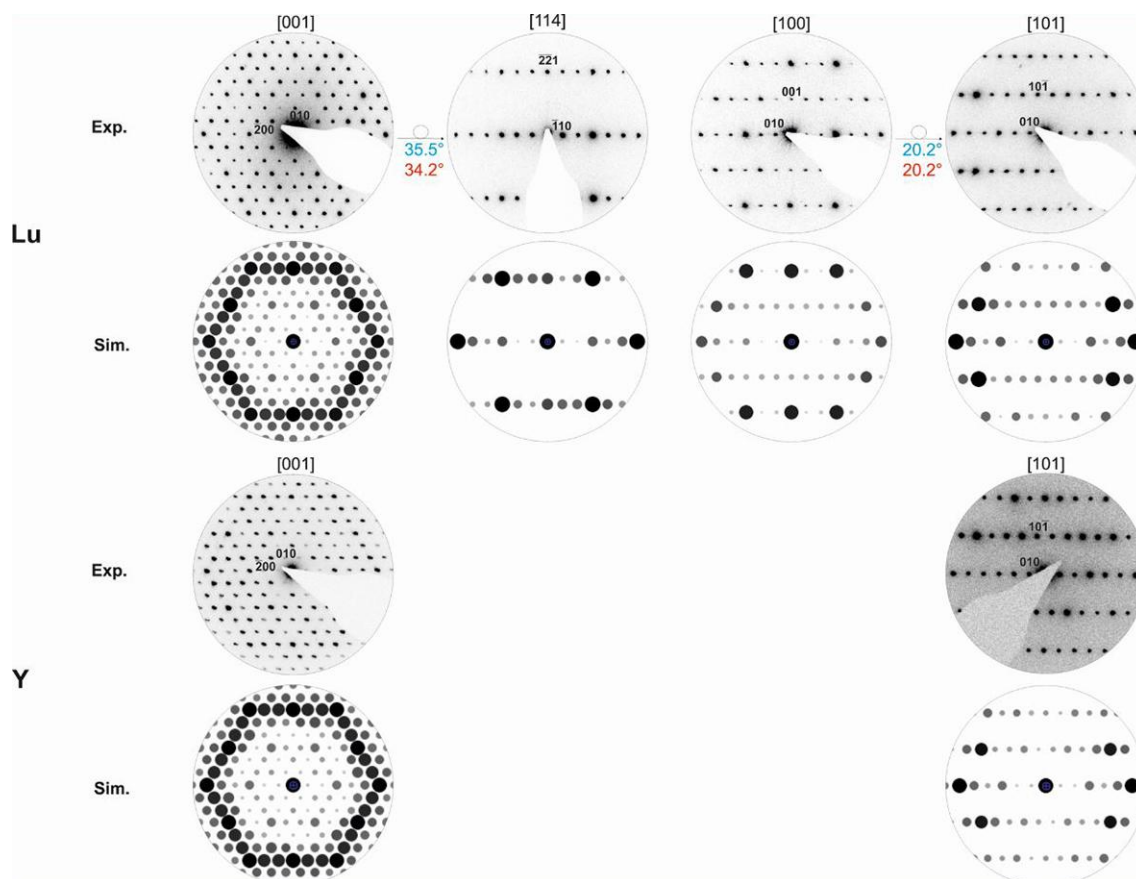
Figure S7. SAED patterns of Lu$_4$Ba$_2$[Si$_{12}$O$_2$N$_{16}$C$_3$] (top) and Y$_4$Ba$_2$[Si$_{12}$O$_2$N$_{16}$C$_3$] (bottom) with simulations and experimental tilt angles (blue) and theoretical tilt angles (red).

Table S9. Wyckoff positions, fractional atomic coordinates, isotropic displacement parameters [Å^2] and site occupancy factors for $Lu_4Ba_2[Si_{12}O_2N_{16}C_3]$ from single-crystal X-ray diffraction data (standard deviations in parentheses). The isotropic displacement parameters for the Si atoms and the C/O/N atoms were constrained to be of the same values, respectively.

Site	Wyckoff	x	y	z	U_{eq}/U_{iso}	s.o.f
Lu1	3d	0.18417(5)	0.42197(5)	0.4997(8)	0.00629(12)	1
Lu2	3d	0.24661(5)	0.13679(5)	0.9998(7)	0.00660(12)	1
Lu3	3d	0.59619(5)	0.09000(5)	0.0009(8)	0.00712(12)	1
Lu4	1c	2/3	1/3	0.0030(13)	0.0123(2)	1
Lu5	1b	1/3	2/3	0.5027(14)	0.0123(2)	1
Lu6	1a	0	0	0.0001(13)	0.0106(2)	1
Ba1	3d	0.03140(8)	0.36458(8)	0.0038(11)	0.0123(2)	1
Ba2	3d	0.33154(8)	0.30131(8)	0.5032(12)	0.0118(2)	1
Si1	3d	0.0940(7)	0.2047(8)	0.7603(15)	0.007(2)	1
Si2	3d	0.0943(7)	0.2076(7)	0.2491(14)	0.004(2)	1
Si3	3d	0.1196(3)	0.0686(3)	0.500(4)	0.0059(7)	1
Si4	3d	0.1284(7)	0.5875(7)	0.7454(15)	0.007(2)	1
Si5	3d	0.1315(7)	0.5913(7)	0.2578(15)	0.004(2)	1
Si6	3d	0.2545(3)	0.3580(3)	0.999(4)	0.0062(8)	1
Si7	3d	0.2582(3)	0.5486(3)	0.990(2)	0.0051(9)	1
Si8	3d	0.3009(3)	0.0573(3)	0.503(4)	0.0048(8)	1
Si9	3d	0.4616(3)	0.0237(3)	0.497(4)	0.0059(8)	1
Si10	3d	0.4643(7)	0.1909(7)	0.7558(14)	0.004(2)	1
Si11	3d	0.4663(8)	0.1892(7)	0.249(2)	0.008(2)	1
Si12	3d	0.6403(3)	0.2179(3)	0.491(3)	0.0062(8)	1
C1	3d	0.0173(10)	0.1831(10)	0.490(6)	0.0030(15)	1
C2	3d	0.3307(10)	0.4913(10)	0.998(14)	0.0030(15)	1
C3	3d	0.5122(10)	0.1543(10)	0.485(4)	0.0030(15)	1
N1	3d	0.3458(17)	0.1390(15)	0.732(4)	0.0088(7)	0.9375
O1	3d	0.3458(17)	0.1390(15)	0.732(4)	0.0088(7)	0.0625
N2	3d	0.0248(10)	0.1710(10)	0.994(9)	0.0088(7)	0.9375
O2	3d	0.0248(10)	0.1710(10)	0.994(9)	0.0088(7)	0.0625
N3	3d	0.161(2)	0.1457(15)	0.718(3)	0.0088(7)	0.9375
O3	3d	0.161(2)	0.1457(15)	0.718(3)	0.0088(7)	0.0625
N4	3d	0.497(2)	0.3096(14)	0.273(3)	0.0088(7)	0.9375
O4	3d	0.497(2)	0.3096(14)	0.273(3)	0.0088(7)	0.0625
N5	3d	0.014(2)	0.5161(15)	0.267(4)	0.0088(7)	0.9375
O5	3d	0.014(2)	0.5161(15)	0.267(4)	0.0088(7)	0.0625
N6	3d	0.182(2)	0.3300(2)	0.765(4)	0.0088(7)	0.9375

O6	3*d*	0.182(2)	0.3300(2)	0.765(4)	0.0088(7)	0.0625
N7	3*d*	0.186(2)	0.3175(15)	0.239(4)	0.0088(7)	0.9375
O7	3*d*	0.186(2)	0.3175(15)	0.239(4)	0.0088(7)	0.0625
N8	3*d*	0.5057(10)	0.1691(10)	0.997(12)	0.0088(7)	0.9375
O8	3*d*	0.5057(10)	0.1691(10)	0.997(12)	0.0088(7)	0.0625
N9	3*d*	0.341(2)	0.1221(14)	0.256(4)	0.0088(7)	0.9375
O9	3*d*	0.341(2)	0.1221(14)	0.256(4)	0.0088(7)	0.0625
N10	3*d*	0.2110(15)	0.5455(15)	0.753(3)	0.0088(7)	0.9375
O10	3*d*	0.2110(15)	0.5455(15)	0.753(3)	0.0088(7)	0.0625
N11	3*d*	0.1798(15)	0.5184(15)	0.227(3)	0.0088(7)	0.9375
O11	3*d*	0.1798(15)	0.5184(15)	0.227(3)	0.0088(7)	0.0625
N12	3*d*	0.3470(10)	0.5130(10)	0.491(7)	0.0088(7)	0.9375
O12	3*d*	0.3470(10)	0.5130(10)	0.491(7)	0.0088(7)	0.0625
N13	3*d*	0.0227(10)	0.3642(11)	0.515(4)	0.0088(7)	0.9375
O13	3*d*	0.0227(10)	0.3642(11)	0.515(4)	0.0088(7)	0.0625
N14	3*d*	0.1253(15)	0.1207(15)	0.248(3)	0.0088(7)	0.9375
O14	3*d*	0.1253(15)	0.1207(15)	0.248(3)	0.0088(7)	0.0625
N15	3*d*	0.5311(15)	0.3107(15)	0.746(3)	0.0088(7)	0.9375
O15	3*d*	0.5311(15)	0.3107(15)	0.746(3)	0.0088(7)	0.0625
N16	3*d*	0.010(2)	0.504(2)	0.735(4)	0.0088(7)	0.9375
O16	3*d*	0.010(2)	0.504(2)	0.735(4)	0.0088(7)	0.0625
N17	1*c*	2/3	1/3	0.410(5)	0.0088(7)	1
N18	1*b*	1/3	2/3	0.074(5)	0.0088(7)	1
N19	1*a*	0	0	0.577(5)	0.0088(7)	1
O17	3*d*	0.3258(9)	0.3088(9)	0.013(4)	0.0088(7)	1

Table S10. Anisotropic displacement parameters (U_{iy} in Å^2) for the single-crystal structure determination of $Lu_4Ba_2[Si_{12}O_2N_{16}C_3]$ (standard deviations in parentheses).

Atom	U_{11}	U_{22}	U_{33}	U_{23}	U_{13}	U_{12}
Lu1	0.0058(2)	0.0057(2)	0.0071(2)	−0.0004(12)	0.0026(12)	0.0027(2)
Lu2	0.0068(2)	0.0079(2)	0.0059(2)	−0.0007(14)	0.0011(12)	0.0043(2)
Lu3	0.0063(3)	0.0073(3)	0.0070(2)	0.0012(14)	0.0005(14)	0.0028(2)
Lu4	0.0142(4)	0.0142(4)	0.0085(5)	0	0	0.0071(2)
Lu5	0.0142(3)	0.0142(3)	0.0085(5)	0	0	0.0071(2)
Lu6	0.0123(3)	0.0123(3)	0.0074(5)	0	0	0.0061(2)
Ba1	0.0110(4)	0.0103(4)	0.0108(4)	0.000(2)	0.006(2)	0.0017(3)
Ba2	0.0103(4)	0.0142(4)	0.0111(4)	0.000(2)	0.000(2)	0.0062(3)
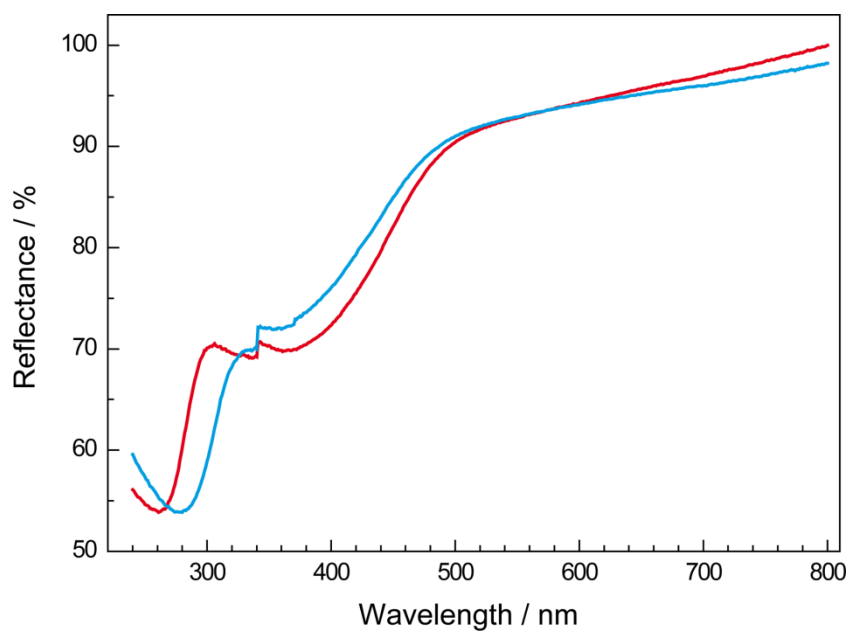
Figure S8. Diffuse reflectance UV/Vis spectra of doped samples of $Lu_4Ba_2[Si_{12}O_2N_{16}C_3]$:$Eu^{2+}$ (red) and $Y_4Ba_2[Si_{12}O_2N_{16}C_3]$:$Eu^{2+}$ (blue). The artifacts around 340 nm correspond to the lamp-switch.

References

[1]   Schlieper, T.; Milius, W.; Schnick, W. Nitridosilicate. II: Hochtemperatur-Synthesen und Kristallstrukturen von $Sr_2Si_5N_8$ und $Ba_2Si_5N_8$. *Z. Anorg. Allg. Chem.* **1995**, *621*, 1380–1384.

[2]   Hoppe, R. Madelung constants. *Angew. Chem., Int. Ed. Engl.* **1966**, *5*, 95–106; Über Madelungfaktoren. *Angew. Chem.* **1966**, *78*, 52–63.

[3]   Hoppe, R. The Coordination Number – an "Inorganic Chameleon". *Angew. Chem., Int. Ed. Engl.* **1970**, *9*, 25–34; Die Koordinationszahl – ein „anorganisches Chamäleon". *Angew. Chem.* **1970**, *82*, 7–16.

[4]   Hübenthal, R. *Maple, Program for the Calculation of MAPLE values, version 4*, University of Gießen: Gießen, Germany, 1993.

[5]   Klemm, W.; Winkelmann, G. Zur Kenntnis der Nitride der Seltenen Erden. *Z. Anorg. Allg. Chem.* **1956**, *288*, 87–90.

[6]   Ghebouli, M. A.; Ghebouli, B.; Bouhemadou, A.; Fatmi, M.; Bouamama, K. Structural, electronic, optical and thermodynamic properties of $Sr_xCa_{1-x}O$, $Ba_xSr_{1-x}O$ and $Ba_xCa_{1-x}O$ alloys. *J. Alloys Compd.* **2011**, *509*, 1440–1447.

[7]   Gomes de Mesquita, A. H. Refinement of the crystal structure of SiC type 6*H*. *Acta Crystallogr.* **1967**, *23*, 610–617.

[8]   Yang, P.; Fun, H.-K.; Rahman, I. A.; Saleh, M. I. Two phase refinements of the structures of α-Si_3N_4 and β-Si_3N_4 made from rice husk by Rietveld analysis. *Ceram. Int.* **1995**, *21*, 137–142.

[9]   Zeuner, M.; Pagano, S.; Schnick, W. Nitridosilicates and Oxonitridosilicates: From Ceramic Materials to Structural and Functional Diversity. *Angew. Chem., Int. Ed.* **2011**, *50*, 7754–7775; Nitridosilicate und Oxonitridosilicate: von keramischen Materialien zu struktureller und funktioneller Diversität. *Angew. Chem.* **2011**, *123*, 7898–7920.

[10]   Höppe, H. A.; Kotzyba, G.; Pöttgen, R.; Schnick, W. High-temperature synthesis, crystal structure, optical properties, and magnetism of the carbidonitridosilicates $Ho_2[Si_4N_6C]$ and $Tb_2[Si_4N_6C]$. *J. Mater. Chem.* **2001**, *11*, 3300–3306.

[11]   Momma, K.; Izumi, F. VESTA 3 for Three-Dimensional Visualization of Crystal, Volumetric and Morphology Data. *J. Appl. Crystallogr.* **2011**, *44*, 1272–1276.

[12]   Hoppe, R.; Voigt, S.; Glaum, H.; Kissel, J.; Müller, H. P.; Bernet, K. A new route to charge distributions in ionic solids. *J. Less-Common Met.* **1989**, *156*, 105–122.

11.5 Supporting Information for Chapter 6

Oxonitridosilicate Oxides $RE_{26}Ba_6[Si_{22}O_{19}N_{36}]O_{16}$:Eu^{2+} ($RE$ = Y, Tb) with a Unique Layered Structure and Orange-Red Luminescence for RE = Y

Christian Maak, Constantin Hoch, Peter J. Schmidt, and Wolfgang Schnick

Inorg. Chem. **2018**, 57, 2242–2248
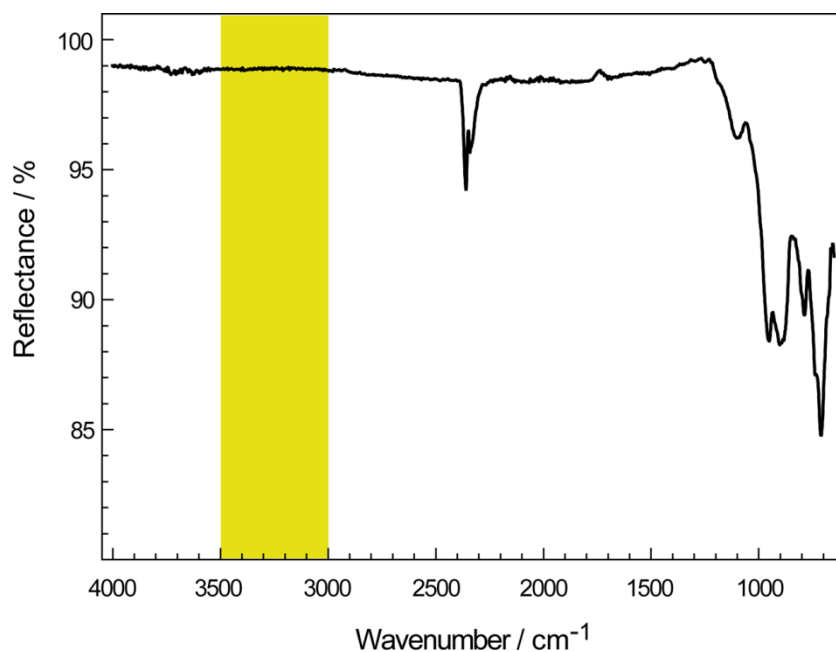
Figure S1. ATR-FTIR spectrum of a $Y_{26}Ba_6[Si_{22}O_{19}N_{36}]O_{16}$:Eu^{2+} powder sample. Typical region for N–H and O–H vibrations colored yellow. Bands at 2345 cm^{-1} belong to the asymmetric stretch vibration of CO_2.
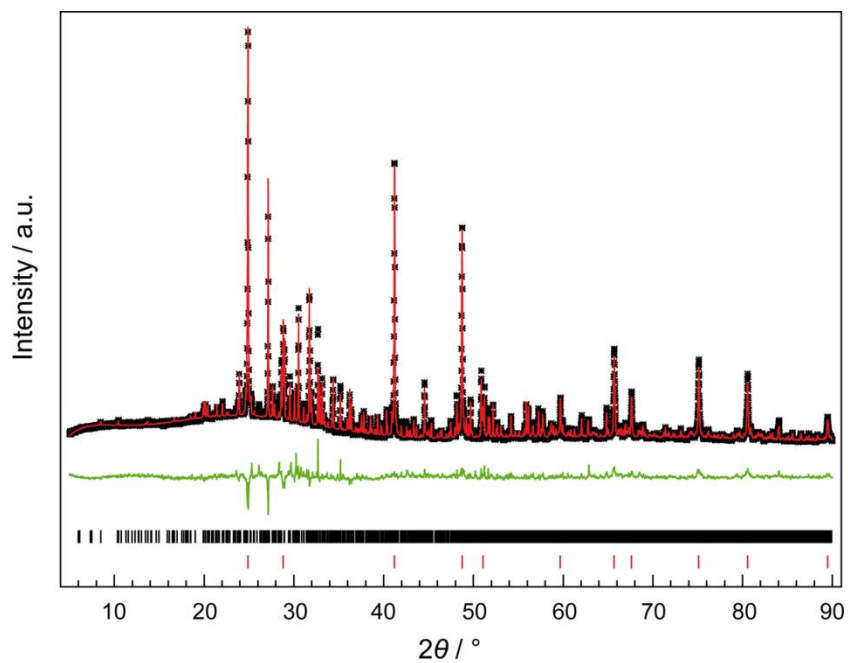
Figure S2. Rietveld refinement of data collected for an unwashed $Y_{26}Ba_6[Si_{22}O_{19}N_{36}]O_{16}$:$Eu^{2+}$ sample. Experimental data as black stars, Rietveld fit as red line and difference plot as green line. Reflection positions for $Y_{26}Ba_6[Si_{22}O_{19}N_{36}]O_{16}$:$Eu^{2+}$ (black bars, 70 wt%) and BaF_2 (red bars, 30 wt%).

Table S1. Data for Rietveld refinements of a washed and an unwashed $Y_{26}Ba_6[Si_{22}O_{19}N_{36}]O_{16}{:}Eu^{2+}$ sample. Structure data from single-crystal X-ray data were used. Only lattice parameters and profile parameters were refined (standard deviations in parentheses).

	Washed sample	Unwashed sample
formula mass / $g{\cdot}mol^{-1}$	4818.04	
crystal system	monoclinic	
space group	Pm (no. 6)	
lattice parameters / Å, °	$a = 16.42947(14)$, $b = 20.8563(2)$ $c = 16.9237(5)$, $\beta = 119.052(3)$	$a = 16.4317(4)$, $b = 20.8595(4)$ $c = 16.9271(8)$, $\beta = 119.052(4)$
volume / $Å^3$	5069.4(2)	5071.9(3)
formula units/cell	3	
X-ray density / $g{\cdot}cm^{-3}$	4.7342(1)	4.7319(3)
diffractometer, detector	Stoe StadiP, MYTHEN 1K	
radiation	Cu Kα_1 (λ = 1.54056 Å)	
monochromator	Ge(111)	
$F(000)$	6570	
2θ range, increment / °	5–90, 0.015	
data points	5695	
number of observed reflections	4374	
number of parameters	25	31
program used	TOPAS Academic V4.1	
background function	Shifted Chebyshev 12 polynomials	
R_{wp}	0.0522	0.0600
R_{exp}	0.0235	0.0265
R_p	0.0373	0.0446
R_{Bragg}	0.0310	0.0479
χ^2	2.220	2.265

Table S2. Si, N, O, and O/N atom groups with constrained isotropic displacement parameters. Left column: Chemically equivalent group of atoms. Right column: Affected atoms, compare with Tables S3 and S4.

Si in Q^1-type tetrahedra	Si2, Si8, Si18
Si in Q^2-type tetrahedra	Si19, Si30, Si35, Si37, Si38, Si39, Si40, Si41, Si42
Si in Q^3-type tetrahedra	Si3, Si4, Si9, Si10, Si14, Si15, Si21,Si22, Si26, Si27, Si31, Si32
Si in Q^4-type tetrahedra	Si1, Si5, Si6, Si7, Si11, Si12, Si13, Si16, Si17, Si20, Si23, Si24, Si25, Si28, Si29, Si33, Si34, Si36
Twofold bridging N atoms	N1–N60
Noncondensed O atoms	O1–O24
N/O in Q^1-type tetrahedra	N/O61, N/O62, N/O63, N/O66, N/O67,N/O68, N/O71 N/O72, N/O73
N/O in Q^2-type tetrahedra	N/O76, N/O77, N/O80, N/O81, N/O84, N/O85, N/O89, N/O90, N/O88, N/O91, N/O92, N/O93
N/O in Q^3-type tetrahedra	O/N64, N/O65, N/O69, N/O70, N/O74, N/O75, N/O78, N/O79, N/O82, N/O83, N/O86, N/O87

Table S3. Atomic coordinates, isotropic displacement parameters (in $\mathring{A}^2$), and site occupancy factors (*s.o.f.*) of $Y_{26}Ba_6[Si_{22}O_{19}N_{36}]O_{16}:Eu^{2+}$ with standard deviations in parentheses.

Atom	Wyckoff	x	y	z	U_{eq}	s.o.f.
Ba1	1*a*	0.0001(2)	0	0.0002(2)	0.0381(7)	1
Ba2	1*a*	0.9971(2)	0	0.49882(12)	0.0149(4)	1
Ba3	1*a*	0.1692(2)	0	0.3352(2)	0.0310(6)	1
Ba4	1*a*	0.3327(2)	0	0.6649(2)	0.0338(6)	1
Ba5	1*a*	0.50203(13)	0	0.9759(2)	0.0172(4)	1
Ba6	1*a*	0.30565(13)	0	0.15954(12)	0.0122(4)	1
Ba7	1*a*	0.6606(2)	0	0.82683(13)	0.0169(4)	1
Ba8	1*a*	0.68776(12)	0	0.35694(12)	0.0105(4)	1
Ba9	1*a*	0.8359(2)	0	0.6700(2)	0.0236(5)	1
Ba10	1*b*	0.8116(2)	1/2	0.83008(13)	0.0178(4)	1
Ba11	1*b*	0.96436(14)	1/2	0.68621(14)	0.0195(5)	1
Ba12	1*b*	0.7723(2)	1/2	0.3141(2)	0.0300(6)	1
Ba13	1*b*	0.62896(14)	1/2	0.0200(2)	0.0207(5)	1
Ba14	1*b*	0.45683(12)	1/2	0.16358(12)	0.0091(4)	1
Ba15	1*b*	0.13195(13)	1/2	0.00852(13)	0.0133(4)	1
Ba16	1*b*	0.2907(2)	1/2	0.3239(2)	0.0267(5)	1
Ba17	1*b*	0.4397(2)	1/2	0.6465(2)	0.0267(5)	1
Ba18	1*b*	0.1420(2)	1/2	0.49012(13)	0.0166(4)	1
Y1	2*c*	0.0384(2)	0.87316(13)	0.8319(2)	0.0376(8)	1

Y2	2c	0.16429(14)	0.88631(10)	0.70277(12)	0.0064(4)	1
Y3	2c	0.29271(14)	0.11275(10)	0.95935(13)	0.0079(4)	1
Y4	2c	0.3667(2)	0.87377(13)	0.4868(2)	0.0308(6)	1
Y5	2c	0.50141(14)	0.11505(10)	0.36594(13)	0.0068(4)	1
Y6	2c	0.62117(13)	0.88784(10)	0.62063(12)	0.0062(4)	1
Y7	2c	0.69721(14)	0.87921(10)	0.1585(2)	0.0114(4)	1
Y8	2c	0.82940(14)	0.11392(10)	0.03390(13)	0.0070(4)	1
Y9	2c	0.95384(13)	0.88826(10)	0.28859(13)	0.0056(4)	1
Y10	2c	0.40984(14)	0.83261(11)	0.82746(12)	0.0103(4)	1
Y11	2c	0.74522(13)	0.83227(11)	0.49787(12)	0.0092(4)	1
Y12	2c	0.2315(2)	0.24997(12)	0.8332(2)	0.0064(3)	1
Y13	2c	0.07541(13)	0.83359(11)	0.16146(12)	0.0079(4)	1
Y14	2c	0.27403(14)	0.77087(10)	0.60989(12)	0.0074(4)	1
Y15	2c	0.16304(13)	0.77260(10)	0.37783(12)	0.0065(4)	1
Y16	2c	0.29813(13)	0.73172(10)	0.27704(12)	0.0066(4)	1
Y17	2c	0.17562(13)	0.72841(10)	0.04524(13)	0.0074(4)	1
Y18	2c	0.51036(13)	0.72440(10)	0.71209(12)	0.0065(4)	1
Y19	2c	0.63157(14)	0.27566(10)	0.94320(12)	0.0071(4)	1
Y20	2c	0.5648(2)	0.74939(12)	0.4999(2)	0.0064(3)	1
Y21	2c	0.49745(14)	0.22362(10)	0.04697(12)	0.0055(4)	1
Y22	2c	0.60570(13)	0.22367(10)	0.27691(12)	0.0061(4)	1
Y23	2c	0.83229(14)	0.77299(10)	0.71325(12)	0.0061(4)	1
Y24	2c	0.93964(14)	0.76948(10)	0.94446(12)	0.0072(4)	1
Y25	2c	0.84357(13)	0.27599(10)	0.38078(12)	0.0062(4)	1
Y26	2c	0.96673(14)	0.72560(11)	0.61091(12)	0.0074(4)	1
Y27	2c	0.89520(11)	0.75121(8)	0.16651(12)	0.0056(4)	1
Y28	2c	0.04820(13)	0.33261(11)	0.83071(12)	0.0079(4)	1
Y29	2c	0.16078(14)	0.61483(10)	0.69909(13)	0.0072(4)	1
Y30	2c	0.29512(13)	0.38851(10)	0.95315(12)	0.0048(4)	1
Y31	2c	0.4178(2)	0.37809(11)	0.8208(2)	0.0158(5)	1
Y32	2c	0.37979(13)	0.33291(11)	0.49329(12)	0.0083(4)	1
Y33	2c	0.62862(14)	0.61235(10)	0.62484(13)	0.0075(4)	1
Y34	2c	0.50117(13)	0.38677(10)	0.36892(12)	0.0058(4)	1
Y35	2c	0.7567(2)	0.37773(12)	0.4965(2)	0.0214(5)	1
Y36	2c	0.71307(14)	0.33171(11)	0.16309(13)	0.0090(4)	1
Y37	2c	0.96043(14)	0.61239(10)	0.29022(13)	0.0084(4)	1
Y38	2c	0.82820(14)	0.61436(10)	0.03448(13)	0.0075(4)	1
Y39	2c	0.0828(2)	0.37099(13)	0.1589(3)	0.0425(9)	1
Si1	2c	0.0273(3)	0.8012(2)	0.4922(3)	0.0054(2)	1
Si2	2c	0.1573(3)	0.8943(2)	0.4952(3)	0.0063(4)	1

Si3	2c	0.8426(4)	0.8726(3)	0.3916(3)	0.0039(2)	1
Si4	2c	0.9463(3)	0.8744(3)	0.5959(3)	0.0039(2)	1
Si5	1a	0.8186(5)	0	0.2603(4)	0.0054(2)	1
Si6	1a	0.0590(5)	0	0.7289(5)	0.0054(2)	1
Si7	2c	0.6936(3)	0.8010(2)	0.8245(3)	0.0054(2)	1
Si8	2c	0.8235(3)	0.8943(2)	0.8270(3)	0.0063(4)	1
Si9	2c	0.5074(3)	0.8734(3)	0.7225(3)	0.0039(2)	1
Si10	2c	0.6127(3)	0.8734(2)	0.9259(3)	0.0039(2)	1
Si11	1a	0.4864(5)	0	0.5909(4)	0.0054(2)	1
Si12	1a	0.7233(5)	0	0.0585(5)	0.0054(2)	1
Si13	2c	0.4257(3)	0.2998(2)	0.1578(3)	0.0054(2)	1
Si14	2c	0.5094(3)	0.3734(3)	0.0572(3)	0.0039(2)	1
Si15	2c	0.6094(3)	0.3737(3)	0.2614(3)	0.0039(2)	1
Si16	1b	0.4009(5)	1/2	0.9243(4)	0.0054(2)	1
Si17	1b	0.6308(5)	1/2	0.3949(5)	0.0054(2)	1
Si18	2c	0.2988(4)	0.3931(3)	0.1605(3)	0.0063(4)	1
Si19	2c	0.9538(3)	0.5788(2)	0.4962(3)	0.0055(3)	1
Si20	2c	0.0795(3)	0.6687(2)	0.4857(3)	0.0054(2)	1
Si21	2c	0.1771(3)	0.6274(2)	0.3872(3)	0.0039(2)	1
Si22	2c	0.2749(3)	0.6260(3)	0.5928(3)	0.0039(2)	1
Si23	1b	0.0641(5)	1/2	0.2615(5)	0.0054(2)	1
Si24	1b	0.2915(5)	1/2	0.7223(4)	0.0054(2)	1
Si25	2c	0.3659(3)	0.1677(2)	0.1500(3)	0.0054(2)	1
Si26	2c	0.1720(3)	0.1283(2)	0.0554(3)	0.0039(2)	1
Si27	2c	0.2798(3)	0.1258(3)	0.2606(3)	0.0039(2)	1
Si28	1a	0.3940(5)	0	0.3893(4)	0.0054(2)	1
Si29	1a	0.1591(5)	0	0.9296(5)	0.0054(2)	1
Si30	2c	0.5050(3)	0.0769(3)	0.1635(3)	0.0055(3)	1
Si31	2c	0.9438(3)	0.6252(3)	0.9295(3)	0.0039(2)	1
Si32	2c	0.8448(3)	0.6283(3)	0.7231(3)	0.0039(2)	1
Si33	1b	0.9586(5)	1/2	0.0585(5)	0.0054(2)	1
Si34	1b	0.7346(5)	1/2	0.5964(5)	0.0054(2)	1
Si35	2c	0.6211(3)	0.5787(2)	0.8306(3)	0.0055(3)	1
Si36	2c	0.7474(3)	0.6684(2)	0.8205(3)	0.0054(2)	1
Si37	1a	0.2756(5)	0	0.8321(5)	0.0055(3)	1
Si38	1a	0.9359(5)	0	0.1612(5)	0.0055(3)	1
Si39	1a	0.6056(5)	0	0.4945(5)	0.0055(3)	1
Si40	1b	0.1847(5)	1/2	0.8266(5)	0.0055(3)	1
Si41	1b	0.8498(5)	1/2	0.1638(5)	0.0055(3)	1
Si42	1b	0.5186(5)	1/2	0.4973(5)	0.0055(3)	1

N1	1a	0.502(2)	0	0.3923(14)	0.0088(3)	1
N2	2c	0.9613(10)	0.5675(8)	0.0077(10)	0.0088(3)	1
N3	2c	0.0970(10)	0.6788(7)	0.3926(9)	0.0088(3)	1
N4	2c	0.7990(10)	0.8121(7)	0.8275(10)	0.0088(3)	1
N5	2c	0.1333(10)	0.8124(7)	0.4947(9)	0.0088(3)	1
N6	2c	0.8138(10)	0.9285(8)	0.3068(9)	0.0088(3)	1
N7	2c	0.5955(10)	0.8259(8)	0.7291(10)	0.0088(3)	1
N8	1b	0.856(2)	1/2	0.064(2)	0.0088(3)	1
N9	1a	0.922 (2)	0	0.2548(14)	0.0088(3)	1
N10	2c	0.6994(10)	0.8285(8)	0.9230(10)	0.0088(3)	1
N11	1a	0.062(2)	0	0.831(2)	0.0088(3)	1
N12	2c	0.5274(11)	0.9049(8)	0.8262(10)	0.0088(3)	1
N13	2c	0.4562(10)	0.4298(7)	0.9724(9)	0.0088(3)	1
N14	1b	0.732(2)	1/2	0.497(2)	0.0088(3)	1
N15	2c	0.6914(8)	0.5950(6)	0.7891(8)	0.0088(3)	1
N16	2c	0.4849(10)	0.9283(8)	0.6413(9)	0.0088(3)	1
N17	1b	0.188(2)	1/2	0.7237(13)	0.0088(3)	1
N18	1b	0.532(2)	1/2	0.403(2)	0.0088(3)	1
N19	1b	0.057(2)	1/2	0.162(2)	0.0088(3)	1
N20	1a	0.723(2)	0	0.159(2)	0.0088(3)	1
N21	1b	0.628(2)	1/2	0.593(2)	0.0088(3)	1
N22	1a	0.831(2)	0	0.064(2)	0.0088(3)	1
N23	1a	0.5900(2)	0	0.5859(14)	0.0088(3)	1
N24	2c	0.6349(11)	0.4309(8)	0.3423(10)	0.0088(3)	1
N25	1a	0.2647(16)	0	0.927(2)	0.0088(3)	1
N26	2c	0.6685(10)	0.9298(8)	0.0060(9)	0.0088(3)	1
N27	1b	0.397(2)	1/2	0.8234(14)	0.0088(3)	1
N28	1a	0.5265(14)	0	0.1742(12)	0.0088(3)	1
N29	2c	0.4516(11)	0.2202(8)	0.1596(10)	0.0088(3)	1
N30	2c	0.5183(10)	0.3300(8)	0.2564(10)	0.0088(3)	1
N31	2c	0.1191(10)	0.5680(8)	0.3083(9)	0.0088(3)	1
N32	2c	0.0075(10)	0.9283(8)	0.6757(9)	0.0088(3)	1
N33	2c	0.8526(10)	0.6701(7)	0.9207(9)	0.0088(3)	1
N34	2c	0.2638(11)	0.5986(9)	0.4962(11)	0.0088(3)	1
N35	2c	0.7634(10)	0.6774(7)	0.7278(9)	0.0088(3)	1
N36	2c	0.8626(11)	0.9041(9)	0.4969(11)	0.0088(3)	1
N37	2c	0.0033(10)	0.7200(7)	0.4935(9)	0.0088(3)	1
N38	2c	0.9303(10)	0.8275(8)	0.3967(10)	0.0088(3)	1
N39	1b	0.9386(13)	1/2	0.5043(12)	0.0088(3)	1
N40	2c	0.5948(12)	0.4025(9)	0.1615(11)	0.0088(3)	1

N41	2c	0.2951(10)	0.5691(8)	0.6708(9)	0.0088(3)	1
N42	2c	0.9309(11)	0.5999(8)	0.8295(11)	0.0088(3)	1
N43	2c	0.6706(10)	0.7201(7)	0.8273(10)	0.0088(3)	1
N44	1b	0.956(2)	1/2	0.258(2)	0.0088(3)	1
N45	2c	0.4251(11)	0.3299(8)	0.0637(10)	0.0088(3)	1
N46	2c	0.1946(12)	0.0989(9)	0.1632(11)	0.0088(3)	1
N47	2c	0.0308(11)	0.8294(8)	0.5906(10)	0.0088(3)	1
N48	2c	0.3643(10)	0.1703(7)	0.2518(9)	0.0088(3)	1
N49	1b	0.6072(13)	1/2	0.8418(12)	0.0088(3)	1
N50	2c	0.3927(8)	0.0942(6)	0.1229(8)	0.0088(3)	1
N51	2c	0.3392(10)	0.0701(7)	0.3350(9)	0.0088(3)	1
N52	2c	0.1827(10)	0.6713(7)	0.5844(9)	0.0088(3)	1
N53	2c	0.0232(8)	0.5953(6)	0.4540(8)	0.0088(3)	1
N54	2c	0.7882(10)	0.4296(8)	0.6426(9)	0.0088(3)	1
N55	2c	0.1554(11)	0.0701(8)	0.9793(10)	0.0088(3)	1
N56	2c	0.3217(11)	0.3142(8)	0.1602(10)	0.0088(3)	1
N57	1a	0.390(2)	0	0.4899(14)	0.0088(3)	1
N58	2c	0.2562(9)	0.1805(6)	0.0595(9)	0.0088(3)	1
N59	1b	0.294(2)	1/2	0.9154(14)	0.0088(3)	1
N60	1a	0.167(2)	0	0.737(2)	0.0088(3)	1
O1	2c	0.6001(9)	0.2015(6)	0.4023(8)	0.0077(4)	1
O2	2c	0.2624(9)	0.8011(6)	0.7301(9)	0.0077(4)	1
O3	2c	0.3152(9)	0.7723(7)	0.4964(9)	0.0077(4)	1
O4	2c	0.3628(9)	0.1955(6)	0.9291(8)	0.0077(4)	1
O5	2c	0.6473(9)	0.2214(6)	0.1664(8)	0.0077(4)	1
O6	2c	0.9829(9)	0.7722(7)	0.8332(9)	0.0077(4)	1
O7	2c	0.8303(9)	0.1514(7)	0.1621(9)	0.0077(4)	1
O8	2c	0.1954(9)	0.3052(6)	0.9300(9)	0.0077(4)	1
O9	2c	0.5279(9)	0.3049(6)	0.5961(9)	0.0077(4)	1
O10	2c	0.8604(9)	0.3042(6)	0.2631(8)	0.0077(4)	1
O11	2c	0.4976(9)	0.8474(7)	0.4924(8)	0.0077(4)	1
O12	2c	0.0278(9)	0.8062(6)	0.2627(8)	0.0077(4)	1
O13	2c	0.6275(9)	0.6531(7)	0.5003(9)	0.0077(4)	1
O14	2c	0.9529(9)	0.6553(6)	0.1616(9)	0.0077(4)	1
O15	2c	0.2913(9)	0.3458(7)	0.8245(8)	0.0077(4)	1
O16	2c	0.1688(9)	0.1515(7)	0.8315(9)	0.0077(4)	1
O17	2c	0.6957(9)	0.8046(6)	0.5969(9)	0.0077(4)	1
O18	2c	0.4290(9)	0.3016(6)	0.3958(9)	0.0077(4)	1
O19	2c	0.9295(9)	0.8012(6)	0.0650(9)	0.0077(4)	1
O20	2c	0.0973(9)	0.2984(6)	0.7343(8)	0.0077(4)	1

O21	2*c*	0.8136(9)	0.7240(6)	0.5008(8)	0.0077(4)	1
O22	2*c*	0.1442(9)	0.7294(7)	0.1648(9)	0.0077(4)	1
O23	2*c*	0.7616(9)	0.2993(6)	0.0662(8)	0.0077(4)	1
O24	2*c*	0.4783(9)	0.7243(7)	0.8322(8)	0.0077(4)	1
N61 / O61	2*c*	0.2447(9)	0.9062(6)	0.4783(9)	0.0272(10)	0.1364 / 0.8636
N62 / O62	2*c*	0.1750(9)	0.9273(7)	0.5865(9)	0.0272(10)	0.1364 / 0.8636
N63 / O63	2*c*	0.0727(9)	0.9307(7)	0.4108(9)	0.0272(10)	0.1364 / 0.8636
N64 / O64	2*c*	0.7541(10)	0.8210(7)	0.3601(9)	0.0110(6)	0.1364 / 0.8636
N65 / O65	2*c*	0.8944(9)	0.8211(6)	0.6322(8)	0.0110(6)	0.1364 / 0.8636
N66 / O66	2*c*	0.9056(9)	0.9031(6)	0.8027(9)	0.0272(10)	0.1364 / 0.8636
N67 / O67	2*c*	0.7379(9)	0.9300(7)	0.7454(9)	0.0272(10)	0.1364 / 0.8636
N68 / O68	2*c*	0.8467(9)	0.9267(7)	0.9207(9)	0.0272(10)	0.1364 / 0.8636
N69 / O69	2*c*	0.4137(9)	0.8230(7)	0.6868(9)	0.0110(6)	0.1364 / 0.8636
N70 / O70	2*c*	0.5609(9)	0.8196(7)	0.9627(8)	0.0110(6)	0.1364 / 0.8636
N71 / O71	2*c*	0.1957(9)	0.4065(7)	0.1410(9)	0.0272(10)	0.1364 / 0.8636
N72 / O72	2*c*	0.3022(9)	0.4312(7)	0.0767(10)	0.0272(10)	0.1364 / 0.8636
N73 / O73	2*c*	0.3706(10)	0.4259(7)	0.2550(10)	0.0272(10)	0.1364 / 0.8636
N74/ O74	2*c*	0.6964(9)	0.3214(7)	0.2952(8)	0.0110(6)	0.1364 / 0.8636
N75 / O75	2*c*	0.5685(9)	0.3228(7)	0.0273(9)	0.0110(6)	0.1364 / 0.8636
N76 / O76	2*c*	0.9981(8)	0.6073(5)	0.6021(8)	0.0175(7)	0.1364 / 0.8636
N77 / O77	2*c*	0.8528(8)	0.6079(6)	0.4341(8)	0.0175(7)	0.1364 / 0.8636
N78 / O78	2*c*	0.3644(9)	0.6778(7)	0.6323(8)	0.0110(6)	0.1364 / 0.8636
N79 / O79	2*c*	0.2349(8)	0.6713(6)	0.3460(8)	0.0110(6)	0.1364 / 0.8636
N80 / O80	2*c*	0.5399(8)	0.1072(6)	0.0978(8)	0.0175(7)	0.1364 / 0.8636
N81 / O81	2*c*	0.5672(8)	0.1086(6)	0.2690(8)	0.0175(7)	0.1364 / 0.8636
N82 / O82	2*c*	0.0740(8)	0.1744(6)	0.0138(8)	0.0110(6)	0.1364 / 0.8636
N83 / O83	2*c*	0.2297(9)	0.1774(6)	0.3002(8)	0.0110(6)	0.1364 / 0.8636
N84 / O84	2*c*	0.6639(8)	0.6086(6)	0.9352(8)	0.0175(7)	0.1364 / 0.8636
N85 / O85	2*c*	0.5211(8)	0.6064(6)	0.7658(8)	0.0175(7)	0.1364 / 0.8636
N86 / O86	2*c*	0.0339(9)	0.6745(7)	0.9696(9)	0.0110(6)	0.1364 / 0.8636
N87 / O87	2*c*	0.9021(9)	0.6753(6)	0.6872(8)	0.0110(6)	0.1364 / 0.8636
N88 / O88	2*c*	0.6597(11)	0.0696(8)	0.4974(10)	0.0175(7)	0.1364 / 0.8636
N89 / O89	2*c*	0.3277(11)	0.0697(8)	0.8324(10)	0.0175(7)	0.1364 / 0.8636
N90 / O90	2*c*	0.9896(11)	0.9308(8)	0.1625(10)	0.0175(7)	0.1364 / 0.8636
N91 / O91	2*c*	0.7952(11)	0.4310(8)	0.1669(10)	0.0175(7)	0.1364 / 0.8636
N92 / O92	2*c*	0.4651(11)	0.4309(8)	0.5003(10)	0.0175(7)	0.1364 / 0.8636
N93 / O93	2*c*	0.1302(11)	0.4316(8)	0.8286(10)	0.0175(7)	0.1364 / 0.8636

Table S4. Atomic coordinates, isotropic displacement parameters (in Å^2), and site occupancy factors (*s.o.f.*) of $Tb_{26}Ba_6[Si_{22}O_{19}N_{36}]O_{16}:Eu^{2+}$ with standard deviations in parentheses.

Atom	Wyckoff	x	y	z	U_{eq}	s.o.f.
Ba1	1*a*	0.0008(4)	0	-0.0001(4)	0.0425(13)	1
Ba2	1*a*	0.9950(3)	0	0.4984(2)	0.0201(9)	1
Ba3	1*a*	0.1697(3)	0	0.3353(3)	0.0354(11)	1
Ba4	1*a*	0.3352(4)	0	0.6669(4)	0.0402(13)	1
Ba5	1*a*	0.5018(3)	0	0.9761(3)	0.0203(9)	1
Ba6	1*a*	0.3025(2)	0	0.1589(2)	0.0141(8)	1
Ba7	1*a*	0.6583(3)	0	0.8257(2)	0.0216(9)	1
Ba8	1*a*	0.6878(2)	0	0.3556(2)	0.0104(7)	1
Ba9	1*a*	0.8367(3)	0	0.6677(3)	0.0335(11)	1
Ba10	1*b*	0.8133(3)	1/2	0.8299(3)	0.0248(10)	1
Ba11	1*b*	0.9626(3)	1/2	0.6844(3)	0.0240(9)	1
Ba12	1*b*	0.7726(4)	1/2	0.3150(4)	0.0334(12)	1
Ba13	1*b*	0.6271(3)	1/2	0.0179(3)	0.0242(10)	1
Ba14	1*b*	0.4575(2)	1/2	0.1629(2)	0.0120(8)	1
Ba15	1*b*	0.1313(2)	1/2	0.0075(3)	0.0187(8)	1
Ba16	1*b*	0.2915(3)	1/2	0.3253(3)	0.0311(11)	1
Ba17	1*b*	0.4413(4)	1/2	0.6480(4)	0.0353(12)	1
Ba18	1*b*	0.1435(3)	1/2	0.4895(3)	0.0223(9)	1
Tb1	2*c*	0.0384(2)	0.8746(2)	0.8311(2)	0.0398(8)	1
Tb2	2*c*	0.16451(14)	0.88702(11)	0.70173(12)	0.0079(5)	1
Tb3	2*c*	0.29481(13)	0.11176(11)	0.96050(11)	0.0078(5)	1
Tb4	2*c*	0.3675(2)	0.87519(14)	0.4883(2)	0.0353(7)	1
Tb5	2*c*	0.50004(13)	0.11360(11)	0.36427(12)	0.0074(4)	1
Tb6	2*c*	0.6224(2)	0.88867(11)	0.62207(12)	0.0077(5)	1
Tb7	2*c*	0.6970(2)	0.87987(12)	0.1584(2)	0.0157(5)	1
Tb8	2*c*	0.82901(14)	0.11329(11)	0.03328(12)	0.0087(5)	1
Tb9	2*c*	0.95478(14)	0.88870(11)	0.28947(12)	0.0066(5)	1
Tb10	2*c*	0.40909(14)	0.83527(12)	0.82706(12)	0.0112(5)	1
Tb11	2*c*	0.74467(14)	0.83518(12)	0.49734(12)	0.0112(5)	1
Tb12	2*c*	0.2310(2)	0.25005(13)	0.8327(2)	0.0081(3)	1
Tb13	2*c*	0.07550(13)	0.83659(12)	0.16147(12)	0.0113(5)	1
Tb14	2*c*	0.27424(14)	0.77164(12)	0.61056(12)	0.0089(5)	1
Tb15	2*c*	0.16225(14)	0.77260(11)	0.37726(12)	0.0079(5)	1
Tb16	2*c*	0.2983(2)	0.73078(11)	0.27794(12)	0.0086(4)	1
Tb17	2*c*	0.17600(14)	0.72863(11)	0.04487(12)	0.0080(5)	1
Tb18	2*c*	0.51052(14)	0.72531(11)	0.71132(12)	0.0074(5)	1

Tb19	2c	0.63137(14)	0.27475(11)	0.94357(12)	0.0080(5)	1
Tb20	2c	0.5642(2)	0.74973(14)	0.4991(2)	0.0083(3)	1
Tb21	2c	0.49610(14)	0.22404(11)	0.04608(12)	0.0062(4)	1
Tb22	2c	0.60623(14)	0.22436(11)	0.27748(12)	0.0067(4)	1
Tb23	2c	0.83077(14)	0.77283(11)	0.71273(12)	0.0076(5)	1
Tb24	2c	0.94047(14)	0.77064(12)	0.94535(12)	0.0086(5)	1
Tb25	2c	0.84402(14)	0.27508(11)	0.38002(12)	0.0070(5)	1
Tb26	2c	0.96660(14)	0.72646(12)	0.61178(12)	0.0084(5)	1
Tb27	2c	0.89528(9)	0.75092(7)	0.16590(9)	0.0073(6)	1
Tb28	2c	0.04775(14)	0.33589(12)	0.83011(12)	0.0102(5)	1
Tb29	2c	0.1611(2)	0.61380(11)	0.69737(12)	0.0087(5)	1
Tb30	2c	0.29565(12)	0.38871(11)	0.95415(11)	0.0053(4)	1
Tb31	2c	0.4187(2)	0.37863(13)	0.8211(2)	0.0207(5)	1
Tb32	2c	0.37972(13)	0.33593(12)	0.49314(12)	0.0100(5)	1
Tb33	2c	0.62874(14)	0.61183(11)	0.62621(12)	0.0079(5)	1
Tb34	2c	0.50078(13)	0.38696(11)	0.36850(11)	0.0066(5)	1
Tb35	2c	0.7571(2)	0.37810(14)	0.4968(2)	0.0259(6)	1
Tb36	2c	0.71278(13)	0.33439(12)	0.16238(12)	0.0111(5)	1
Tb37	2c	0.96001(14)	0.61159(11)	0.29180(13)	0.0099(5)	1
Tb38	2c	0.8276(2)	0.61335(11)	0.03305(12)	0.0091(5)	1
Tb39	2c	0.0835(2)	0.6274(2)	0.1605(2)	0.0444(9)	1
Si1	2c	0.0296(5)	0.8015(4)	0.4932(5)	0.0079(3)	1
Si2	2c	0.1577(6)	0.8941(4)	0.4947(6)	0.0131(7)	1
Si3	2c	0.8439(7)	0.8732(6)	0.3928(6)	0.0051(3)	1
Si4	2c	0.9476(7)	0.8738(6)	0.5966(6)	0.0051(3)	1
Si5	1a	0.8202(9)	0	0.2613(9)	0.0079(3)	1
Si6	1a	0.0608(10)	0	0.7290(9)	0.0079(3)	1
Si7	2c	0.6957(5)	0.8016(4)	0.8248(5)	0.0079(3)	1
Si8	2c	0.8241(6)	0.8947(5)	0.8275(5)	0.0131(7)	1
Si9	2c	0.5072(6)	0.8738(5)	0.7225(6)	0.0051(3)	1
Si10	2c	0.6132(7)	0.8727(5)	0.9272(6)	0.0051(3)	1
Si11	1a	0.4879(9)	0	0.5918(8)	0.0079(3)	1
Si12	1a	0.7235(11)	0	0.0593(9)	0.0079(3)	1
Si13	2c	0.4272(6)	0.3000(5)	0.1586(6)	0.0079(3)	1
Si14	2c	0.5090(7)	0.3749(6)	0.0589(6)	0.0051(3)	1
Si15	2c	0.6088(7)	0.3741(5)	0.2611(6)	0.0051(3)	1
Si16	1b	0.4015(9)	1/2	0.9266(8)	0.0079(3)	1
Si17	1b	0.6320(11)	1/2	0.3952(9)	0.0079(3)	1
Si18	2c	0.2979(7)	0.3945(5)	0.1604(6)	0.0131(7)	1
Si19	2c	0.9546(5)	0.5799(4)	0.4951(5)	0.0077(4)	1

Si20	2c	0.0812(5)	0.6681(4)	0.4868(4)	0.0079(3)	1
Si21	2c	0.1767(6)	0.6268(5)	0.3884(6)	0.0051(3)	1
Si22	2c	0.2747(6)	0.6260(6)	0.5934(6)	0.0051(3)	1
Si23	1b	0.0643(10)	1/2	0.2622(9)	0.0079(3)	1
Si24	1b	0.2924(9)	1/2	0.7228(8)	0.0079(3)	1
Si25	2c	0.3668(5)	0.1680(4)	0.1515(4)	0.0079(3)	1
Si26	2c	0.1732(6)	0.1276(5)	0.0565(6)	0.0051(3)	1
Si27	2c	0.2811(7)	0.1255(5)	0.2611(6)	0.0051(3)	1
Si28	1a	0.3951(9)	0	0.3894(8)	0.0079(3)	1
Si29	1a	0.1601(10)	0	0.9293(9)	0.0079(3)	1
Si30	2c	0.5032(6)	0.0753(5)	0.1624(6)	0.0077(4)	1
Si31	2c	0.9423(7)	0.6251(6)	0.9295(6)	0.0051(3)	1
Si32	2c	0.8442(7)	0.6271(6)	0.7252(6)	0.0051(3)	1
Si33	1b	0.9581(9)	1/2	0.0583(8)	0.0079(3)	1
Si34	1b	0.7337(10)	1/2	0.5974(9)	0.0079(3)	1
Si35	2c	0.6214(5)	0.5792(4)	0.8300(5)	0.0077(4)	1
Si36	2c	0.7490(5)	0.6679(4)	0.8221(4)	0.0079(3)	1
Si37	1a	0.2750(10)	0	0.8299(9)	0.0077(4)	1
Si38	1a	0.9359(11)	0	0.1609(9)	0.0077(4)	1
Si39	1a	0.6074(10)	0	0.4943(9)	0.0077(4)	1
Si40	1b	0.1850(10)	1/2	0.8270(9)	0.0077(4)	1
Si41	1b	0.8494(11)	1/2	0.1624(9)	0.0077(4)	1
Si42	1b	0.5196(10)	1/2	0.4964(9)	0.0077(4)	1
N1	1a	0.502(3)	0	0.396(3)	0.0103(5)	1
N2	2c	0.966(2)	0.5727(14)	0.009(2)	0.0103(5)	1
N3	2c	0.097(2)	0.6778(13)	0.396(2)	0.0103(5)	1
N4	2c	0.797(2)	0.8114(12)	0.829(2)	0.0103(5)	1
N5	2c	0.131(2)	0.8111(12)	0.496(2)	0.0103(5)	1
N6	2c	0.815(2)	0.9295(14)	0.306(2)	0.0103(5)	1
N7	2c	0.596(2)	0.827(2)	0.731(2)	0.0103(5)	1
N8	1b	0.856(3)	1/2	0.066(3)	0.0103(5)	1
N9	1a	0.916(2)	0	0.254(2)	0.0103(5)	1
N10	2c	0.697(2)	0.8303(14)	0.9200(2)	0.0103(5)	1
N11	1a	0.064(3)	0	0.832(3)	0.0103(5)	1
N12	2c	0.527(2)	0.905(2)	0.826(2)	0.0103(5)	1
N13	2c	0.454(2)	0.4306(14)	0.973(2)	0.0103(5)	1
N14	1b	0.733(3)	1/2	0.497(3)	0.0103(5)	1
N15	2c	0.6961(13)	0.5902(9)	0.7938(13)	0.0103(5)	1
N16	2c	0.489(2)	0.931(2)	0.642(2)	0.0103(5)	1
N17	1b	0.187(3)	1/2	0.726(2)	0.0103(5)	1

N18	1*b*	0.532(3)	1/2	0.404(3)	0.0103(5)	1
N19	1*b*	0.062(3)	1/2	0.164(3)	0.0103(5)	1
N20	1*a*	0.725(3)	0	0.161(3)	0.0103(5)	1
N21	1*b*	0.624(3)	1/2	0.594(3)	0.0103(5)	1
N22	1*a*	0.825(3)	0	0.066(3)	0.0103(5)	1
N23	1*a*	0.590(3)	0	0.587(3)	0.0103(5)	1
N24	2*c*	0.633(2)	0.4308(14)	0.338(2)	0.0103(5)	1
N25	1*a*	0.265(3)	0	0.928(3)	0.0103(5)	1
N26	2*c*	0.668(2)	0.930(2)	0.008(2)	0.0103(5)	1
N27	1*b*	0.397(3)	1/2	0.825(3)	0.0103(5)	1
N28	1*a*	0.528(2)	0	0.173(2)	0.0103(5)	1
N29	2*c*	0.451(2)	0.2150(13)	0.162(2)	0.0103(5)	1
N30	2*c*	0.516(2)	0.3303(14)	0.255(2)	0.0103(5)	1
N31	2*c*	0.117(2)	0.5708(14)	0.3049(14)	0.0103(5)	1
N32	2*c*	0.007(2)	0.9296(14)	0.672(2)	0.0103(5)	1
N33	2*c*	0.851(2)	0.673(2)	0.923(2)	0.0103(5)	1
N34	2*c*	0.260(2)	0.600(2)	0.499(2)	0.0103(5)	1
N35	2*c*	0.764(2)	0.6777(13)	0.732(2)	0.0103(5)	1
N36	2*c*	0.865(2)	0.9076(15)	0.4999(18)	0.0103(5)	1
N37	2*c*	0.007(2)	0.7227(11)	0.496(2)	0.0103(5)	1
N38	2*c*	0.931(2)	0.827(2)	0.398(2)	0.0103(5)	1
N39	1*b*	0.938(2)	1/2	0.503(2)	0.0103(5)	1
N40	2*c*	0.592(2)	0.403(2)	0.161(2)	0.0103(5)	1
N41	2*c*	0.301(2)	0.5714(14)	0.672(2)	0.0103(5)	1
N42	2*c*	0.925(2)	0.599(2)	0.827(2)	0.0103(5)	1
N43	2*c*	0.673(2)	0.7220(11)	0.829(2)	0.0103(5)	1
N44	1*b*	0.953(3)	1/2	0.256(3)	0.0103(5)	1
N45	2*c*	0.426(2)	0.330(2)	0.064(2)	0.0103(5)	1
N46	2*c*	0.196(2)	0.095(2)	0.163(2)	0.0103(5)	1
N47	2*c*	0.030(2)	0.8288(14)	0.587(2)	0.0103(5)	1
N48	2*c*	0.364(2)	0.1704(14)	0.254(2)	0.0103(5)	1
N49	1*b*	0.608(2)	1/2	0.840(2)	0.0103(5)	1
N50	2*c*	0.3927(13)	0.0904(9)	0.1298(13)	0.0103(5)	1
N51	2*c*	0.340(2)	0.0666(12)	0.3330(14)	0.0103(5)	1
N52	2*c*	0.182(2)	0.672(2)	0.587(2)	0.0103(5)	1
N53	2*c*	0.0253(13)	0.5909(9)	0.4576(12)	0.0103(5)	1
N54	2*c*	0.787(2)	0.429(2)	0.646(2)	0.0103(5)	1
N55	2*c*	0.167(2)	0.0640(12)	0.985(2)	0.0103(5)	1
N56	2*c*	0.322(2)	0.3140(14)	0.162(2)	0.0103(5)	1
N57	1*a*	0.395(3)	0	0.490(3)	0.0103(5)	1

N58	2c	0.257(2)	0.1780(13)	0.062(2)	0.0103(5)	1
N59	1b	0.289(3)	1/2	0.914(2)	0.0103(5)	1
N60	1a	0.166(3)	0	0.735(3)	0.0103(5)	1
O1	2c	0.598(2)	0.2006(10)	0.4042(13)	0.0070(5)	1
O2	2c	0.261(2)	0.8004(11)	0.7314(14)	0.0070(5)	1
O3	2c	0.316(2)	0.7733(12)	0.498(2)	0.0070(5)	1
O4	2c	0.363(2)	0.1940(12)	0.9290(14)	0.0070(5)	1
O5	2c	0.648(2)	0.2207(11)	0.1679(13)	0.0070(5)	1
O6	2c	0.982(2)	0.7753(12)	0.8319(14)	0.0070(5)	1
O7	2c	0.829(2)	0.1543(12)	0.1628(14)	0.0070(5)	1
O8	2c	0.193(2)	0.3071(11)	0.9285(14)	0.0070(5)	1
O9	2c	0.526(2)	0.3063(11)	0.5967(14)	0.0070(5)	1
O10	2c	0.859(2)	0.3056(11)	0.2646(13)	0.0070(5)	1
O11	2c	0.499(2)	0.8452(12)	0.4930(14)	0.0070(5)	1
O12	2c	0.028(2)	0.8048(12)	0.2638(14)	0.0070(5)	1
O13	2c	0.630(2)	0.6498(12)	0.5022(13)	0.0070(5)	1
O14	2c	0.956(2)	0.6504(12)	0.1645(14)	0.0070(5)	1
O15	2c	0.292(2)	0.3487(13)	0.8250(14)	0.0070(5)	1
O16	2c	0.171(2)	0.1533(12)	0.8341(14)	0.0070(5)	1
O17	2c	0.695(2)	0.8042(13)	0.596(2)	0.0070(5)	1
O18	2c	0.429(2)	0.3036(13)	0.398(2)	0.0070(5)	1
O19	2c	0.928(2)	0.8021(12)	0.0672(14)	0.0070(5)	1
O20	2c	0.098(2)	0.3000(11)	0.7352(14)	0.0070(5)	1
O21	2c	0.813(2)	0.7236(12)	0.5016(13)	0.0070(5)	1
O22	2c	0.142(2)	0.7296(11)	0.163(2)	0.0070(5)	1
O23	2c	0.763(2)	0.2992(11)	0.0658(14)	0.0070(5)	1
O24	2c	0.477(2)	0.7256(12)	0.8343(14)	0.0070(5)	1
N61 / O61	2c	0.2387(14)	0.9039(10)	0.4735(14)	0.034(2)	0.1364 / 0.8636
N62 / O62	2c	0.1792(14)	0.9273(11)	0.5857(14)	0.034(2)	0.1364 / 0.8636
N63 / O63	2c	0.0721(14)	0.9319(11)	0.4130(14)	0.034(2)	0.1364 / 0.8636
N64 / O64	2c	0.754(2)	0.823(2)	0.360(2)	0.0139(9)	0.1364 / 0.8636
N65 / O65	2c	0.896(2)	0.8234(13)	0.632(2)	0.0139(9)	0.1364 / 0.8636
N66 / O66	2c	0.9015(14)	0.8998(10)	0.7957(14)	0.034(2)	0.1364 / 0.8636
N67 / O67	2c	0.7388(14)	0.9313(11)	0.7481(14)	0.034(2)	0.1364 / 0.8636
N68 / O68	2c	0.8475(14)	0.9263(11)	0.9194(14)	0.034(2)	0.1364 / 0.8636
N69 / O69	2c	0.413(2)	0.8253(13)	0.6830(14)	0.0139(9)	0.1364 / 0.8636
N70 / O70	2c	0.561(2)	0.8230(14)	0.966(2)	0.0139(9)	0.1364 / 0.8636
N71 / O71	2c	0.1925(14)	0.4040(10)	0.1345(14)	0.034(2)	0.1364 / 0.8636
N72 / O72	2c	0.3051(14)	0.4323(12)	0.080(2)	0.034(2)	0.1364 / 0.8636
N73 / O73	2c	0.363(2)	0.4248(11)	0.254(2)	0.034(2)	0.1364 / 0.8636

N74/ O74	2*c*	0.695(2)	0.3215(12)	0.2936(14)	0.0139(9)	0.1364 / 0.8636
N75 / O75	2*c*	0.565(2)	0.3228(14)	0.026(2)	0.0139(9)	0.1364 / 0.8636
N76 / O76	2*c*	0.9941(12)	0.6025(9)	0.5979(12)	0.0208(11)	0.1364 / 0.8636
N77 / O77	2*c*	0.8532(12)	0.6074(9)	0.4342(12)	0.0208(11)	0.1364 / 0.8636
N78 / O78	2*c*	0.365(2)	0.6770(14)	0.632(2)	0.0139(9)	0.1364 / 0.8636
N79 / O79	2*c*	0.2344(14)	0.6737(12)	0.3473(14)	0.0139(9)	0.1364 / 0.8636
N80 / O80	2*c*	0.5355(12)	0.1069(9)	0.0964(12)	0.0208(11)	0.1364 / 0.8636
N81 / O81	2*c*	0.5672(12)	0.1067(9)	0.2667(11)	0.0208(11)	0.1364 / 0.8636
N82 / O82	2*c*	0.0774(14)	0.1725(12)	0.0161(14)	0.0139(9)	0.1364 / 0.8636
N83 / O83	2*c*	0.231(2)	0.1722(13)	0.303(2)	0.0139(9)	0.1364 / 0.8636
N84 / O84	2*c*	0.6600(12)	0.6062(9)	0.9312(11)	0.0208(11)	0.1364 / 0.8636
N85 / O85	2*c*	0.5225(12)	0.6051(9)	0.7661(12)	0.0208(11)	0.1364 / 0.8636
N86 / O86	2*c*	0.033(2)	0.6758(14)	0.968(2)	0.0139(9)	0.1364 / 0.8636
N87 / O87	2*c*	0.901(2)	0.6775(13)	0.691(2)	0.0139(9)	0.1364 / 0.8636
N88 / O88	2*c*	0.658(2)	0.070(2)	0.495(2)	0.0208(11)	0.1364 / 0.8636
N89 / O89	2*c*	0.325(2)	0.070(2)	0.829(2)	0.0208(11)	0.1364 / 0.8636
N90 / O90	2*c*	0.988(2)	0.932(2)	0.161(2)	0.0208(11)	0.1364 / 0.8636
N91 / O91	2*c*	0.793(2)	0.433(2)	0.163(2)	0.0208(11)	0.1364 / 0.8636
N92 / O92	2*c*	0.462(2)	0.432(2)	0.497(2)	0.0208(11)	0.1364 / 0.8636
N93 / O93	2*c*	0.128(2)	0.433(2)	0.829(2)	0.0208(11)	0.1364 / 0.8636

Table S5. Anisotropic displacement parameters (U_{ij} in Å^2) of $Y_{26}Ba_6[Si_{22}O_{19}N_{36}]O_{16}$:$Eu^{2+}$ with standard deviations in parentheses.

Atom	U_{11}	U_{22}	U_{33}	U_{23}	U_{13}	U_{12}
Ba1	0.0312(12)	0.0206(11)	0.084(2)	0	0.0447(13)	0
Ba2	0.0220(10)	0.0093(9)	0.0142(8)	0	0.0094(7)	0
Ba3	0.0214(10)	0.0176(10)	0.058(2)	0	0.0226(11)	0
Ba4	0.0346(12)	0.0215(11)	0.071(2)	0	0.0462(13)	0
Ba5	0.0124(8)	0.0089(9)	0.0362(11)	0	0.0165(8)	0
Ba6	0.0151(9)	0.0058(8)	0.0175(8)	0	0.0094(7)	0
Ba7	0.0313(11)	0.0100(9)	0.0176(9)	0	0.0184(8)	0
Ba8	0.0089(8)	0.0081(8)	0.0157(8)	0	0.0069(7)	0
Ba9	0.0169(9)	0.0162(9)	0.0389(12)	0	0.0145(9)	0
Ba10	0.0209(10)	0.0070(8)	0.0189(9)	0	0.0044(8)	0
Ba11	0.0102(8)	0.0131(9)	0.0332(11)	0	0.0090(8)	0
Ba12	0.0396(13)	0.0112(10)	0.063(2)	0	0.0438(13)	0
Ba13	0.0127(9)	0.0134(9)	0.0358(12)	0	0.0117(8)	0
Ba14	0.0039(8)	0.0064(8)	0.0174(8)	0	0.0055(7)	0
Ba15	0.0045(7)	0.0140(8)	0.0205(9)	0	0.0053(6)	0
Ba16	0.0182(10)	0.0205(11)	0.056(2)	0	0.0295(11)	0
Ba17	0.0352(12)	0.0137(10)	0.0512(14)	0	0.0367(11)	0
Ba18	0.0193(9)	0.0074(8)	0.0179(9)	0	0.0050(7)	0
Y1	0.0231(14)	0.0144(13)	0.091(2)	0.0013(14)	0.040(2)	0.0022(11)
Y2	0.0099(9)	0.0049(10)	0.0055(9)	0.0016(8)	0.0046(7)	0.0015(8)
Y3	0.0100(10)	0.0047(10)	0.0072(9)	−0.0012(7)	0.0027(8)	−0.0002(8)
Y4	0.0206(12)	0.0148(12)	0.074(2)	0.0019(12)	0.0362(13)	0.0036(10)
Y5	0.0109(9)	0.0032(9)	0.0092(9)	−0.0004(7)	0.0072(7)	0.0002(7)
Y6	0.0052(9)	0.0058(10)	0.0065(9)	0.0007(7)	0.0020(7)	−0.0006(7)
Y7	0.0054(9)	0.0052(10)	0.0241(11)	0.0010(8)	0.0076(8)	0.0009(8)
Y8	0.0103(9)	0.0037(10)	0.0067(9)	−0.0001(7)	0.0040(7)	0.0018(8)
Y9	0.0046(9)	0.0058(10)	0.0063(8)	0.0009(7)	0.0026(7)	0.0001(7)
Y10	0.0072(9)	0.0187(12)	0.0045(9)	−0.0004(8)	0.0025(7)	−0.0056(9)
Y11	0.0050(9)	0.0183(12)	0.0038(9)	0.0000(8)	0.0017(7)	−0.0061(8)
Y12	0.0055(7)	0.0050(7)	0.0099(7)	−0.0010(6)	0.0047(6)	0.0004(6)
Y13	0.0070(9)	0.0132(11)	0.0042(8)	−0.0006(8)	0.0032(7)	−0.0038(8)
Y14	0.0084(9)	0.0094(10)	0.0035(8)	−0.0019(7)	0.0022(7)	0.0003(7)
Y15	0.0067(9)	0.0087(10)	0.0040(8)	0.0033(7)	0.0024(7)	0.0030(7)
Y16	0.0065(8)	0.0088(9)	0.0049(8)	0.0016(7)	0.0031(7)	0.0007(7)
Y17	0.0036(9)	0.0099(10)	0.0075(8)	−0.0017(8)	0.0016(7)	0.0013(7)
Y18	0.0065(9)	0.0072(10)	0.0053(8)	−0.0027(7)	0.0027(7)	−0.0016(7)

Y19	0.0073(9)	0.0087(10)	0.0059(8)	0.0003(7)	0.0037(7)	0.0002(7)
Y20	0.0059(7)	0.0051(7)	0.0101(7)	0.0001(6)	0.0053(6)	−0.0004(6)
Y21	0.0085(9)	0.0052(9)	0.0037(8)	−0.0017(7)	0.0036(7)	0.0002(7)
Y22	0.0057(9)	0.0059(10)	0.0037(8)	0.0003(7)	−0.0001(7)	0.0017(7)
Y23	0.0071(8)	0.0067(10)	0.0058(8)	0.0027(7)	0.0042(7)	0.0021(7)
Y24	0.0080(9)	0.0092(10)	0.0037(8)	−0.0017(7)	0.0022(7)	−0.0002(7)
Y25	0.0046(9)	0.0074(10)	0.0055(8)	0.0009(7)	0.0015(7)	0.0006(7)
Y26	0.0069(8)	0.0109(10)	0.0051(8)	0.0000(7)	0.0034(7)	−0.0008(7)
Y27	0.0046(10)	0.0029(11)	0.0105(10)	−0.0014(8)	0.0045(8)	−0.0008(9)
Y28	0.0037(9)	0.0108(11)	0.0086(9)	−0.0013(8)	0.0026(7)	0.0038(8)
Y29	0.0055(9)	0.0065(10)	0.0078(9)	−0.0002(7)	0.0018(7)	0.0001(7)
Y30	0.0030(8)	0.0057(10)	0.0054(8)	−0.0002(7)	0.0018(7)	−0.0014(7)
Y31	0.0130(10)	0.0111(11)	0.0320(12)	0.0032(9)	0.0179(9)	0.0012(8)
Y32	0.0061(9)	0.0117(11)	0.0077(9)	−0.0001(8)	0.0039(8)	0.0033(8)
Y33	0.0070(9)	0.0082(10)	0.0083(9)	0.0003(8)	0.0043(7)	0.0023(8)
Y34	0.0058(9)	0.0055(10)	0.0065(9)	0.0014(7)	0.0033(8)	−0.0014(8)
Y35	0.0155(11)	0.0134(12)	0.045(2)	0.0004(11)	0.0222(11)	0.0002(9)
Y36	0.0069(9)	0.0149(11)	0.0054(8)	0.0001(8)	0.0033(7)	0.0055(9)
Y37	0.0084(9)	0.0075(10)	0.0085(9)	−0.0015(8)	0.0035(7)	−0.0007(8)
Y38	0.0075(9)	0.0067(10)	0.0077(9)	−0.0004(7)	0.0032(7)	0.0003(8)
Y39	0.0287(14)	0.0128(12)	0.113(3)	0.003(2)	0.055 (2)	−0.0020(11)

Table S6. Anisotropic displacement parameters (U_{ij} in Å^2) of $Tb_{26}Ba_6[Si_{22}O_{19}N_{36}]O_{16}$:$Eu^{2+}$ with standard deviations in parentheses.

Atom	U_{11}	U_{22}	U_{33}	U_{23}	U_{13}	U_{12}
Ba1	0.038(2)	0.021(3)	0.094(4)	0	0.052(2)	0
Ba2	0.034(2)	0.0082(19)	0.0141(16)	0	0.0083(14)	0
Ba3	0.0225(19)	0.022(2)	0.065(3)	0	0.024(2)	0
Ba4	0.048(3)	0.023(3)	0.083(3)	0	0.058(3)	0
Ba5	0.0162(16)	0.012(2)	0.040(2)	0	0.0187(15)	0
Ba6	0.0202(17)	0.0007(16)	0.0312(17)	0	0.0202(14)	0
Ba7	0.048(2)	0.0080(18)	0.0186(16)	0	0.0236(15)	0
Ba8	0.0114(15)	0.0087(16)	0.0126(13)	0	0.0071(11)	0
Ba9	0.0174(17)	0.018(2)	0.056(3)	0	0.0115(17)	0
Ba10	0.032(2)	0.0059(19)	0.0285(19)	0	0.0080(15)	0
Ba11	0.0123(16)	0.0156(18)	0.038(2)	0	0.0073(14)	0
Ba12	0.047(3)	0.012(2)	0.071(3)	0	0.052(2)	0
Ba13	0.0111(15)	0.0130(19)	0.044(2)	0	0.0101(15)	0
Ba14	0.0051(15)	0.0113(18)	0.0181(15)	0	0.0044(12)	0
Ba15	0.0096(14)	0.0191(18)	0.0274(16)	0	0.0091(12)	0
Ba16	0.0233(19)	0.023(2)	0.065(3)	0	0.036(2)	0
Ba17	0.050(3)	0.017(2)	0.066(3)	0	0.049(2)	0
Ba18	0.0240(17)	0.0053(18)	0.0256(17)	0	0.0025(14)	0
Tb1	0.0251(14)	0.0186(15)	0.093(2)	−0.0011(15)	0.0422(15)	−0.0003(12)
Tb2	0.0106(9)	0.0070(12)	0.0044(8)	0.0022(8)	0.0022(7)	0.0018(9)
Tb3	0.0103(10)	0.0067(12)	0.0053(9)	−0.0008(8)	0.0029(8)	−0.0015(9)
Tb4	0.0258(12)	0.0200(15)	0.0798(18)	−0.0037(13)	0.0410(12)	−0.0026(11)
Tb5	0.0103(9)	0.0056(11)	0.0097(8)	0.0006(8)	0.0075(7)	−0.0006(8)
Tb6	0.0107(10)	0.0051(11)	0.0088(8)	0.0000(8)	0.0058(7)	0.0010(9)
Tb7	0.0099(10)	0.0081(12)	0.0320(11)	0.0015(9)	0.0126(9)	0.0007(8)
Tb8	0.0108(10)	0.0057(12)	0.0081(9)	−0.0023(8)	0.0033(8)	−0.0019(9)
Tb9	0.0069(9)	0.0061(12)	0.0066(8)	−0.0005(8)	0.0032(7)	0.0008(8)
Tb10	0.0082(10)	0.0201(14)	0.0049(9)	−0.0006(9)	0.0030(7)	−0.0068(10)
Tb11	0.0075(10)	0.0210(14)	0.0056(9)	−0.0001(9)	0.0037(7)	−0.0057(10)
Tb12	0.0068(7)	0.0062(8)	0.0123(7)	−0.0004(6)	0.0055(6)	0.0008(6)
Tb13	0.0072(10)	0.0182(14)	0.0088(9)	−0.0002(9)	0.0042(8)	−0.0058(9)
Tb14	0.0074(10)	0.0129(13)	0.0040(8)	−0.0034(7)	0.0008(7)	−0.0006(8)
Tb15	0.0077(9)	0.0101(12)	0.0046(8)	0.0017(7)	0.0021(7)	0.0018(8)
Tb16	0.0100(9)	0.0100(11)	0.0059(8)	0.0028(8)	0.0039(7)	0.0011(8)
Tb17	0.0079(9)	0.0089(12)	0.0070(8)	0.0004(8)	0.0034(7)	0.0022(8)
Tb18	0.0072(9)	0.0096(12)	0.0041(8)	−0.0006(7)	0.0017(7)	−0.0018(8)

Tb19	0.0102(9)	0.0086(12)	0.0050(8)	−0.0010(7)	0.0036(7)	−0.0003(8)
Tb20	0.0081(8)	0.0059(8)	0.0127(7)	−0.0004(6)	0.0066(6)	−0.0012(6)
Tb21	0.0083(9)	0.0056(10)	0.0047(8)	−0.0008(7)	0.0031(7)	0.0012(8)
Tb22	0.0072(9)	0.0059(11)	0.0051(8)	0.0013(7)	0.0016(7)	0.0003(8)
Tb23	0.0069(8)	0.0100(12)	0.0069(8)	0.0005(7)	0.0042(7)	0.0025(8)
Tb24	0.0062(9)	0.0125(12)	0.0059(8)	−0.0027(7)	0.0020(7)	−0.0011(8)
Tb25	0.0050(9)	0.0088(11)	0.0056(8)	−0.0004(7)	0.0012(7)	0.0007(8)
Tb26	0.0082(9)	0.0120(12)	0.0061(8)	0.0008(7)	0.0043(7)	0.0001(8)
Tb27	0.0074(12)	0.0044(14)	0.0113(11)	−0.0008(9)	0.0056(9)	−0.0010(11)
Tb28	0.0064(10)	0.0166(14)	0.0074(9)	−0.0006(9)	0.0031(7)	0.0034(9)
Tb29	0.0096(10)	0.0059(11)	0.0102(9)	0.0003(8)	0.0046(7)	0.0003(9)
Tb30	0.0040(8)	0.0068(11)	0.0068(8)	0.0022(7)	0.0040(7)	0.0000(8)
Tb31	0.0187(10)	0.0148(13)	0.0390(11)	0.0021(9)	0.0222(9)	0.0016(9)
Tb32	0.0071(10)	0.0163(14)	0.0059(9)	0.0007(8)	0.0027(7)	0.0045(10)
Tb33	0.0069(9)	0.0075(12)	0.0072(8)	−0.0001(8)	0.0017(7)	0.0000(9)
Tb34	0.0065(10)	0.0080(13)	0.0039(8)	0.0002(8)	0.0016(7)	−0.0005(9)
Tb35	0.0183(12)	0.0152(14)	0.0539(15)	−0.0003(12)	0.0253(11)	0.0000(10)
Tb36	0.0064(10)	0.0191(14)	0.0060(9)	0.0003(9)	0.0017(8)	0.0061(10)
Tb37	0.0088(9)	0.0073(12)	0.0113(9)	−0.0009(8)	0.0031(7)	0.0000(9)
Tb38	0.0081(9)	0.0081(12)	0.0102(9)	−0.0002(8)	0.0038(7)	0.0000(9)
Tb39	0.0300(14)	0.0154(15)	0.114(2)	0.0032(14)	0.0551(16)	0.0061(11)
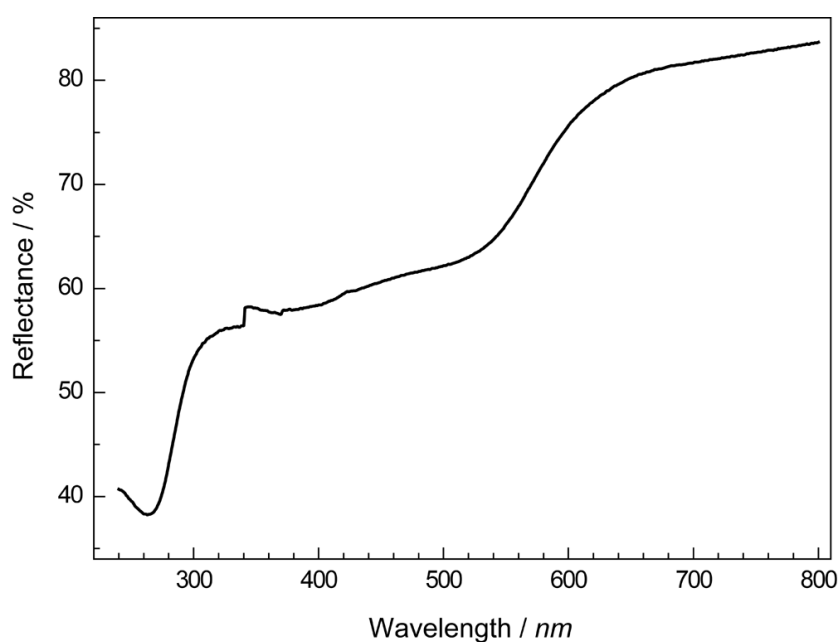
Figure S3. Diffuse reflectance UV/Vis spectrum of $Y_{26}Ba_6[Si_{22}O_{19}N_{36}]O_{16}$:$Eu^{2+}$.

11.6 Supporting Information for Chapter 7

$Y_{23}Sr_{17}[Si_{38}O_{18}N_{67}]O_9$ – An Oxonitridosilicate Oxide with a Unique Layered Structure

Christian Maak, Robin Niklaus, Oliver Oeckler, and Wolfgang Schnick

Z. Anorg. Allg. Chem. **2019**, *645*, 182–187

Table S1. Results in atom% for 15 EDX point measurements of 15 different $Y_{23}Sr_{17}[Si_{38}O_{18}N_{67}]O_9$ crystals.

	Y	Sr	Si	O	N
1	14.1	9.8	22.3	17.7	36.0
2	12.0	9.2	21.4	18.4	39.2
3	13.4	10.2	26.5	17.3	32.6
4	16.0	11.5	21.6	16.8	34.1
5	14.3	10.3	29.7	15.6	30.1
6	14.3	10.5	28.3	16.3	30.5
7	15.3	11.0	22.6	15.1	36.0
8	13.6	10.4	24.3	13.7	38.1
9	12.6	9.5	23.9	17.1	36.9
10	10.5	7.2	18.8	19.7	43.9
11	11.6	8.8	21.3	19.2	39.2
12	15.9	9.0	23.0	18.2	33.9
13	14.6	8.3	21.4	18.5	37.2
14	15.3	8.6	22.3	18.2	35.6
15	15.2	8.6	22.4	18.5	35.2
Average	13.9	9.5	23.3	17.4	35.9
Deviation	1.6	1.1	2.9	1.6	3.5
Theory	13.4	9.9	22.1	15.7	39.0
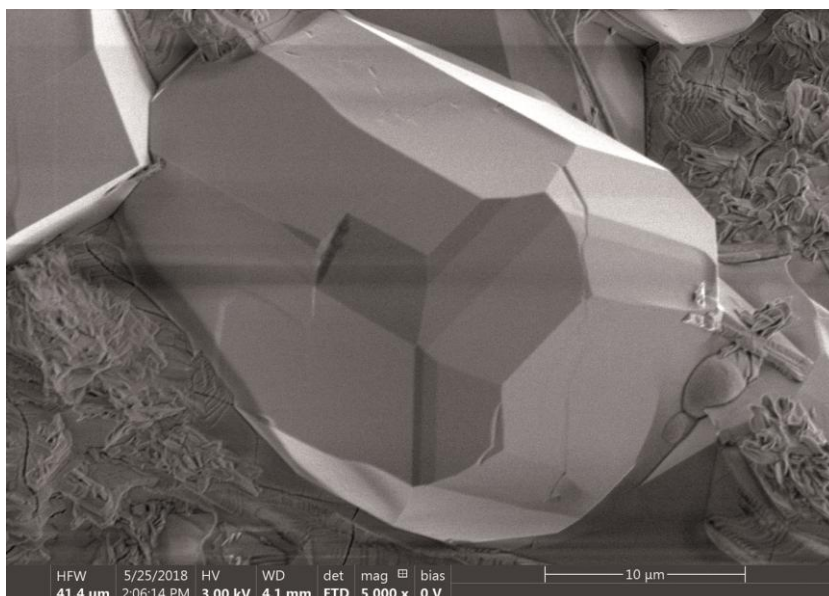
Figure S1. Representative SEM image of a $Y_{23}Sr_{17}[Si_{38}O_{18}N_{67}]O_9$ crystal.
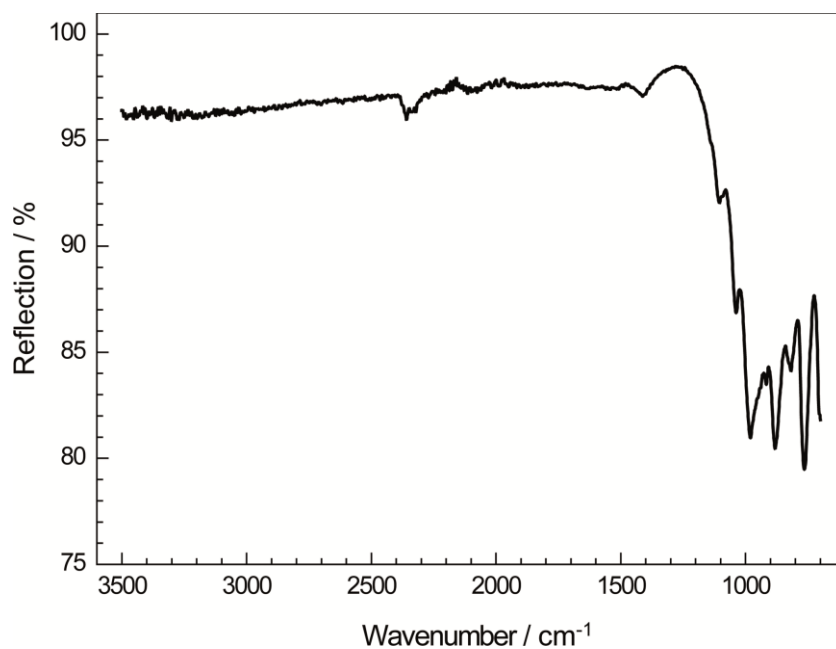
Figure S2. ATR-FTIR spectrum of a $Y_{23}Sr_{17}[Si_{38}O_{18}N_{67}]O_9$ powder sample. No N−H and O−H bands are observed in the typical region.

Table S2. Data for Rietveld refinement of $Y_{23}Sr_{17}[Si_{38}O_{18}N_{67}]O_9$ (least squares standard deviations in parentheses). The structure model obtained from single-crystal X-ray diffraction data was used. Only lattice parameters were refined for $Y_{23}Sr_{17}[Si_{38}O_{18}N_{67}]O_9$.

formula	$Y_{23}Sr_{17}[Si_{38}O_{18}N_{67}]O_9$
formula mass / g·mol^{-1}	5972.56
crystal system	hexagonal
space group	$P6_3/m$ (no. 176)
lattice parameters / Å	$a = 16.5696(2)$ $c = 18.6070(2)$
volume / Å^3	4424.14(10)
formula units/cell	2
X-ray density / g·cm^{-3}	4.48305(10)
diffractometer	Stoe StadiP
radiation	Cu Kα_1 ($\lambda = 1.54056$ Å)
monochromator	Ge(111)
detector	MYTHEN 1K
$F(000)$	5520
2θ range / °	5–100
data points	6365
observed reflections	1618
number of parameters	45
software	TOPAS Academic V4.1
structure refinement	Rietveld-Method
background function	Shifted Chebyshev
	24 polynomials
R_{wp}	0.0345
R_{exp}	0.0237
R_p	0.0251
R_{Bragg}	0.0157
χ^2	1.479

Table S3. Fractional atomic coordinates, equivalent displacement parameters, and site occupancies for $Y_{23}Sr_{17}[Si_{38}O_{18}N_{67}]O_9$, standard deviations in parentheses.

Atom	Wyckoff	x	y	z	U_{eq}	s.o.f.
Y1	12i	0.07984(2)	0.53821(3)	0.07790(2)	0.00499(7)	1
Y2	12i	0.28798(3)	0.01139(3)	0.00712(2)	0.00748(9)	1
Y3	4f	1/3	2/3	0.00518(3)	0.00487(12)	1
Y4	4f	1/3	2/3	0.16845(3)	0.00423(12)	1
Y5	4f	1/3	2/3	0.66651(3)	0.00722(12)	1
Y6/Sr6	12i	0.20576(3)	0.42400(2)	0.10777(2)	0.00538(8)	5/6 / 1/6
Sr1	12i	0.22342(2)	0.11593(3)	0.13755(2)	0.00904(8)	1
Sr2	6h	0.10866(5)	0.22725(4)	1/4	0.01209(11)	1
Sr3	6h	0.42956(4)	0.21550(5)	1/4	0.01310(11)	1
Sr4	6h	0.53513(5)	0.05617(4)	1/4	0.02272(15)	1
Sr5	2b	0	0	0	0.0359(3)	1
Si1	12i	0.10770(10)	0.21365(7)	0.08931(5)	0.0059(2)	1
Si2	12i	0.31808(9)	0.32313(9)	0.16939(6)	0.0032(2)	1
Si3	12i	0.32149(9)	0.00200(9)	0.16819(6)	0.0037(2)	1
Si4	12i	0.47815(9)	0.33275(9)	0.07282(6)	0.0047(3)	1
Si5	12i	0.48063(9)	0.15188(9)	0.06606(6)	0.0047(3)	1
Si6	6h	0.14023(13)	0.48240(13)	1/4	0.0035(4)	1
Si7	6h	0.33384(13)	0.48236(13)	1/4	0.0032(3)	1
Si8	4e	0	0	0.16317(9)	0.0068(3)	1
O1	12i	0.1084(2)	0.4210(2)	0.0067(2)	0.0149(8)	1
O2	12i	0.2211(2)	0.1150(3)	0.00062(14)	0.0159(6)	1
O3	12i	0.2310(2)	0.5720(2)	0.08827(15)	0.0125(7)	1
O4	12i	0.3138(2)	0.4428(2)	0.0209(2)	0.0112(7)	1
O5	6h	0.5870(3)	0.2200(3)	1/4	0.0172(12)	1
N1	12i	0.0548(3)	0.1091(2)	0.1277(2)	0.0282(10)	1
N2	12i	0.0596(3)	0.2775(3)	0.1210(2)	0.0074(8)	1
N3	12i	0.0680(3)	0.4392(3)	0.1746(2)	0.0055(8)	1
N4	12i	0.2244(3)	0.2761(3)	0.1111(2)	0.0068(8)	1
N5	12i	0.3598(3)	0.4419(3)	0.1728(2)	0.0062(8)	1
N6	12i	0.3801(2)	0.0958(3)	0.1130(2)	0.0058(7)	1
N7	12i	0.4004(3)	0.2992(3)	0.1411(2)	0.0137(9)	1
N8	12i	0.5395(2)	0.2718(3)	0.07833(15)	0.0063(6)	1
N9	12i	0.5482(3)	0.0992(2)	0.0685(2)	0.0169(7)	1
N10	6h	0.0363(10)	0.010(2)	1/4	0.031(5)	1/3
N11	6h	0.2057(3)	0.6025(4)	1/4	0.0049(8)	1
N12	6h	0.2152(4)	0.4392(3)	1/4	0.0100(9)	1
N13	6h	0.2781(4)	0.2640(4)	1/4	0.0069(11)	1
N14	6h	0.2989(4)	0.0374(3)	1/4	0.0061(11)	1

Table S4. Anisotropic displacement parameters (U_{ij} in $\mathring{A}^2$) of $Y_{23}Sr_{17}[Si_{38}O_{18}N_{67}]O_9$ with standard deviations in parentheses. The site N10 was refined with an isotropic displacement parameter.

| Atom	U_{11}	U_{22}	U_{33}	U_{23}	U_{13}	U_{12}
Y1	0.00654(16)	0.0031(2)	0.00600(15)	0.00002(18)	−0.00147(13)	0.00288(19)
Y2	0.0072(2)	0.0089(2)	0.00700(17)	0.00400(16)	0.00098(17)	0.00462(19)
Y3	0.00549(17)	U_{11}	0.0036(3)	0	0	0.00275(9)
Y4	0.00479(17)	U_{11}	0.0031(3)	0	0	0.00239(9)
Y5	0.00857(19)	U_{11}	0.0045(3)	0	0	0.00429(9)
Y6/Sr6	0.0051(2)	0.00522(17)	0.00674(16)	−0.00183(13)	−0.00074(18)	0.00330(17)
Sr1	0.01112(18)	0.0066(2)	0.01127(16)	−0.00002(19)	−0.00017(13)	0.0058(2)
Sr2	0.0104(3)	0.0249(3)	0.0067(2)	0	0	0.0131(3)
Sr3	0.0125(3)	0.0072(3)	0.0210(3)	0	0	0.0061(3)
Sr4	0.0083(4)	0.0064(3)	0.0528(4)	0	0	0.0031(3)
Sr5	0.0518(5)	U_{11}	0.0040(4)	0	0	0.0259(2)
Si1	0.0048(6)	0.0047(5)	0.0080(5)	−0.0005(3)	−0.0002(5)	0.0023(6)
Si2	0.0036(6)	0.0031(6)	0.0026(5)	−0.0011(5)	−0.0004(5)	0.0016(5)
Si3	0.0035(6)	0.0036(6)	0.0041(5)	−0.0004(5)	−0.0002(5)	0.0017(5)
Si4	0.0032(6)	0.0055(6)	0.0059(6)	−0.0004(5)	0.0001(5)	0.0026(5)
Si5	0.0037(6)	0.0044(6)	0.0065(6)	0.0001(5)	0.0002(5)	0.0024(5)
Si6	0.0026(8)	0.0039(9)	0.0047(8)	0	0	0.0023(7)
Si7	0.0030(8)	0.0015(8)	0.0038(8)	0	0	0.0003(7)
Si8	0.0068(5)	U_{11}	0.0070(8)	0	0	0.0034(3)
O1	0.0133(17)	0.0098(17)	0.0131(18)	0.0036(14)	0.0023(13)	−0.0006(14)
O2	0.0262(16)	0.0135(18)	0.0109(13)	0.0030(15)	0.0091(11)	0.0123(17)
O3	0.0081(16)	0.0142(17)	0.0046(15)	−0.0007(13)	−0.0005(12)	−0.0024(14)
O4	0.0158(17)	0.0055(16)	0.0101(15)	0.0006(13)	−0.0039(13)	0.0038(14)
O5	0.023(3)	0.007(2)	0.011(2)	0	0	0.000(2)
N1	0.007(2)	0.0085(17)	0.066(3)	0.0100(18)	−0.002(3)	0.001(2)
N2	0.007(2)	0.008(2)	0.0081(19)	0.0035(16)	0.0017(16)	0.0047(16)
N3	0.0045(19)	0.008(2)	0.0050(19)	0.0012(15)	0.0003(15)	0.0034(17)
N4	0.0080(19)	0.0076(19)	0.0034(17)	−0.0018(16)	−0.0024(15)	0.0029(17)
N5	0.009(2)	0.0020(18)	0.0062(19)	0.0007(14)	0.0040(16)	0.0016(16)
N6	0.0058(18)	0.0068(17)	0.0057(17)	0.0048(15)	0.0028(15)	0.0038(15)
N7	0.014(2)	0.015(2)	0.016(2)	0.0063(17)	0.0110(17)	0.0101(18)
N8	0.0054(14)	0.0028(19)	0.0096(14)	−0.0012(18)	0.0014(12)	0.0013(18)
N9	0.007(2)	0.0105(16)	0.033(2)	0.0013(15)	0.002(2)	0.0039(18)
N11	0.004(2)	0.004(3)	0.005(2)	0	0	0.000(3)
N12	0.003(3)	0.004(2)	0.022(2)	0	0	0.001(2)
N13	0.009(3)	0.008(3)	0.005(2)	0	0	0.006(2)
N14	0.008(3)	0.004(3)	0.007(2)	0	0	0.004(2)
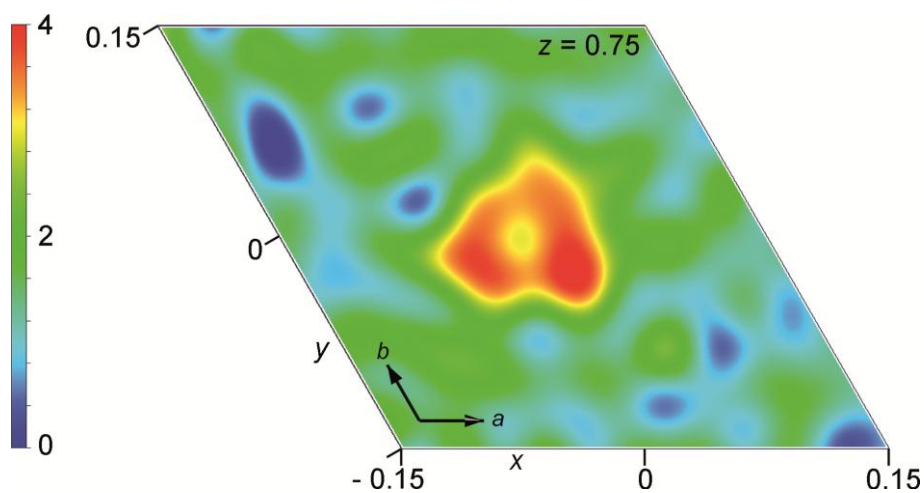
Figure S3. Residual electron density ($F_{obs} - F_{calc}$) around 0,0,3/4 for the refinement in space group $P2_1/m$.
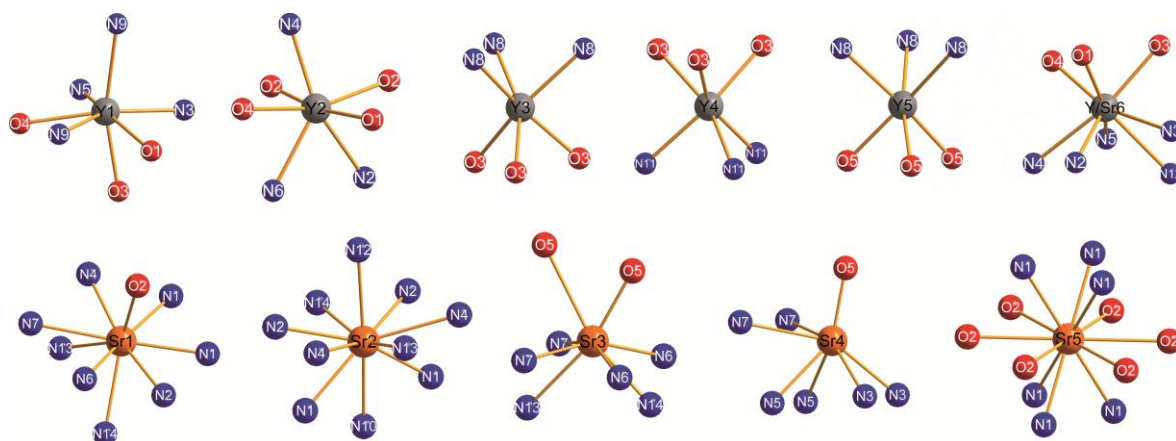

Figure S4. Coordination spheres of Y, Y/Sr, and Sr sites.

Table S5. Metal–Ligand distances for the Y, Y/Sr, and Sr sites in $Y_{23}Sr_{17}[Si_{38}O_{18}N_{67}]O_9$ in Å. Standard deviations in parentheses.

Y1–O3	2.285(3)	Sr1–O2	2.550(3)
Y1–N3	2.377(4)	Sr1–N4	2.692(4)
Y1–O4	2.410(3)	Sr1–N1	2.747(5)
Y1–N5	2.433(4)	Sr1–N6	2.816(4)
Y1–N9	2.577(3)	Sr1–N1	2.823(5)
Y1–O1	2.583(4)	Sr1–N2	2.881(4)
Y1–N9	2.739(4)	Sr1–N7	2.988(4)
Y2–O1	2.218(3)	Sr1–N13	3.001(4)
Y2–N4	2.337(4)	Sr1–N14	3.045(4)
Y2–O4	2.378(3)	Sr2–N13	2.559(5)
Y2–N2	2.421(4)	Sr2–N14	2.750(5)
Y2–N6	2.457(4)	Sr2–N2	2.793(3)
Y2–O2	2.470(4)	Sr2–N2	2.793(3)
Y2–O2	2.539(4)	Sr2–N1	2.841(4)
Y3–O3	2.252(3)	Sr2–N1	2.841(4)
Y3–O3	2.252(3)	Sr2–N10	2.90(3)
Y3–O3	2.252(3)	Sr2–N12	3.043(4)
Y3–N8	2.399(3)	Sr2–N4	3.077(4)
Y3–N8	2.399(3)	Sr2–N4	3.077(4)
Y3–N8	2.399(3)	Sr3–O5	2.573(5)
Y4–O3	2.216(3)	Sr3–N7	2.634(4)
Y4–O3	2.216(3)	Sr3–N7	2.634(4)
Y4–O3	2.216(3)	Sr3–N14	2.648(5)
Y4–N11	2.380(3)	Sr3–N13	2.995(5)
Y4–N11	2.380(3)	Sr3–N6	3.080(4)
Y4–N11	2.380(3)	Sr3–N6	3.080(4)
Y5–O5	2.282(3)	Sr3–O5	3.325(4)
Y5–O5	2.282(3)	Sr4–O5	2.405(4)
Y5–O5	2.282(3)	Sr4–N3	2.829(4)
Y5–N8	2.456(3)	Sr4–N3	2.829(4)
Y5–N8	2.456(3)	Sr4–N5	2.887(4)
Y5–N8	2.456(3)	Sr4–N5	2.887(4)
Y/Sr6–O3	2.302(3)	Sr4–N7	3.186(4)
Y/Sr6–O4	2.315(3)	Sr4–N7	3.186(4)
Y/Sr6–N2	2.438(4)	Sr5–N1	2.846(4)
Y/Sr6–O1	2.463(3)	Sr5–N1	2.846(4)
Y/Sr6–N4	2.621(4)	Sr5–N1	2.846(4)
Y/Sr6–N12	2.6573(5)	Sr5–N1	2.846(4)
Y/Sr6–N5	2.705(4)	Sr5–N1	2.846(4)
Y/Sr6–N3	2.720(4)	Sr5–N1	2.846(4)
		Sr5–O2	3.175(3)
		Sr5–O2	3.175(3)
		Sr5–O2	3.175(3)
		Sr5–O2	3.175(3)
		Sr5–O2	3.175(3)
		Sr5–O2	3.175(3)

11.7 Supporting Information for Chapter 8

Ultra-Narrow-Band Blue-Emitting Oxoberyllates AELi$_2$[Be$_4$O$_6$]:Eu^{2+} (AE = Sr, Ba) Paving the Way to Efficient RGB pc-LEDs

Philipp Strobel, Christian Maak, Volker Weiler, Peter J. Schmidt, and Wolfgang Schnick

Angew. Chem., Int. Ed. **2018**, *57*, 8739–8743; *Angew. Chem.* **2018**, *130*, 8875–8879

Synthesis

Single crystals of AELi$_2$[Be$_4$O$_6$]:Eu^{2+} (AE = Sr, Ba) (1 mol% Eu nominal composition) were obtained by a solid-state reaction in Ta ampules. 1 mmole of AECO$_3$ (SrCO$_3$: Merck, 99%, 147.6 mg; BaCO$_3$: Philips, 197.3 mg), 1.33 mmole Be$_3$N$_2$ (73.2 mg, synthesized from Be (ABCR, 99+%, 325. mesh) in a radiofrequency (rf) furnace under N$_2$-atmosphere at 1300 °C), 2 mmole Li$_2$O (Schuchardt, 98%, 59.8 mg). The reaction mixture was filled in Ta ampules and heated in 3 h to 950 °C in evacuated silica ampules. The temperature was kept for 24 h and then cooled down to 500 °C in 3 h.

Powder samples of AELi$_2$[Be$_4$O$_6$]:Eu^{2+} (AE = Sr, Ba) were synthesized by heating a stoichiometric mixture of AEO (SrO: Sigma Aldrich, 99.9%; BaO: Sigma Aldrich, 99.99%), Li$_2$O (Schuchardt, 98%), BeO (Alfa Aesar, 99.95%), and Eu$_2$O$_3$ ((ABCR, 99.99%) for 2 h to 1100 °C in Ar gas atmosphere. The starting materials were thoroughly ground in a mortar under Ar and filled in a tungsten crucible. The product is obtained as colorless powder, which is stable in 0.1M HCl.

Luminescence

Luminescence investigations on single crystals of AELi$_2$[Be$_4$O$_6$]:Eu^{2+} (AE = Sr, Ba) have been performed with a Horiba Fluoromax4 spectrofluorimeter system attached to an Olympus BX51 microscope via fiber optics. Photoluminescence measurements on powder samples were carried out with an in-house-built system based on a 5.300 integrating sphere and a spectrofluorimeter equipped with a 150 W Xe lamp, two 500 mm Czerny-Turner monochromators, 1800 1/mm lattices and 250/500 nm lamps, with a spectral range from 230 to 820 nm. Low-temperature emission spectra of powder samples were recorded with an Ocean Optics HR2000 C ES spectrometer (2048 pixels, grating UA (200–1100 nm), slit-50) with the samples mounted in a closed-cycle He cryostat. The samples were measured on PTFE sample holders. The excitation wavelength was 410 nm with a spectral width of 10 nm. The emission spectra were recorded in the wavelength range

between 460 nm and 820 nm with 1 nm step size. Excitation spectra were monitored at 470 nm under an excitation wavelength range from 380 to 450 nm with 2 nm step size. For photoluminescence quantum efficiency measurements a manufactured $SrSi_2O_2N_2:Eu^{2+}$ reference with internal quantum efficiency of 95% excited at 440 nm was used.

Elemental Analysis

For the determination of the chemical composition of different crystallites EDS spectroscopy and ICP-OES analysis was applied. For EDS, a Dualbeam Helios Nanolab G3 UC scanning electron microscope (SEM, FEI) with X-Max 80 SDD detector (Oxford Instruments) was used. The EDS data were collected from several particles with an accelerating voltage of 20 kV. Additionally, SEM was used to collect images of particles to investigate the morphology. Inductively coupled plasma optical emission spectrometry (ICP-OES) was conducted with a Varian Vista RL spectrometer, to determine the Sr, Li, Be, and Eu ratio.

Table S1. Elemental Analysis via energy dispersive X-ray spectroscopy (EDS) of $AELi_2[Be_4O_6]:Eu^{2+}$ (1% Eu, AE = Sr, Ba).

		AE	Eu	Li	Be	O
$SrLi_2[Be_4O_6]:Eu^{2+}$	EDS	1	-	-	-	5
	ICP	1	< 0.01	1.5	3.6	-
$BaLi_2[Be_4O_6]:Eu^{2+}$	EDS	1	-	-	-	6
	ICP	1	< 0.01	1.7	3.8	-

NMR spectroscopy

Solid-state MAS-NMR experiments were performed at 11.74 T on a Bruker 500 Avance III FT spectrometer equipped with a commercial 4 mm triple-resonance MAS probe at a ^{6}Li frequency of 73.6 MHz, ^{7}Li frequency of 194.4 MHz, and ^{9}Be frequency of 70.3 MHz. All experiments were performed in ZrO_2 rotors at room temperature. The chemical shift of ^{6}Li, ^{7}Li, and ^{9}Be is reported using the frequency ratios published by IUPAC [δ-scale relative to 1% tetramethylsilane (TMS) in $CDCl_3$].[1]

The [6]Li MAS-NMR spectrum was acquired with a 90° pulse length of 2.5 µs and a recycle delay of 128000 s, the ^{7}Li MAS-NMR spectrum was acquired with a 90° pulse length of 5.0 µs and a recycle delay of 4096 s and the [9]Be MAS-NMR spectrum was acquired with a 90° pulse length of 2.5 µs and a recycle delay of 8192 s. The spinning frequency for all measurements was 10 kHz.
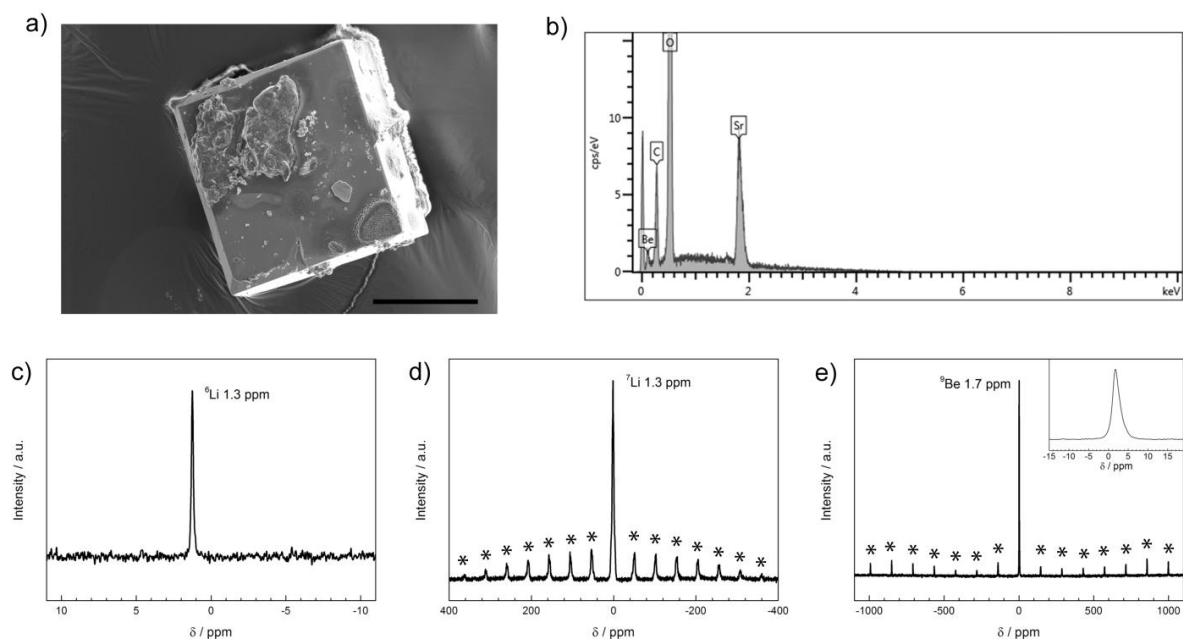

Figure S1. Morphology and composition of ultra-narrow band blue emitting AELi$_2$[Be$_4$O$_6$]:Eu^{2+} (AE = Sr, Ba). (a) SEM image of a SLBO single crystal. Scale bar 100 µm. (b) EDS scan of SLBO single crystal, coated with C. (c) [6]Li solid-state MAS-NMR spectrum of BLBO (rotation frequency 10 kHz). (d) ^{7}Li solid-state MAS-NMR spectrum of BLBO. Rotation side-bands are indicated by asterisks (rotation frequency 10 kHz). (e) [9]Be solid-state MAS-NMR spectrum of BLBO. Rotation side-bands are indicated by asterisks (rotation frequency 10 kHz).

X-ray Diffraction

The crystal structures of AELi$_2$[Be$_4$O$_6$] (AE = Sr, Ba) were determined by single-crystal X-ray diffraction on a Bruker D8 Venture diffractometer (Mo Kα radiation, rotating anode generator, graphite monochromator). Blue luminescent single crystals of AELi$_2$[Be$_4$O$_6$]:Eu^{2+} (AE = Sr, Ba) were placed on micromounts (MiTeGen) for measurements. Integration and multi-scan absorption correction was applied using the program APEX3.[2] The crystal structure was solved using direct methods with SHELXS.[3] The refinement of the structure was carried out with a least-squares algorithm using

SHELXL.[4,5] The crystal structure was refined with the Rietveld method on the powder X-ray diffraction data. PXRD data were collected on a STOE STADI P diffractometer (Cu Kα_1 radiation, Ge(111) monochromator, position sensitive detector) in transmission geometry. Rietveld refinement was carried out using the TOPAS 4.1 package.[6]

Further details of the crystal structure investigations can be obtained from the Fachinformationszentrum Karlsruhe, 76344 Eggenstein-Leopoldshafen, Germany (Fax, (+49)7247-808-666; email, crysdata@fiz-karlsruhe.de) upon quoting the depository numbers CSD-434376 (BaLi$_2$[Be$_4$O$_6$]) and CSD-434377 (SrLi$_2$[Be$_4$O$_6$]).

Table S2. Single-crystal X-ray diffraction data for AELi$_2$[Be$_4$O$_6$] (AE = Sr, Ba). Standard deviations in parentheses.

	SrLi$_2$[Be$_4$O$_6$]	BaLi$_2$[Be$_4$O$_6$]
formula mass / g·mol^{-1}	233.54	283.26
crystal system / space group	tetragonal / $P4/ncc$ (no. 130)	
lattice parameters / Å	a = 7.1659(2) c = 8.9085(6)	a = 7.2770(4) c = 8.8872(5)
cell volume / Å^3	457.45(4)	470.62(6)
formula units per cell Z	4	
X-ray density / g·cm^{-1}	3.391	3.998
absorption coefficient / μ·mm^{-1}	11.730	8.385
F(000)	432	504
crystal dimensions / mm^3	0.246 × 0.150 × 0.059	0.08 × 0.03 × 0.02
diffractometer	D8 Quest	
radiation	Mo Kα (λ = 0.71073 Å)	
temperature / K	297(2)	
absorption correction	multiscan	
θ range / °	4.022–29.999	3.960–29.974
measured reflections	8810	8043
independent reflections	339 [R_{int} = 0.0365]	349 [R_{int} = 0.0347]
observed reflections	306	310
min./max. transmission	0.466/1.000	0.837/1.000
refined parameters	33	33
GoF	1.194	1.098
R indices ($F_o^2 \geq 2\sigma(F_o^2)$)	$R$1 = 0.0174, wR2 = 0.0473	$R$1 = 0.0121, wR2 = 0.0365
R indices (all data)	$R$1 = 0.0193, wR2 = 0.0487	$R$1 = 0.0137, wR2 = 0.0374
min./max. residual electron density / e·Å^{-3}	−0.906/0.506	−0.848/0.499

Table S3. Atomic coordinates and equivalent isotropic displacement parameters of $SrLi_2[Be_4O_6]$ and $BaLi_2[Be_4O_6]$. Standard deviations in parentheses.

	Atom (Wyckoff)	*x*	*y*	*z*	U_{eq} (Å^2)	*s.o.f*
$SrLi_2[Be_4O_6]$	Sr1 (4*c*)	1/4	1/4	0.34572(3)	0.00909(17)	1
	Li1 (8*f*)	0.3697(4)	0.6303(4)	1/4	0.0122(7)	1
	Be1 (16*g*)	0.1197(3)	0.5311(3)	0.0776(2)	0.0059(3)	1
	O1 (16*g*)	0.50309(13)	0.16231(15)	0.04168(10)	0.0064(2)	1
	O2 (8*f*)	0.59096(15)	0.40904(15)	1/4	0.0088(3)	1
$BaLi_2[Be_4O_6]$	Ba1 (4*c*)	1/4	1/4	0.32551(2)	0.00909(17)	1
	Li1 (8*f*)	0.3665(4)	0.6335(4)	1/4	0.0120(7)	1
	Be1 (16*g*)	0.1207(3)	0.5337(3)	0.0766(2)	0.0066(4)	1
	O1 (16*g*)	0.50530(15)	0.15991(16)	0.04538(12)	0.0061(2)	1
	O2 (8*f*)	0.59636(15)	0.40364(15)	1/4	0.0075(3)	1

Table S4. Selected bond lengths and angles in $SrLi_2[Be_4O_6]$ and $BaLi_2[Be_4O_6]$. Standard deviations in parentheses.

|	$SrLi_2[Be_4O_6]$	$BaLi_2[Be_4O_6]$
Bond	Bond length / Å	
Sr/Ba1–O1 (4x)	2.5945(10)	2.7749(11)
Sr/Ba1–O2 (4x)	2.8276(5)	2.8378(6)
Be1–O1 (1x)	1.607(2)	1.633(3)
Be1–O2 (1x)	1.608(2)	1.617(2)
Be1–O1 (1x)	1.646(2)	1.650(2)
Be1–O1 (1x)	1.673(2)	1.704(3)
Li1–O2 (2x)	2.017(3)	1.985(3)
Li1–O1 (2x)	2.0802(14)	2.0527(15)
Li1–O2 (1x)	2.242(4)	2.365(5)
Li1–Li1 (1x)	2.427(8)	2.399(9)
Angle	Angle / °	
O1-Sr/Ba1-O1 (4x)	63.08(2)	60.27(2)
O1-Sr/Ba1-O1 (2x)	95.43(4)	90.47(4)
O1-Sr/Ba1-O2 (4x)	154.76(2)	148.68(2)
O1-Sr/Ba1-O2 (4x)	105.98(3)	102.74(3)
O2-Sr/Ba1-O2 (4x)	84.782(3)	86.794(2)
O2-Sr/Ba1-O2 (2x)	144.895(12)	152.642(9)
O2-Be1-O1	110.35(11)	107.73(12)
O2-Be1-O1	113.54(12)	114.42(13)
O1-Be1-O1	115.86(12)	117.16(12)
O2-Be1-O1	109.66(12)	109.21(14)
O1-Be1-O1	111.68(13)	113.19(15)
O1-Be1-O1	94.76(10)	94.56(10)
O2-Li1-O2	106.0(2)	105.6(2)
O2-Li1-O1 (2x)	116.69(7)	117.57(8)
O2-Li1-O1 (2x)	80.18(4)	81.10(5)
O1-Li1-O1	153.2(2)	150.5(2)
O2-Li1-O2 (2x)	126.98(10)	127.18(10)
O1-Li1-O2 (2x)	76.60(11)	75.23(12)
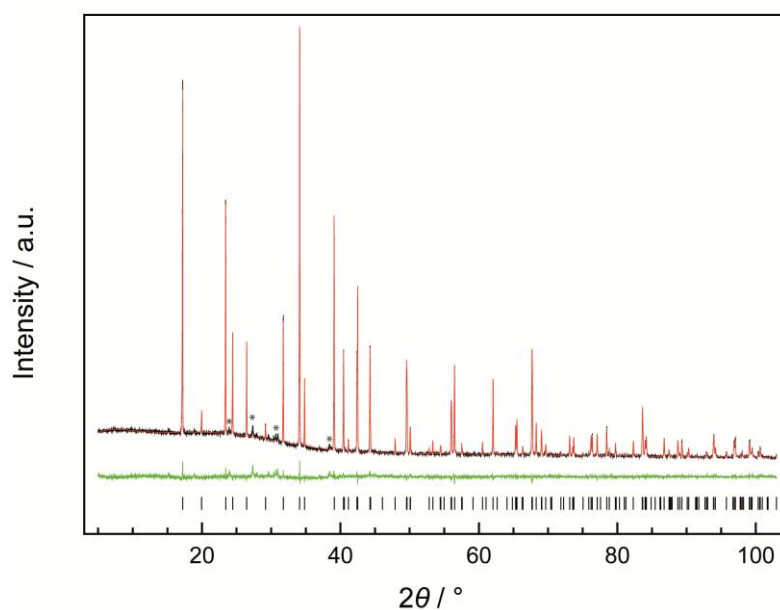
Figure S2. Crystal structure characterization of ultra-narrow band blue emitting AELi$_2$[Be$_4$O$_6$]:Eu^{2+} (AE = Sr, Ba). X-ray powder diffractogram (Cu Kα_1 radiation) of BLBO with the measured data (black line), calculated pattern based on Rietveld refinement data (red line), difference curve (green line), and tick marks (black) that give positions of Bragg reflections of BLBO; unknown side-phases are marked with asterisks.

MAPLE Calculations

Table S5. Results of MAPLE calculations [kJ/mol] for SrLi$_2$[Be$_4$O$_6$]; Δ = MAPLE sum of constituting binary/ternary nitrides / MAPLE sum compound.

	SrLi$_2$[Be$_4$O$_6$]
Sr^{2+}	1594
Li$^+$	641
Be^{2+}	2920
O^{2-}	2445–2527
Total	**29600**
Δ	**0.7%**
Total MAPLE: Li$_2$O + SrBe$_3$O$_4$ + BeO = 29795 kJ/mol	

The deviation $\Delta = 0.7\%$ can be explained by the change of the coordination of Be. While Be is in trigonal planar coordination in $SrBe_3O_4$, it is tetrahedrally coordinated in $SrLi_2[Be_4O_6]$, leading to an increased deviation. This can be seen when applying the MAPLE concept for $SrBe_3O_4$. The partial MAPLE value for the trigonal planar coordinated Be yields decreased values (2880 kJ/mol) when compared to tetrahedrally coordinated (O^{2-} ligands) Be (2980 kJ/mol).

UV/Vis Spectroscopy

UV/Vis reflectance data were obtained to investigate the optical band gap of $AELi_2[Be_4O_6]:Eu^{2+}$ (AE = Sr, Ba). Reflectance spectra of Eu^{2+} doped and undoped powder samples were obtained with an Edinburgh Photonics FLS920-s spectrometer equipped with a 450 W Xe900 arc lamp (single photon-photomultiplier detector, Czerny-Turner monochromator with triple grating turret). The spectra were measured in the wavelength range from 230 nm to 780 nm (5 nm step size).
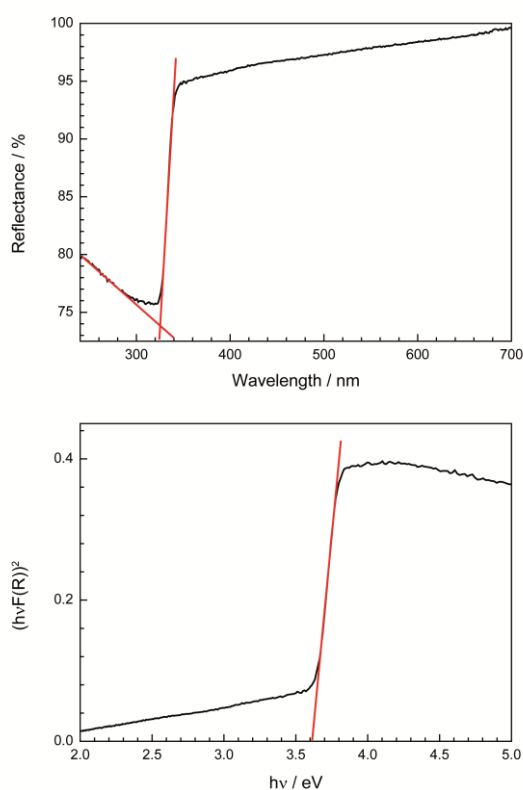

Figure S3. Top: Reflectance spectrum of undoped $BaLi_2[Be_4O_6]$. Bottom: Tauc plot (n = 1/2) for $BaLi_2[Be_4O_6]$. The band gap is estimated with both methods and is found in a range from 3.6–3.8 eV.

Temperature dependent luminescence

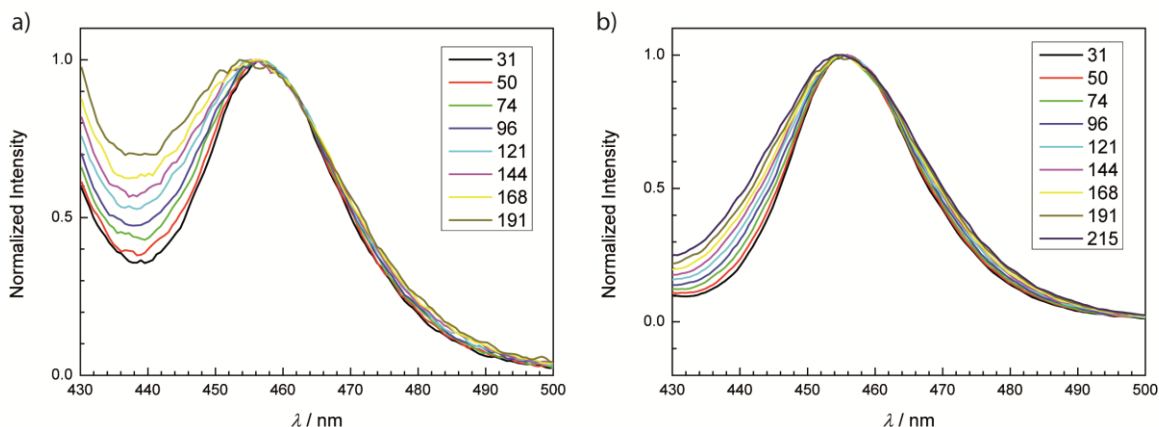**Figure S4.** Temperature dependent luminescence spectra of (a) $SrLi_2[Be_4O_6]$:Eu^{2+} and (b) $BaLi_2[Be_4O_6]$:Eu^{2+}. At increased temperatures, resulting in decreased emission intensity, spectra are additionally broadened by excitation light. This effect is strong especially for $SrLi_2[Be_4O_6]$:Eu^{2+}. The data are obtained at the temperatures (in °C) given in the inset.

References

[1]   Harris, R. K.; Becker, E. D.; Cabral de Menezes, S. M.; Goodfellow, R.; Granger, P. NMR nomenclature: nuclear spin properties and conventions for chemical shifts. IUPAC Recommendations 2001. International Union of Pure and Applied Chemistry. Physical Chemistry Division. Commission on Molecular Structure and Spectroscopy. *Magn. Reson. Chem.* **2002**, *40*, 489–505.

[2]   BrukerAXS, *APEX3 v2016.5-0*: Billerica, 2016.

[3]   Sheldrick, G. M. *SHELXS-97: A Program for Crystal Structure Solution*; University of Göttingen: Göttingen, Germany, 1997.

[4]   Sheldrick, G. M. A short history of SHELX. *Acta Crystallogr., Sect. A: Found. Crystallogr.* **2008**, *64*, 112–122.

[5]   Sheldrick, G. M. *SHELXL-97: A Program for Crystal Structure Refinement*; University of Göttingen: Göttingen, Germany, 1997.

[6]   Coelho, A. A. *TOPAS, v. 4.1: A program for Rietveld refinement*; Coelho Software: Brisbane, Australia, 2007.

12 Publications

12.1 List of Publications within this Thesis

1. Unprecedented Deep-Red Ce^{3+} Luminescence of the Nitridolithosilicates Li$_{38.7}$*RE*$_{3.3}$Ca$_{5.7}$[Li$_2$Si$_{30}$N$_{59}$]O$_2$F (*RE* = La, Ce, Y)

Christian Maak, Philipp Strobel, Volker Weiler, Peter J. Schmidt, and Wolfgang Schnick

Chem. Mater. **2018**, *30*, 5500–5506

For this contribution, sample syntheses, structure determination based on single-crystal and powder X-ray diffraction data, elemental analysis, lattice energy calculations, measurement of diffuse reflectance data, literature screening, image preparation, and writing of the main part of the manuscript was performed by Christian Maak, supported by Philipp Strobel. Luminescence investigations were done at the LPC Aachen, supported by Volker Weiler and Peter Schmidt. Interpretation of measured spectra and values was done by Christian Maak, Volker Weiler, and Peter J. Schmidt. Supervision of the research project was carried out by Wolfgang Schnick. All authors have revised the manuscript.

2. Narrow-Band Yellow-Orange Emitting La$_{3-x}$Ca$_{1.5x}$Si$_6$N$_{11}$:Eu^{2+} (*x* ≈ 0.77): A Promising Phosphor for Next-Generation Amber pcLEDs

Christian Maak, Dajana Durach, Christoph Martiny, Peter J. Schmidt, and Wolfgang Schnick

Chem. Mater. **2018**, *30*, 3552–3558

For this contribution, conceptualization and literature screening were conducted by Christian Maak and Dajana Durach. Writing the main part of the manuscript, image preparation, sample syntheses, elemental analysis, structure determination based on single-crystal X-ray diffraction data, and Rietveld refinement was performed by Christian Maak. Luminescence investigations were done at the LPC Aachen, supported by Christoph Martiny and Peter Schmidt. Interpretation of measured values was carried out by Christian Maak, Christoph Martiny, and Peter J. Schmidt.

Supervision of the research project was carried out by Wolfgang Schnick. All authors have revised the manuscript.

3.   Efficient Yellow-Orange Phosphor Lu$_4$Ba$_2$[Si$_9$ON$_{16}$]O:Eu^{2+} and Orange-Red Emitting Y$_4$Ba$_2$[Si$_9$ON$_{16}$]O:Eu^{2+}: Two Oxonitridosilicate Oxides with Outstanding Structural Variety

Christian Maak, Robin Niklaus, Franziska Friedrich, Andre Mähringer, Peter J. Schmidt, and Wolfgang Schnick

Chem. Mater. **2017**, *29*, 8377–8384

For this contribution, sample syntheses, elemental analysis, structure elucidation from single-crystal X-ray diffraction data, and Rietveld refinements were carried out by Christian Maak supported by Franziska Friedrich and Andre Mähringer. Literature screening, image preparation, and writing the main part of the manuscript was performed by Christian Maak. DFT calculations were performed by Robin Niklaus. Luminescence investigations were done at the LPC Aachen, supported by Peter Schmidt. Interpretation of luminescence properties was carried out by Christian Maak and Peter J. Schmidt. Supervision of the research project was carried out by Wolfgang Schnick. All authors have revised the manuscript.

4.   *RE*$_4$Ba$_2$[Si$_{12}$O$_2$N$_{16}$C$_3$]:Eu^{2+} (*RE* = Lu,   Y):   Green-Yellow   Emitting Oxonitridocarbidosilicates with a Highly Condensed Network Structure Unraveled through Synchrotron Microdiffraction

Christian Maak, Lucien Eisenburger, Jonathan P. Wright, Markus Nentwig, Peter J. Schmidt, Oliver Oeckler, and Wolfgang Schnick

Inorg. Chem. **2018**, *57*, 13840–13846

For this contribution, literature research, writing of the main part of the manuscript, sample preparation, Rietveld refinements, lattice energy calculations, and band gap determination was carried out by Christian Maak. Elemental analysis and preparation of graphical material was performed by Christian Maak and Lucien Eisenburger. TEM investigations were carried out by Lucien Eisenburger under the supervision of Oliver Oeckler. Single-crystal X-ray diffraction data were collected by Jonathan P. Wright, supported by Lucien Eisenburger, Markus Nentwig and Oliver

Oeckler. Diffraction data reduction was performed by Markus Nentwig under the supervision of Oliver Oeckler. The crystal structure elucidation was conducted by Oliver Oeckler. Luminescence investigations were done at the LPC Aachen, supported by Peter Schmidt. Interpretation of measured values was carried out by Christian Maak and Peter J. Schmidt. Supervision of the research project was carried out by Oliver Oeckler and Wolfgang Schnick. All authors have revised the manuscript.

5.   Oxonitridosilicate Oxides $RE_{26}Ba_6[Si_{22}O_{19}N_{36}]O_{16}$:Eu^{2+} ($RE$ = Y, Tb) with a Unique Layered Structure and Orange-Red Luminescence for RE = Y

Christian Maak, Constantin Hoch, Peter J. Schmidt, and Wolfgang Schnick

Inorg. Chem. **2018**, *57*, 2242–2248

For this contribution, sample syntheses, elemental analysis, band gap determination, literature screening, image preparation, and writing of the main part of the manuscript was performed by Christian Maak. The structure determination based on single-crystal and powder X-ray diffraction data was conducted by Christian Maak, supported by Constantin Hoch. Luminescence investigations were done at the LPC Aachen, supported by Peter J. Schmidt. Interpretation of measured spectra and values was done by Christian Maak and Peter J. Schmidt. Supervision of the research project was carried out by Wolfgang Schnick. All authors have revised the manuscript.

6. $Y_{23}Sr_{17}[Si_{38}O_{18}N_{67}]O_9$ – An Oxonitridosilicate Oxide with a Unique Layered Structure

Christian Maak, Robin Niklaus, Oliver Oeckler, and Wolfgang Schnick

Z. Anorg. Allg. Chem. **2019**, *645*, 182–187

For this publication, sample syntheses, powder X-ray diffraction analyses, Rietveld refinement, elemental analysis, lattice energy calculations, diffuse reflectance spectroscopy, writing the main part of the manuscript, image preparation, and literature research was performed by Christian Maak. The crystal structure determination from single-crystal X-ray diffraction data was conducted by Christian Maak, supported by Oliver Oeckler. DFT calculations were carried out by Robin

Niklaus. Supervision of the research project was carried out by Wolfgang Schnick. All authors have revised the manuscript.

7.   Ultra-Narrow-Band Blue-Emitting Oxoberyllates *AE*Li$_2$[Be$_4$O$_6$]:Eu^{2+} (*AE* = Sr, Ba) paving the Way to Efficient RGB pc-LEDs

Philipp Strobel, Christian Maak, Volker Weiler, Peter J. Schmidt, and Wolfgang Schnick

Angew. Chem., Int. Ed. **2018**, *57*, 8739–8743; *Angew. Chem.* **2018**, *130*, 8875–8879

For this contribution, writing the manuscript main part, sample syntheses, structure determination based on single-crystal X-ray diffraction data, elemental analysis and image preparation was performed by Philipp Strobel, supported by Christian Maak. Luminescence investigations were done at the LPC Aachen, supported by Volker Weiler and Peter J. Schmidt. Interpretation of measured values was done by Philipp Strobel, Volker Weiler, and Peter J. Schmidt. Supervision of the research project was carried out by Wolfgang Schnick. All authors have revised the manuscript.

12.2 Other Publications

1. **Ammonothermal Synthesis, Optical Properties, and DFT Calculations of Mg$_2$PN$_3$ and Zn$_2$PN$_3$**
    Mathias Mallmann, Christian Maak, Robin Niklaus, and Wolfgang Schnick
    Chem. - Eur. J. **2018**, *24*, 13963–13970

2. **Framework Structures of Interconnected Layers in Calcium Iron Arsenides**
    Tobias Stürzer, Christine Hieke, Catrin Löhnert, Fabian Nitsche, Juliane Stahl, Christian Maak, Roman Pobel, and Dirk Johrendt
    Inorg. Chem. **2014**, *53*, 6235–6240

3. **New Polymorph of the Highly Efficient LED-Phosphor SrSi$_2$O$_2$N$_2$:Eu^{2+} – Polytypism of a Layered Oxonitridosilicate**
    Markus Seibald, Tobias Rosenthal, Oliver Oeckler, Christian Maak, Andreas Tücks, Peter J. Schmidt, Detlef Wiechert, and Wolfgang Schnick
    Chem. Mater. **2013**, *25*, 1852–1857

12.3 Conference Contributions

1. **La$_{3-x}$Ca$_{1.5x}$Si$_6$N$_{11}$:Eu^{2+} – Ein Nitridosilicat mit schmalbandiger Lumineszenz (talk)**
Christian Maak, and Wolfgang Schnick
4. Obergurgl-Seminar Festkörperchemie, January 29 – February 1, 2019.

2. **Crystal Structure and Luminescence of Li$_{38.7}$*RE*$_{3.3}$Ca$_{5.7}$[Li$_2$Si$_{30}$N$_{59}$]O$_2$F:Ce^{3+} (*RE* = Y, La) and Li$_{38.7}$Ce$_{3.3}$Ca$_{5.7}$[Li$_2$Si$_{30}$N$_{59}$]O$_2$F (talk)**
Christian Maak, and Wolfgang Schnick
3. Obergurgl-Seminar Festkörperchemie, January 23–26, 2018.

3. **Y$_{26}$Ba$_6$[Si$_{22}$O$_{19}$N$_{36}$]O$_{16}$:Eu^{2+} – An Orange-Red Emitting Oxonitridosilicate Oxide with a Unique Layered Structure (poster)**
Christian Maak, Constantin Hoch, Peter J. Schmidt, and Wolfgang Schnick
European Conference on Solid State Chemistry, Glasgow (UK), July 23–26, 2017.

4. **Y$_{23}$Sr$_{17}$[Si$_{38}$O$_{18}$N$_{67}$]O$_9$ – A Layered Oxonitridosilicate Oxide (talk)**
Christian Maak, and Wolfgang Schnick
2. Obergurgl-Seminar Festkörperchemie, January 26–29, 2017.

5. **Crystal Structure and Luminescence Properties of the novel Oxonitridosilicate Oxide Y$_4$Ba$_2$[Si$_9$ON$_{16}$]O (poster)**
Franziska Friedrich, Christian Maak, and Wolfgang Schnick
Undergraduate Research Conference on Molecular Sciences (URCUP), Kloster Irsee (Germany), July 2–3, 2016.

6. **Absence of superconductivity in metastable Ca$_{1-x}$Pr$_x$Fe$_2$As$_2$ (*x* = 0–1) synthesized under high pressure conditions (poster)**
Roman Pobel, Katharina Strobl, Christian Maak, and Dirk Johrendt
European Conference on Solid State Chemistry, Vienna (Austria), August 23–26, 2015.

12.4 Deposited Crystallographic Data

Crystallographic Information Files (CIF) of the investigated compounds were deposited at the Fachinformationszentrum (FIZ) Karlsruhe, 76344 Eggenstein-Leopoldshafen, Germany (fax: +49-7247-808-666, e-mail: crysdata@fizkarlsruhe.de) or at the Cambridge Crystallographic Data Centre (CCDC), CB2 1EZ Cambridge, United Kingdom, and are available on quoting the following CSD/CCDC depository numbers.

Compound	CSD/CCDC-Number
$Li_{38.7}Y_{3.3}Ca_{5.7}[Li_2Si_{30}N_{59}]O_2F$	CCDC-1840986
$Li_{38.7}Ce_{3.3}Ca_{5.7}[Li_2Si_{30}N_{59}]O_2F$	CCDC-1840987
$Li_{38.7}La_{3.3}Ca_{5.7}[Li_2Si_{30}N_{59}]O_2F$	CCDC-1840988
$La_{2.23}Ca_{1.16}Si_6N_{11}$	CCDC-1821482
$Y_4Ba_2[Si_9ON_{16}]O$	CSD-433302
$Lu_4Ba_2[Si_9ON_{16}]O$	CSD-433303
$Lu_4Ba_2[Si_{12}O_2N_{16}C_3]$	CSD-1860785
$Y_{26}Ba_6[Si_{22}O_{19}N_{36}]O_{16}$	CCDC-1812427
$Tb_{26}Ba_6[Si_{22}O_{19}N_{36}]O_{16}$	CCDC-1812428
$Y_{23}Sr_{17}[Si_{38}O_{18}N_{67}]O_9$	CSD-434652
$BaLi_2[Be_4O_6]$	CSD-434376
$SrLi_2[Be_4O_6]$	CSD-434377